

ION IMPLANTATION AND CHEMICAL MODIFICATION OF CuO NANOPARTICLES AND THEIR ELECTROCHEMICAL APPLICATIONS

Ph.D. THESIS

by

Umesh Chandra Bind



**CENTRE OF NANOTECHNOLOGY
INDIAN INSTITUTE OF TECHNOLOGY ROORKEE
ROORKEE - 247667 (INDIA)
JULY, 2018**

ION IMPLANTATION AND CHEMICAL MODIFICATION OF CuO NANOPARTICLES AND THEIR ELECTROCHEMICAL APPLICATIONS

A THESIS

*Submitted in partial fulfilment of the
requirements for the award of the degree*

of

DOCTOR OF PHILOSOPHY

in

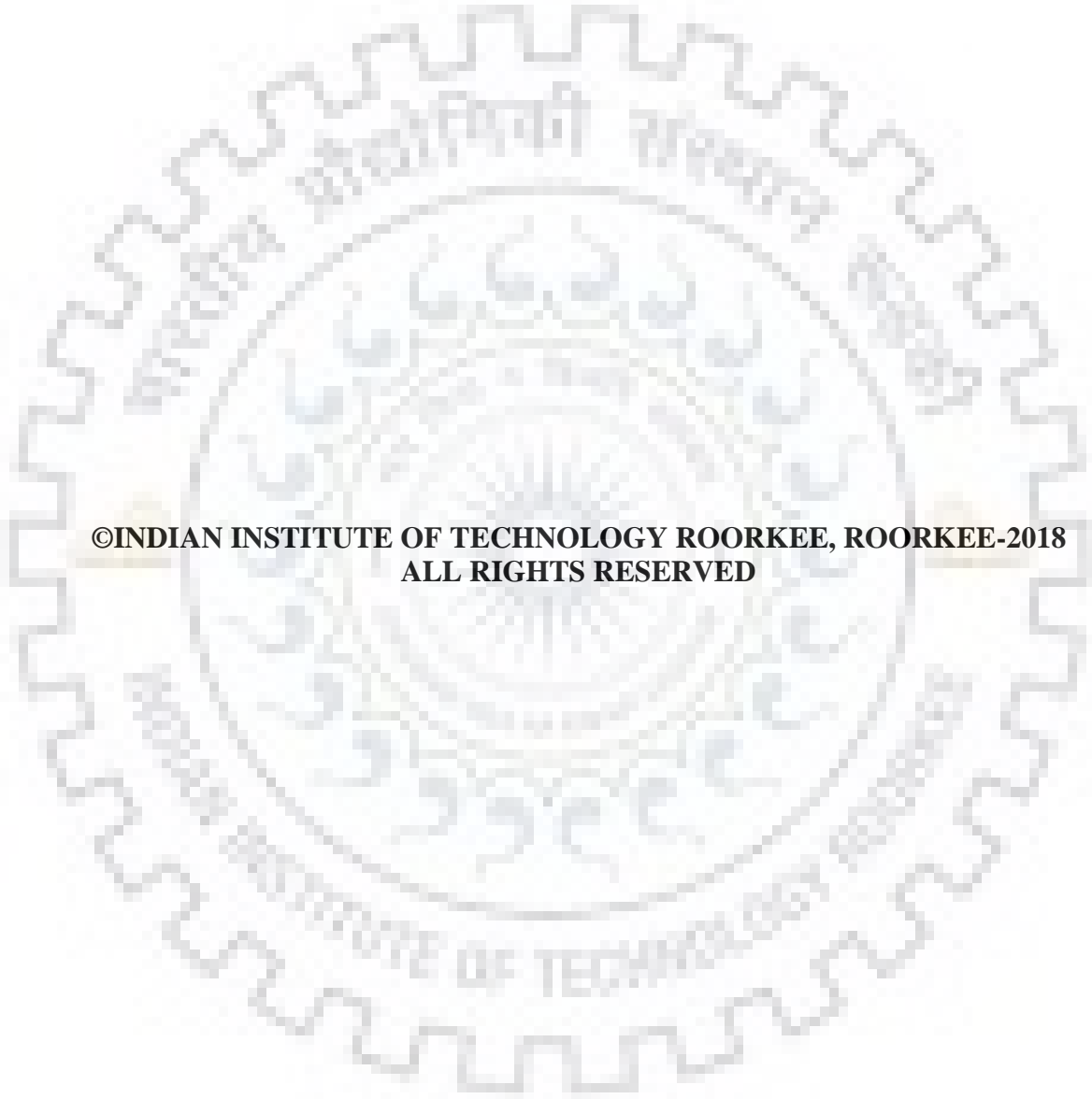
NANOTECHNOLOGY

by

UMESH CHANDRA BIND



**CENTRE OF NANOTECHNOLOGY
INDIAN INSTITUTE OF TECHNOLOGY ROORKEE
ROORKEE – 247667 (INDIA)
JULY, 2018**



**©INDIAN INSTITUTE OF TECHNOLOGY ROORKEE, ROORKEE-2018
ALL RIGHTS RESERVED**



INDIAN INSTITUTE OF TECHNOLOGY ROORKEE ROORKEE

CANDIDATE'S DECLARATION

I hereby certify that the work which is being presented in the thesis entitled “**ION IMPLANTATION AND CHEMICAL MODIFICATION OF CuO NANOPARTICLES AND THEIR ELECTROCHEMICAL APPLICATIONS**” in partial fulfilment of the requirements for the award of Degree of Doctor of Philosophy and submitted in the Centre of Nanotechnology of the Indian Institute of Technology Roorkee, Roorkee is an authentic record of my own work carried out during a period from January 2013 to July 2018 under the supervision of Dr. R.K. Dutta, Associate Professor, Department of Chemistry and Head, Centre of Nanotechnology, Indian Institute of Technology Roorkee, Roorkee.

The matter presented in the thesis has not been submitted by me for the award of any other degree of this or any other Institution.

(**Umesh Chandra Bind**)

This is to certify that above statement made by the candidate is correct to the best of my knowledge.

(**R.K. Dutta**)
Supervisor

The Ph. D. Viva-Voce Examination of **Mr. Umesh Chandra Bind**, Research Scholar, has been held on 28.12.2018.

Chairman, SRC

Signature of External Examiner

This is to certify that the student has made all the corrections in the thesis.

Signature of Supervisor

Head of Centre

ABSTRACT

Metal oxide nanoparticles (NPs) are finding wide range of applications in all the major domains of science and technology, e.g. energy, environment, catalysis, sensors and magnetism. Metal oxides for energy applications are further classified into different categories, viz. as fuel cells, solar cells, batteries, photoelectrochemical cells and as supercapacitors to meet the future energy demands. In view of these metal oxides, particularly ruthenium oxide exhibited very good supercapacitor behavior. Furthermore modification of these metal oxides revealed improved supercapacitor behavior. Owing to high cost of the ruthenium precursors alternate metal oxides are being explored. The variable valency of manganese led to development of manganese oxide as supercapacitors. Though copper also exhibit variable valency, but CuO and its nanoparticles are not widely studied as supercapacitor. This thesis work is therefore focused on the studies of modified CuO NPs to establish it as supercapacitor.

The thesis comprises of FIVE chapters. The **Chapter 1** consists of general introduction about different types of modified metal oxide nanoparticles and their applications. The focus has been on CuO NPs as it is known to exhibit excellent conductivity and has tremendous potential to be a supercapacitor and electrochemical sensor. The basic concepts involved in electrochemical properties for glucose sensing and supercapacitor behaviors are discussed. A brief literature survey on CuO NPs as electrocatalytic sensor and as supercapacitor is discussed. The importance of modifying the surface and lattice environment of metal oxide has been outlined in the context of their electrochemical properties. The focus has been on modification by irradiating metal oxides with low energy (keV) ion beams and by suitable capping and doping. From these discussions, the aim and scope of present thesis work is identified and the research objectives are outlined.

The **Chapter 2** deals with the effect of low ion implantation of 50 keV N^{5+} on copper oxide thin films. Pulsed laser deposition technique was used with different partial pressure of oxygen for preparing batches of copper oxide thin films on glass substrates kept at 350 °C. The N^{5+} ion beams of particle fluences of 2.5×10^{15} , 1.0×10^{16} and 4×10^{16} were used. The as-deposited thin films were characterized by X-ray diffraction (XRD), field emission scanning electron microscopy (FE-SEM) and atomic force microscopy (AFM). Their optical properties were studied by measuring the transmittance spectra in the UV-Vis-NIR region and the band gap of the materials were determined from Tauc's plot using diffused reflectance spectroscopy (DRS) data. The as-deposited copper oxide thin film corresponding to 80 mTorr partial pressure of oxygen was transformed to single Cu_2O phase of crystallite size 20.2 nm when implanted at 1.0×10^{16} particles/cm². On the other hand the film deposited at 100 mTorr partial pressure of oxygen resulted in formation of mixed Cu_2O and CuO phases. Interestingly, this film upon implantation with 2.5×10^{15} particles/cm² resulted in conversion to a single Cu_2O phase with enhanced crystallinity and larger crystallite size (23.5 nm). The phase transformation is attributable to thermal effect due to stopping of incident beam. Implantation with higher particle fluence led to transformation to CuO phase with decrease in crystallinity and increase in electrical conductivity.

Chapter 3 deals with synthesis, characterization and electrochemical applications of CuO NPs. Different capping agents e.g., triphenylphosphine oxide (TPPO), Mercaptoacetic acid (MAA), Triton X-100, polyvinyl alcohol (PVA) and polyvinylpyrrolidone (PVP) were used for preparing respective batches of capped CuO NPs by precipitation method. These as-synthesized batches of capped CuO NPs were characterized by XRD that revealed monoclinic phase with crystallite size in the range of 7.1 nm to 11.4 nm. The FE-SEM and TEM images

revealed cluster of nanoparticles of sizes similar to crystallite sizes. The photoluminescence studies revealed more defects in MAA capped and PVP capped CuO NPs as compared to rest batches of capped CuO NPs. All these batches of capped CuO NPs were investigated by cyclic voltammetry (CV), galvanostatic charge-discharge (GCD) and electrochemical impedance spectroscopy (EIS) studies. The CV plot was quasi-rectangular in shape and the specific capacitance was high (i.e., 94 F/g and 103 F/g) for TPPO capped and MAA capped CuO NPs at the scan rate of 5 mV/s. The CV studies revealed involvement of both electric double layer capacitance (EDLC) and pseudocapacitance (PC) characters. The supercapacitor behavior of the capped CuO NPs was studied by recording potential vs. time plot at different current densities. The conductivity of CuO NPs and electrolyte ion interactions with electrode material were analyzed by EIS spectrum. However, the cyclic stability of the TPPO capped CuO NPs (highest specific capacitance) was poor. Because of this, the capped CuO NPs were calcined at 450 °C for 3 hours. All the electrochemical studies were repeated. The specific capacitance for calcined TPPO capped CuO NPs was 125 F/g at the current density of 0.2 A/g and its capacitance retention was significantly improved to 102%. Better specific capacitance for TPPO capped CuO NPs was attributed to lesser defects which are likely to be the charge tapping sites. The supercapacitor behavior was mostly due to pseudocapacitance character which is attributed to faradic process. Hence these capped CuO NPs were used as anode for electrochemical sensing of glucose. The limits of detection for calcined TPPO capped and MAA capped CuO NPs were 0.04 μM and 0.33 μM , respectively. Their linear detection range were 9 μM to 4.2 μM (for MAA capped) and 9 μM to 3.2 μM (for TPPO capped). The batches of calcined MAA capped and TPPO capped CuO NPs were for glucose determination in human blood and urine samples.

Chapter 4 deals with synthesis, characterization and supercapacitor behavior of increasing concentration of selenium doped (Se-doped) in CuO NPs. The exact concentrations of doped selenium in different batches were determined by inductive coupled plasma optical emission spectroscopy (ICP-OES). The XRD measurements revealed formation of monoclinic phase of CuO with minor shift in the 2θ value due to lattice modification by Se species. The FE-SEM and TEM studies confirmed morphology and size distribution of the nanoparticles. All the batches of Se-doped CuO NPs were investigated for supercapacitor behavior by recording CV, GCD and EIS spectra. The batch corresponding to 0.45 wt% Se-doped CuO NPs revealed maximum specific capacitance of 140 F/g at current density of 0.2 A/g. However the capacitance retention after 500 cycles was poor. For this reason, as-synthesized Se-doped CuO NPs were calcined at 450 °C and were further characterized and investigated as supercapacitor. The supercapacitor behavior was mostly due to pseudocapacitance character. Furthermore, the supercapacitor behavior of the calcined 0.45 wt% Se-doped CuO NPs was studied for its performance at elevated cell temperature, i.e., in the range of 25 °C to 75 °C. The CV plots reflected the role of pseudocapacitance behavior due to faradic processes. The stability studies at respective cell temperature were performed for 500 cycles at 3 A/g. The capacitance retention after 500 cycles was 98% for cell temperature upto 55 °C.

Chapter 5 deals with synthesis, characterization and supercapacitor studies of different batches of cobalt doped (Co-doped) CuO NPs. The exact concentrations of doped cobalt were determined by ICP-OES. The as-synthesized batches of Co-doped CuO NPs were characterized by XRD, FE-SEM, TEM, BET surface area. The photoluminescence spectroscopy study revealed the vacancy based defects due to Co-doping. Similarly, supercapacitor behaviors of these Co-doped CuO NPs were studied from CV, GCD, EIS spectra. The best result was

obtained for 5.77 wt% Co-doped CuO NPs which corresponded to 160 F/g specific capacitance at current density of 0.2 A/g. However due to poor cyclic stability, this batch of Co-doped CuO NPs was calcined at 450 °C and was studied for supercapacitor behavior. As expected, the calcined batch of Co-doped CuO NPs revealed high specific capacitance (140 F/g) and high capacitance retention of 92-95%. Such high specific capacitance and excellent capacitance retention are so far better specifications than those available in literature. For this reason, the batches of calcined 5.77 wt% Co-doped CuO NPs was used for fabricating a symmetric solid state supercapacitor and successfully tested between a working potential window of 0 and 2.0 V. The energy density was determined as 5.2 Wh/kg at a current density of 0.2 A/g. This is an encouraging result for optimizing Co-doped CuO NPs for real time application as supercapacitor.

This thesis work has been concluded by summarizing the salient features of modification of CuO NPs and their impact towards electrochemical applications e.g., as glucose sensing and as supercapacitor.



ACKNOWLEDGEMENTS

At the outset, I wish to express my deepest sense of gratitude and reverence to my mentor and supervisor **Dr. R.K. Dutta** present Head of Centre of Nanotechnology for introducing me to this present area of research. His invaluable and meticulous guidance with lots of constructive criticisms have served as a vital source of inspiration for bringing the present work in the final shape. His affectionate treatment and magnanimity made it feasible to bring the present work to conclusion.

I also take this opportunity to express my sincere thanks to **Prof. V. Agarwala**, **Prof. R. Jayagathan** and **Prof. S.K. Nath** previous Heads of the Centre of Nanotechnology for extending all the necessary research facilities. I express my special thanks to my Research Committee members **Prof. R.P. Singh**, **Prof. Anirban Mitra**, **Prof. Rajdeep Chatterjee**, and **Prof. B.S.S Daniel** for taking time out of their schedules to advise me on my dissertation. I feel privileged to express unfeigned thanks to **Prof. M.R. Maurya**, Head of Department of Chemistry, for extending the department's research facilities. I am also thankful to the staff of the Centre of Nanotechnology and Department of Chemistry for providing countless assistance over these years. I express my sincere gratitude to **Prof. A.K. Sen**, Head of the Institute Instrumentation Centre of IIT Roorkee for their assistance in using experimental facility.

Further, I am extremely grateful to **Dr. J.B.M. Krishna**, **Dr. P.Y. Nabhiraj**, **Dr. Ranjini Menon**, and staff of VECC Kolkata and UGC DAE CSR Kolkata centre for their keen interest in this work. I would also like to extend special thanks to **Prof. K.L. Yadav**, Head of the Department of Physics for guidance and providing the thin film fabrication facility.

It goes without saying that the contribution of friends matters a lot in according such arduous tasks. I express my sincere thanks and regards to my friends especially Shashank Shekhar, Manoj Kumar Yadav, Kirandeep Singh and Shiv Kumar for their kind help and motivation round the clock. I convey my heartfelt thanks to all my colleagues, especially, Bhawani, Ambika, Swati, Soumita, Aarti, Subhashish, Azfar, Dipika, Atika and Gandharv without who's uncompromising and relentless cooperation, this work would not have seen the light of the day in its truest sense.

Further, I would like to thank the Almighty, without Him I could do nothing. I want to express my heartfelt gratitude to my parents for their endless love, blessings, support and for always being with me. I also appreciate the love and support from my brother Guru Sharan Bind, Satya Dev Bind, Devdutt Bind, Devanand Bind, Lal Bahadur Bind and lovely Sisters Meera Bind, Kamala Bind, Dev Shree Bind along with cute daughter Anusha Bind, who constantly inspired me to achieve this hallmark.

All the words not sum up the pain and hardship that my father **R.D. Bind** and mother **Shashi Kala Devi** along with my uncle **Ram Shish Kashyap** had to face in my accent for this achievement. Their sacrifice and love has been the guiding principles of my life. Despite the agony and inconvenience, they provided me everything throughout my academics. Their unlimited faith and confidence has made me whatever I am today. Their blessings are the great kinetic force which always lighted my path towards success. In last very special thanks to PITAJI.

I would like to acknowledge Ministry of Human Resource and Development (MHRD) India for awarding me fellowship for carrying out my research work at IIT Roorkee.

(Umesh Chandra Bind)

CONTENTS

	Page no.
Candidate's Declaration	
Abstract	i
Acknowledgement	vii
Contents	ix
List of Figures	xv
List of Tables	xxv
Abbreviations	xxvii
List of Publication	xxix
CHAPTER 1 GENERAL INTRODUCTION	
1.1 General introduction	1
1.2 Modification of metal oxide nanoparticles	1
1.3 Working principle of supercapacitors	4
1.4 Working principle of non-enzymatic glucose sensing	5
1.5 Modified metal oxide nanostructures for supercapacitors	6
1.6 Modification in copper oxide nanoparticles	11
1.7 Modification of CuO by physical and chemical methods	19
1.7.1 Ion implantation modifications in copper oxide nanoparticles	19
1.7.2 Capping assisted modifications in copper oxide nanoparticles	20
1.7.2.1 CuO nanoparticles for sensing	22
1.7.3 Doping resulted modifications in copper oxide nanoparticles	23
1.8 Aim and scope of this thesis work	32
CHAPTER 2 ION IMPLANTATION OF COPPER OXIDE NPs	
2.1 Introduction	35
2.2 Experimental	38
2.2.1 Preparation of copper oxide thin film	38
2.2.2 Low energy N^{5+} ion implantation	38
2.2.3 Structural, surface and optical analyses	38

2.3	Results and Discussion	39
2.3.1	Structural study of pristine and ion implanted thin films	39
2.3.2	Surface morphology	44
2.3.3	Optical properties	47
2.3.4	Electrical properties	50
2.4	Conclusions	51

CHAPTER 3 SYNTHESIS OF CAPPED CUO NPS AND THEIR ELECTROCHEMICAL APPLICATIONS

3.1	Introduction	53
3.2	Materials and methods	54
3.2.1	Chemicals	54
3.2.2	Synthesis of capped CuO NPs	56
3.2.4	Sample preparation for TEM measurement	56
3.2.5	Characterization techniques	56
3.3	Result and discussion of capped CuO NPs	57
3.3.1	X-ray diffraction	57
3.3.2	Surface morphology	59
3.3.3	Fourier transformed infrared (FT-IR) spectroscopy	63
3.3.4	Optical studies	64
3.3.4.1	Diffuse reflectance spectroscopy	64
3.3.4.2	Photoluminescence studies	66
3.3.5	Surface area and pore size	67
3.3.6	Capped CuO nanoparticles as supercapacitor	68
3.3.6.1	Electrode fabrication	69
3.3.6.2	Cyclic voltammetry	70
3.3.6.3	EDLC vs. PC contributions	73
3.3.6.4	Galvanostatic charge –discharge (GCD) studies	74
3.3.6.5	Electrochemical Impedance spectroscopy	78
3.3.6.6	Cycle stability	80
3.4	Studies of calcined capped CuO NPs	81
3.5	Result and discussion of calcined capped CuO NPs	82

3.5.1 X-ray diffraction	82
3.5.2 Surface morphology	83
3.5.3 BET Surface area and pore size	85
3.5.4 Electrochemical study of calcined capped CuO NPs	85
3.5.4.1 Cyclic voltammetry studies	85
3.5.4.2 EDLC vs. PC contributions	88
3.5.4.3 Galvanostatic charge-discharge studies	89
3.5.4.4 Cyclic stability	91
3.6 Capped and calcined capped CuO NPs as glucose sensor	92
3.6.1 Effect of glucose concentration	93
3.6.2 Sensitivity	95
3.6.3 Limit of detection (LoD)	97
3.6.4 Amperometric study	98
3.6.4.1 Sensitivity	98
3.6.4.2 Selectivity	100
3.6.4.3 Real time analysis	101
3.7 Conclusions	103
CHAPTER 4 SYNTHESIS OF SE-DOPED CUO NPS AND THEIR APPLICATION AS A SUPERCAPACITOR	
4.1 Introduction	105
4.2 Materials and Methods	105
4.2.1 Chemicals	105
4.2.2 Synthesis of Se-doped CuO NPs	105
4.2.3 Characterization techniques	106
4.3 Result and discussion of Se doped CuO NPs	107
4.3.1 Analysis of Se doped CuO NPs	107
4.3.2 X-ray diffraction	107
4.3.3 Surface morphology	109
4.3.4 Optical studies	112
4.3.4.1 Diffuse reflectance spectroscopy (DRS)	113
4.3.4.2 Photoluminescence studies	114

4.3.5 Se-doped CuO NPs as supercapacitor	114
4.3.5.1 Cyclic voltammetry studies	115
4.3.5.2 EDLC vs. PC contributions	115
4.3.5.3 Galvanostatic charge–discharge (GCD) studies	119
4.3.5.4 Electrochemical Impedance spectroscopy (EIS) studies	119
4.3.5.5 Cyclic stability	121
4.4 Result and discussion of calcined Se-doped CuO NPs	123
4.4.1 X-ray diffraction	123
4.4.2 Surface morphology	124
4.4.3 Calcined Se-doped CuO NPs as supercapacitor	125
4.4.3.1 Cyclic voltammetry studies	125
4.4.3.2 Galvanostatic charge-discharge studies	126
4.4.3.3 Cyclic stability	126
4.5 Calcined Se doped CuO NPs as elevated temperature supercapacitor	127
4.5.1 Cyclic voltammetry studies	127
4.5.2 EDLC vs. PC contributions	132
4.5.3 Electrochemical impedance spectroscopy studies	134
4.5.4 Cycle stability at elevated temperature	136
4.6 Conclusion	137
CHAPTER 5 SYNTHESIS OF CO-DOPED CUO NPS AND THEIR APPLICATION AS A SUPERCAPACITOR	
5.1 Introduction	139
5.2 Materials and methods	139
5.2.1 Chemicals	139
5.2.2 Synthesis of Co-doped CuO NPs	139
5.2.3 Fabrication of symmetric solid state supercapacitor	140
5.3 Result and discussion of Co-doped CuO NPs	141
5.3.1 Analysis of Co doped CuO NPs	141
5.3.2 X-ray diffraction	141
5.3.3 Surface morphology	143
5.3.4 Optical studies	147

5.3.4.1 Diffuse reflectance spectroscopy (DRS)	147
5.3.4.2 Photoluminescence studies	148
5.3.5 Electrochemical studies of Co-doped CuO NPs	149
5.3.5.1 Cyclic voltammetry study	149
5.3.5.2 EDLC vs. PC contributions	151
5.3.5.3 Galvanostatic charge-discharge (GCD) studies	153
5.3.5.4 Electrochemical impedance spectroscopy	155
5.3.5.5 Cyclic stability	157
5.4 Characterization of calcined Co-doped CuO NPs	158
5.4.1 XRD studies	158
5.4.2 Surface morphology	159
5.4.3 Electrochemical study of calcined Co-doped CuO NPs	160
5.4.3.1 Cyclic voltammetry studies	160
5.4.3.2 Galvanostatic charge-discharge studies	161
5.4.3.3 Cyclic stability	162
5.5 Symmetric solid state supercapacitor	163
5.5.1 Cyclic voltammetry	164
5.5.2 Charge-discharge study	166
5.6 Conclusion	167
SUMMARY AND FUTURE SCOPE	169-173
REFERENCES	175-198



LIST OF FIGURES

	Page no.
Fig. 1.1 Different types of metal oxide and their modified metal oxide systems studied as supercapacitors	7
Fig. 1.2 Pie chart diagram showing distribution of various metal oxides published as supercapacitor up to 2016	10
Fig. 1.3 Pie chart showing metal oxide nanoparticles used in electrocatalytic glucose sensing.	10
Fig. 1.4 Schematic flow chart of objective	34
Fig. 2.1 Schematic illustration showing changes in the grains of thin film during post treatment.	35
Fig. 2.2 A representation of nuclear and electronic energy loss profile of the incident ion as a function of ion energy	37
Fig. 2.3 X-ray diffraction patterns of the Copper oxide thin films as-deposited and N^{5+} ion implanted at 80 mTorr oxygen partial pressure (a) pristine and (b) 1×10^{16} particles/cm ² .	40
Fig. 2.4 X ray diffraction patterns of copper oxide thin films of pristine and N^{5+} ion implanted films as deposited at 100 m Torr oxygen partial pressure (a) pristine (b) 2.5×10^{15} particles/cm ² (c) 1×10^{16} particles/cm ² and (d) 4×10^{16} particles/cm ² .	41
Fig. 2.5 A schematic representation of the events that took place during low energy ion implantation on amorphous/mixed phase copper oxide thin film and its impact on atomic level is presented. (oxygen; copper and N^{5+} ion beam)	43
Fig. 2.6 Field emission scanning electron microscopy images of pristine and implanted copper oxide thin films (a) pristine thin film as deposited at 80 mTorr oxygen partial pressure (b) 80 mTorr as deposited film implanted with fluence 1×10^{16} particles/cm ² (c) Energy dispersive X-ray analysis of copper oxide thin film (d) cross sectional view of film (e) pristine thin film as deposited at 100 mTorr oxygen partial pressure and (f) 80 mTorr as deposited film implanted with fluence 1×10^{16} particles/cm ² .	45

Fig. 2.7	Atomic force microscopy images of copper oxide thin film: as deposited at 80 mTorr oxygen partial pressure (a) pristine (b) 1×10^{16} particles/cm ² and as deposited at 100 mTorr oxygen partial (c) pristine (d) 2.5×10^{15} particles/cm ² ; (e) 1×10^{16} particles/cm ² , (f) 4.0×10^{16} particles/cm ² .	46
Fig. 2.8	Transmittance spectra of the copper oxide thin films: (a) as deposited at 80 mTorr oxygen partial pressure and ion implanted thin film with fluence 1×10^{16} particles/cm ² ; (b) as deposited at 100 mTorr oxygen partial pressure and ion implanted thin film with different particle fluence 2.5×10^{15} , 1×10^{16} , 4.0×10^{16} particles/cm ² .	48
Fig. 2.9	Diffused reflectance spectroscopy of the copper oxide thin films: (a) as deposited at 80 mTorr oxygen partial pressure and ion implanted thin film with fluence 1×10^{16} particles/cm ² ; (b) as deposited at 100 mTorr oxygen partial pressure and ion implanted thin film with different particle fluence 2.5×10^{15} , 1×10^{16} , 4.0×10^{16} particles/cm ² .	49
Fig. 2.10	$I_D - V_{DS}$ plot of pristine and ion implanted thin films comprising copper oxide phases	50
Fig. 3.1	XRD pattern corresponding to the monoclinic structure of bare, TPPO capped, MAA capped, TRX capped, PVP capped and PVA capped CuO NPs.	58
Fig. 3.2	Field Emission Scanning Electron Microscopy images of (a) Bare, (b) TPPO, (c) MAA, (d) TRX, (e) PVP, (f) PVA capped CuO NPs and their corresponding energy dispersive X-ray analysis spectrum of representative nanoparticles showing characteristic K and L X-rays and atomic% of Cu and O.	61
Fig. 3.3	Transmission Electron Microscopy images of (a) bare, (b) TPPO capped (c) MAA capped CuO NPs with their respective SAED image in the inset. High resolution images of (d) bare, (e) TPPO capped (f) MAA capped CuO NPs.	62
Fig. 3.4	High resolution scanning electron microscope images of TPPO capped CuO nanoparticles.	63

Fig. 3.5	Fourier-transform infrared (FT-IR) spectra of bare, TPPO capped, MAA capped, TRX capped, PVP capped and PVA capped CuO NPs.	64
Fig. 3.6	Tauc plot obtained from diffuse reflectance spectroscopy of bare, TPPO capped, MAA capped, TRX capped, PVP capped and PVA capped CuO NPs.	65
Fig. 3.7	Photoluminescence spectra of bare, TPPO capped, MAA capped, TRX capped, PVP capped and PVA capped CuO NPs.	67
Fig. 3.8	BET isotherm of TPPO capped CuO NPs. Inset represent pore size distribution plot.	68
Fig. 3.9	(a) Optimization of active mass of prepared CuO NPs by recording GCD plot of different total mass material on electrode at constant current density (b) photograph of fabricated electrode with CuO NPs.	69
Fig. 3.10	Cyclic voltammograms of (a) bare, (b) TPPO capped, (c) MAA capped, (d) TRX capped, (e) PVP capped, (f) PVA capped CuO NPs. (g) Cyclic voltammograms of bare and all capped CuO NPs at scan rate of 10 mV/s (h) Specific capacitance at different scan rates.	72
Fig. 3.11	(a) I/q vs. $v^{1/2}$ and (b) q vs. $v^{-1/2}$ dependence of bare and capped CuO NPs.	73
Fig. 3.12	Galvanostatic charge-discharge curves of (a) bare, (b) TPPO capped, (c) MAA capped, (d) TRX capped, (e) PVP capped, (f) PVA capped CuO NPs. and (g) Galvanostatic charge-discharge curves of bare and all capped CuO NPs at current density 0.2 A/g.	77
Fig. 3.13	(a) Electrochemical impedance spectroscopy of bare and batches of capped CuO NPs. (b) represent the zoom EIS of all sample in higher frequency range.	78
Fig. 3.14	Capacitance retention (in %) of bare (a) TPPO capped (b) and MAA capped (c) for 500 cycles of GCD at current density of 1 A/g. and EIS of samples before and after the 500 cycles inset in respective figures.	80
Fig. 3.15	XRD pattern corresponding to the monoclinic structure of bare, TPPO capped, MAA capped, TRX capped, PVP capped and PVA capped CuO NPs after calcination.	82

Fig. 3.16	Field Emission Scanning Electron Microscopy images showing morphology of (a) Bare, (b) TPPO, (c) MAA, (d) TRX, (e) PVP, (f) PVA capped CuO NPs after calcination and their corresponding energy dispersive X-ray analysis spectrum of representative nanoparticles showing characteristic K and L X-rays and atomic% of Cu and O.	84
Fig. 3.17	BET isotherm of calcined TPPO capped CuO NPs. Inset represent pore size distribution plot.	85
Fig. 3.18	Cyclic voltammograms of (a) bare, (b) TPPO capped, (c) MAA capped, (d) TRX capped, (e) PVP capped, (f) PVA capped CuO NPs. (g) Cyclic voltammograms of calcined bare and all batches of calcined capped CuO NPs at 10 mV/s scan rate. (h) Specific capacitance vs. scan rates plot.	87
Fig. 3.19	(a) $1/q$ vs. $v^{1/2}$ and (b) q vs. $v^{-1/2}$ dependence of calcined bare and calcined capped CuO NPs.	88
Fig. 3.20	Galvanostatic charge-discharge curves of (a) bare, (b) TPPO capped, (c) MAA capped, (d) TRX capped, (e) PVP capped, (f) PVA capped CuO NPs, (g) Galvanostatic charge-discharge curves of calcined bare and all batches of calcined capped CuO NPs at current density 0.2 A/g.	91
Fig. 3.21	Cycling stability test (a) calcined bare (b) calcined TPPO capped and (c) calcined MAA capped CuO NPs at current density 1 A/g. Inset shows the Nyquist impedance spectrum of samples before and after 500 cycles.	92
Fig. 3.22	CV curves of graphite sheet and, (a) bare, (b) TPPO capped, (c) MAA capped, (d) calcined bare, (e) calcined TPPO and (f) calcined MAA capped CuO NPs electrode in the presence and absence of glucose in 0.1 M NaOH solution at scan rate of 50 mV/s.	94
Fig. 3.23	The electrochemical behavior of glucose oxidation on the calcined TPPO capped CuO NPs electrode recorded in 0.1 M NaOH solution containing 1 mM glucose concentration at different scan rates ranging from 20 mV/s to 300 mV/s. Inset shows the dependence of the peak oxidation current on the square root of the scan rate.	95
Fig. 3.24	CV curves of bare, TPPO capped, MAA capped, calcined bare, calcined	96

TPPO and calcined MAA capped CuO NPs electrode recorded at scan rate of 50 mV/s in 0.1 M NaOH solution with successive addition of different concentration of glucose. Inset showing plot of change in anodic current versus potential.

- Fig. 3.25** Calibration curve of all six batches CuO NPs electrodes based on current recorded on successive addition of different amount of glucose concentration into 0.1 M NaOH solution at different oxidation potential e.g., 0.5 V for pristine, TPPO capped and MAA capped CuO NPs electrodes, 0.4 V for calcined pristine and calcined TPPO capped CuO NPs, and 0.45 V for calcined MAA capped CuO NPs. 97
- Fig. 3.26** Amperometric current responses of the all the batches of CuO NPs electrode at different oxidation potentials in 0.1 M NaOH solution with dropwise addition of 2.5 μ M, 5.0 μ M and 10.0 μ M glucose. 100
- Fig. 3.27** Amperometric current responses of glucose oxidation with interfering compounds such as starch, sucrose, H₂O₂, ascorbic acid (AA), dopamine (DA) and uric acid (UA) in 0.1 M NaOH solution. 101
- Fig. 3.28** Amperometric current response of blood sample over calcined TPPO capped CuO NPs electrode (a) and urine sample (b) over calcined MAA capped CuO NPs electrode in 0.1 M NaOH solution. 102
- Fig. 3.29** CV curves of blood samples (a) over the calcined TPPO capped CuO NPs electrode and urine (b) over the calcined MAA capped CuO NPs electrode in 0.1 M NaOH solution at scan rate of 50 mV/s. 102
- Fig. 3.30** CV curves showing re-usability of calcined TPPO capped CuO NPs electrode for glucose determination in urine samples. 105
- Fig. 4.1** (a) XRD pattern corresponding to the monoclinic structure of pristine and Se doped CuO NPs, (b) Zoom XRD of Se doped CuO NPs 108
- Fig. 4.2** Field Emission Scanning Electron Microscopy images of (a) Pristine, (b) 0.14 wt% Se doped, (c) 0.23 wt% Se doped, (d) 0.45 wt% Se doped and (e) 0.31 wt% Se doped CuO NPs and their corresponding energy dispersive X-ray analysis spectrum of representative nanoparticles showing characteristic K and L X-rays and atomic% of Cu and O. 111

Fig. 4.3	Transmission Electron Microscopy (TEM) images of (a) pristine, (b) high resolution image of pristine, (c) Se doped CuO NPs and (d) high resolution image of Se-doped CuO NPs.	112
Fig. 4.4	Tauc plot obtained from diffuse reflectance spectroscopy of pristine and the batches of Se doped CuO NPs.	113
Fig. 4.5	Photoluminescence spectra of pristine and batches of Se doped CuO NPs.	114
Fig. 4.6	Cyclic voltammetry plots of (a) pristine, (b) 0.14 wt% Se (c) 0.23 wt% Se (d) 0.45 wt% Se, (e) 0.31 wt% Se doped CuO NPs, and (f) specific capacitance vs. scan rate plot.	116
Fig. 4.7	(a) $1/q$ vs. $v^{1/2}$ and (b) q vs. $v^{-1/2}$ dependence of the batches of Se doped CuO NPs	117
Fig. 4.8	Galvanostatic charge-discharge curves of (a) pristine, (b) 0.14 wt% Se doped, (c) 0.23 wt% Se doped, (d) 0.45 wt% Se doped, (e) 0.31 wt% Se doped CuO NPs and (f) Comparison study of GCD of the batches of Se-doped CuO NPs at current density of 0.2 A/g.	118
Fig. 4.9	(a) Electrochemical impedance spectroscopy of pristine and Se doped CuO NPs, (b) represent the zoom EIS of all the batches of CuO NPs in higher frequency range.	120
Fig. 4.10	Capacitance retention of (a) pristine and (b) 0.45 wt% Se-doped CuO NPs, inset showing EIS plot of samples before and after the 500 cycles at current density 1 A/g.	122
Fig. 4.11	XRD pattern corresponding to the monoclinic structure of calcined pristine and calcined Se doped CuO NPs.	123
Fig. 4.12	Field Emission Scanning Electron Microscopy images of (a) calcined pristine, (b) calcined 0.45 wt% Se doped CuO NPs and their corresponding energy dispersive X-ray analysis spectrum of representative nanoparticles showing characteristic K and L X-rays and atomic% of Cu and O.	124
Fig. 4.13	Cyclic voltammograms of (a) calcined pristine (b) calcined 0.45 wt% Se doped CuO NPs. Galvanostatic charge-discharge curves of (c) calcined	125

	pristine and (d) calcined 0.45 wt% Se doped CuO NPs.	
Fig. 4.14	Capacitance retention of (a) calcined pristine and (b) calcined Se doped CuO NPs, inset showing EIS plot of samples before and after the 500 cycles at current density 1 A/g.	127
Fig. 4.15	Cyclic voltammetry of calcined pristine CuO NPs at (a) 25 °C, (b) 35 °C, (c) 45 °C, (d) 55 °C, (e) 65 °C, and (f) 75 °C.	129
Fig. 4.16	Cyclic voltammetry of calcined Se-doped CuO NPs at (a) 25 °C, (b) 35 °C, (c) 45 °C, (d) 55 °C, (e) 65 °C, and (f) 75 °C.	130
Fig. 4.17	(a) Comparison plot of CV curves of calcined pristine CuO NPs at different temperature at scan rate of 10 mV/s (b) capacitance vs. scan rate plot, (c) Comparison plot of CV curves of calcined Se doped CuO NPs at different temperature at scan rate of 10 mV/s and (d) capacitance vs. scan rate plot.	131
Fig. 4.18	(a) I/q vs. $v^{1/2}$, (b) q vs. $v^{-1/2}$ dependence of calcined pristine CuO NPs on temperature, (c) I/q vs. $v^{1/2}$ and (d) q vs. $v^{-1/2}$ dependence of calcined Se doped CuO NPs on temperature.	132
Fig. 4.19	Electrochemical impedance spectroscopy (EIS) of (a) pristine (b) Se doped CuO NPs at different temperature.	135
Fig. 4.20	Cycle stability of (a) pristine and (b) Se doped CuO NPs at 25 °C, (c) pristine and (d) Se doped CuO NPs at 55 °C after 500 cycles at current density 3 A/g. The inset in each figure represent EIS plot of pristine and Se doped CuO NPs recorded at respective cell temperatures.	136
Fig. 5.1	(a) XRD pattern corresponding to the monoclinic structure of pristine and Co-doped CuO NPs, (b) Zoom XRD of Co-doped CuO NPs	142
Fig. 5.2	Field Emission Scanning Electron Microscopy images of (a) Pristine, (b) 1.14 wt% Co doped, (c) 4.10 wt% Co doped, (d) 5.77 wt% Co doped; and(e) 8.33 wt% Co doped CuO NPs. Their corresponding energy dispersive X-ray analysis spectrum are given next to the respective FE-SEM images, which revealed characteristic K and L X-rays and atomic% of Cu, Co and O.	145
Fig. 5.3	Transmission Electron Microscopy (TEM) images of (a) pristine; (b)	146

pristine high resolution images; (c) Co-doped CuO NPs; and (d) high resolution images of Co-doped CuO NPs.

- Fig. 5.4** Tauc plot obtained from diffuse reflectance spectroscopy of pristine and the respective batches of Co-doped CuO NPs. 147
- Fig. 5.5** Photoluminescence spectra of pristine and the batches of Co-doped CuO NPs. 149
- Fig. 5.6** Cyclic voltammetry plots of (a) pristine; (b) 1.14 wt% Co (c) 4.10 wt% Co (d) 5.77 wt% Co and (e) 8.33 wt% Co doped CuO NPs, (f) specific capacitance vs. scan rate plot. 150
- Fig. 5.7** (a) I/q vs. $v^{1/2}$ and (b) q vs. $v^{-1/2}$ dependence of the batches of Co-doped CuO NPs 152
- Fig. 5.8** Galvanostatic charge-discharge curves of (a) pristine, (b) 1.14 wt% Co-doped, (c) 4.10 wt% Co-doped, (d) 5.77 wt% Co-doped, (e) 8.33 wt% Co-doped CuO NPs and (f) Comparison study of GCD of all batches of CuO NPs at current density of 0.2 A/g. 154
- Fig. 5.9** (a) Electrochemical impedance spectroscopy of pristine and Co-doped CuO NPs, (b) represent the zoom EIS of all the batches of CuO NPs in higher frequency range. 155
- Fig. 5.10** Capacitance retention of (a) pristine and (b) Se doped CuO NPs, inset shows EIS plot of samples before and after the 500 cycles at current density 1 A/g. 158
- Fig. 5.11** XRD pattern corresponding to the monoclinic structure of calcined pristine and calcined Co doped CuO NPs. 159
- Fig. 5.12** Field Emission Scanning Electron Microscopy images of (a) calcined pristine, (b) calcined 5.77 wt% Co doped CuO NPs. Their corresponding energy dispersive X-ray analysis spectrum of representative nanoparticles showing characteristic K and L X-rays and atomic% of Cu, Co and O. 160
- Fig. 5.13** Cyclic voltammograms of (a) calcined pristine (b) calcined 5.77 wt% Co-doped CuO NPs. Galvanostatic charge-discharge curves of (c) calcined pristine and (d) calcined 5.77 wt% Co-doped CuO NPs 161

- Fig. 5.14** Capacitance retention of (a) calcined pristine and (b) calcined Co-doped CuO NPs, inset showing EIS of samples before and after 500 cycles at current density 1 A/g. 163
- Fig. 5.15** Photograph of symmetric solid state supercapacitor made of 5.77 wt% Co-doped CuO NPs 164
- Fig. 5.16** CV curve of symmetric solid state supercapacitor at different scan rate in the cell voltage range 0 to 1.0 V 165
- Fig. 5.17** CV curves of symmetric solid state supercapacitor at fixed scan rate of 20 mV/s in the different cell voltage range 0 to 3.5 V 165
- Fig. 5.18** CV curves of symmetric solid state supercapacitor at 20 mV/s scan rate in the different cell voltage range of 0 to 2.4 V. 166
- Fig. 5.19** Galvanostatic charge-discharge curve of symmetric solid state supercapacitor at 0.2 A/g current density in the cell voltage range 0 to 2.0 V. 167



LIST OF TABLES

	Page no.
Table 1.1 Different types of modified CuO nanomaterial and their applications as supercapacitor	14
Table 1.2 Doping assisted modifications in copper oxide nanostructures for several applications	26
Table 3.1 The chemical structures and chemical formula of the capping agents	55
Table 3.2 Crystallite size, band gap, surface area and specific capacitance of bare and capped CuO NPs	58
Table 3.3 Summary of maximum total charge (q_t), double layer charge (q_{dl}), and charge associated with pseudocapacitance (q_p) of bare and capped CuO NPs in 1 M Na ₂ SO ₄ solution.	74
Table 3.4 Specific capacitance of reported CuO nanostructures in literature	77
Table 3.5 Crystallite size, band gap, surface area (for Bare and TPPO capped) and specific capacitance of calcined bare and calcined capped CuO NPs	87
Table 3.6 Summary of maximum total charge (q_t), double layer charge (q_{dl}), and charge associated with pseudocapacitance(q_p) of calcined bare and calcined capped CuO NPs after calcinations in 1 M Na ₂ SO ₄ solution.	89
Table 3.7 Characteristic features of glucose sensors of all batches of CuO NPs electrodes	98
Table 3.8 Comparison of studied CuO NPs electrode as glucose sensor reported in literature.	99
Table 4.1 Concentration of selenium taken during synthesis of Se-doped CuO NPs	106
Table 4.2 Crystallite size, band gap, surface area and specific capacitance of pristine and Se-doped CuO NPs	109
Table 4.3 Summary of maximum total charge (q_t), double layer charge (q_{dl}), and charge associated with pseudocapacitance (q_p) of pristine and Se doped CuO NPs in 1 M Na ₂ SO ₄ solution.	117
Table 4.4 Summary of maximum total charge (q_t), double layer charge (q_{dl}), and charge associated with pseudocapacitance (q_p) of calcined pristine and calcined Se doped CuO NPs in 1 M Na ₂ SO ₄ solution.	133

Table 5.1	Concentration of cobalt taken during synthesis of Co-doped CuO NPs	140
Table 5.2	Crystallite size, band gap, surface area and specific capacitance of pristine and Co-doped CuO NPs	141
Table 5.3	Summary of maximum total charge (q_t), double layer charge (q_{dl}), and charge associated with pseudocapacitance (q_p) of pristine and Co doped CuO NPs in 1 M Na ₂ SO ₄ solution	152



ABBREVIATIONS

AFM	Atomic Force Microscopy
AA	Ascorbic Acid
BET	Brunauer–Emmett–Teller
CV	Cyclic Voltammetry
CTAB	Cetyltrimethylammonium bromide (CTAB)
DRS	Diffuse Reflectance Spectroscopy
DA	Dopamine
EDLC	Electric Double Layer Capacitance
EIS	Electrochemical Impedance Spectroscopy
EDAX	Energy Dispersive X-ray Analysis
ESR	Equivalent Series Resistance
FT-IR	Fourier Transform Infrared Spectroscopy
FWHM	Full-Width at Half Maximum
FDA	Food And Drug Administration
FE-SEM	Field Emission Scanning Electron Microscopy
GCD	Galvanostatic Charge-Discharge
ITO	Indium Tin Oxide
JCPDS	Joint Committee Powder Diffraction Standard
LoD	Lower Detection Limit
MAA	Mercapto Acetic Acid
MWCNT	Multiwall Carbon Nanotube
PC	Pseudocapacitance
PEG	Polyethylene Glycol
PVP	Polyvinyl Alcohol
PLD	Pulsed Laser Deposition
PVA	Polyvinyl Alcohol
PL	Photoluminescence
PVP	Polyvinyl Pyrrolidone
RTFM	Room Temperature Ferromagnetism
SILAR	Successive Ionic Adsorption and Reaction

SDS	Sodium Dodecyl Sulphate
SC	Specific Capacitance
TEM	Transmission Electron Microscopy
TPPO	Triphenylphosphine Oxide
TRX	Triton X-100
UA	Uric acid
XPS	X-ray Photoelectron Spectroscopy
XRD	X-Ray Diffraction



LIST OF PUBLICATIONS

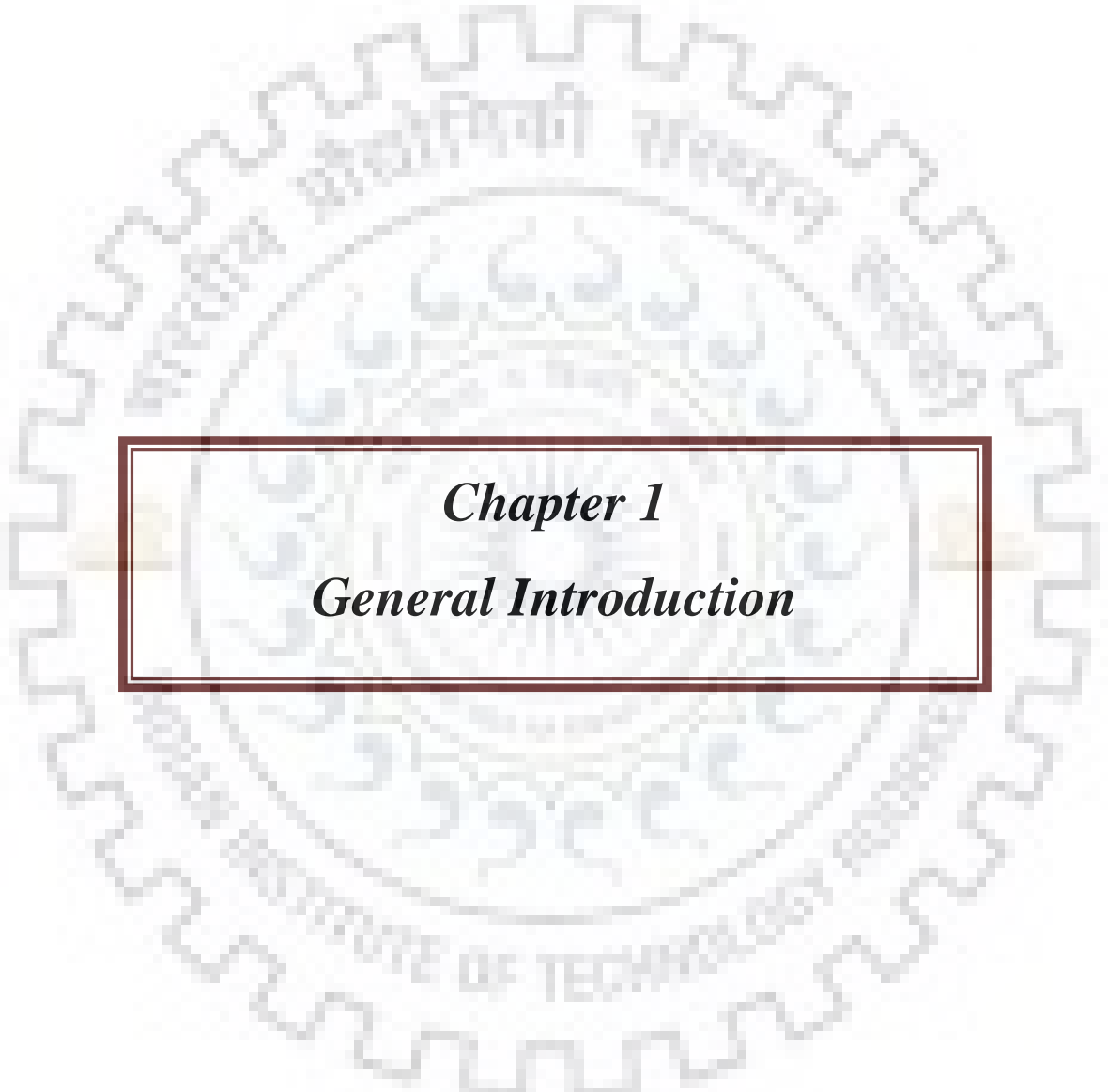
- **Bind, U.C.**, Dutta, R.K., Sekhon, G.K., Yadav, K.L., Krishna, J.B.M., Menon, R., Nabhiraj, P.Y. Ion implantation induced phase transformation and enhanced crystallinity of as deposited copper oxide thin films by pulsed laser deposition. *Superlattices and Microstructures*, 84, (2015), 24-35. (Impact factor **2.090**).
- Dutta, R.K., **Bind, U.C.**, Krishna, J.B.M., Sinha, A.K., Taki, G.S. Ion beam irradiation of ZnS dispersed in PMMA and its photocatalytic application. *Journal of Radioanalytical and Nuclear Chemistry*, 302(2), (2014), 819-824. (Impact factor **1.181**)
- **Bind, U.C.**, Dutta, R.K. Enhanced pseudocapacitance performances for elevated cell temperature by selenate doped CuO nanoparticles. (Manuscript to be submitted)
- **Bind, U.C.**, Dutta, R.K. Cobalt doped CuO nanoparticles as efficient symmetric solid state supercapacitor (Manuscript under preparation).
- **Bind, U.C.**, Dutta, R.K. Improvement in the sensitivity and selectivity of glucose sensing by calcined-capped CuO nanoparticles (Manuscript under preparation)

Conferences

1. **Oral presentation** on “Effect of surfactants and dopants on structural, morphological and electrochemical properties of CuO nanoparticles prepared by precipitation method” **Bind, U.C.**, Dutta, R.K. in International Conference on Nanotechnology: Ideas, Innovations & Initiatives-2017 (ICN:3I-2017) Indian Institute of Technology Roorkee, Roorkee Uttarakhand held on 06-08 Dec 2017.
2. Participated in “International Professional Development Course: Insider Threats and Security Culture” program for nuclear security organized by Amity University Uttar Pradesh in partnership with King’s College London during 1st – 5th of June and 24th – 28th of August 2015.
3. Participated in, one day workshop on “nano drug delivery system (industry/academia interaction)” organized by Centre of excellence: nanotechnology, Indian Institute of Technology Roorkee, Roorkee on 10 Jan 2015.

4. **Poster presentation** on “Synthesis and characterization of magnetic nanofibers of PVA-pectin” Roy, P., **Bind, U.C.**, Dutta, R.K. in a national conference on Science: Emerging Scenario & Future Challenges-II (SESFC-II) organized by Himachal Science Congress Association (HSCA), Himanchal Pradesh, India on May 17-18, 2014.
5. **Oral presentation** on “Low energy ion implantation studies on nanomaterial” **Bind, U.C.**, Krishna, J.B.M., Nabhiraj, P.Y., Yadav, K.L., Dutta, R.K. in Research Scholar’s Workshop on Physics of Materials, held at UGC-DAE Consortium for Scientific Research Indore, Madhya Pradesh in Dec 23-24, 2013.





Chapter 1
General Introduction

1.1. Introduction

Nanomaterials have made tremendous impact in various domains of Science and Technology. The credit for conceptualizing versatility of nanomaterials is attributed to Nobel Prize winner Richard Feynman in 1959 for mentioning that “there is plenty of room at the bottom” and introduced the possibility manoeuvring material atom by atom [1]. In 1974, the term “nanotechnology” was first used by Norio Taniguchi at an International Conference on Industrial Production in Tokyo where he described the processing, separation, consolidation, and deformation of materials by one atom or one molecule [2]. The growth in nanotechnology occurred with the advent of sophisticated probes to image nanoscale materials and discovery of techniques for manipulation of surfaces with atomic resolution. Since then wide range of nanoscale materials are being synthesized and their applications are found in almost all the major areas of Science and Technology [3-8]. In this regard, metal oxide nanoparticles have attracted wide attention in the scientific community owing to unique tuneable properties, e.g., optical, electrical, magnetic, mechanical, structural, thermal and chemical properties. These properties are utilized for wide range of applications. Some selected applications are catalysts [9], photocatalysts [10, 11], sensors [12], antibacterial [13], Li ion batteries [14], solar cells [15], pyroelectric, piezoelectric, ferroelectric, magnetic [16], supercapacitors [17], photoelectrochemical cell [18]. The other salient features of metal oxide nanoparticles over their bulk counterparts are high surface to volume ratio, manipulation of their size, shape, surface area, porosity strength and stability in different environment. Different shapes and morphologies, e.g., spherical, nanorods, nanowires, nanocubes, nanobelts and nanotubes, nanoflowers, prism have been developed [19, 20]. This has been achieved by developing various novel synthesis methods, such as chemical precipitation, sol-gel process, hydrothermal process, solvothermal process, sonochemical process, electrochemical deposition, pulse laser deposition and thermal decomposition [21, 22].

1.2.1 Modification of metal oxide nanoparticles

The metal oxide nanoparticles are found to exhibit enhanced properties by suitable modification of its composition and structure. For example, TiO₂ nanoparticles are essentially large band gap materials and therefore exhibit photocatalytic properties when photoexcited by UV light. But by doping TiO₂ with Cu and Fe, it has been possible to reduce the band gap and turn it into a visible light photocatalyst [23, 24]. On the other hand, though the band gaps of

CuO nanoparticles are in the visible region, but they were inefficient visible light photocatalyst. Whereas, CuO nanoparticles when modified by incorporating ZnO or graphene oxide or doped with Se, revealed excellent photocatalytic activity [25-28]. These examples are very encouraging for exploring the benefits if modified metal oxides for other applications as well, particularly about energy storage and sensing applications.

Modification of nanoparticles can be broadly done by physical and by chemical methods. Ion implantation or ion beam irradiation is one of the well established techniques for modifying materials including the nanoparticles or nanostructured materials [29-32]. In addition energetic proton beams can also be used for patterning nanostructures [33-36]. Ion implantation is a unique technique for doping atoms of interest with precise concentration and depth of a material. The major advantage of ion implantation over conventional chemical method or thermal diffusion method is the ability to introduce any atom of interest in a material as long as a stable ion beam can be generated from a particle accelerator. Several studies are reported on tuning of nanostructures with different surface properties and optical properties due to defects induced by ion-implantation [37-41]. Further, low energy ion beam induced modifications tailored the ultrafine grains of material and lattice structures, which was dependent on ion flux and fluence [42-43]. Such ion implanted materials were found to be good for some devices and healthcare applications [44-47].

Chemical modification method can be classified into two categories, i.e., (a) chemical doping and (b) surface modification by with suitable ligands. There are several examples of doping wide range of p, d and f block elements in wide range of metal oxide nanoparticles [4, 48]. Such studies resulted in introduction of additional energy levels within the forbidden gap. In many cases, the doped atoms acted as a charge carrier and influenced the conducting nature of the host materials [49, 50]. Doping of d-block elements with unpaired electrons, e.g., cobalt in diamagnetic host material resulted in inducing magnetic property [51, 53]. Similarly, properties of nanoparticles can be modified by choosing suitable ligands as capping agent. Here the purpose of capping agent is two folds. They are used for stabilizing the nanoparticles. In addition, the functional groups in the capping agents can play important role in enhancing adsorption property by selective interaction with metal ions of interest [53]. Similarly, electron rich or electron deficient systems can be used as capping agent to manipulate the charge density in nanoparticles for inducing electrical conducting property [53].

Nagarajan et al. [54] have modified powder and thin film of CuCrO_2 , which have moderated conductivity due to presence of holes with 5% Mg doping. They observed that the conductivity of doped CuCrO_2 powder and thin film is enhanced by 1000 times and 220 time, with respect to their counterpart sample, respectively. In another doped assisted modification they have studied effect of replacing Pb^{2+} of electrical insulating polycrystalline PbCu_2O_2 pellets by 3% Na^+ , which exhibited 6 fold increase in the electrical conductivity [55]. Further, they have studied heavy F-doping assisted modification in SnO_2 nanocrystal via simple and novel synthesis route with single-source precursor (KSnF_3). They observed 21% of F ion in the sizes 5-7 nm nanocrystals of SnO_2 , which enhanced the photocatalytic activity of SnO_2 due to introducing oxygen vacancies in the nanocrystals [56]. *Mishra et al.* [57, 58] have modified pure titania by zirconium oxide and $\text{TiO}_2\text{-SiO}_2$ by N-doping, which were observed to be thermally stables at high temperature and exhibited enhanced photocatalytic activity towards the reduction of Se(VI) to Se(0) owing to synergetic effect of N-doping, high surface area and oxygen vacancy. They have used hydrazine as N-dopant precursor which controlled surface area and oxygen vacancy density. In another study, *Mishra et al.*[59] have prepared Cr-doped titania nanotube in presence of ethylene glycol by electrochemical anodization of Ti-Cr alloy, where 0.02 At% Cr doped sample followed by annealing with 450 °C revealed maximum photocurrent response due to increase in crystallinity and decrease in electron-holes recombination after doping. Apart from doping in mixed oxide, *Mishra et al.* [60] have studied surfactant assisted modification of mixed oxide nanoparticles with cetyltrimethylammonium bromide (CTAB) and reported that 2 mol% CTAB yielded spherically shaped silica and zirconia mixed titania which were stabilized at even at high temperature i.e., 900 °C and exhibited good photocatalytic activity. *Biswal et al.* [61] have also reported surfactant assisted effect on catalytic activity of manganese dioxide, in which they claimed that surfactants increased the surface area of the nanoparticles and consequently enhanced the electrochemical performances. *Kumar et al.* [62] have reported ultra-violet absorption assisted modification in Al-doped ZnO bulk and thin films transport properties, where they have explained that UV absorption gave smooth conduction in thin film which enhanced the current response of heterojunction. Further, incorporation of very small amount (e.g. 0.02 At% doping) impacted the whole environment and chemical compositions [63, 64].

These above discussions on modification in metal oxide nanoparticles by different way such a capping, doping, ion implantation, effect of precursors, etc, suggested that these modified nanoparticles can be used in used/utilized in several fields of general life such as gas sensing, photocatalytic, biosensors, antibacterial applications, etc [4, 24, 66-67]. These applications as based on surface area, conductivity, oxidation active sites, porous structure of the metal oxide. These properties in a material are also favorable for electrochemical applications [18, 68-72]. Therefore the performances of electrochemical applications, e.g., supercapacitor and molecular sensing by metal oxide nanoparticles as an electrode can be enhanced by modification. For achieving best electrochemical performances the modified nanomaterials must follow the principle of supercapacitor and molecular sensing based on redox reactions at the electrode surface, which are discussed here.

1.3 Working principle of supercapacitors

The energy storage in the supercapacitors is based on the charge storage/accumulation processes, which could be achieved by two different ways; (a) by formation of electric charge layer on the electrode material surface, known as electric double layer capacitance (EDLC) mechanism and (b) by charge transfer between electrolyte and electrode material through interface, referred to as pseudo-capacitance (PC) mechanism. In EDLC mechanism, energy storage takes place by reversible accumulation of electrolyte ions at the electrolyte/electrode material interface. The specific capacitance of EDLCs mainly depends on the specific surface area of the electrode materials which is available for accumulation of electrolyte ions. The EDLC behavior is mostly found in carbon materials, which depends on surface or interface area of the porous material used as electrode. When a potential is applied between electrodes the cations move toward the negatively polarized electrode/electrolyte interface, while negatively charged ions (anions) move towards the positively polarized electrode/electrolyte interface to neutralize the generated holes in the electrode materials. The hydrodynamic motion of the ionic species in the diffused layer and subsequent accumulation of ions at the close proximity of the electrode surface is given by Stern model, which takes into account of Helmholtz model and Gouy-Chapman model. The total capacitance of such an electrode can be derived from the equation: [73]

$$1/C_t = 1/C_H + 1/C_d$$

where, C_H and C_d represents capacitance due to Helmholtz layer and capacitance due to double layer, respectively.

On the other hand, pseudocapacitance is a faradaic process where the electrolyte ions undergo fast and reversible redox reactions with electroactive species at the electrode material surface/interface when potential is applied across the electrodes. Here charges are transferred from electrolyte ions to electroactive species. The conducting polymers, transition metals, metal oxides and metal hydroxides reveal pseudo-capacitance behavior due to presence of electroactive sites for faradaic reactions. Transition metal oxides/hydroxides have attracted much attention as pseudocapacitor materials due to their good electrical conductivity, multivalent oxidation states and free intercalation of the protons inside or outside of the oxide/hydroxide electrode materials during the redox reaction [4].

1.4 Working principle of non-enzymatic glucose sensing

The non-enzymatic glucose sensing by electrochemical method is performed via oxidation of glucose on the surface of electrode. The analyte, i.e., the glucose is adsorbed on to the electrode surface. Here the d-electrons of the metal substrate presumably form a suitable bond with the adsorbate [18]. It has been evident in numerous publications [75–79] that electrooxidation of glucose and many other organic molecules coincide with the onset of adsorbed OH_{ads} . But it does not take into account the role of hydroxyl radicals. *Burke* [80] discussed the importance of this hydrous oxide layer on the electrocatalytic process, and proposed the ‘Incipient Hydrous oxide adatom Mediator’ model (IHOAM). This was based on the observation that ‘active’ surface metal atoms undergo a pre-monolayer oxidation step that forms an incipient hydrous oxide layer of reactive OH_{ads} mediating oxidation and inhibiting reduction of kinetically slow electrode reactions. Considering this effect, both the activated chemisorption model and the IHOAM model can be implemented onto different metal-based glucose sensors; such as Pt, Au, Ni, Cu, etc, metal alloy-based sensors like, Au-Pt, Cu-Ni, Pt-Ir, Cu-Ni etc, carbon based materials such as MWCNTs, SWCNT, Cu-CNTs-GCE, Cu NPs/SWCNTs/GC, etc and metal-metal-oxide based materials such as, CuO NWs-Cu modified GCE, Cu-TiO₂, Au-Ni(OH)₂, Cu-Cu₂S etc. Among all different types of glucose sensing material Cu-based materials are found to be one of the promising candidates due to their availability and outstanding catalytic ability. The electrocatalytic oxidation of glucose on

copper based materials was proposed by Fleischmann et al., who claimed that the copper II/III transition occurs at 0.65 V vs. SCE potential on 0.1 M KOH solution. This oxidation potential was too close to bulk oxygen evolution. But, the observations revealed a clear indication of copper (III) in the apparent charge under the peaks. However, other redox peaks of copper clearly identified with the oxidation of copper (I) to copper (II) states and corresponding reduction evident in CV studies [81–83].

1.5 Modified metal oxide nanostructures for supercapacitors

Supercapacitor principle indicates the role of charge/energy storage in the materials. This can be appropriately, done with a materials which have large surface area, uniform distribution of pores and excellent conductivity to reduce charge transport time, etc. This can be achieved by an appropriate modification of material. The modification can tune the properties of nanoparticle metal oxides that are being used extensively for energy storage due to different types of nanostructures of increased specific surface area and multioxidation states ions owing to enhanced redox reaction. The architecture related modifications in metal oxide nanoparticles has been well discussed by Jiang et al. for electrochemical performance [18]. They have discussed several types of schemes such as metal oxide/metal hydroxides, metal oxide@carbon/conducting polymers, metal oxides and conducting textiles/paper, metal oxides@conducting substrates and pure phase metal oxide nanostructure, as given in Fig. 1.1 and concluded that pure phase metal oxides revealed lower electrochemical performance as compared to their modified counterparts.

RuO₂ is well known single phase material for electrochemical performances i.e., for supercapacitor. Zheng et al. [84] demonstrated the specific capacitance of 720 F/g for hydrous RuO₂ and further they enhanced its supercapacitance performance by modifying it with hydrogen. Before Zheng et al., Conway et al. [85] was the first person who introduced the concept of supercapacitance to scientific community in 1975 by explaining the cyclic voltammetric curve nature of RuO₂. They purposed that redox reactions are taking place in successive electron transfer process at reaction centres (Ru²⁺, Ru³⁺ and Ru⁴⁺), whereas proton transfer process involves the conversion of OH⁻ to O²⁻ sites in the metal oxides. Further explanations of charge storage mechanism of hydrous RuO₂ demonstrated the charge storage is not limited to ion diffusion process as generally observed in battery applications, and the

electrochemical impedance spectroscopy (EIS) of RuO₂ based materials did not revealed electrostatic capacitance behavior. Conway et al. has explained the difference between battery and supercapacitor behavior by demonstrating different oxidation/reduction of Ru taking place at different potentials. Moreover, *Sugimoto et al.* [86] reported different types of RuO₂ nanostructures developed by the use of layered and colloidal ruthenic acid as promising candidate for supercapacitor which comprised of higher kinetics than conventional battery type electrodes.

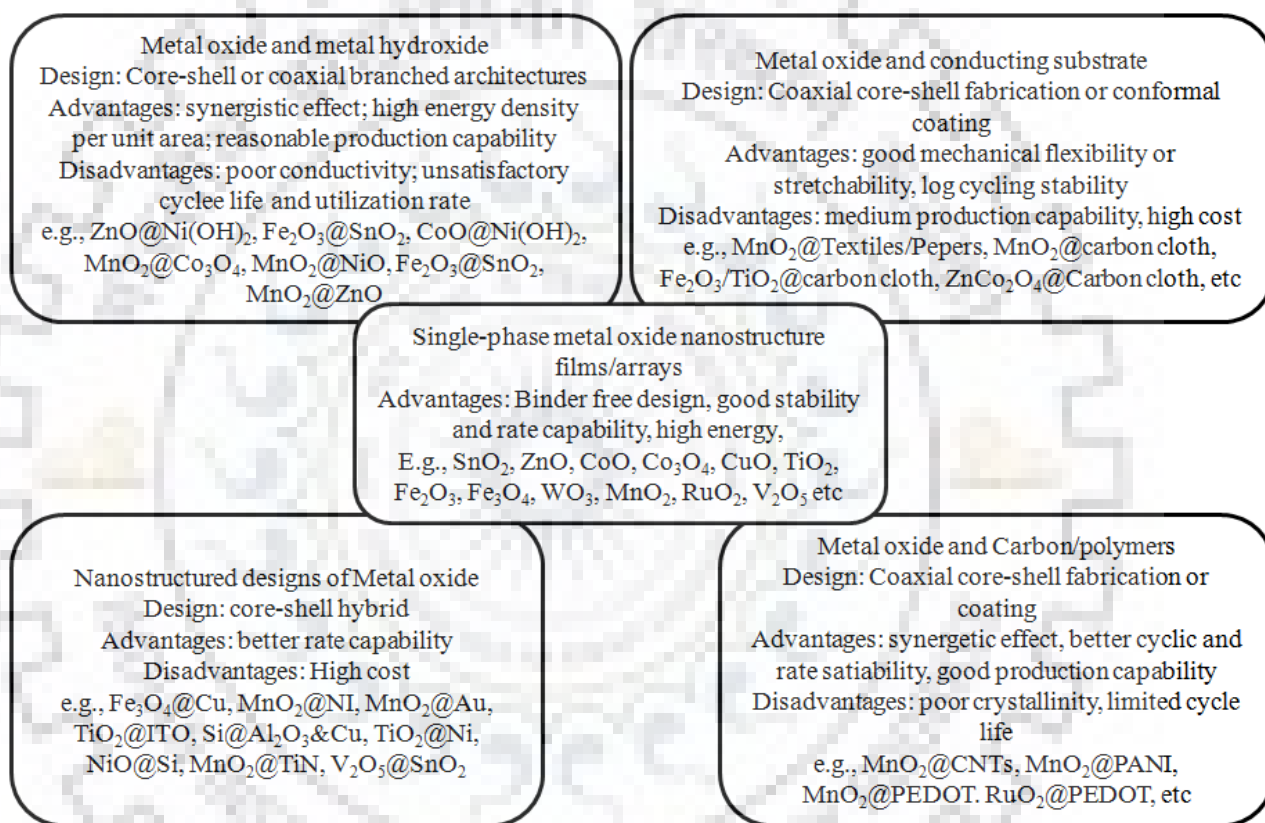


Fig. 1.1 Different types of metal oxide and their modified metal oxide systems studied as supercapacitors ⁷⁴

This was the key invention on supercapacitor which demonstrated that supercapacitor can have higher energy density than conventional battery. Owing to overcome the energy density problem of battery, researchers started working on supercapacitors. *Hu et al.* [87] reported maximum specific capacitance of 1340 F/g for RuO_x.nH₂O at scan rate of 25 mV/s. Further RuO₂ has been used for supercapacitors with different metal oxide such as, SnO₂, WO₃, MnO₂, NiO, VO_x, TiO₂ to formed composite electrode [88–90]. However Ru based electrodes are expensive and are also toxic, which forced scientific community to develop alternate low

cost and environmental friendly electrode material as supercapacitor. The Mn-based materials were found to be alternative of Ru-based electrode materials owing to their theoretical specific capacitance ranging from 1100 to 1300 F/g. It has multi oxidation/reduction potential in neutral electrolyte such as Na_2SO_4 , K_2SO_4 or NaCl [91]. Thus MnO_2 also exhibited desirable rectangular CV curve in neutral aqueous electrolyte solution in the working potential window range of 0 to 0.9 V vs. Ag/AgCl [91]. This charge storage mechanism was explained on the basis of CV and X-ray photoelectron spectroscopy studies which revealed variation of surface oxidation states from III to IV in CV measurements. In another words, the charge storage process of MnO_2 involved only surface redox reactions not the bulk parts of the materials. The scientific community made tremendous effort and studied supercapacitor behavior of different morphologies of MnO_2 nanostructures with different supporting materials like CNT, graphene, metal oxide composites, etc. In this regard, *Chen et al* [91] fabricated nanostructured/ MnO_2 supercapacitor which showed very good 1230 F/g specific capacitance and 96% capacitance retention after 10000 cycles at current density of 5 A/g. Cheng et al. [92] reported an asymmetric supercapacitor made up of graphene as negative electrode and $\text{MnO}_2/\text{graphene}$ as positive electrode, which could work in the potential window range 0-2.0 V and revealed 30.4 Wh/kg energy density. *Bhagwan et al.* [93] reported supercapacitance of Mn_3O_4 nanoparticles in two different electrolytes, where they concluded that nanostructured material with high surface area revealed maximum specific capacitance in both the electrolytes but this was higher for KCl electrolyte as compared to Na_2SO_4 due to smaller size of K^+ ion than Na^{2+} ion. In another study based on nanostructured nanofibers of Mn_3O_4 , the same group fabricated a symmetric solid state supercapacitor device which revealed 75 Wh/kg and 2 kW/kg energy density and power density, respectively and 93% capacitance retention after 1500 cycles [94].

The solid state supercapacitors can be fabricated in three different ways; (i) symmetric supercapacitor which typically consists both electrodes of same material with same mass loading. Most of the commercial supercapacitors are made of carbon materials in symmetric configuration that can work in larger potential window 0 to 2.7 V [68]. (ii) Asymmetric supercapacitors which are made of two different electrode materials, i.e., these can be of same material with different mass loading or may be of two types of materials. (iii) Hybrid supercapacitor that consist electrodes of two different charge storage behavior, i.e., one must

have electric double layer capacitance behavior and other should be of pseudocapacitance behavior.

In addition to the above process, ion implantation has also been used to tune the electrochemical performances of these metal oxides. *Tian et al.* [44] has modified indium tin oxide electrode with 20 keV nickel ions at a particle fluence of 5×10^{16} ions/cm² and they observed nickel NPs with average sizes of 25-35 nm developed on the surface of ITO electrode played important role. The Ni nanoparticles were characterized by scanning electron microscopy (SEM) and X-ray photoelectron spectroscopy (XPS). They used the ion implanted electrode for non-enzymatic glucose sensing application. The pristine ITO did not revealed any glucose oxidation peak while modified ITO revealed oxidation peak at 0.55 V. The Ni/ITO electrode revealed 189.5 $\mu\text{AmM}^{-1}\text{cm}^{-2}$ and linear detection range from 1 μM to 350 μM with lower detection limit of 0.5 μM . Further such studies were done by same group (Hu and coworkers) [95-97] by doping Ni, Pt, and Ag particles with ion beam induced modifications in indium tin oxide (ITO) thin film at different particle fluencies and energies and investigated their electrochemical performance by observing electrocatalytic oxidation of formaldehyde and electrocatalytic activity towards methanol.

Based on the above discussions, we can conclude that the metal oxides having multi-oxidation states and good conductivity; can be used for applications involving electrocatalytic activity like, energy storage and sensing. In view of this, a comprehensive literature search was done in Scopus using keyword: 'metal oxides as supercapacitor' in documents: Articles, Abstracts and Keywords. A total of 2779 documents till 2016 were obtained. A pie chart was constructed to find out the frequency distribution of the published work on different metal oxides as supercapacitor. Notably, manganese oxide and nickel oxide were most widely studied (Fig. 1.2). The category of "other metal oxide given in the Pie chart corresponded to mixed oxide, and modified oxides. Notably, the number of publications on CuO as supercapacitor was very small (i.e., 0.35%), in spite of higher theoretical capacitance (~1800 F/g) as compared to MnO₂ (theoretical capacitance = 1100-1300 F/g). Furthermore, copper oxide abundant and it is a well known conducting semiconductor material. It can exist as multioxidation states and therefore satisfies all the conditions to behave as a good supercapacitor.

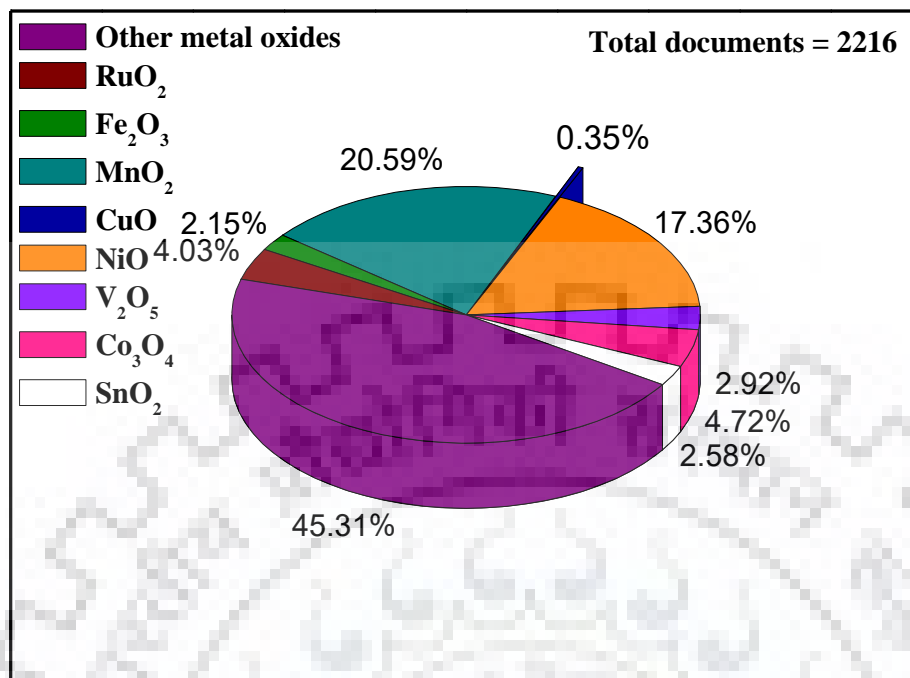


Fig. 1.2 Pie chart diagram showing distribution of various metal oxides published as supercapacitor up to 2016

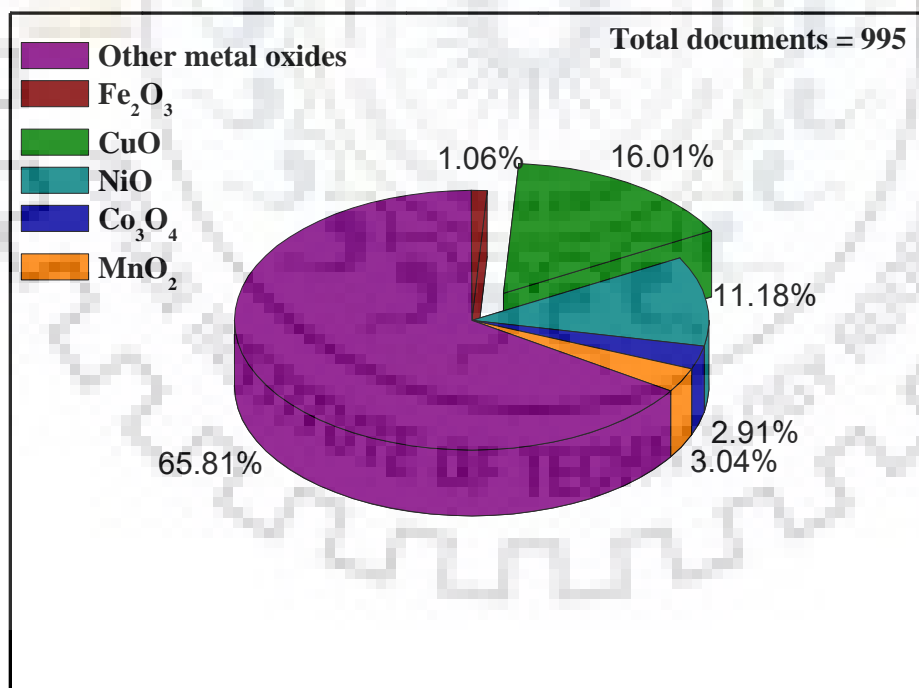


Fig. 1.3 Pie chart showing metal oxide nanoparticles used in electrocatalytic glucose sensing.

This suggested that modifications in CuO nanoparticles can enhance the specific capacitance behavior, and it might be used for commercial applications like MnO₂ and NiO based supercapacitors. Therefore we have selected this to enhance supercapacitor behavior through chemical modifications.

However, compared to supercapacitor applications, the use of CuO nanoparticles as glucose sensor are more. This is reflected to the pie chart showing distribution of various metal oxides as glucose sensor published up to 2016, revealed from Scopus search (Fig. 1.3). It appears that CuO offer excellent electrocatalytic property based on which the glucose sensing was done.

1.6 Modification in copper oxide nanoparticles

Like other metal oxides, copper oxide nanoparticles have attracted much scientific attention as it favour tuning of its properties such as electrical conductivity, stability, surface area, nanostructures, etc, by modifications to enhance the performances in wide range of applications, e.g. gas sensing, biosensors, thermal conductors, photodetectors, supercapacitors, lithium ion batteries, storage media, pollutant removal/degradation systems [98-105]. Therefore, the studies of modified copper oxide properties have been under taken by several scientists. For example, *Li et al.*[106] have reported array of nanoflower-like, nanowires and nanosheets of CuO grown over Cu foam by anodization of copper foam followed by thermal treatments and used it for electrochemical performances. They observed that specific capacitance of CuO nanostructures depends upon surface morphology and dimensions of the nanostructures. The maximum specific capacitance observed for CuO nanosheet structure was 212 F/g at current density of 0.41 mA/mg as compared to specific capacitance of nanoflower and nanowires of CuO (159 F/g and 102 F/g, respectively). The difference in specific capacitance was attributed to surface morphology of CuO nanostructures which basically influence the specific capacitance by three ways; (a) the electrical resistance; (b) the electrolyte ion diffusion inside the pores; and (c) the specific surface area of CuO thin film. The capacitance retention was found to be 85% for nanosheet CuO nanostructure after 850 cycles at current density of 0.41 mA/mg in charge-discharge process, while nanowire CuO nanostructure showed 86% after 600 cycles and nanoflowers revealed 98.3% capacitance retention after 400 cycles at same current density. Mostly the decrease in the specific capacitance during the initial

50 cycles was around 8.1%. *Pendashteh et al.* [107] reported anchored CuO nanoparticles on graphene oxide nanosheet via an electrostatic coprecipitation method followed by thermal treatment and their applications as a supercapacitor. They have studied electrochemical behavior of different symmetric configurations of CuO and GO such as; layer-by-layer coated CuO on GO network (GO/CuO), and composite electrodes along with their individual electrochemical performances. They observed that composite system revealed better specific capacitance (245 F/g) at current density of 0.1 A/g as compared to the respective pure components of CuO (125 F/g) and GO (120 F/g), and the layer-by-layer coated electrodes (155 F/g). The capacitance retention of the composite electrode was found to be 79% after 1000 cycles at current density of 0.25 A/g. Lower specific capacitance of layer-by-layer coated CuO on GO network (CuO/GO) attributed to poor electrical contact of nanoparticles with GO as also reflected from cyclic stability studies. The GO was used for providing a conductive network to the CuO nanoparticles for better electron transfer process. *Nwanya et al.* [108] have developed binderless and without capped nanosheet-like and nanorod-like CuO nanostructured thin film on indium tin oxide (ITO) substrate by successive ionic adsorption and reaction (SILAR) method for a good pseudocapacitor electrode application. They have studied two batches of CuO nanostructured thin films deposition, i.e., (1) 10 cycles for nanosheet-like nanostructure and (2) 40 cycles for nanorod-like nanostructure. They found that the nanostructured CuO thin film revealed average grain of size 30-50 nm for the batch of 10 and 40 cycles of deposition. The average pore size distribution was 12.0 nm and 12.5 nm, for 10 cycles and 40 cycles deposited CuO nanostructured thin films, respectively. They observed maximum specific capacitance 566.33 F/g for nanosheet-like CuO nanostructured thin film, while 211.87 F/g for nanorods-like CuO nanostructured thin film at scan rate of 5 mV/s. The nanosheet-like CuO nanostructured thin film electrode revealed long-term cyclic stability (capacitance retention) 100% at current density of 50 A/g for 1000 cycles which was attributed to no loss of redox reactions. Further the specific energy and specific power of the nanosheet-like CuO thin film were determined as 127.29 Wh/kg and 53.13 kW/kg at current density of 6.25 A/g and 50 A/g, respectively. Some other literature reports published on CuO nanostructures with different modification like, deposition on conducting substrates, composite with carbon materials, deposition on carbon materials, different types of nanostructures and different types of metal oxides composites are presented in Table 1.1. The improvement in the supercapacitor properties and the reason for improvement are categorically discussed.

Similarly, a few studies are reported on the uses of copper oxide nanoparticles and copper-vanadium mixed oxide for Li-ion batteries [102, 109]. In addition CuO and Cu₂O are also being studied for photochemical energy conversion application and solar water splitting applications, respectively [110, 111].

Besides energy applications, copper oxide nanoparticles were also explained for alternate electrochemical applications. In this regard, CuO grown on Cu was synthesized by hydrothermal method revealed excellent glucose sensing property. Different morphologies e.g. chrysanthemum-like, candock-like and dandelion-like revealed efficient sensitivity 3252 $\mu\text{A mM}^{-1} \text{cm}^{-2}$, 4078 $\mu\text{A mM}^{-1} \text{cm}^{-2}$ and 5368 $\mu\text{A mM}^{-1} \text{cm}^{-2}$, respectively. All different nanostructured non-enzymatic glucose sensors revealed good interference property with dopamine, ascorbic acid, uric acid, and other carbohydrate compounds [112].



Table 1.1 Different types of modified CuO nanomaterial and their applications as supercapacitor

Materials	Fabrication	Factor effecting properties	Improvement in its properties	Reason for improvement	Ref
Cu ₂ O@Cu	Electro-chemical deposition	Nanoneedle arrays	Energy storage, cyclic stability, high capacitance of 862.4 F/g and excellent cycling stability upto 20000 cycles; asymmetric capacitance, energy density = 35.6 Wh/kg at 0.9 kW/kg	Needle arrays led to enhancement in surface area resulted in increase in the number of electrolyte ion interaction, copper oxide development on Cu led to binder free electrode resistance free charge conduction	113
Cu ₂ O/CuO/rGO nanocomposite	Hydrothermal	Nanostructure grown on rGO nanosheet	Rate capability and cyclic stability; only 21.4% of the capacity loss while changing discharge current from 1 A/g (173.4 F/g) to 10 A/g (136.3 F/g)	Consist of pair of redox counterparts and conductivity enhanced due to rGO	101
CuO nanoparticles	Precipitation	Anchoring of CuO NPs on N-doped rGO, Surface area and conductivity	The CuO/n-rGO composite with 15.1 wt% CuO loading revealed 340 F/g specific capacitance at current density of 0.5 A/g in a wide potential window 1.4 V in 6 mol dm ⁻³ KOH electrolyte and 80% capacitance retention after 500 cycles at current density of 1 A/g	In situ development on N doped rGO led to increase in its conductivity as well as surface area	114
CuO/rGO composite	Hydrothermal	Conductivity and surface area	Specific capacitance was 326 F/g at current density of 0.5 A/g and symmetric hybrid capacitor capacitance 97 F/g at current density of 0.2 A/g	rGO composite formation with CuO by hydrothermal route led to increase in ionic conductivity, improved cyclic stability	115

CuO/grapheme	Hydrothermal	Leaf like CuO nanostructure, mechanical strength	Specific capacitance was 331.9 and 305 F/g at current density 0.6 and 2 A/g, respectively; Revealed high capacitance retention 95.1% after 1000 cycles	Improvement in electrical contact and mechanical stability due to graphene and improved specific capacitance due to layer-by-layer structure	116
Cu ₂ O microstructures	Simple polyol reduction methods using different copper salts	Different morphology e.g. cubes, flower-like, and microspheres	The maximum specific capacitance was 144 F/g at current density of 0.1 A/g and reported GCD cyclic stability of 99% for only 100 cycles at current density of 0.1 A/g	The supercapacitor behavior is attributed to larger volume charge during the electrochemical reaction owing to its smaller size nanoparticles.	117
CuO hierarchical nanostructures on Cu substrate	In-situ crystallization of Cu foil under alkaline medium	Electro-chemical properties are improved	cyclic voltammetry revealed the maximum specific capacitance 94 F/g at scan rate of 5 mV/s and electrochemical impedance spectroscopy revealed conductivity and the electrolyte ion interaction with CuO nanostructures	Hierarchical nanostructure provide more excess to electrolyte ions for interaction with material	118
Copper oxide multilayer nanosheets thin films	Chemical bath deposition (CBD) method	morphological study, optical And wettability test	FE-SEM images revealed hierarchical structure which have contact angle of 53° with liquid interface and optical band gap was 2.18 eV. The copper oxide electrode revealed specific capacitance of 43 F/g at scan rate of 10 mV/s.	Good wettability due to the strong cohesive force between the water droplet and hydroxide present in the copper oxide compound. High value of capacitance may be due to hydrous nature of copper oxide in present case.	119

CuO Nanoflowers on Carbon Fiber Fabric i.e., CuO/CFF	Hydrothermal method	Electrochemical properties	CuO/CFF electrode revealed specific capacitance 839 F/g at scan rate of 1 mV/s with high energy density of 10.05 Wh/kg and large power density 1304.3 W/kg. Fabricated solid state capacitor with CuO/CFF revealed 131.34 F/g at scan rate of 1 mV/s with power density of 145.12 W/kg and good capacitance retention of 91% after 2000 cycles.	Synergetic action between the CuO and CFF in the charge storage. Three green LED of 2.3 V and 20 mA burned for 5 min through addition of three solid supercapacitors in series	69
Porous and amorphous CuO thin films on stainless steel	Electro-deposition method	Structural, morphological and electrochemical properties	Specific capacitance increases with increase in film thickness. Maximum specific capacitance of 36 F/g was exhibited for the 0.6959 mg cm ⁻² film thickness at scan rate of 20 mV/s	Increase in thickness enhanced the number of faradaic redox reaction sites in the electrode	120
CuO Nano-flowers on flexible copper foil	Chemical bath deposition method	Morphology and electrochemical properties	Nanoflower shaped CuO thin film revealed maximum specific capacitance 498 F/g at scan rate of 5 mV/s, with a high energy density of 26 Wh/kg in KOH electrolyte and 84% of capacitance retention after 2000 cycles at scan rate of 100 mV/s.	Nanoflower provides more pores for electrolyte ions	121
CuO nanosheets, micro-rose and micro-woolen like nanostructures	Chemical bath deposition method	surface morphology, and electrochemical properties	Maximum specific capacitances of nanosheets, micro-roses and micro-woolen like CuO nanosheets = 303 F/g, 279 F/g and 346 F/g, respectively at scan rate of 5 mV/s with high capacitance retention	High specific capacitance attributable to facile electrolyte ions penetration into uniformly distributed pores which lowered ion diffusion resistance and enhanced Faradaic processes in the well-arranged structures made up of layered nanosheets	122

2D & 3D CuO ordered architectures	Solvothermal with mixed solution of ethylene glycol and n-butylamine	3D ordered architecture reflect higher surface area, more convenient electron/ionic mobility, high structural stability	2D and 3D architecture showed 541 and 585 F/g specific capacitance at 1A/g current density, capacity retaining 81% and 79% at 20 A/g, with 85.3% and 86.8% capacitance retention respectively after 8000 cycles	Ordered nanoporous architecture provide ideal route for enhancing comprehensive performance	123
CuO nanobelts	Wet chemical	High surface area, small crystal grains, mixing of CuO with SWCNT	Flexible hybrid (CuO NBs on SWCNT) electrode showed specific capacitance higher than 62 F/g after 1000 cycles while pure SWCNT showed 23.6 F/g at current density 5 A/g	Enhancement in conductivity and ionic mobility due to mixing/support of SWCNT	124
3D porous gear like copper oxide	Hydrothermal	Porous structure, conductive Cu substrate	Specific capacitance = 348 F/g at current density of 1 A/g, excellent cycling stability	Gear-like structure with number of holes formed on edge developed on Cu substrate resulted for high ionic conductivity	125
CuO-poly (acrylic) acid (PAA) hybrid thin film	Spin coating	Morphology changes with annealing temperature	Specific capacitance increases from 41 to 136 F/g with increase in annealing temperature of film	With increase in the annealing temperature island like structure increased and finally became prominent due to decomposition of PAA and resulted in the formation of CuO surrounded by PAA grafted ring	126
3D ordered nanoporous CuO	Hydrothermal	Surface area and interconnected pores	Specific capacitance 131 F/g (1.51 F cm ⁻²) at 3.5 mA cm ⁻² with retention over 70% after operating at 70 mA cm ⁻²	High surface area with interconnected nanopores attributed in ion transportation within it, short ion and electron transport pathway	127

CuO thin film	Chemical bath deposition	Surfactant mediated morphological change	The maximum specific capacitance was 396 F/g for CuO nanobuds nanostructure at scan rate of 5mV/s, which revealed better spercapacitor than woolen clumps and stacked nanosheets CuO	Surfactant nature provides guideline to the surface morphology, high surface area and mesoporous structure	128
CuO nanoflakes	Oxidation of Copper	Structure, morphology and oxidation states	Specific capacitance = 190 F/g at 2 mA cm ⁻² current density in 1.0 M NaOH, 67% cyclic stability after 2000 cycles	Interconnected nanoflakes create pores and crevices which allow large surface area for electrolyte ion diffusion	129
CuO nanowires	Thermal evaporation method	Structure and morphology	Bicrystal structure of CuO nanowire reflected from HRTEM, two step nanowire formation reflected from XRD	Morphology of nanowire changes with growth condition, seems to be vapor-solid mechanism	130
CuO/Cu ₂ O/Cu composite	Hydrothermal	Binder free, nanostructure grow on Cu substrate	Specific capacitance 878 F/g at current density of 1.67 A/g and 545 F/g at current density of 16.7 A/g. Asymmetric supercapacitor formation revealed energy density 42 Wh/kg and power density 0.44 kW/kg.	Multi oxidation state of Cu and Cu ₂ O, CuO nanostructure grown on Cu substrate	131

Therefore, our work will focus on the modification in copper oxide nanoparticles by ion implantation and chemical precipitation techniques. In the following section we will discuss about types of modification like structural, morphological, electrical, magnetic and optical has been done to modify copper oxide nanoparticles and their different applications.

1.7 Modification of CuO by physical and chemical methods

1.7.1 Ion implantation modifications in copper oxide nanoparticles

Nanostructured fabrications or modifications can be precisely controlled by ion implantation techniques [44, 95-97]. The modification depth profile can be controlled by controlling the energy of the ion beam. So, for the thick or penetrated modifications, high energy ion beam revealed good result and for surface and subsurface related modifications low energy ion implantation exhibited excellent results owing to ion beam energy loss associated with nuclear energy process, in which implanted ion collides with lattice atoms and replace it or modified its surface states by influencing its chemical environment [132]. Low energy ion implantation on transition metal oxides nanostructure can leads to change the conductivity, change the phases, optical properties such as band gap and photoluminescence, and produce lattice disorder resulted for the development of defects [133, 134]. Few ion implantation studies of copper oxide are reported such as, *Balamurugan et al.* [135] have modified the nanocrystalline properties such as structure, size, and surface states of copper oxide thin film prepared by activated reactive evaporation technique with high energy (120 MeV) Ag^{9+} ion beam. They have observed that Cu_2O thin film phase, size and surface states changes with implanted ion fluence. The ion beam modified cubic phase is more stable in higher temperature environment. The crystallinity of implanted thin film was found to be improved with irradiation. Implanted thin films showed increase in photoluminescence spectra is attributed to removal of surface states. *Parretta et al.* [135] have modified copper oxide thin film during deposition by reactive RF magnetron sputtering via varying partial oxygen pressure. They observed that there is sudden increase in sputtering rate above 0.08 Pa oxygen partial pressure and above 0.2 Pa sputtering rate became independent of oxygen partil pressure. This variation in sputtering rate resulted for the change in copper oxide thin film phase modification. The thin film prepared till oxygen pressure 0.11 Pa revealed cupric phase while above that oxygen partial pressure prepared thin revealed CuO phase. This phase modification leads to change in their conductivity.

1.7.2 Capping assisted modifications in copper oxide nanoparticles

Modifications can be easily implemented during the synthesis of nanoparticles. In the nanoparticle synthesis process, nucleation takes place followed by growth process of nanoparticles. After completion of this process, nanoparticles start agglomerating to minimize their surface energy and attain stability. However, agglomeration reduces the size of nanoparticles and therefore size dependent properties are not obtained. Therefore, it is necessary to protect the agglomeration of nanoparticles. But it is very challenging task to synthesize agglomeration free nanoparticles. To overcome this issue, researchers have proposed two main stabilization mechanisms: (a) electrostatic in which the system is at kinetic equilibrium and (b) steric stabilization which the system is in thermodynamic equilibrium. Electrostatic equilibrium mechanism was given by Derjaguin, Landua, Verwey and Overbeek, known as DLVO theory, on the basis of electrostatic interaction and van der Waals attractions which explained the interaction between two approaching particles [136]. There are numbers of organic molecules or polymers, which has hydrophilic head and hydrophobic tail or cavity gaps or ionic feature in their structure to protect nanoparticles from their agglomeration during synthesis. These organic molecules and polymers are named as **capping agent**. The capping agent with hydrophilic head gets absorbed on the nanoparticles surface while its hydrophobic tail repels the nanoparticles to avoid their agglomeration. For this it is necessary that capping agent must have hydrophilic head which can bind with nanoparticles tightly and hydrophobic tail long enough than characteristics size of nanoparticles. The capping agents whose cavity play important role in order to protect nanoparticles agglomeration forms a kind of network structure while dispersing in the solvent. This network structure provides space in the cavity for nanoparticles to grow. The ionic nature capping agents offers a repulsive environment between the growing nanoparticles which protect them from their agglomeration. Some capping agent forms a layer on the nanoparticles in order to avoid their agglomeration. Some commonly used capping agents reported in the literature are CTAB, ascorbic acid, tween 80, triton X-100, mercaptoacetic acid, TPPO, polyethylene glycol, thioglycol, dendrimers, PVP, PVA etc [53, 137, 138]. This complicated possibilities ruled by capping agent leads to development of unique feature surface morphology and size of the nanoparticles. Moreover, large amount of capping agent in the reaction medium leads to formation of spherical shape nanoparticles because excess amount of capping agent leads to development of steric resistance for the diffusion [53].

The shapes, size, conductivity and morphology of nanoparticles are reported to be fundamental requirement for a material and their applications e.g., as photocatalyst, electrocatalyst, sensors, energy storage materials, etc [139-141]. For these types of applications of nanoparticles, the reactivity/interaction of the surface atoms of the nanoparticles plays an important role [66]. For example, the reactivity or interaction play a role in the degradation of pollutants, detection of foreign molecules and enhancement in the energy storage behavior like supercapacitor, lithium ion battery, etc. The interaction with foreign molecule by the surface atoms of nanoparticles influences the electronic environment of the surface atom. These phenomena used for applications like catalyst, sensor, micro/nanodevices [66]. The performance of the device depends on the time taken by a generated electron or hole in transportation [142, 143]. For that purpose modifications is one of the ways to solve this issue properly by different ways e.g., with the use of conducting substrate like Pt, Au, Ag etc, with blending of conducting materials like CNT, activated carbon, graphene etc [112, 144-148].

Unlike TiO₂ or ZnO, there are only a few studies on capped CuO nanoparticles synthesis and their applications. *Dubal et. al.*, have reported capping assisted chemical bath deposition of copper oxide thin film. They observed that capping agent triton X-100 and polyvinyl alcohol (PVA) played important role in modification of structure, morphology, pore size distribution and surface area of copper oxide thin film. They have measured its supercapacitive properties and found that all CuO samples exhibited high power density, high performance and excellent cycle stability. They observed maximum specific capacitance 411 F/g at 5 mV/s scan rate for triton X-100 assisted CuO thin film sample [149]. Siddiqui et. al., have prepared CuO nanocrystals with the use of three different type of capping agent, sodium dodecyl sulphate (SDS) as anionic, cetyltrimethylammonium bromide (CTAB) as an cationic and polyethylene glycol (PEG) as nonionic capping agent, by chemical process. They observed different sizes of nanocrystals ranging from 16-20 nm with cube, leaf and flower like nanostructures which were found to be good for optical applications [150]. Zhang et al. has reported the morphology dependent electrochemical properties of CuO prepared by chemical precipitation method. They reported that the flower like CuO exhibited higher specific capacitance as compared to CuO sheets and CuO globular, which exhibited good cycle stability at high current density. The efficient supercapacitive properties of flower like CuO nanostructure was attributed to enhancement in surface area [151]. In another study, CuO nanosheet grown on Ni by template free growth method exhibited high

specific capacitance of 569 F/g at current density of 5 mA/cm². They attributed their results to the unique structure of the CuO nanosheet which resulted in superior electrolyte ion diffusion [152].

1.7.2.1 CuO nanoparticles for sensing

Diabetes is one of the most frequently occurring fatal diseases which needs constant monitoring and medication [153]. In this regard various glucose sensing techniques are developed which address important sensing features e.g., sensitivity, response time and selectivity. These are often achieved through the modification of sensors [146, 154, 155]. A number of studies have been reported on copper oxide nanoparticles for the detection of glucose with the help of several conducting substrate or conducting material to enhance sensitivity and concentration range [147, 156, 157]. Some of the noteworthy studies are discussed here. *Zhuang et al.* have developed Cu(OH)₂ nanowire on the Cu substrate. They have used this material for glucose sensing which showed very fast response (less than 1 sec), good sensitivity and selectivity of glucose [145]. Multiwall carbon nanotube (MWCNT) coated CuO composite were prepared by chemical precipitation method which exhibited excellent sensitivity 664.3 $\mu\text{A mM}^{-1}\text{cm}^{-2}$ and good detection limit of 5.7 μM towards glucose sensing. This excellent performance as a glucose sensor was attributed to unique structure with high surface area [158]. CuO nanocubes and graphene nanocomposite modified with glassy carbon electrode was developed by electrochemical deposition technique it was observed that nanocomposite of graphene-CuO nanocube exhibited higher current response of glucose oxidation with faster response time and long term stability, good reproducibility due to increase in surface area and faster electron transfer rate as compared to CuO nanocubes and graphene, individually [159]. Different morphologies like chrysanthemum, candock and dandelion CuO micro/nanostructures hierarchical thin films have also been used in determination of glucose. It has been found that these chrysanthemum, candock and dandelion like structures showed enhanced electrocatalytic activity toward glucose oxidation 3252 $\mu\text{A mM}^{-1}\text{cm}^{-2}$, 4078 $\mu\text{A mM}^{-1}\text{cm}^{-2}$ and 5368 $\mu\text{A mM}^{-1}\text{cm}^{-2}$. They have also reflected excellent anti-interference properties and good stability. These excellent features of CuO nanostructures towards glucose oxidation are attributed to more electron transfer passages, lower charge transfer resistance, and high surface area of CuO as modified a CuO nanostructure, which provides more reaction sites and better sensitivity [112]. However, studies on developing electrode made with capped CuO NPs are not well reported. The challenges in this approach are understood but it would make glucose

sensing procedure simpler of suitable methodology is developed for preparing electrode made of CuO NPs synthesized by chemical precipitation method by stabilizing with suitable capping agent.

1.7.3 Doping resulted modifications in copper oxide nanoparticles

Present status of research has shown that simple copper oxide nanostructures could not comply with all demands like, photocatalysts, supercapacitors, sensors, etc [3, 160]. For this reason the nanoparticles are modified in forms of nanocomposites with other materials. These types of modifications have been done by researchers to enhance its conductivity and increase multi-components in the system. Apart from nanocomposite formation, multi-components can also be incorporated in the nanoparticles matrix with very less amount addition of other elements named as **doping**. The addition of other elements as dopants in host nanoparticles is very well known for the enhancement of conductivity owing to production of defects and vacancies [3, 161]. The addition of elements as a dopant in the host metal oxide nanoparticles could be reason for the development of other oxide microstructure [4]. For this purpose dopant could be noble metals, transition metal, alkaline atoms and inert impurities. These kinds of dopant can alter the catalytic activity, stabilized the catalytic reduction, support for the formation of active phase or increase the electron exchange rate of metal oxide nanoparticles. These dopants can lead to alter the concentration of charge carriers, physicochemical properties, surface potential and phase composition, crystallite size of metal oxide nanoparticles. Doping in the metal oxide nanoparticles may also effect the electronic and physical-chemical properties of the surface of nanoparticles i.e., electronic spectra of surface states, adsorption and desorption energy, sticking coefficients etc [163, 164]. Alkali and alkaline earth elements as a dopant are well known as electron exchange promoters due to the presence of high charge on the neighboring oxygen atom, whereas, transition elements as a dopant are good for generating active sites in the metal oxide nanoparticles [164-166]. The active sites may signify the presence of cations in the metal oxide nanoparticles. Rare earth element as dopant are also studied to promote the separation of electron holes pair under UV light illumination and increase the photocurrent response and enhances catalytic activities of the metal oxide nanoparticles [167, 168].

Chaudhary et al. has prepared polycrystalline Co-doped CuO samples by solid state method in presence of oxygen. The structural analysis revealed monoclinic phase structure and CuO samples volume decrease as function of cobalt dopant concentration. The Co-doped CuO

samples revealed a marginal increase in ordering temperature at high temperature AFM and decrease for low temperature. Further Co-doped CuO samples revealed giant dielectric constant without any signature peak of ferroelectricity due to presence of multi valence states of Cu and Co in doped samples [169]. *Baturay et al.* has prepared Ni-doped CuO thin film with different concentration e.g. 2, 4, 6 and 10% by spin coating on glass substrates and studied the electrical and optical properties. The XRD analysis revealed polycrystalline, the preferential growth in the (002), (111) and (-311) directions and SEM images revealed the agglomeration of nanoparticles. The Hall Effect measurement confirmed that the free charge carrier decreases as function of Ni dopant concentration, while holes mobility increases with Ni-doping in CuO. The optical study revealed that initially the band gap decreases with increase in Ni concentration from 2.03 to 1.96 eV and then increase to 2.22 eV for 10% Ni concentration [170]. *Bhuvaneshawari et al.* has reported monoclinic phase of Cr-doped CuO nanoboats preparation by hydrothermal rout with 2 At% and 6 At% of Cr and their application as ammonia sensor. They observed deep level emission in the range of 350-610 nm attributed to oxygen revealed from photoluminescence study. They found that 6 at% Cr-doped CuO nanoboats exhibited 2.5 fold enhancements in ammonia response at room temperature and maximum 180% sensitivity at 75 °C for 600 ppm of ammonia as compared to undoped CuO nanoboats ammonia response range of 100-600 ppm at room temperature. This enhanced ammonia response was attributed to increase in surface area, surface charge and oxygen vacancies developed due to Cr dopping [171].

Huang et al. have grown monoclinic phase Ag-doped CuO nanosheet array of average thickness 150 nm on nickel foam via template free growth method and studied their supercapacitance performances. The Ag was doped in CuO nanosheet array via silver mirror reaction. They observed that the Ag-doped CuO nanosheet array revealed specific capacitance of 689 F/g at current density of 1 A/g and 299 F/g at current density of 10 A/g, much higher than that of un-doped CuO nanosheet array (specific capacitance 418 F/g at current density of 1 A/g and 127 F/g at current density of 10 A/g). They have found smaller semicircle for Ag-doped CuO nanosheet array as compared to un-doped CuO nanosheet array counterpart in electrochemical impedance spectroscopy (EIS) studies which was attributed to lower charge transfer resistance. The mid frequency region of Ag-doped CuO nanosheet array was at higher frequency region as compared to un-doped CuO nanosheet array which implied the lower diffusion resistance of Ag-doped CuO sample. They have studied cyclic stability for 2000 cycles at current density of 1 A/g

in 6.0 mol dm^{-3} KOH solution and found 61% capacitance retention for Ag-doped CuO nanosheet array sample. This enhancement in supercapacitance behavior was attributed to presence of Ag particles coated the CuO nanosheet array which improved the electrical conductivity [172].

Shaikh et al. have reported ruthenium doped CuO nanostructure thin film on stainless steel prepared by colloidal solution method followed by spin coating for supercapacitor application with 1 M solution electrolyte of Bronsted acidic (3-carboxymethyl-1-methylimidazolium bisulfate [CMIM] [HSO₄]) ionic liquid. They found that Ru-doped CuO thin films exhibited higher specific capacitance with larger working potential window as compared to un-doped CuO thin films sample. The 15 vol% Ru-doped CuO thin film sample exhibited maximum specific capacitance of 406 F/g at scan rate of 10 mV/s. They have studied the cyclic stability of un-doped and Ru-doped CuO thin film by 2000 cycles of CV at scan rate of 40 mV/s in potential window range of 0-0.3 V and -0.2-0.5 V, respectively in 1 M Na₂SO₄ electrolyte solution, which revealed their good stability. This improved supercapacitor performance was attributed to increase in electrical conductivity with increase in concentration of ruthenium [173].

On the basis of above literature survey the effect of dopant on metal oxide nanoparticles can be summarized as follows;

1. Doping impacts useful structural properties in a metal oxide for versatile and efficient applications. For example dopant can produce a defect and strain in the crystal structure which could enhance the conductivity of the metal oxide nanoparticles.
2. An optimum amount of dopant can lead to maximum change in properties of the metal oxide nanoparticles.
3. Doping may cause the formation of new compound with fundamentally different physicochemical properties.
4. Dopant can tune the structural, optical, electrical and magnetic properties of the host metal oxide nanoparticles matrix.

Table 1.2 Doping assisted modifications in copper oxide nanostructures for several applications

Materials	Fabrication	Factor effecting properties	Improvement in its properties	Reason for improvement	Application	Ref.
Mn-doped CuO nanoflakes	Wet chemical	Surface defects, oxygen vacancies	Pristine CuO exhibit room temperature ferromagnetism (RTFM) while doped don't show RTFM, CuO is more ethanol sensitive than Mn-doped CuO	presence of surface spin initiating from defects and oxygen vacancies, thus surface defect played important role in magnetism as well as ethanol sensing	Ethanol sensing	174
CuO doped with Li, Ni, Co, Ag, Zn and Mg,	Flame spray pyrolysis (FSP)	Conductivity of doped materials and photo-electrode resistance	doping of Li, Ni, Co, Ag, Zn and Mg, into CuO thin film leads to increase in the conductivity by two orders of magnitude while addition of Cr, Fe, and Mn leads to lower conductivity, by 100 times. dopant influence the photocurrent density	Photocurrent density was found to be independent of conductivity because once the conductivity reaches to a level after which material can produce electron but due to less surface area these were not involving in the process	Water splitting	175
Pd (IV)-doped CuO oxide composite nanofibers (PCNF)	Electro-spinning	Electro-catalytic activity towards the oxidation of glucose	lower oxidation voltage (0.32 V) and ultrafast (1 s) and ultrasensitive current ($1061.4 \text{ l AmM}^{-1} \text{ cm}^{-2}$) lower detection limit (LoD) of 19 nM, good selectivity, reproducibility and stability	Pd sites acts as Lewis acid sites in the PCNFs for for adsorption of polar glucose molecules, because of lower electron occupancy in their 3d orbitals in comparison to the Cu sites, which works as Lewis bases, due to their	Glucose sensing	176

				non-bonded electron pairs. This increased residence time for the reactant species within the electrified interface at the electrode surface resulted for enhanced in the glucose oxidation		
Fe-doped CuO thin film	spray pyrolysis	Structural, optical, electrical and magnetic properties	Monoclinic structure with cubic CuFe_2O_4 impurities. The direct band gap estimation revealed blue shift and indirect band gap estimation revealed red shift in doped thin film samples. The activation energy in doped thin films was reduced. The magnetization of the CuO:Fe (10%) films at 300 K showed a hysteresis behavior with large coercivity.	The reduced activation energy attributed to deep donor levels developed due to Fe-doping.	No application reported	177
Fe and Ni codoped CuO nano-composites	chemical concentration precipitation method	effects of doped magnetic Ni ions on the exchange bias field and coercivity	Ferromagnetic MFe_2O_4 (M = Cu, Ni) particles in the antiferromagnetic CuO matrix, in which with the increase of Ni content, the exchange bias field increases monotonously but the	doped Ni ions promotes the formation of domain state in AFM and hence increases exchange bias field. But the behavior of coercivity is attributed to existence of the soft magnetic NiFe_2O_4 phase	No application reported	178

			coercivity first decreases.			
Ni-doped and (La, Ni) co-doped CuO films.	sol-gel spin coating	Structural, morphological properties, optical and wettability properties	Ni doping improved the (002) preferential orientation with crystallite size 24.2 nm and La co-doping reduced the crystallite size to 11.4 nm. Wettability enhanced with thickness and La codoping	Ni and La co-doping could efficiently control transmittance, optical band gap, and the refractive index of the films. Wettability enhance due to La codoping resulted deterioration in the film crystallinity owing to affect the surface free energy	No application reported	179
Pb doped CuO nanostructures	Successive Ionic Layer Adsorption and Reaction (SILAR) method	Structural, optical, morphological study	The morphology of the film surface changed from plate-like to coral-like nanostructures with increasing Pb concentration. The band gap increased suddenly with a small Pb doping (0.27 at.%) and then decreased slowly with increasing doping concentration	Pb doping concentration	No application reported	180
Mn-doped CuO nanostructures	SILAR method	morphological, compositional, structural and optical properties	The thickness of thin film increases and size of nanostructure decrease with Mn-doping concentration. Optical band gap of the films increases with increasing Mn-doping concentrations.	Due to substitution of Mn on Cu lattice sites	No application reported	156

Li doped CuO film	Flame spray pyrolysis followed by spin coating	Doping and film thickness	The photocurrent density and photon-to-hydrogen conversion efficiency enhanced by 5-10 folds in doped sample and charge carrier density increased by 2 fold. 2 at% Li-doped CuO film of thickness 1.7 μm at applied voltage of -0.55 V vs. Ag/AgCl in 1 M KOH revealed maximum photocurrent 1.69 mA/cm^2	Due to increase of electric conductivity of the film. Photocurrent density increased with increase in film thickness	Photo-electro-chemical cells	181
Li doped CuO thin films on Si(100) substrate	Pulse laser deposition	Doping concentration, Crystalline nature of the material.	The crystallite size increased from 7 to 14 nm and optical band gap decreased from 2.99 to 2.76 eV as a function of Li concentration	Reduction of band gap because of Li ion substitution at Cu sites in the CuO and band tailing effect	No application reported	182
Zn doped CuO nanostructure	Chemical solutions and rapid thermal annealing process.	Zn doping, structural, morphological, vibrational, chemical, electronic and sensorial properties.	Mixed CuO/Cu ₂ O phases resulted in better sensing properties of the sensors and demonstrated good potential for fabrication of reliable, selective and fast hydrogen sensors with high gas response.	The two mixed phases controlled by Zn-doping during synthesis, Zn doping improved the Hydrogen sensing	Hydrogen and ethanol sensing	183

Ni doped CuO nanostructure	microwave-assisted combustion synthesis method	structural, morphological, optical, and magnetic properties	Morphology transitioned from nanoflower shape to nanoparticles then further to nanocrystal as a function of Ni concentration. The optical band gap increases with Ni-doping concentration, ferromagnetic at room temperature	Due to Ni ²⁺ doping in CuO structure, the change in the band gap was attributed to d-d transitions	No application reported	184
Mn doped CuO nanoparticles	Co-precipitation method	Microstructure and particle size due to calcinations from 250 to 850 °C	Crystalline Cu _{1-x} Mn _x O core surrounded by an amorphous CuO shell, for particles < 22 nm, real glass behavior for 11 & 22 nm particles and ferromagnetic for particles size > 35 nm	Observed ferromagnetic behavior owing to the coexistence of Mn ²⁺ and Mn ³⁺ ions	No application reported	185
Zn doped CuO nanoparticles	Sol-gel	Zn doping, structure and morphology	Shift in XRD peaks, cluster of grapes like morphology of NPs, crystallite size of pure and doped CuO ranges from 13.2 to 31.2 nm and 17.3 to 22.3 nm, respectively	Shift in the XRD peaks corresponds to the Zn ion replacement of Cu site in the lattice structure without affecting its crystal structure	No application reported	186
Fe, Ni Doped CuO	Co-precipitation	Fe and Ni doping, magnetic and structure	Isomorphous structure formation, Neel temperature in the magnetization of Fe (x=0.06) doped CuO reduced from 213 K to 70 K, while no change in it in Ni doped	Change in the structure nature due to the dopant, the decrease in Neel temperature is due to the formation of different electronic structure	No application reported	187

			sample			
Mn doped CuO thin film	Radio-frequency magnetron sputtering	Mn dopping, ferromagnetism, structure	15.2%-29.8% Mn doped CuO thin film showed ferromagnetism between transition temperature 87.0 and 99.5 K due to several interactions between Mn & Cu ions	Ferromagnetism produced due to ferromagnetic coupling between Mn ions mediated by Cu ions	No application reported	188



Thus, the physical and chemical properties of CuO nanostructures strongly depend on the structure, size, shape and chemical composition, which can be tuned by ion implantation and chemical modifications. Therefore, modifications in these parameters of a nanostructures influence the primary need of nanoscience and nanotechnology at a glance. These modifications studies provide basic potential information for both theoretical studies and practical applications in microdevices and nanodevices.

1.8 Aim and scope of this thesis work

1. There exist sufficient scope for developing CuO nanoparticles for electrochemical applications, e.g. as supercapacitor and as an efficient electrode for glucose sensing. The physic-chemical properties of CuO nanostructures strongly depend on their size, shape, structure and chemical composition. These can be tuned by employing different modification strategies, e.g., low energy ion implantation, role of capping agents with different molecular structures and by controlled doping with p & d block elements.
2. Low energy ion implantation induces defect at sub-surface regions. The effect of high charge state ion beam with tens of keV energy would be interesting to study the nature of modification of CuO nanostructure. The energy will be chosen on the basis of the stopping power calculation from SRIM. The CuO films will be deposited by pulsed laser deposition to prepare samples for ion implantation.
3. Capping agents play primarily role to inhibit agglomeration of nanoparticles which are synthesized by chemical routes. However, the molecular structure and the nature of functional group in the capping agents may have an impact in the transportation of charges. The effect of capping agents on the supercapacitor behavior will require systematic studies.
4. Similarly, dopants play important role in incorporating changes in the size, structure and morphology of host nanoparticles. In view of this, the effect of cobalt (a 3d element) and selenium (a 4p element) will be used as dopant. Here, Co is chosen as it an electrocatalytic active element. Similarly Se is chosen as there are no reports on its electrochemical effect due to doping in CuO.
5. The supercapacitor behavior of the capped and doped CuO nanoparticles will be investigated by recording cyclic voltammetry, galvanostatic charge-discharge and electrochemical impedance spectroscopy studies. These modified CuO nanoparticles

will be used to fabricate electrode/device for glucose determination and symmetric solid state supercapacitor.

6. The modified CuO nanoparticles will also be studied as electrode for sensing glucose in human blood and urine matrix.



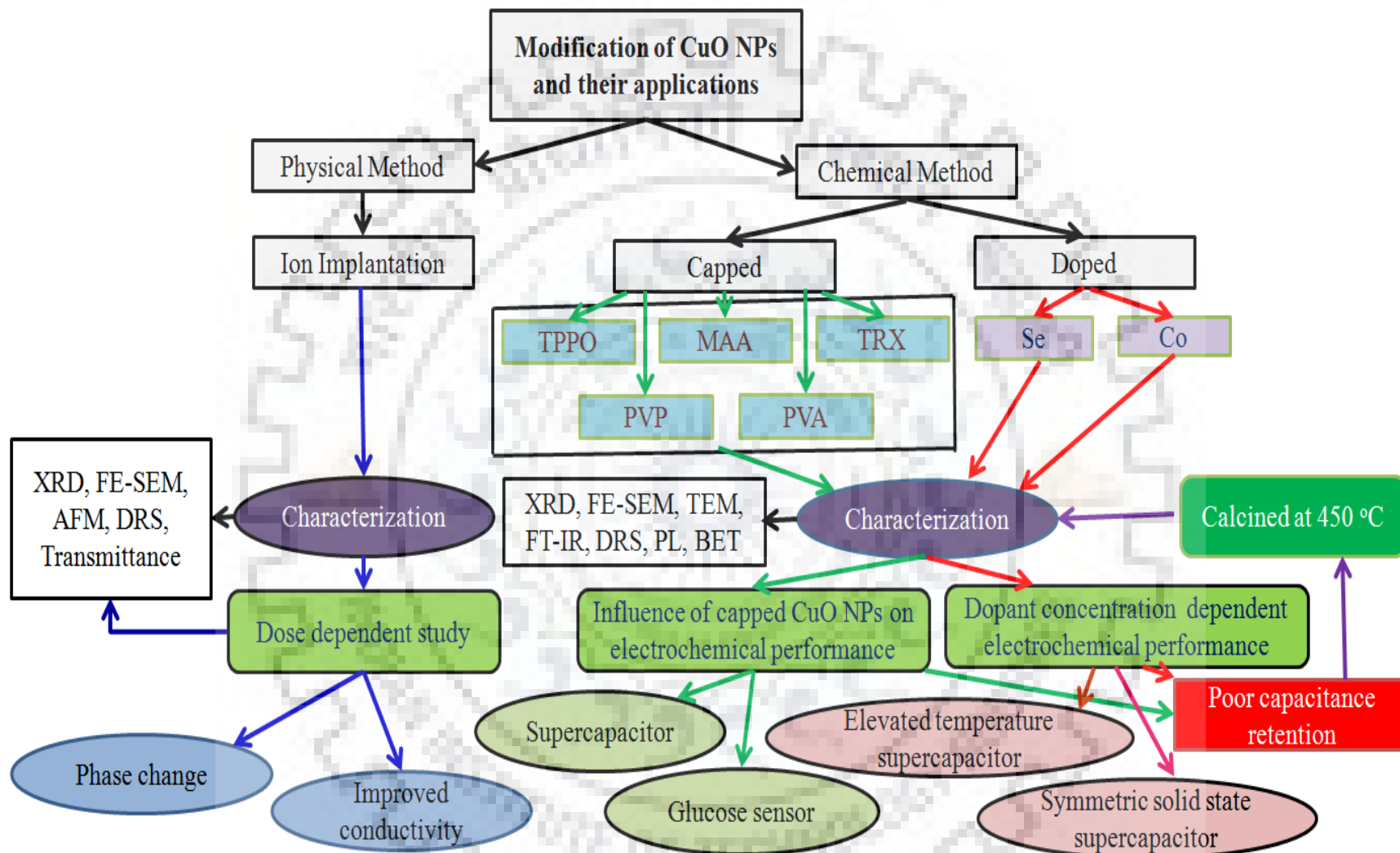
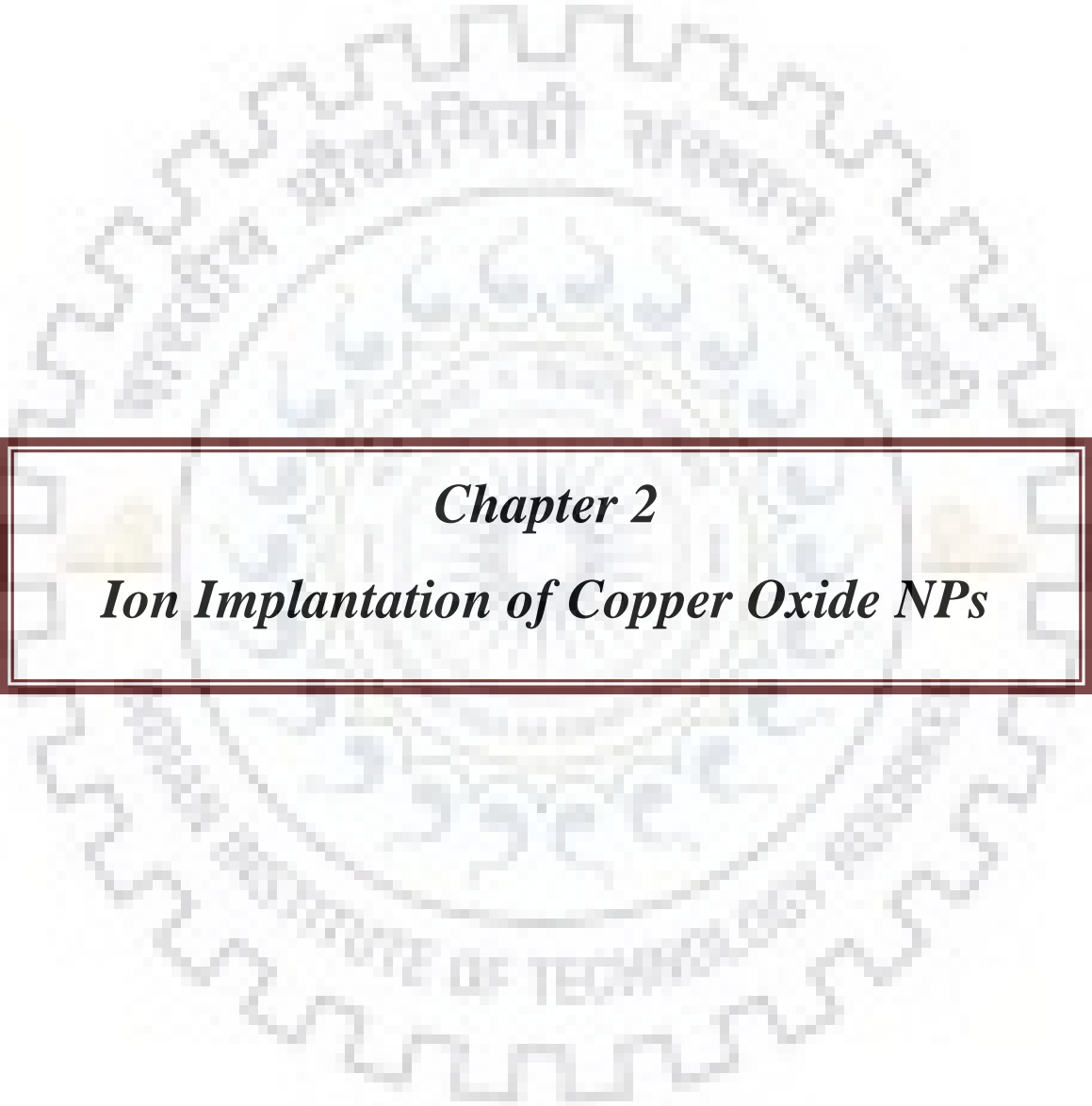


Fig. 1.4 Schematic flow chart of objective.



Chapter 2

Ion Implantation of Copper Oxide NPs

2.1 Introduction

Copper oxide nanoparticles is a versatile material with wide range of applications, e.g., gas sensors, biosensors, thin film transistors, magnetic storage media, high temperature superconductors, energy storage and spintronics [189-195]. It is a potential material for photovoltaic devices owing to its favorable band gap for harnessing visible light of the solar spectrum [196-198]. Copper oxide primarily exist in either of the two well established stoichiometric forms such as Cu_2O and CuO , corresponding to cubic and monoclinic crystal structures, respectively. Both are p-type semiconductors, where the Cu_2O is a preferred choice for solar cell applications owing to its high optical absorption coefficient in visible region than that of CuO [199]. Moreover, Cu_2O is a transparent material and the maximum photocurrent of 14.7 mA cm^{-2} under standard AM 1.5 irradiation [200], with the theoretically calculated energy conversion efficiency of 20% [201]. There is a need for developing methodology for fabricating pure and stable Cu_2O phase [180]. Deposition techniques are most commonly used for growing polycrystalline copper oxide thin films. However this technique suffers for a drawback as it leads to formation of both Cu_2O and CuO phases [135, 202, 203]. Literature reports indicated that post depositional treatments, e.g. thermal annealing improved phase stability and reflected on structural, optical and vibrational properties of the materials [204]. A schematic representation of post depositional treatment effect is illustrated in Fig. 2.1.

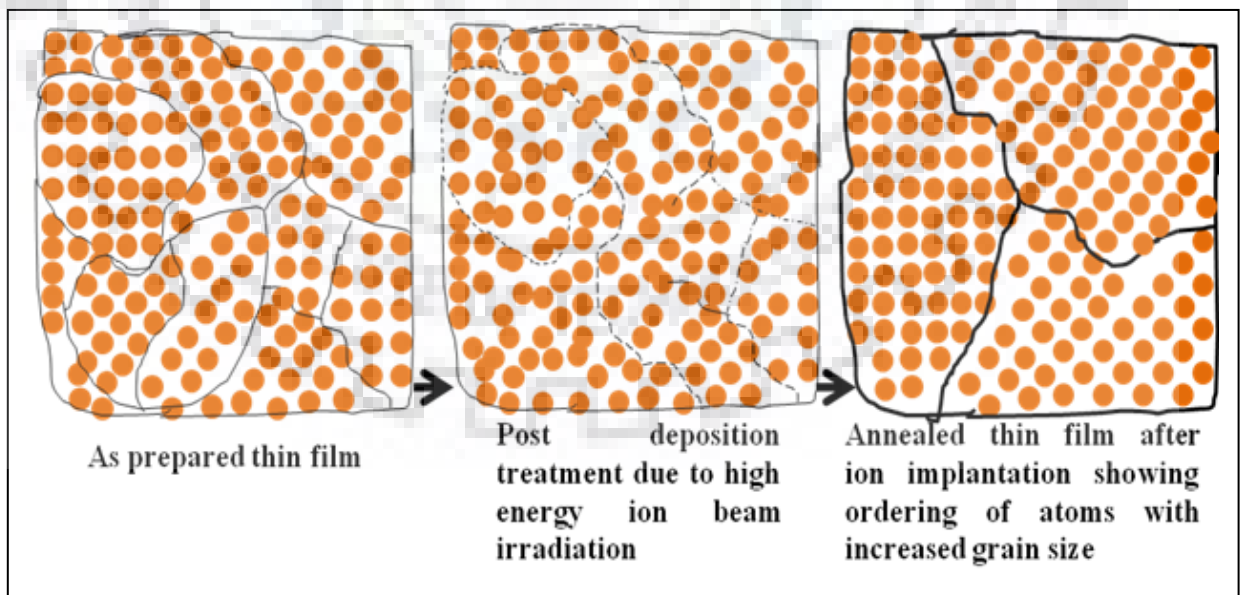


Fig. 2.1 Schematic illustration showing changes in the grains of thin film during post treatment.

However, thermal annealing is associated with temperature gradient across the material thickness which might result in undue crystal growth at higher temperature. This is not suitable for processing nanocrystalline materials, as uncontrolled crystal growth could destroy the nanocrystalline structure. Alternately, high energy incident ions of the order of 100 MeV, has been reported as a post depositional treatment. Here the local temperatures can be potentially raised to the order of 1000 K due to the interaction of such high energy ions with target atoms [204].

The modification of material depends upon the energy of the ion beam, types of ions, fluence, and angle of incidence on the material surface. Each types of ion have its own impression on modified material due to its unique features. These energetic ion beams lose their energy via electronic collision and nuclear collision. The energy loss at lower energy is attributed to nuclear energy loss phenomena while the energy loss at higher energy is attributed to electronic energy loss phenomena. This is schematically represented in Fig. 2.2. The energy loss of ion beam along the depth of the material is defined as “stopping power”, which is represented by dE/dx . The stopping power depends on the composition of the material. The energy loss due to electronic collision is attributed to slowing down of ion beams by inelastic collision with bound electrons. Such collision interaction may change the charge state of implanted ions while traversing through the material. In nuclear energy loss, ion beams lose their energy by elastic collisions between the implanted ions and lattice atoms of material.

Ion implantation by a few tens of keV is different from those by high energy (MeV order) ion beams. The low energy ion beam mostly lose its energy via nuclear energy loss and thus, it has a potential to modify the lattice structure. The modification is restricted to a few layers at surface of the material. On the other hand high energy ions modify the materials at greater depths and they exhibit both electronic as well as nuclear energy loss due to continuous energy loss via cascade of collisions with the materials. Consequently the high energy ion irradiations are more prone to irradiation damage. Therefore, low energy (< 100 keV) ion-implantation is a unique post-depositional treatment suitable for nanoscale materials as the interaction depth of the incident ion matches with the dimensions of the nanoparticles. Such interaction can potentially modify the structural, optical and optoelectronic properties of nanostructured materials due to its precise control over the dopant profile and depth of the implantation owing to energy dependent stopping power phenomenon of energetic ions [205].

The effect of low energy ion implantation is different from that of the high energy ion irradiation owing to differences in the energy loss processes of the incident ions

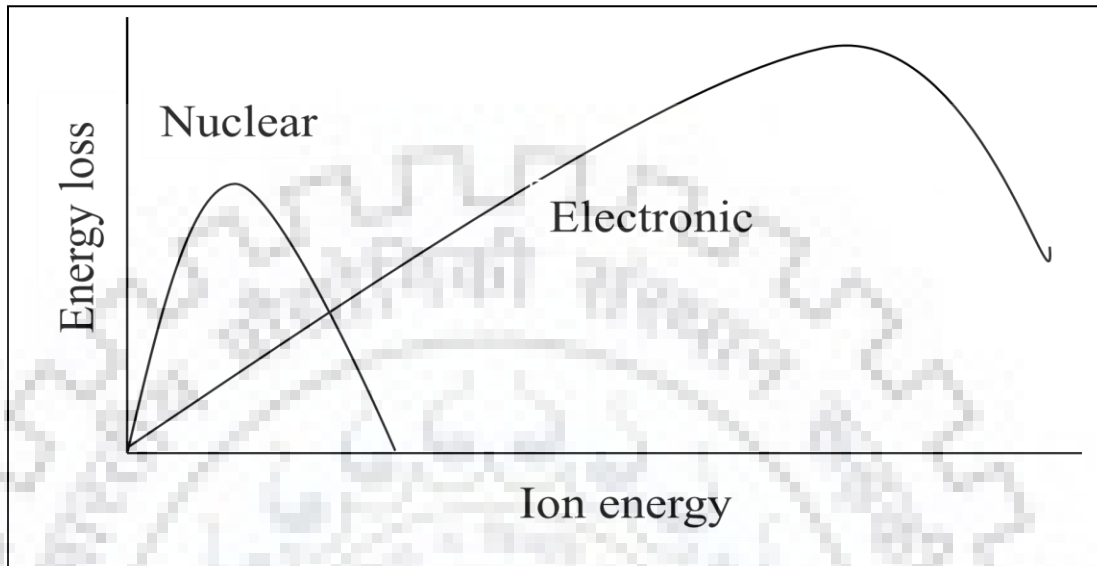


Fig. 2.2 A representation of nuclear and electronic energy loss profile of the incident ion as a function of ion energy.

Contrary to the high energy ion irradiation, which is predominantly associated with electronic energy loss process, the low energy ion implantation is associated with nuclear energy loss process. Consequently, low energy ion implantation in semiconductor type materials might lead to the following three cases: (a) changes in electrical property of the material due to the introduction of implanted species as dopants, (b) changing in optical band gap due to emergence of new energy levels of the dopants and modify optoelectronic property, (c) lattice disorder and change in structure or phases of the implanted materials [133].

Literature search reflected very few studies on effect of low energy ion irradiation on nanoparticles and nanocrystalline thin films [133, 134]. The motivation of the present study is to study the effect of ion implantation using low energy N^{5+} beam as a post deposition method on Cu_2O thin film prepared by pulsed laser deposition technique. The emphasis is on the changes in the structural (phase transformation, morphological change), optical and electrical properties of Cu_2O thin films.

2.2 Experimental

2.2.1 Preparation of copper oxide thin film

The PLD technique (Excel Instruments, India) was used to deposit copper oxide thin films on glass substrate. A Cu_2O target was mounted on a multi-target carousel system provided with stepper motor and DC motors simultaneously. The Nd-YAG laser operating on 355 nm wavelength i.e. the third harmonic of the laser with 100 mJ/pulse energy was used for ablating the target material. The deposition parameters were optimized to fabricate a thin film of stable copper oxide phase on ultrasonically cleaned glass substrates. The substrate temperature was kept at 350 °C with oxygen gas pressure of 100 mTorr.

2.2.2 Low energy N^{5+} ion implantation

Batches of copper oxide films were mounted on a sample ladder in the scattering chamber of the low energy ion implantation facility of Variable Energy Cyclotron Centre (VECC), India equipped with electron cyclotron resonance (ECR) ion source. The samples were implanted with 50 keV N^{5+} ions at an angle 45°. The extraction voltage of the ECR ion source was kept at 10 kV and the Q/m resolution was better than 1 in 40. The ion beam was scanned over 10 x 10 mm² area on the sample using X-Y magnetic beam scanner. The beam current was approximately 1 μA and the recorded particle fluences were 2.5×10^{15} , 1×10^{16} and 4×10^{16} particles/cm².

2.2.3 Structural, surface and optical analyses

The X-ray analysis was performed by using a Bruker D8 Advance diffractometer using CuK_α ($\lambda = 1.54 \text{ \AA}$) radiation for the phase identification, grain size measurement and threshold grain analysis. The scan rate used was 1° min^{-1} and the scan range was from 15° to 80° . The optical studies of the pristine and the implanted copper oxide were studied by measuring their transmittance spectra (using UV-Vis-NIR spectrophotometer, Cary 5000) in the range 300 to 2500 nm. The surface morphology of the pristine and the batches of implanted thin films was studied using Atomic Force Microscopy (AFM, NT-MDT, Ntegra) operated in semi-contact (tapping) mode and by field emission scanning electron microscopy (FESEM). The batches of pristine and implanted samples were sputter coated with gold and the FESEM images were recorded with Zeiss Ultra Plus operated at 15 kV. The elemental composition of the thin films

was determined by energy dispersive X-ray spectrometer (EDX) attached with SEM. The electron backscatter diffraction was used to obtain the grain size distribution of thin films.

The electrical conductivity of the pristine and post depositional ion implanted samples was studied by measuring electrical sheet resistance using a two point probe system (Keithley Model 4200 SCS). Very thin layer (10 nm) of gold was sputter coated at selected positions on the surface of the pristine as well as batches of implanted sample through a shadow mask to form respective circular gold dots of 1 mm diameter, separated by 3 mm. These dots were used as electrodes for measuring sheet resistance by applying voltage in the range ± 10 V.

2.3 Results and Discussion

2.3.1 Structural study of pristine and ion implanted thin films

The X-ray diffraction (XRD) pattern of the pristine thin film prepared by pulsed laser deposition at 80 mTorr partial pressure of oxygen and 350 °C substrate temperature exhibited amorphous signature (Fig. 2.3a). The post deposition treatment of thin film was performed by ion implantation method by using 50 keV N^{5+} ion beam. It was found that the amorphous nature of the pristine thin film prepared at 80 mTorr was modified to a well crystalline Cu_2O after implantation with particle fluence of 1.0×10^{16} particles/cm². The XRD pattern of the implanted sample given in Fig. 2.3b revealed sharp peaks at 2θ values 36.3°, 42.1°, 61.2° and 73.4° corresponding to the (111), (200), (220) and (311) planes of cubic phase of Cu_2O (matched with JCPDS No. 00-005-0667). The crystallite size (δ) of the Cu_2O phase was calculated by Debye Scherrer method given as [206]:

$$\delta = 0.9\lambda/b\cos\theta,$$

where λ is the wavelength of the X-ray, ' b ' is the line broadening measured at half height of the most intense diffraction peak, θ is the Bragg angle of the particles.

The crystallite size (δ) of Cu_2O in the implanted sample was determined to be 20.2 nm. The improvement in the crystalline nature of the Cu_2O phases in the post depositional ion implanted sample can be attributed to ordering of the constituent atoms in the unit cell. A similar enhanced crystalline nature of ZnS nanoparticles has been reported by our research group earlier using low energy ion implantation [207]. The ordering of the atoms in the as

deposited samples is likely to be due to transfer of thermal energy arising due to energy loss process via cascade collisions of energetic incident ions with the constituents of the thin film.

Theoretical calculations revealed that the total energy deposition by 1×10^{16} particles/cm² was 80 J/cm² over a depth of ~89 nm, derived from SRIM calculation [208] in copper oxide matrix for 50 keV nitrogen ion beam.

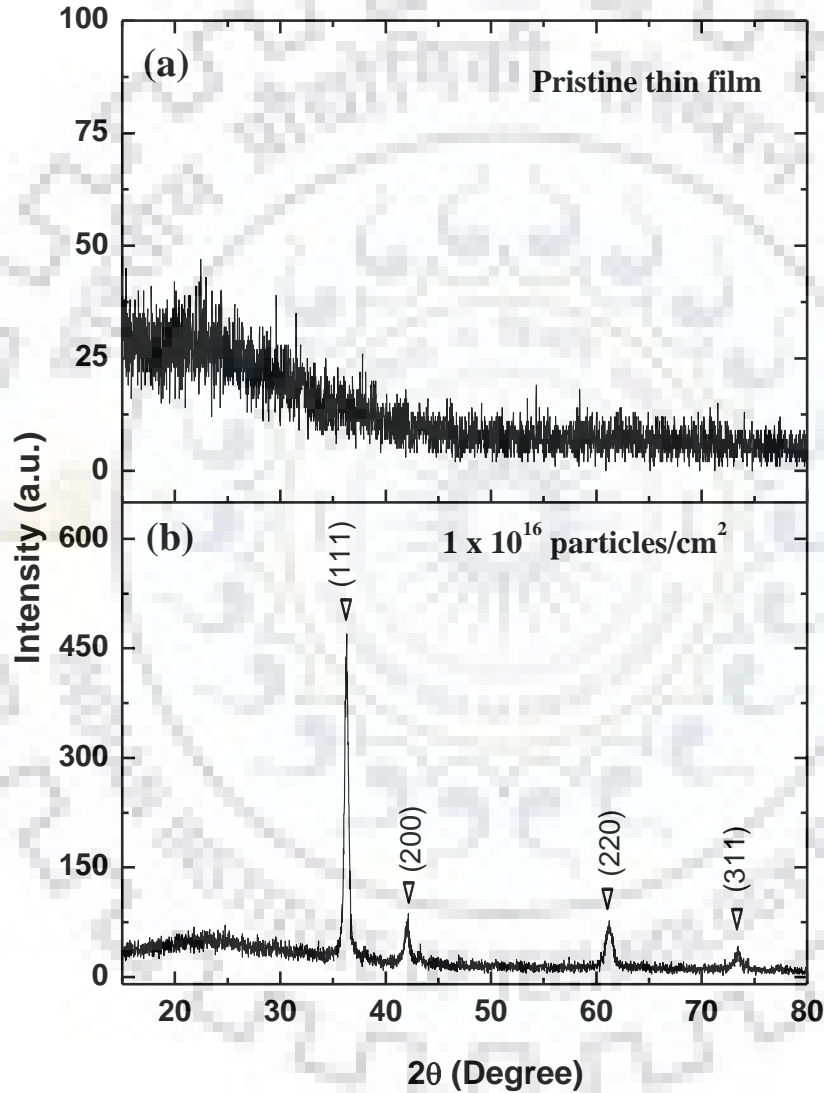


Fig. 2.3 X-ray diffraction patterns of the Copper oxide thin films as-deposited and N^{5+} ion implanted at 80 m Torr oxygen partial pressure (a) pristine and (b) 1×10^{16} particles/cm².

The pristine thin film deposited at 100 mTorr oxygen pressure revealed formation of weak crystalline phases of Cu_2O and CuO (Fig. 2.4a). The diffraction peaks at 2θ values 36.3° ,

42.0° 61.1° and 73.3° corresponded to (111), (200), (220) and (311) planes of Cu₂O phase, respectively (matched with JCPDS No. 00-005-0667). Similarly the diffraction peaks at 2θ values 35.3°, 38.6° corresponded to (002), (111) planes of CuO phase, respectively (matched with JCPDS 00-045-0937). The crystallite size (δ) of Cu₂O and CuO phases was determined as 14.5 nm and 16.9 nm, respectively.

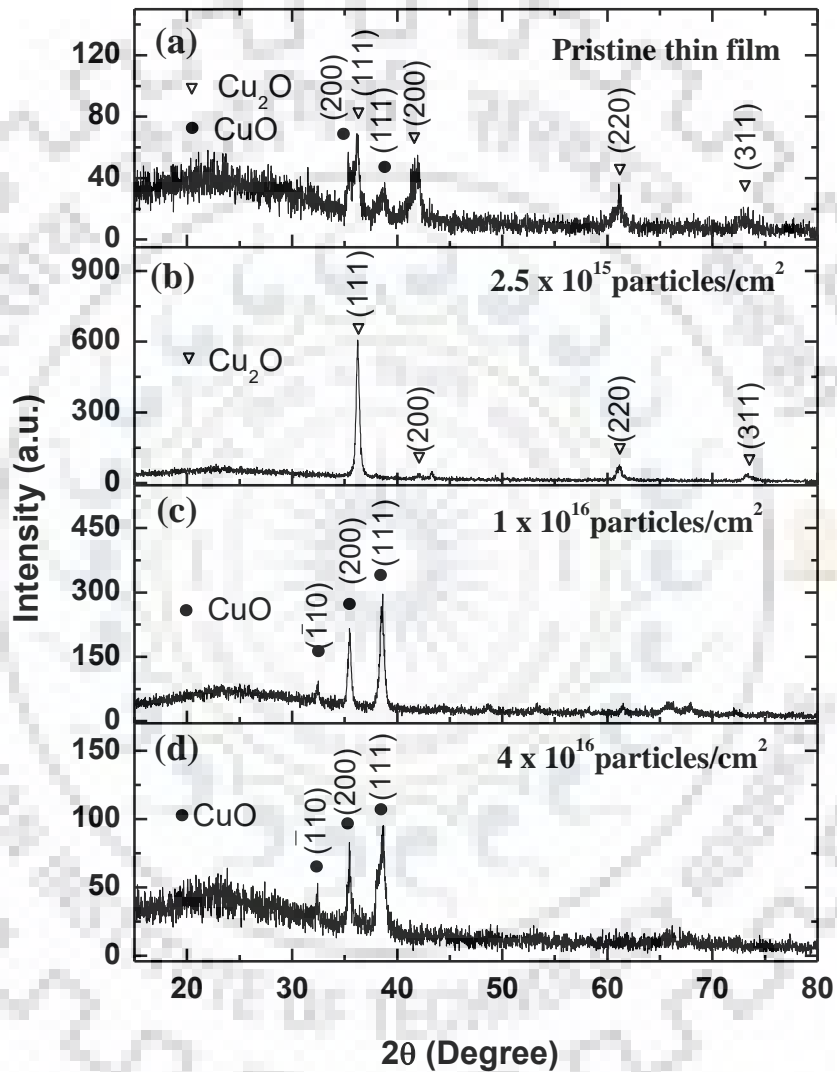
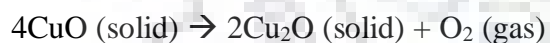


Fig. 2.4 X ray diffraction patterns of copper oxide thin films of pristine and N⁵⁺ ion implanted films as deposited at 100 mTorr oxygen partial pressure (a) pristine (b) 2.5×10^{15} particles/cm² (c) 1×10^{16} particles/cm² and (d) 4×10^{16} particles/cm².

It may be remarked here that the formation of copper oxide phase by deposition technique would depend on the concentration oxygen which is proportional to the ambient

partial pressure of oxygen and the substrate temperature. In PLD technique, the oxides of copper are formed when the ambient partial pressure of oxygen is larger than the dissociation pressure of the oxygen in equilibrium with copper. At higher oxygen pressure, the Cu – O phase diagram reflects formation of both Cu₂O and CuO phases during oxidation [209]. In our investigation, no crystalline phase of copper oxide was formed at 80 mTorr while Cu₂O was formed as the major component in the thin film fabricated at 100 mTorr partial pressure of oxygen, and the results are consistent with recent studies [210].

The post depositional ion implantation thin film implanted with 2.5×10^{15} particles/cm² revealed formation of a single Cu₂O phase. The XRD studies of the implanted sample revealed diffraction peaks at $2\theta = 36.2^\circ, 42.0^\circ, 61.1^\circ$ and 73.3° corresponding to (111), (200), (220) and (311) planes of cubic Cu₂O phase which matched with JCPDS No. 00-005-0667. (Fig. 2.4b), and the crystallite size was measured as 23.5 nm. An equivalent energy of 20 J/cm² was transferred during implantation with 2.5×10^{15} particles/cm². The transformation of mixed copper oxide phases to single Cu₂O phase by ion implantation is attributable to thermal effect owing to stopping of the incident energetic ion beam in the target. A schematic representation of ion implanted induced modification is demonstrated in Fig. 2.5. In this case the CuO phase, which is the minor component in the pristine sample, presumably reduced to Cu₂O by temperature dependent disproportionation type of reaction given as:



Such type of reaction is reported to occur at temperatures higher than 450 °C and at limited oxygen pressure [211, 212]. The required criteria were likely to be achieved by the rise in temperature during ion implantation under vacuum of the order of 10^{-6} Torr. The grain size of Cu₂O in the implanted sample was measured to be 23.5 nm. Notably, the measured grain size was greater than that of the Cu₂O developed during implantation of the thin film deposited at 80 mTorr.

It was found that the post depositional ion implantation of the batches of thin films prepared at 100 mTorr and implanted with higher particle fluencies e.g., 1×10^{16} and 4×10^{16} particles/cm² revealed phase transformation to CuO phase (Fig 2.4c, 2.4d). This was confirmed from the XRD studies of the respective implanted samples which revealed diffraction peaks at 2θ values $32.5^\circ, 35.5^\circ$ and 38.6° values corresponding to ($\bar{1}10$), (200) and (111) planes of

monoclinic CuO phase, matched with the JCPDS No. 00-045-0937. It implied that the Cu₂O phase, which was the major component in the pristine sample prepared at 100 mTorr oxygen partial pressure, was oxidized during ion implantation at higher particle fluence owing to higher rate of transfer of energy to the target. The local temperature in the sample was apparently higher for larger particle fluence. It is found from literature that transformation of Cu₂O phase to CuO could occur at 900 °C where the (111) plane of CuO is preferably oriented [213].

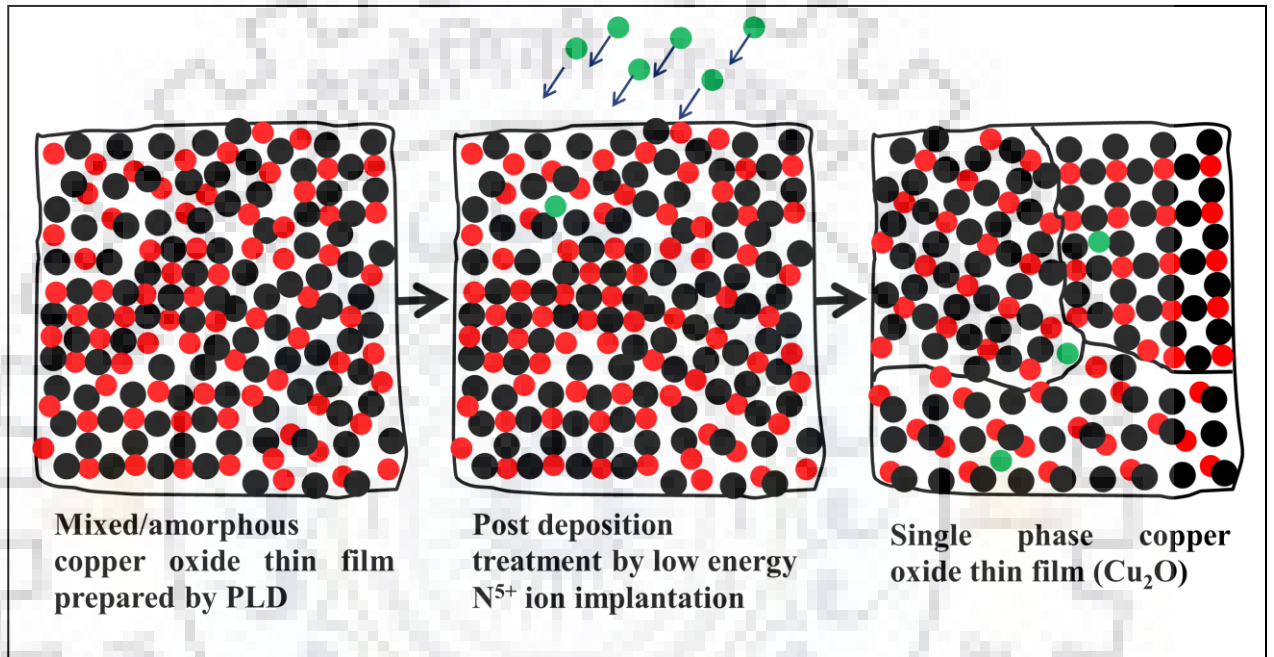


Fig. 2.5 A schematic representation of the events that took place during low energy ion implantation on amorphous/mixed phase copper oxide thin film and its impact on atomic level is presented. (● oxygen; ● copper and ● N⁵⁺ ion beam)

Notably, the XRD of the ion planted sample revealed maximum intensity in the (111) plane and the corresponding grain size of CuO in the implanted samples were determined to be 19.4 nm. Though rise in temperature in the sample during implantation was not measured, but it is quite likely that transfer of such large energy (80 J/cm² for 1 × 10¹⁶ particles /cm²) was the key towards the observed phase transformation of copper oxide. However, the sample implanted at 4 × 10¹⁶ particles/cm² reflected reduction in the intensity of the characteristic diffraction peaks of CuO (Fig. 2.4d). The corresponding crystallite size of CuO in the implanted samples was determined to be 9.4 nm. The decrease in the grain size is an indication

of radiation damage of the of the crystal structure owing to transfer of 320 J/cm^2 for 4×10^{16} particles/cm². Such reduction in crystallinity due to radiation damage by high particle fluence is a common phenomenon [214].

2.3.2 Surface morphology

The FE-SEM surface morphology of pristine and implanted thin film samples were shown in Fig. 2.6.

The pristine thin film deposited at 80 mTorr oxygen pressure exhibited no grain boundaries and is in good agreement with the amorphous nature recorded by XRD (Fig. 2.6a). The post depositional ion implanted thin films exhibited formation of distinct grains (Fig. 2.6b). The EDX analysis of these structures revealed characteristic X-ray peaks of Cu and O, corresponding to the Cu₂O phase, confirmed from the XRD studies Fig. 2.6c. The thickness of the ion implanted thin film was measured to be 271 nm by scanning the cross-sectional view of the tilted sample Fig. 2.6d. Similarly, the thin film deposited at 100 mTorr oxygen pressure exhibited grain like structure (Fig. 2.6e). However the grain boundaries were not sharp which can be attributed to low order of crystallinity of the copper oxide phase as confirmed by XRD studies. The post depositional ion implanted thin film implanted with 2.5×10^{15} particles/cm² exhibited well defined grains similar to Fig. 2.3b. On the other hand, the thin film implanted with 1×10^{16} particles/cm² exhibited thin films with well defined grain boundaries (Fig. 2.6f).

The EDAX analysis of these thin films revealed characteristic peaks of Cu and O together with the constituents of glass substrate, which confirmed the fabrication of CuO phase as confirmed by XRD studies. Further, the observation of well defined grain boundaries indicated enhanced crystallinity of the copper oxide phase which was consistent with the XRD studies.

The detailed surface morphology of the pristine and the implanted samples was obtained from AFM studies measured in tapping mode. The pristine thin film (80 mtorr) exhibited very small average roughness = 5.75 nm, with rms value of 1.89 nm Fig. 2.7a. On other hand, the AFM image of the thin film implanted with 1.0×10^{16} particles/cm² exhibited average roughness of 50.54 nm with rms of 6.29 nm (Fig. 2.7b).

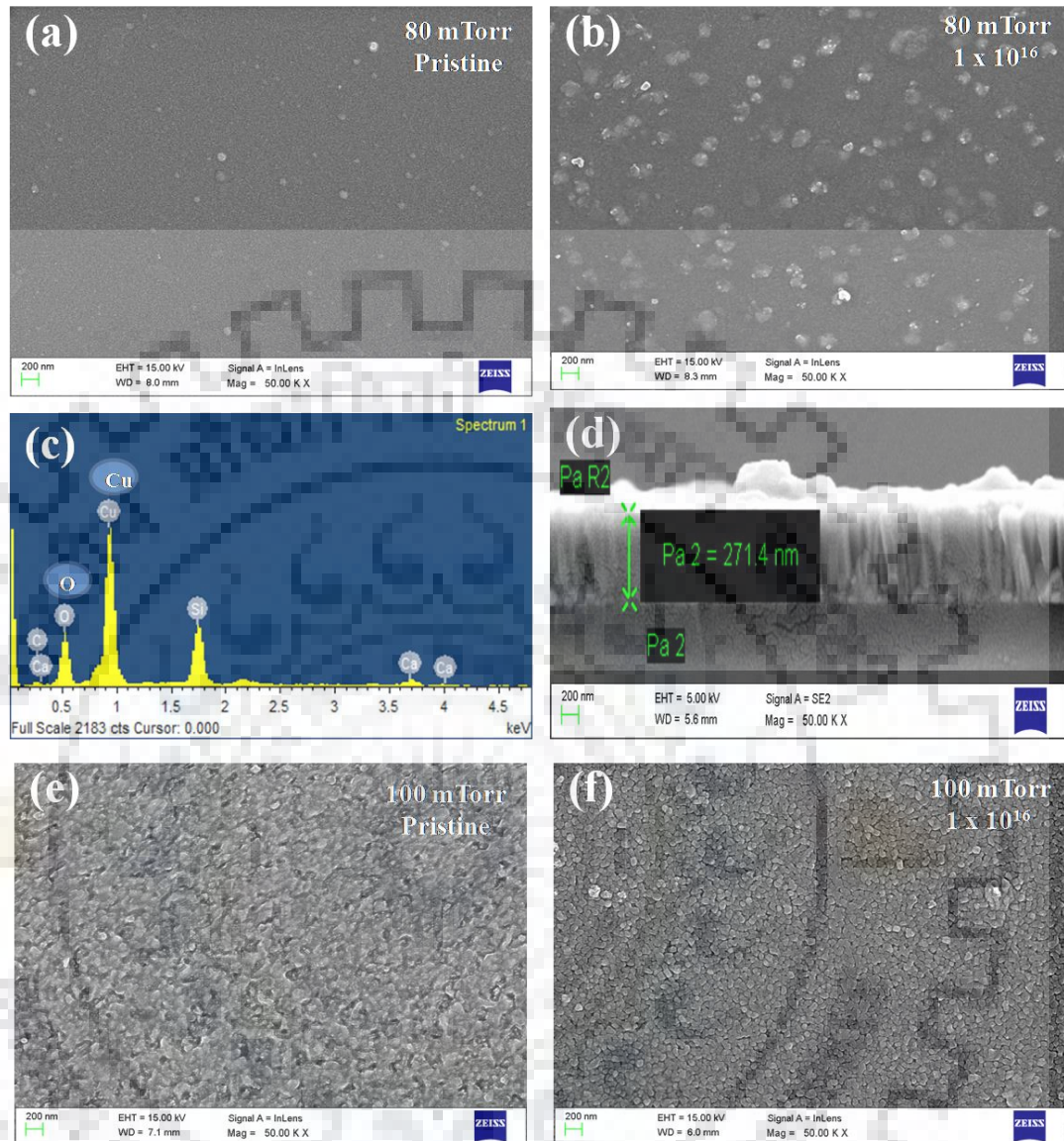


Fig. 2.6 Field emission scanning electron microscopy images of pristine and implanted copper oxide thin films (a) pristine thin film as deposited at 80 mTorr oxygen partial pressure (b) 80 mTorr as deposited film implanted with fluence 1×10^{16} particles/cm² (c) Energy dispersive X-ray analysis of copper oxide thin film (d) cross sectional view of film (e) pristine thin film as deposited at 100 mTorr oxygen partial pressure and (f) 80 mTorr as deposited film implanted with fluence 1×10^{16} particles/cm².

The increase in the surface roughness is the effect of ion implantation which induced the transformation of as-deposited amorphous copper oxide phase to crystalline Cu₂O phase, which is consistent with our XRD studies. The surface roughness was larger than the grain size

determined from Debye Scherrer formula. This is attributable to aggregation of nanoparticles. In the case of AFM studies of thin film (100 mTorr oxygen) both pristine and implanted batches exhibited aggregated nanoparticles of copper oxide whose surface roughness was similar to that of ion implanted thin film (80 mTorr oxygen), given in Fig. 2.7c-2.7f.

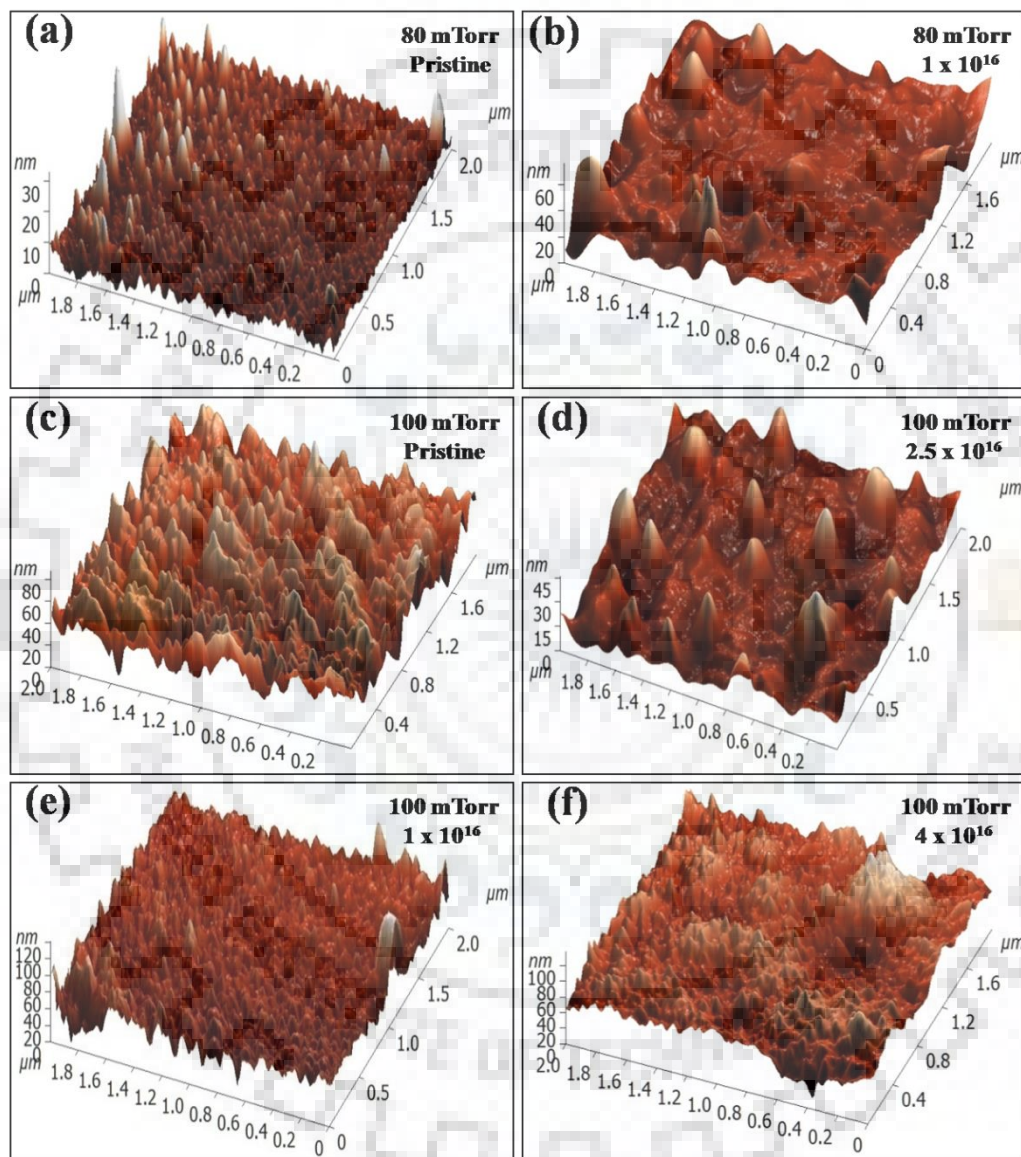


Fig. 2.7 Atomic force microscopy images of copper oxide thin film: as deposited at 80 mTorr oxygen partial pressure (a) pristine (b) 1×10^{16} particles/cm² and as deposited at 100 mTorr oxygen partial (c) pristine (d) 2.5×10^{15} particles/cm²; (e) 1×10^{16} particles/cm², (f) 4.0×10^{16} particles/cm².

2.3.3 Optical properties

Fig. 2.8 revealed optical transmittance spectra of the as-deposited pristine thin film and those of the ion implanted thin films with different particle fluence. The pristine samples deposited at 80 mTorr and at 100 mTorr exhibited high transmittance ($\sim 70\%$) in the near infrared region (NIR). In general, the transmittance profiles of the post depositional ion implanted thin films were different from the pristine thin films. Compared to the pristine sample the transmittance in the ion implanted samples was reduced in the NIR region. The reduction in the transmittance in the NIR region is attributable to enhanced scattering of photons owing to increase in the grain size of copper oxide phase as confirmed from the XRD analysis. The implanted samples (except the one corresponding to 4×10^{16} particles/cm²) exhibited sharp fall in the transmittance in the wavelength region of 400 – 550 nm. This can be attributed optical transitions corresponding to the band gap of the copper oxide phases in the implanted thin films. Further, decrease in the transparency in the visible region can occur due to incorporation of N as dopants in the thin films due to ion implantation, which is consistent with transmittance spectra of ion implanted samples [216]. Moreover, strong absorption of glass substrate in the UV region also contributed to decreased transmittance in the UV region. This indicated that the ion implantation modified the thin film deposited by PLD, which may be attributed to improved crystallinity and phase transformation as confirmed from XRD. The transmittance spectrum of the thin film implanted with very high particles fluence (i.e, 4×10^{16} particles/cm²), exhibited gradual increase in the transmittance profile up to 1250 nm followed by a decrease in the transmittance in the wavelength region 1250 to 2500 nm. The unusual transmittance profile in the band gap region could be due to lowering of crystallinity of the copper oxide phase due to collapsing of band structure, which is consistent with the respective XRD study. The tentative lowering in the crystalline structure at high particle fluence is attributed to effect of radiation damage in solids [216]. The decrease in the transmittance in the NIR region is attributable to biaxial and optical anisotropy exhibited by monoclinic CuO phase as compared to optical isotropy property of Cu₂O [217]. The optically anisotropic CuO phase causes double refraction in NIR region of spectrum.

The optical band gaps of the copper oxide phases formed in the pristine and implanted samples were determined from diffused reflectance spectroscopy studies using Tauc's relationship [218]:

$$(\alpha h\nu)^{1/n} = A(h\nu - E_g) \quad (2.1)$$

Where α : absorption coefficient, h : Planck's constant, ν : frequency of vibration, A : proportionality constant. The parameter ' α ' was calculated using Kubelka-Munk method [219]. Here the value of ' n ' was taken as 0.5 as copper oxide is a direct band gap material.

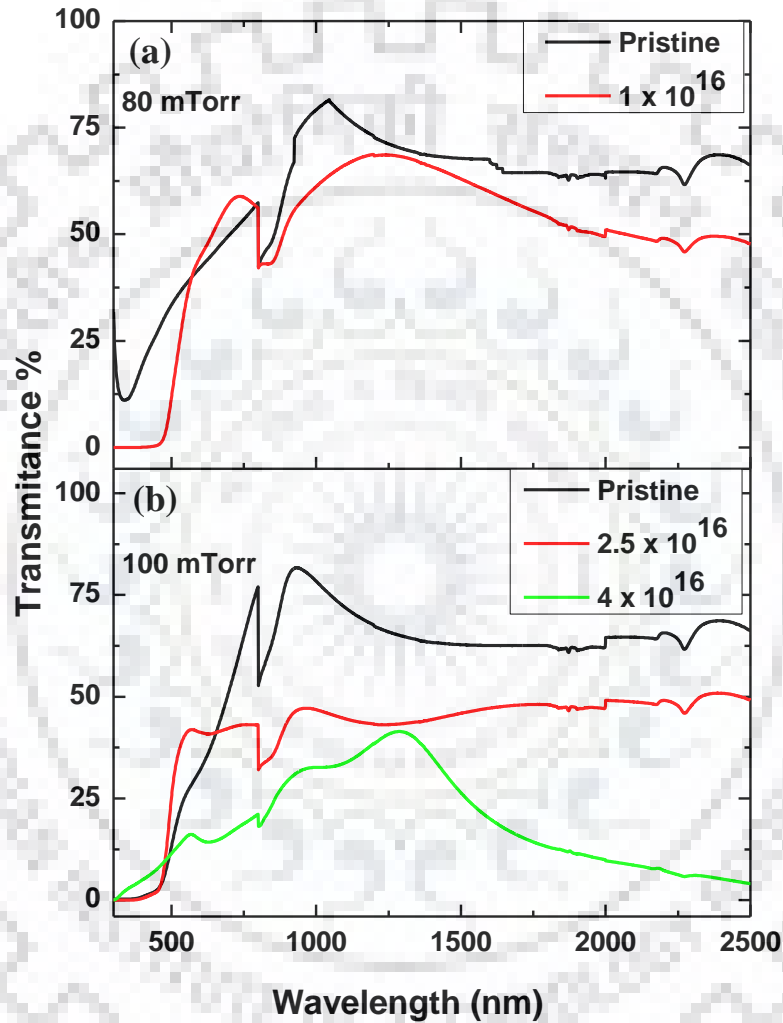


Fig. 2.8 Transmittance spectra of the copper oxide thin films: (a) as deposited at 80 mTorr oxygen partial pressure and ion implanted thin film with fluence 1×10^{16} particles/cm²; (b) as deposited at 100 mTorr oxygen partial pressure and ion implanted thin film with different particle fluence 2.5×10^{15} , 1×10^{16} , 4.0×10^{16} particles/cm².

The plot of $(\alpha h\nu)^2$ versus Energy ($h\nu$) did not reveal any band structure for the pristine sample prepared at 80 mTorr oxygen pressure which is consistent with XRD results (Fig. 2.3a). But the same batch of thin film implanted with 1×10^{16} particles/cm² of N⁵⁺ ion exhibited two distinct

signatures: namely (a) a type of modulated oscillation in the measured near infrared (NIR) region (i.e. 0.88 – 1.72 eV) and (b) characteristic features of band gap of Cu₂O phase (Fig. 2.9a). The oscillation profile observed in our studies was similar to that reported for Cu₂O thin film and attributed to the modulated interference fringes in the transparent region of Cu₂O films [220]. The optical band gap (E_g) was measured to be 2.10 eV and 2.21 eV. The band gap of 2.21 eV and 2.10 eV corresponded to that of different grain sizes of Cu₂O phase. The formation of different grain sizes is supported from XRD and AFM studies, discussed above. The measured band gap for Cu₂O, especially 2.21 eV was larger than that for the bulk Cu₂O. The increase in the band gap is attributed to fabrication of nanosized Cu₂O particles and our result is consistent with literature [180, 202].

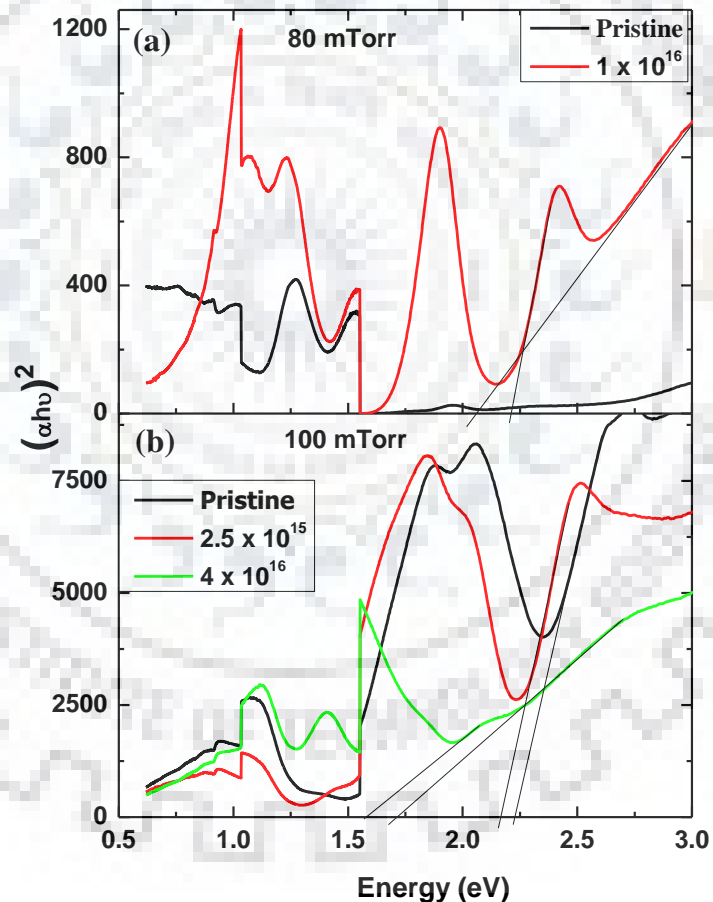


Fig. 2.9 Diffused reflectance spectroscopy of the copper oxide thin films: (a) as deposited at 80 mTorr oxygen partial pressure and ion implanted thin film with fluence 1×10^{16} particles/cm²; (b) as deposited at 100 mTorr oxygen partial pressure and ion implanted thin film with different particle fluence 2.5×10^{15} , 1×10^{16} , 4.0×10^{16} particles/cm².

In the case of thin film prepared at 100 mTorr oxygen pressure, the modulated oscillation in the NIR region was not significant (Fig. 2.9b). The band gap was determined to be 2.21 eV corresponding to Cu_2O phase. It may be remarked that the band structure of CuO was not detected as the CuO phase was a minor phase and its weak signals are likely to be overlapped with that of Cu_2O band structure. The band gap of the same batch of thin film implanted with 2.5×10^{15} particles/ cm^2 was found to be 2.16 eV, which corresponding to Cu_2O phase. The decrease in the band gap was due to increase in the grain size of Cu_2O phase due to ion implantation, which is consistent with the XRD and AFM results. On the other hand, the batch of thin film implanted with 4×10^{16} particles/ cm^2 revealed reduced crystallinity whose band gaps were determined to be 1.51 eV and 1.70 eV. The measured band gaps were attributed to CuO phases of different crystallite size.

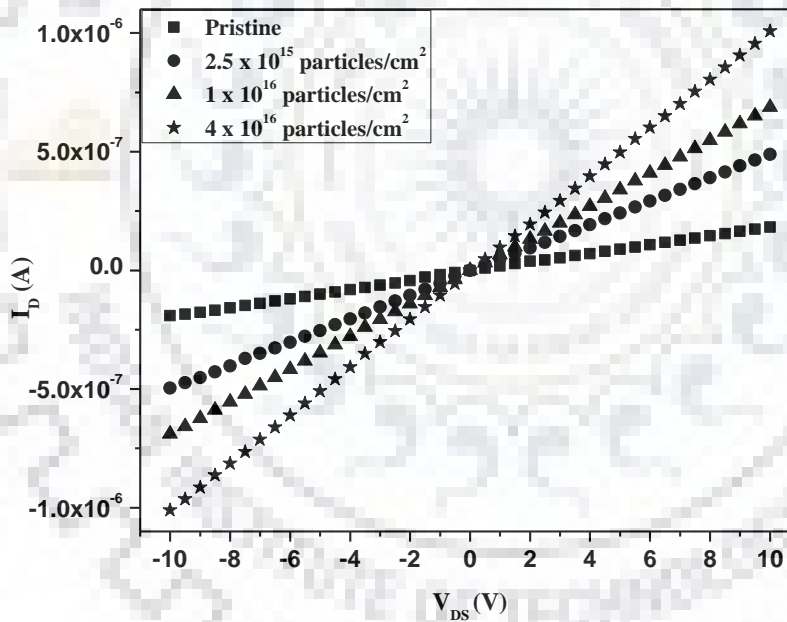


Fig. 2.10 $I_D - V_{DS}$ plot of pristine and ion implanted thin films comprising copper oxide phases

2.3.4 Electrical properties

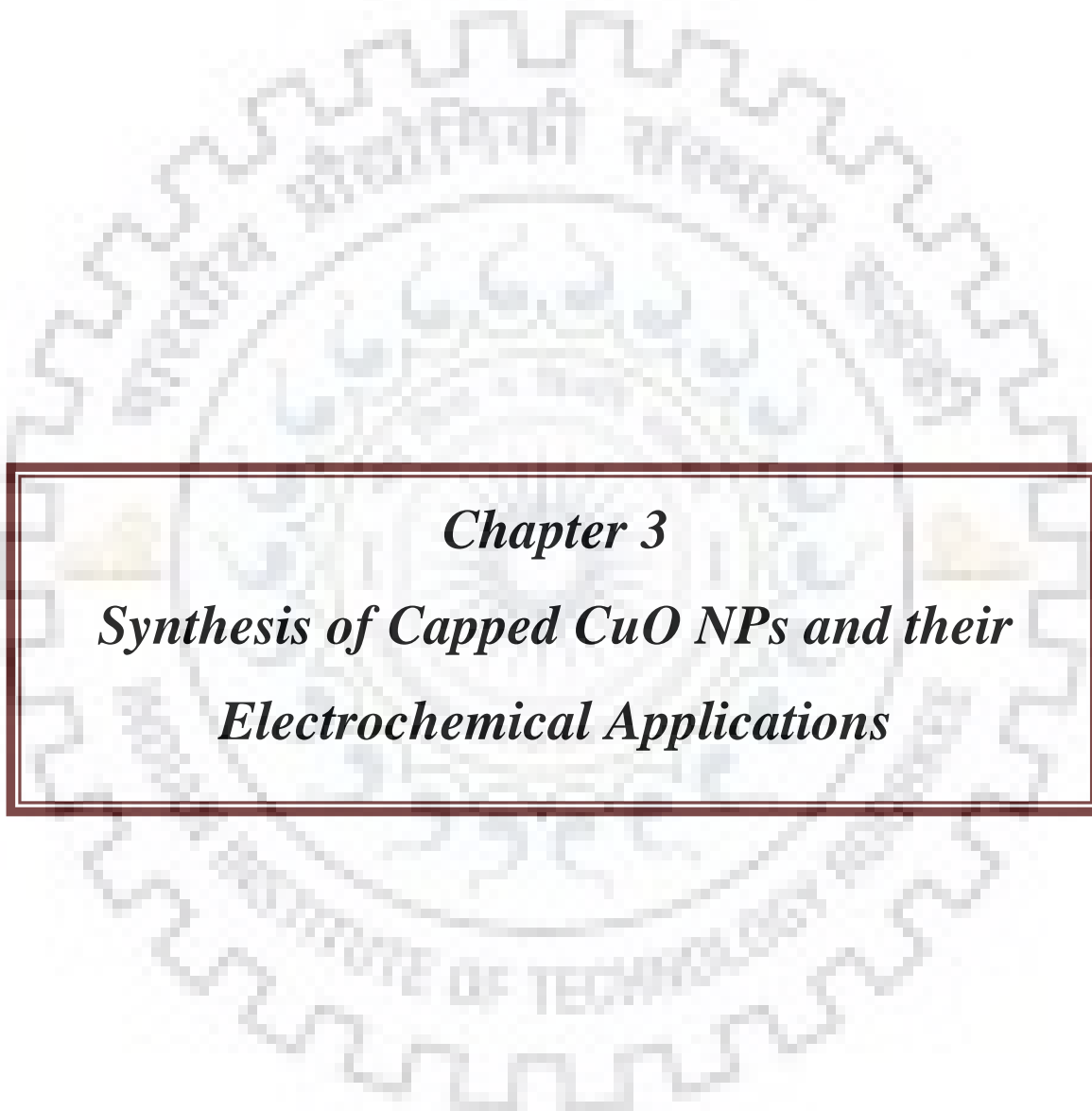
The electrical characterization of the pristine thin film and ion implanted samples deposited at 100 mTorr is given in Fig. 2.7. The plot of $I_D - V_{DS}$ plot revealed ohmic responses and all the cases passed through zero coordinate point. This implied that the resistances were

constant for all the cases. The slope increased with the particles fluence, indicating that the lowest resistance corresponded to the batch implanted with 4×10^{16} particles/cm². The observed decrease in the resistance can be attributed to two phenomenon (a) increase in the dopant concentration due to increase in the fluence and (b) transformation of Cu₂O phase to a CuO phase which exhibits higher electrical conductivity than Cu₂O [221]. From these results, it may be surmised that the optical and the XRD studies were significant to understand the effect of low energy ion implantation as a post depositional method on the copper oxide thin film deposited by PLD technique.

2.4 Conclusions

Low energy (50 keV) ion implantation is demonstrated to be useful method as a post depositional sample treatment for fabricating Cu₂O thin films. The method is sensitive to particle fluence of the incident N⁵⁺ beam, where thin film deposited by pulsed laser deposition (PLD) technique lacking Cu-O stoichiometry is transformed into a polycrystalline Cu₂O phase at 1×10^{16} particles/cm² ion fluence. Similarly, a case was demonstrated where mixed copper oxide phases, i.e., Cu₂O as major and CuO as minor components deposited by PLD technique was transformed to single phase of polycrystalline Cu₂O at 2.5×10^{15} particles/cm² ion fluence and the fabricated Cu₂O phase is characterized by XRD, AFM and optical spectroscopy (UV-vis-NIR). Ion implantation with higher particle fluence caused change in copper oxide phase and also the crystallinity of the copper oxide phase was affected. The band gaps of the respective copper oxide phases measured by diffused reflectance spectroscopy were consistent with the reported values.





Chapter 3

*Synthesis of Capped CuO NPs and their
Electrochemical Applications*

3.1 Introduction

The transition metal oxides are widely being recognized as electrode materials for electrochemical applications. As discussed in Chapter - I, CuO nanoparticles are being less explored as supercapacitor. Due to consistent increase in the demand of energy novel, low cost, easy to fabricated high performance supercapacitors as energy storage devices are being actively pursued in the scientific community. The advantages of supercapacitors are associated with release of high energy density than traditional capacitors, high power density, and longer life than commercial batteries [18, 68]. Supercapacitors are basically of two kinds: (a) electric double layer capacitors (EDLC) and (b) pseudocapacitance (PC). The EDLC type is generally governed by high surface area, good electric conductivity and electrochemical stability [18]. The carbonaceous materials like graphene, carbon nanotube, reduced graphene oxide, etc, were found to exhibit supercapacitor behavior via EDLC mechanism. On the other hand, pseudocapacitance nature involves multi-oxidation states cations and conductivity of the materials.

In this regard, it may be remarked that transition metal oxides fulfill both the conditions for supercapacitor. Among all transition metals, copper is a one of the most abundant materials available on the earth in the form of copper, cupric oxide and cuprous oxide. Cupric oxide (CuO) is a p-type semiconductor material with 1.2 eV indirect band gap. It has good electrical and optical properties. It has excellent thermal stability and has been used in several application like thermal conductor, catalysis and antimicrobials, gas sensors, photocatalytic [3]. It has also been used in the field of energy related applications such solar cell, photovoltaic and lithium ion batteries [102, 222, 223]. Apart from this, theoretical specific capacitance of CuO can be up to 1800 F/g [102], which is more than theoretical specific capacitance of manganese oxide ranging between 1100 and 1300 F/g [91]. It can be synthesized as nanostructures of different shapes such as tubes, wire, belts, rods, sheets, leaves, needles, plates, flowers [3]. Because of this it is a promising candidate for energy applications like supercapacitors. These different types of nanostructures can be obtained by different synthesis routes, e.g. hydrothermal method, deposition methods, etc. In view of this, synthesis of nanoparticles by precipitation method is an easy method to adopt. Recently Shinde et al. reported the polyvinyl alcohol (PVA) and triton X-100 (TRX) assisted different type of morphological Cu(OH)₂/CuO thin film of different supercapacitive behavior by the successive ionic layer adsorption and reaction

(SILAR) method [224]. Our research group has developed triphenylphosphine oxide (TPPO) and polyvinylpyrrolidone (PVP) capped CuO nanoparticles of different photocatalytic behavior [137]. Therefore, capping agents were suitable for tuning several properties of CuO NPs.

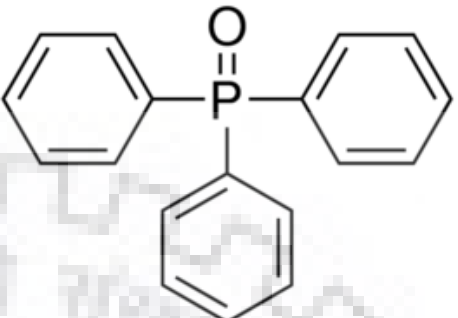
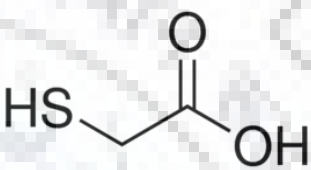
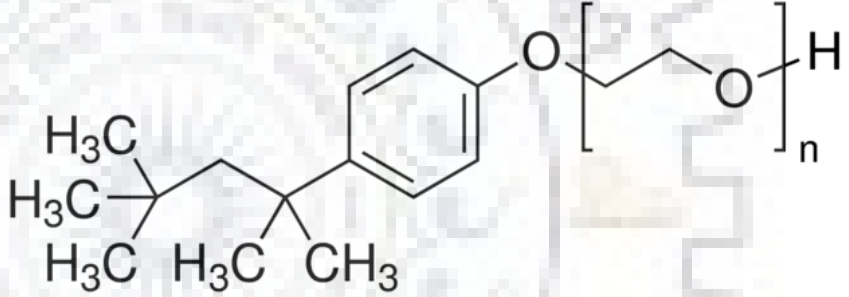
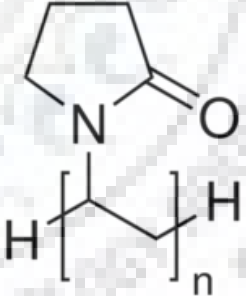
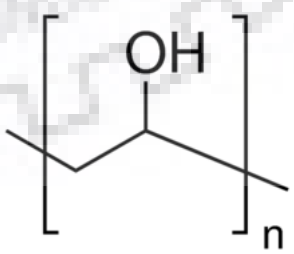
In the present study we have selected five different types of capping agents, e.g., TPPO, MAA, TRX, PVP and PVA for preparing capped CuO nanoparticles by co-precipitation method. TPPO is a large molecule and electron rich capping agent owing to three phenyl group and presence of phosphate. Mercaptoacetic acid (MAA) is an anionic small molecule which forms very small metal ion complexes. Triton X-100 is a non-ionic capping agent that has a hydrophilic polyethylene oxide chain and aromatic hydrocarbon lipophilic or hydrophobic group. Polyvinylpyrrolidone (PVP) is a non-conducting polymer that has polar amide group in polymeric chain which readily attach to the surface of nanoparticles. PVA is a conducting water soluble synthetic polymer. All the batches of capped CuO NPs were well characterized and subjected to electrochemical applications. In addition, these as-synthesized capped CuO NPs were calcined at 450 °C and were investigated for supercapacitor property.

3.2 Materials and methods

3.2.1 Chemicals

Copper acetate ($\text{Cu}(\text{CH}_3\text{COO})_2$, > 98%), acetic acid (CH_3COOH , 99.5%), sodium hydroxide (NaOH , > 98%), Polyvinylpyrrolidone (PVP, average molecular weight 40 000), Polyvinyl alcohol (PVA, average molecular weight), mercaptoacetic acid (MAA, 99%), Glucose, ($\text{C}_6\text{H}_{12}\text{O}_6$, > 99.5%), starch, ($\text{C}_6\text{H}_{10}\text{O}_5$, > 99.5%), sucrose, ($\text{C}_{12}\text{H}_{22}\text{O}_{11}$, > 99.5%), L-Ascorbic acid, (99%-100.5%), Dopamine hydrochloride, (> 98%) and Uric acid, (> 99%). hydrogen peroxide (30% v/v) and ethanol (>99%) were procured from HiMedia Pvt. Ltd., India. Triton X-100 was procured from SDH chemicals Ltd Poole England, Triphenylphosphine oxide (> 98%) were procured from Sigma Aldrich, GmbH, Germany. All reagents and precursors used in this study were of analytical grade and were used without further purification. Analytical grade deionized water (Millipore) was used throughout the study. The chemical structures and chemical formula of the capping agents used in this synthesis is given in Table 3.1.

Table 3.1 The chemical structures and chemical formula of the capping agents

Capping agent	Chemical structure
Triphenylphosphine oxide (TPPO) $OP(C_6H_5)_3$	
Mercaptoacetic acid (MAA) $HSCH_2CO_2H$	
Triton X-100 (TRX) $C_{14}H_{22}O(C_2H_4O)_n$ (n=9-10)	
Polyvinylpyrrolidone (PVP) $(C_6H_9NO)_n$	
polyvinyl alcohol (PVA) $(C_2H_4O)_x$	

3.2.2 Synthesis of capped CuO NPs

The batches of TPPO capped CuO NPs were prepared by adding 0.02 M copper acetate along with 0.1 g of TPPO into 150 mL of water in round-bottomed flask. To this solution, 1 mL of acetic acid was added. The reaction was refluxed at 100 °C for 1 hour. The pH of the reaction medium was maintained between 7.7 and 8.0 with drop wise addition of 1.0 M NaOH solution. The reaction system was allowed to cool down to room temperature. The precipitate formed there in was centrifuged at 5000 rpm and washed three times with ethanol and the final product was dried at 80 °C for 6 to 8 h in a temperature controlled oven. Similar procedure was followed for the synthesis of other batches of CuO NPs with respective capping agent. The capping agents were taken as 50 µl for MAA, 50 µl for triton X-100, 0.1 g for PVP and 0.1 g for PVA.

3.2.4 Sample preparation for TEM measurement

The batch of CuO NPs was dispersed in ethanol for TEM sample preparation. In which 5 mg of CuO NPs were taken in 10 ml of ethanol and kept for ultrasonication for 15 min. After that 0.5 mL of dispersion was taken and diluted in 10 mL ethanol followed by 10 min sonication. The absorbance of diluted sample was kept in the range of 0.15 to 0.20, which was optimized for preparing TEM sample. The diluted sample was then drop casted on a TEM grid (150 mesh) and dried.

3.2.5 Characterization techniques

The X-ray diffraction measurements of different batches of capped CuO NPs and bare CuO NPs were recorded with a Bruker ARS D8 Advance diffractometer. The instrument was operated at 40 kV where graphite-monochromatized Cu-K α X-rays ($\lambda = 1.54 \text{ \AA}$) was scanned at 2°/min in a wide angle region from 30° to 80° on a 2 θ scale. The morphology and particle size distribution of the nanoparticles were studied by transmission electron microscopy (TEM). The TEM studies were carried out using an FEI Technai-G² microscope operated at an acceleration voltage of 200 kV. The Brunauer–Emmett–Teller (BET) specific surface area of the nanoparticles were measured by a Quantachrome Nova 2200 analyzer at liquid-nitrogen temperature using nitrogen adsorption–desorption method. The optical band gap of the as-synthesized batches of capped CuO NPs and bare CuO NPs were determined from their

respective Tauc plots. The Tauc plots were estimated from diffused reflectance spectroscopy (DRS) data, recorded with UV-visible (Shimadzu UV2450) with respect to barium sulphates. The samples for DRS measurements were prepared by mixing CuO NPs and barium sulphate in the ratio of 1:10. The photoluminescence spectra of the nanoparticles were recorded by a Spectrofluorimeter FLS 980 (HORIBA), in the wavelength range of 315–575 nm, using excitation wavelength of 300 nm. The Fourier-transform infrared (FT-IR) spectra were recorded on a Thermo NICOLET 6700 FTIR in KBr pellets. The electrochemical studies were recorded by CHI760E instruments (USA) in three electrode configuration, where the electrode made of capped CuO NPs was taken as working electrode, saturated calomel electrode as reference electrode and platinum wire as counter electrode 1.0 M Na₂SO₄ was used as electrolyte solution. The cyclic voltammetric studies were recorded in the potential window range 0 to 1.0 V at different scan rates. The galvanostatic charge-discharge study was measured at different current density in the potential range 0 to 1.0 V. The electrochemical impedance spectroscopy was recorded in frequency range 0.01 Hz to 1 MHz with 5 mV amplitude at 0.5 V bias voltage.

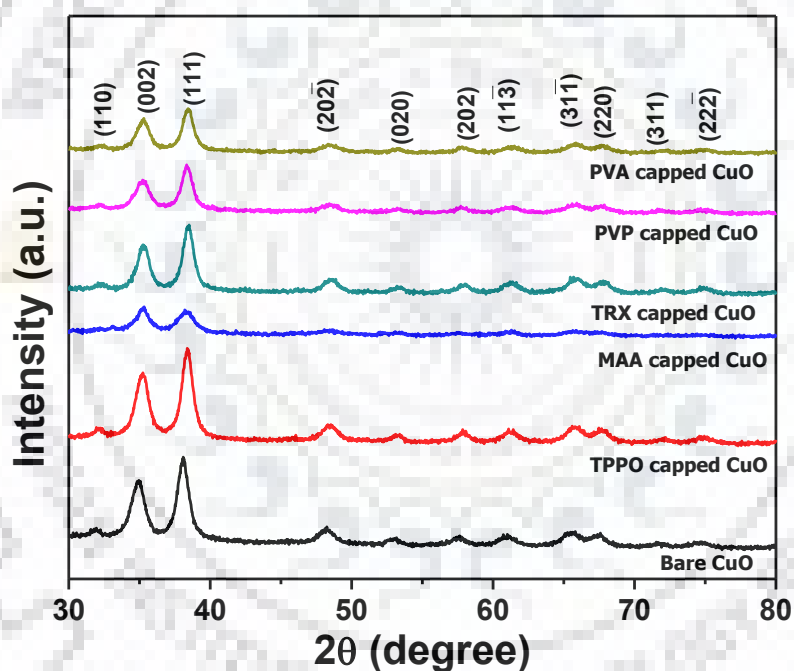
3.3 Results and discussion

3.3.1 X-ray diffraction

The X-ray diffraction patterns of bare and batches of capped CuO NPs prepared with different capping agents, e.g., triphenylphosphine oxide (TPPO), mercaptoacetic acid (MAA), triton X-100 (TRX), polyvinylpyrrolidone (PVP) polyvinyl alcohol (PVA) are given in Fig. 3.1. It revealed Bragg reflection peaks at $2\theta = 32.15^\circ, 35.21^\circ, 38.43^\circ, 48.44^\circ, 53.20^\circ, 57.94^\circ, 61.18^\circ, 65.71^\circ, 67.79^\circ, 72.20^\circ$ and 75.08° for all the batches which corresponded to the (110), (002), (111), (20 $\bar{2}$), (020), (202), (11 $\bar{3}$), (31 $\bar{1}$), (220), (311) and (22 $\bar{2}$) planes of monoclinic phase of CuO nanoparticles. Our XRD results matched well with the JCPDS file card no. 48-1548. The XRD patterns of the capped CuO nanoparticles were same as that of bare CuO and did not reveal any additional peaks, implying that other phases of CuO such as Cu₂O and Cu(OH)₂ were absent. It confirmed formation of pure monoclinic phase of CuO NPs. The XRD patterns of the all batches of capped CuO NPs revealed peak broadening.

Table 3.2 Crystallite size, band gap, surface area and specific capacitance of bare and capped CuO NPs

Sample	Crystallite size (nm)	Band gap (eV)	Surface area (m ² /g)	Specific capacitance (F/g)	
				CV (5 mV/s)	GCD (0.2 A/g)
Bare	11.4	2.76	66	102	139
TPPO capped	11.3	2.90	90	98	134
MAA capped	7.1	3.10	53	102	132
TRX capped	9.3	2.82	79	94	119
PVP capped	9.0	2.80	81	101	131
PVA capped	9.6	2.83	73	88	103

**Fig. 3.1** XRD pattern corresponding to the monoclinic structure of bare, TPPO capped, MAA capped, TRX capped, PVP capped and PVA capped CuO NPs.

The peak broadening is more in the capped CuO NPs as compared to that of bare CuO NPs. The broadening in the capped CuO nanoparticles is attributable to the decrease in crystallite size of nanoparticles [137]. Beside, crystallite size, the broadening could also be attributed to several other reasons, e.g., lesser lattice planes; micro strain/stress in the crystal structure due to dislocation; vacancies and twinning occurring due to capping assisted

modification in the nanoparticles [137, 149, 150]. The crystallite size of the batches of bare and capped CuO NPs were estimated from X-ray peak broadening using Debye Scherrer formula given as

$$D = \frac{0.9\lambda}{\beta \cos(\theta)}$$

where λ is the wavelength of the X-ray source, β is full-width at half maximum (FWHM) of the most intense XRD peak of interest in radians and θ is Bragg's diffraction angle. The crystallite size corresponding to the most intense peak, i.e., (111) plane is determined to be 11.4 nm for bare, 11.3 nm for TPPO capped, 7.1 nm for MAA capped, 9.3 nm for TRX capped, 9.0 nm for PVP capped and 9.6 nm for PVA capped CuO NPs. All data are given in Table 3.2.

3.3.2. Surface morphology

The surface morphology of bare and all the batches of capped CuO NPs were studied by field emission scanning electron microscopy (FE-SEM) & the results are given in Fig. 3.2. The FE-SEM image of bare and the capped batches of CuO NPs revealed agglomeration of the nanoparticles. Among these, the agglomeration is more in MAA capped and PVP capped CuO NPs (Fig. 3.2). The purity of the CuO NPs were reflected from the qualitative compositional analysis by energy dispersive X-ray analysis (EDAX) spectrum, which are given alongside the respective FE-SEM images. They revealed characteristic X-ray peaks of Cu and O. The transmission electron microscopy (TEM) images of bare, representative capped samples e.g., TPPO capped and MAA capped CuO NPs also revealed agglomeration of CuO nanoparticles. The higher resolution TEM images revealed nearly uniform spherical shaped CuO NPs of sizes 12 nm, 13 nm and 8 nm, respectively (Fig. 3.3). A smaller size cluster of small nanoparticles observed in higher resolution FE-SEM image of a representative TPPO capped CuO NPs of size less than 20 nm (Fig. 3.4). The TEM studies revealed size of the nanoparticles, which were consistent with the crystallite size calculated from Debye Scherrer formula. The selected area electron diffraction (SEAD) pattern of the nanoparticles revealed poorly polycrystalline nature of these CuO NPs which were consistent with the lesser intense and broadened XRD results.

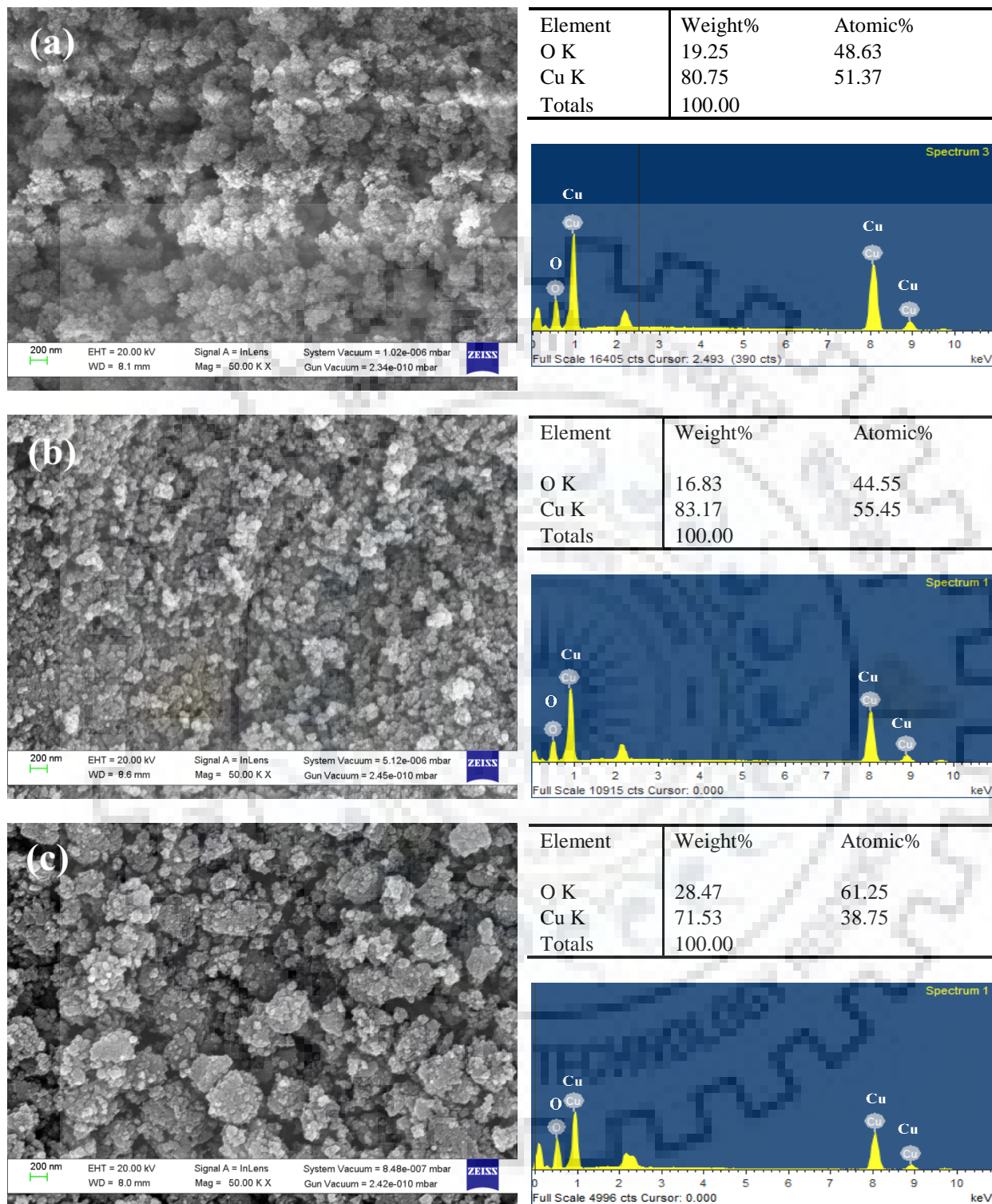


Fig. 3.2 (continued to next page)

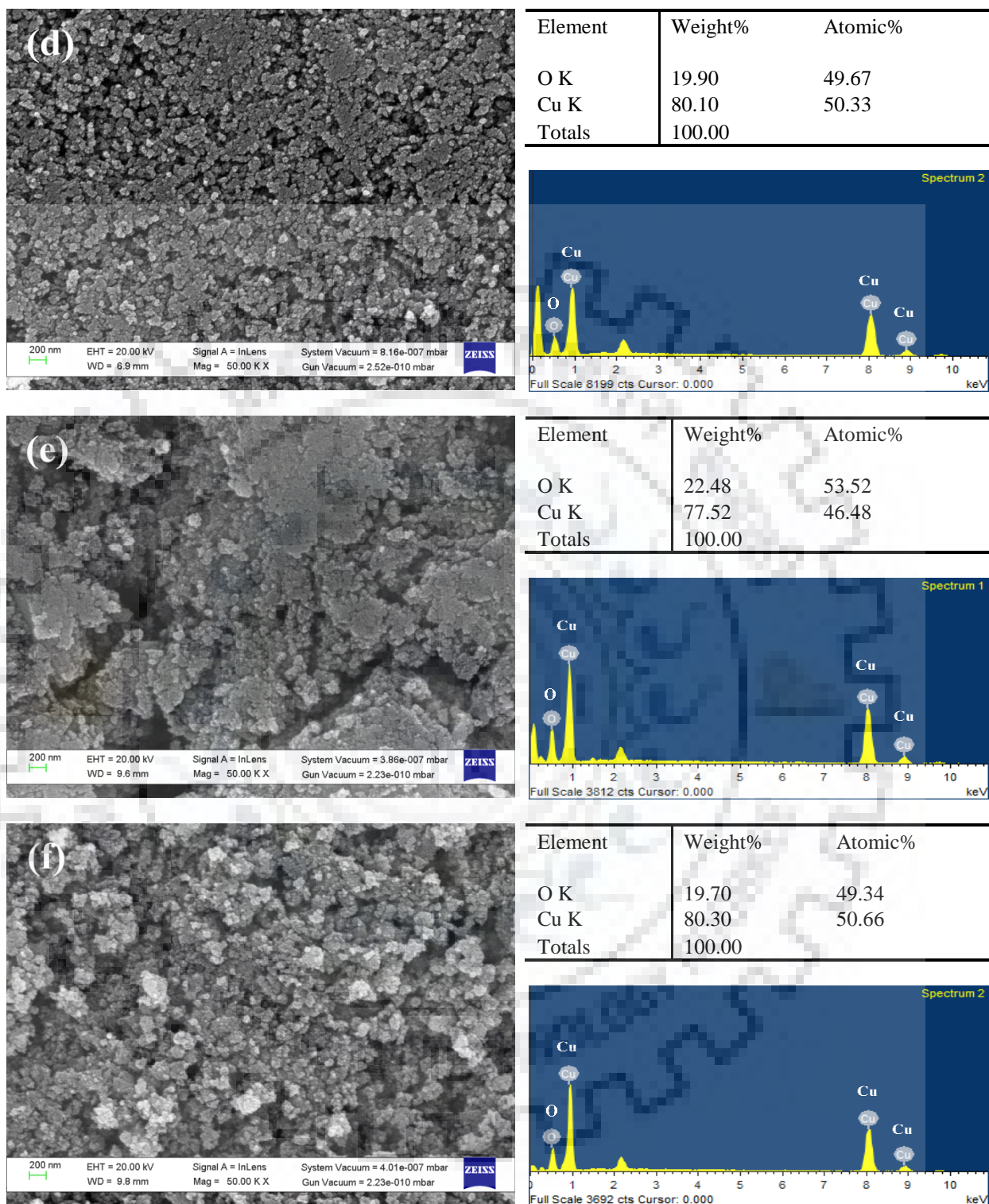


Fig. 3.2 Field Emission Scanning Electron Microscopy images of (a) Bare; (b) TPPO; (c) MAA; (d) TRX; (e) PVP; (f) PVA capped CuO NPs. Their corresponding energy dispersive X-ray analysis spectra are given next the representative FE-SEM images, which revealed characteristic K and L X-rays and atomic% of Cu and O.

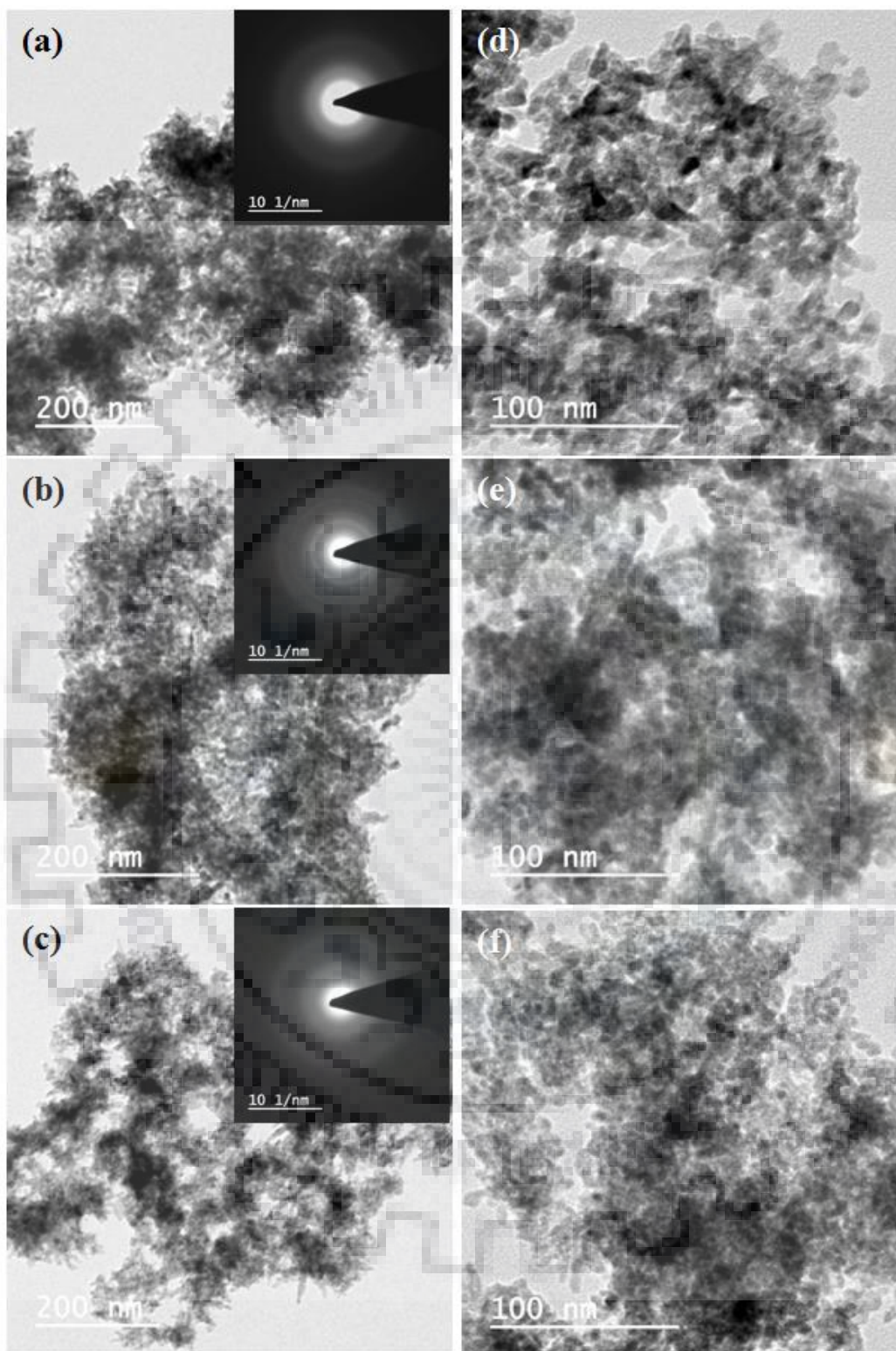


Fig. 3.3 Transmission Electron Microscopy images of (a) bare; (b) TPPO capped; (c) MAA capped CuO NPs with their respective SAED image in the inset. High resolution images of (d) bare; (e) TPPO capped; (f) MAA capped CuO NPs.

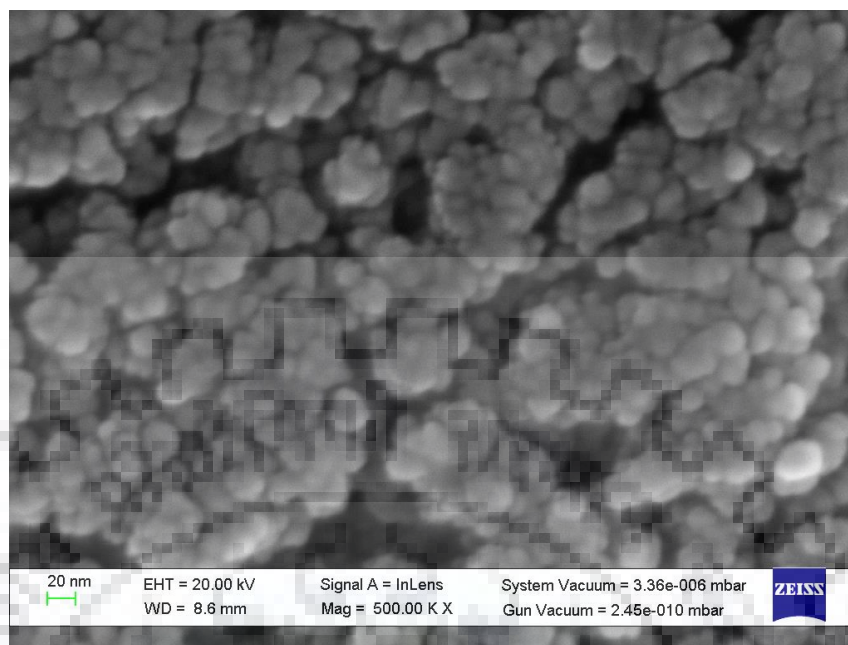


Fig. 3.4 High resolution scanning electron microscope images of TPPO capped CuO nanoparticles.

3.3.3 Fourier transformed infrared (FT-IR) spectroscopy

The FT-IR spectra of bare and all batches of capped CuO NPs were recorded between 400 and 4000 cm^{-1} range. It revealed the signature of capping molecules on CuO NPs (Fig. 3.5). The broad peak observed in the region 3000-3500 cm^{-1} was due to -OH group of the capping agents or absorbed moisture in the NPs. The weak peak at 1078 cm^{-1} in the TPPO capped CuO NPs correspond to the co-ordinate bond between the oxygen atom of P=O bond of TPPO ligand and Cu^{2+} ions. Similar signature peak is also reported in TPPO capped metal oxide NPs [225]. A broad and intense peak was observed in the region 1630-1672 cm^{-1} in the MAA capped CuO NPs which is attributed to carboxylic acid group of MAA. A shallow peak was observed at 1628 cm^{-1} in triton X-100 capped CuO NPs, which is attributable to symmetric stretching bands of benzenoid group. The FT-IR spectrum of PVP capped CuO NPs revealed signature peaks at 1630 cm^{-1} , 1408 cm^{-1} and 1337 cm^{-1} which are attributable to C=O stretching of carbonyl group in pyrrolidone ring and C-N stretching of PVP, respectively. The peak at 1630 cm^{-1} is attributable to interaction of carbonyl bond of PVP with Cu^{2+} ion. Finally, the peaks at 602 cm^{-1} and 527 cm^{-1} are attributable to vibrational frequencies of Cu-O bond. Our results are consistent with literature reports [186].

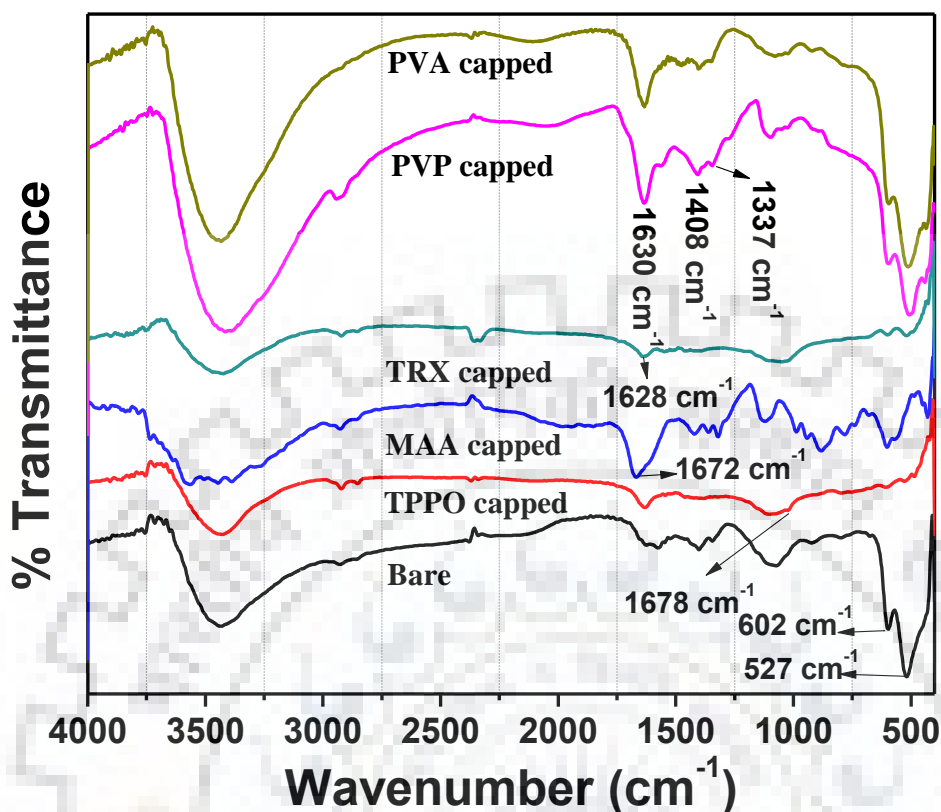


Fig. 3.5 Fourier-transform infrared (FT-IR) spectra of bare, TPPO capped, MAA capped, TRX capped, PVP capped and PVA capped CuO NPs.

3.3.4 Optical studies

The optical properties of bare and the capped CuO NPs were studied by diffuse reflectance spectroscopy (DRS) in the wavelength range 200-800 nm. The band gaps of these nanoparticles were obtained from DRS studies. This study was also useful to select the excitation wavelength for recording photoluminescence spectra of the as synthesized batches of CuO NPs. The photoluminescence spectroscopy studies are carried out in wavelength range of 315-575 nm.

3.3.4.1 Diffuse reflectance spectroscopy

The band gap of bare and batches of capped CuO NPs were determined by modifying the reflectance data to Kubelka–Munk formalism to obtain their absorption spectrum. The

absorption edges of the respective bare and batches of capped CuO NPs were determined by extrapolating the Tauc plot to $(\alpha h\nu)^{1/2} = 0$. The Tauc plot, given as [226],

$$(\alpha h\nu)^{1/n} = A(h\nu - E_g)$$

where, α is absorption coefficient; h is the plank constant; ν is the frequency of incident light; A is the proportionality constant; and E_g represent band gap. The values of n represent the nature of transition that takes place within the material, e.g., direct or indirect transition. The value of n for direct transition and direct band gap material is taken as $1/2$, while $n = 2$ is considered for indirect transition or indirect band gap materials.

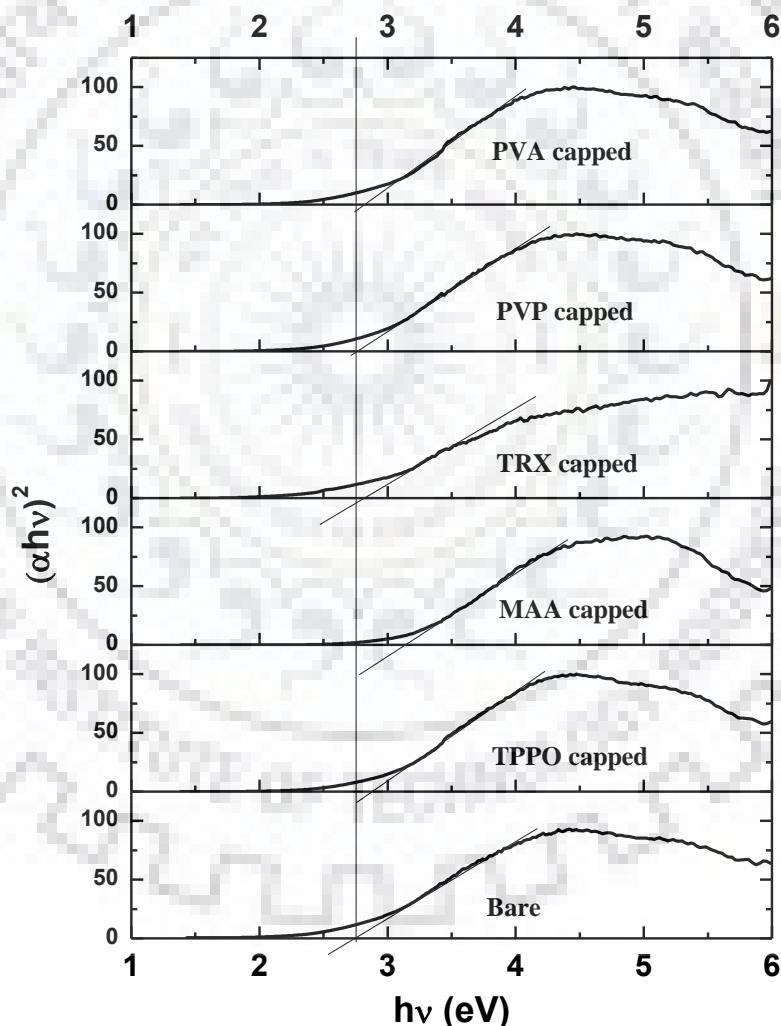


Fig. 3.6 Tauc plot obtained from diffuse reflectance spectroscopy of bare, TPPO capped, MAA capped, TRX capped, PVP capped and PVA capped CuO NPs.

It is found that the as synthesized batches of CuO NPs fitted well with the direct linear transition. The linear region of the Tauc plot was extrapolated $(ah\nu)^2 = 0$, which corresponded to the band gap of the materials. From Fig. 3.6, the band gap of bare, TPPO capped, MAA capped, TRX capped, PVP capped and PVA capped CuO NPs were determined to be 2.76 eV, 2.90 eV, 3.10 eV, 2.82 eV, 2.80 eV and 2.83 eV respectively (Table 3.2). Notably the band gap of all the batches of CuO NPs were larger than the band gap of bulk CuO i.e., 1.2 eV. The increase in the band gap of the as-synthesized batches of capped CuO NPs was attributable to synthesis of particle sizes smaller than the bulk. This is consistent with the characteristic relationship between band gap of a material and its particles size [227].

3.3.4.2 Photoluminescence studies

The photoluminescence (PL) spectra of bare and capped batches of CuO NPs offers important information about band structure of nanoparticles and also reflect the defect corresponding to additional energy levels within the forbidden gap [137]. The PL spectra of bare and batches of capped CuO NPs were recorded using excitation wavelength $\lambda_{ex} = 300$ nm and the results are given in the Fig. 3.7. The PL peak is prominently observed at 397 nm for MAA capped CuO NPs which corresponded to 3.12 eV. This peak energy is very close to the band gap of the NPs (i.e., 3.10 eV). This PL peaks attributable to re-combination of photoexcited electron and holes. The other PL peaks that are prominently observed in MAA as well as PVP capped CuO NPs were at 413 nm, 440 nm, 451 nm, 469 nm, 481 nm, 493 nm and 560 nm. Similar PL spectra of CuO NPs were also reported by other groups [228]. The PL peaks at 413 nm, 440 nm and 451 nm corresponded to near band edge emission in visible region. The peaks at 481 nm and 493 nm are attributable to energy level of defect sites, such as copper vacancy, copper interstitial and oxygen vacancy in CuO NPs [229]. The 560 nm peak is assigned to deep level green emission attributable to the singly ionized oxygen vacancies [53]. These near band edge emission and deep level green emission are signature of structural defects in CuO NPs. Notably, the intensity of the PL peaks of MAA capped and PVA capped CuO NPs were higher as compared to other capped batches of CuO NPs. For other batches, weak intensity peaks were obtained at 469 nm & 560 nm. The weak PL peaks in bare, TPPO capped, TRX capped and PVP capped CuO NPs may be attributed to relaxation of photoexcited electrons & holes via dangling bonds and defects present at the surface of CuO NPs.

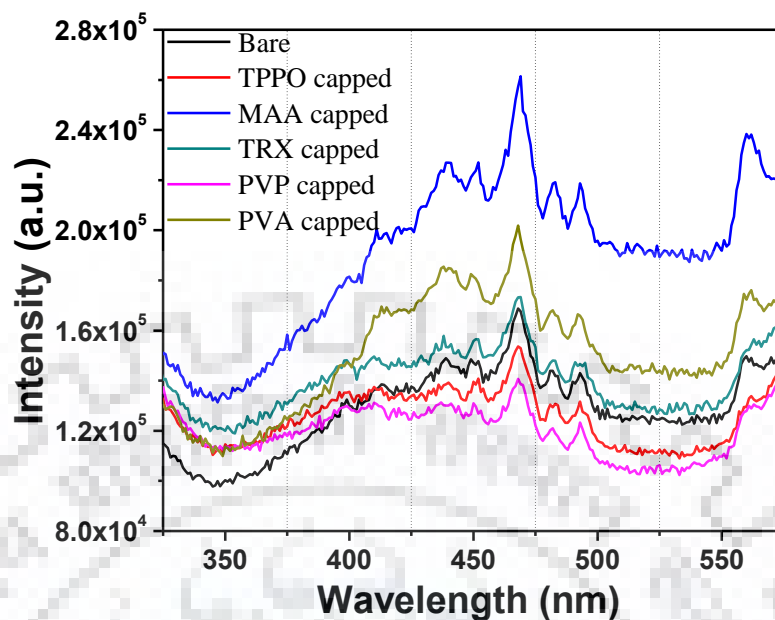


Fig. 3.7 Photoluminescence spectra of bare, TPPO capped, MAA capped, TRX capped, PVP capped and PVA capped CuO NPs.

3.3.5 Surface area and pore size

The Brunauer-Emmett-Teller (BET) surface area of the bare and the batches of capped CuO NPs were investigated by five point measurement at 77 K with N_2 adsorptions desorption process. The nanoparticles for BET measurements were first heated at 150 °C before surface area measurement to remove moisture content in it. The BET surface area of bare, TPPO capped, MAA capped, TRX capped, PVP capped and PVA capped CuO NPs were found to be $66 \text{ m}^2/\text{g}$, $90 \text{ m}^2/\text{g}$, $53 \text{ m}^2/\text{g}$, $79 \text{ m}^2/\text{g}$, $81 \text{ m}^2/\text{g}$ and $73 \text{ m}^2/\text{g}$, respectively and the results are listed in Table 3.2. The surface area of TPPO capped, TRX capped PVP capped and PVA capped are significantly higher than that of bare and MAA capped CuO NPs. This is attributable to changes in the size of the NPs due to nature of capping agents. Notably, MAA capped CuO NPs exhibited highest band gap (3.1 eV) and is expected to exhibit maximum BET surface area. On the other hand, MAA capped CuO NPs exhibited much smaller BET surface area. This could be due to agglomeration of the MAA capped CuO NPs which is also evident from FE-SEM and TEM studies.

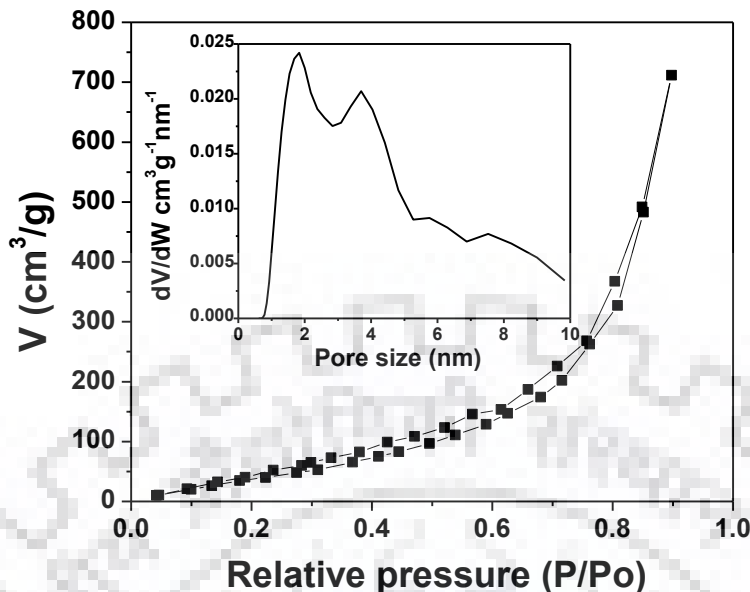


Fig. 3.8 BET isotherm of TPPO capped CuO NPs. Inset represent pore size distribution plot.

The TPPO capped CuO NPs were chosen for a detailed N_2 sorption isotherms Fig. 3.8. It revealed a type IV isotherm, where hysteresis is noted above $P/P_0 = 0.3$ and was extended up to $P/P_0 = 0.8$ indicating mesoporous structure. The pore structure of TPPO capped CuO NPs were further confirmed by pore size distribution analysis. The size of the average pores of TPPO capped CuO NPs was 3.89 nm and pore size distribution is given in Fig. 3.8. Most of the pore sizes were 1.8 nm and 3.6 nm and a fewer pores of sizes 5.8 nm & 7.5 nm were also observed and hence these are refund as mesopores. The pore volume of this CuO NPs was measured to be 0.1147 cc/g.

3.3.6 Capped CuO nanoparticles as supercapacitor

In this section we will discuss the applications of bare and capped CuO NPs as supercapacitor material. It may be remarked that CuO NPs were prepared by chemical precipitation method and using different capping agents. It was possible to control its particles size and morphology on the basis of capping agents. Most importantly both particle size and surface morphology play important role for supercapacitor behavior [3]. So we have recorded the electrochemical properties of these CuO NPs modified by different types of organic capping agent.

The electrochemical performances of bare and the batches of capped CuO NPs were first evaluated by cyclic voltammetry (CV) in 1 M Na₂SO₄ electrolyte solution in three electrode configuration. The CV results were corroborated with the galvanostatic charge-discharge (GCD) studies. The electrochemical impedance spectroscopy (EIS) studies were performed to understand the charge accumulation by the bare and capped nanoparticles and also to monitor the interaction behavior of electrolyte ion and the electrode material prepared with different capped CuO NPs.

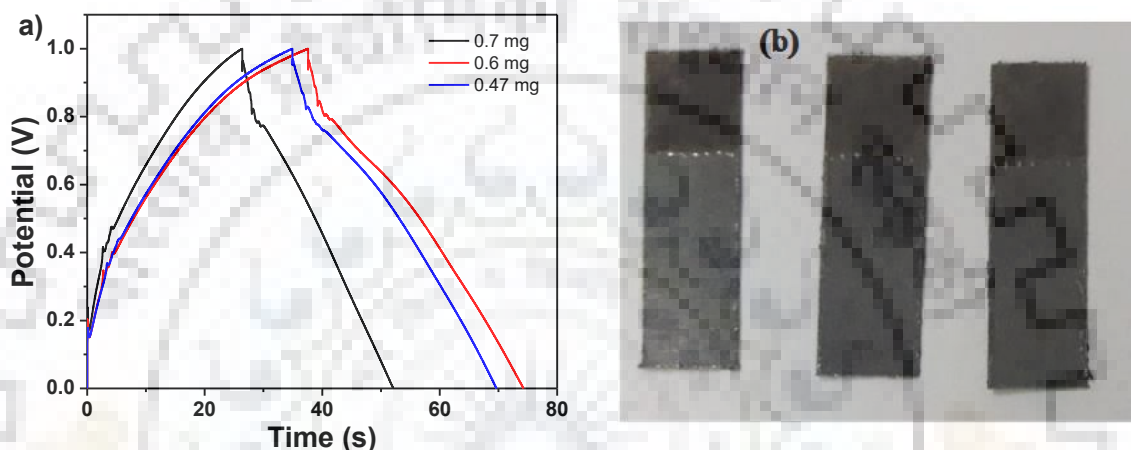


Fig. 3.9 (a) Optimization of active mass of prepared CuO NPs by recording GCD plot of different total mass material on electrode at constant current density (b) photograph of fabricated electrode with CuO NPs.

3.3.6.1 Electrode fabrication

The electrodes were prepared with respective batches of capped CuO NPs by drop casting of slurry made up of respective batches of capped CuO NPs as active material, graphite powder and polyvinylidene difluoride (PVDF) in weight ratios of 75:15:10 in N-methyl 2-pyrrolidone (NMP) solvent i.e., 150 mg of active material, 30 mg of graphite powder and 20 mg of PVDF were dispersed in 2 mL of NMP solvent. This mixed solution was kept for stirred for 12 h for homogeneous slurry. The slurry was coated on surface cleaned graphite sheet in area of 1 cm 1 cm and dried at 90 °C for 12 h to evaporate the solvent. The active material loading for all batches of capped CuO NPs was kept at ~ 0.45 mg. The active material mass was measured as $\text{Active material mass} = \text{Total mass of electrode material} - \text{mass of graphite sheet}$. The masses were measured by a microbalance. The optimization of active mass material was done with GCD measurement

3.3.6.2 Cyclic voltammetry

The cyclic voltammetry (CV) curves for bare and different batches of capped CuO NPs recorded at scan rates e.g., 5 mV/s, 10 mV/s, 20 mV/s, 30 mV/s, 40 mV/s and 50 mV/s are given in Fig. 3.10 a-f. The shapes of CV curves were quasi-rectangular scan rate varying between 5 mV/s to 50 mV/s and were consistent with literature reported on supercapacitor behavior of CuO nanostructure [230]. From this we can infer that the as synthesized batches of capped CuO NPs are favorable as supercapacitor. The specific capacitance (C_s) of the as synthesized bare and capped CuO NPs was calculated using following equation

$$C_s = \frac{\int I dv}{2 \times v \times m \times \Delta V} \quad (3.1)$$

where I , v , m and ΔV represents current changes with respect to scan rate, applied scan rate, active mass of the materials and operating potential window respectively. The specific capacitance (C_s) of bare, TPPO capped, MAA capped, TRX capped, PVP capped and PVA capped CuO NPs were determined as 102 F/g, 98 F/g, 102 F/g, 94 F/g, 101 F/g and 88 F/g respectively at a fixed scan rate of 5 mV/s.

The respective variation in specific capacitance can be attributed to several factors, e.g., porosity, surface area, defects and conductivity of CuO NPs. It is noted that specific capacitance for certain batches of capped CuO NPs e.g., MAA & PVP were similar to that of the bare CuO NPs in spite of their significant differences in the BET surface areas e.g., 53 m²/g for MAA capped & 81 m²/g for PVP capped. Usually, specific capacitance increases with increase in surface area of the electrode material. But the specific capacitance measured in our samples did not follow trend surface area. For example, in this study we found that BET surface area of TPPO capped CuO NPs and MAA capped CuO NPs is significantly different but specific capacitance were similar. Compared to other capped CuO NPs, the specific capacitance of PVA capped CuO NPs was found to be significantly less. This is correlated with intense PL peaks due to metal or oxygen vacancies. So it may be revealed that the vacancies acted as trap sites for neutralizing the charge and decrease the specific capacitances. Further the effect of capping agents on the supercapacitor behavior of CuO NPs can be observed from the CV plots for a fixed scan rate of 10 mV/s (Fig. 3.10).

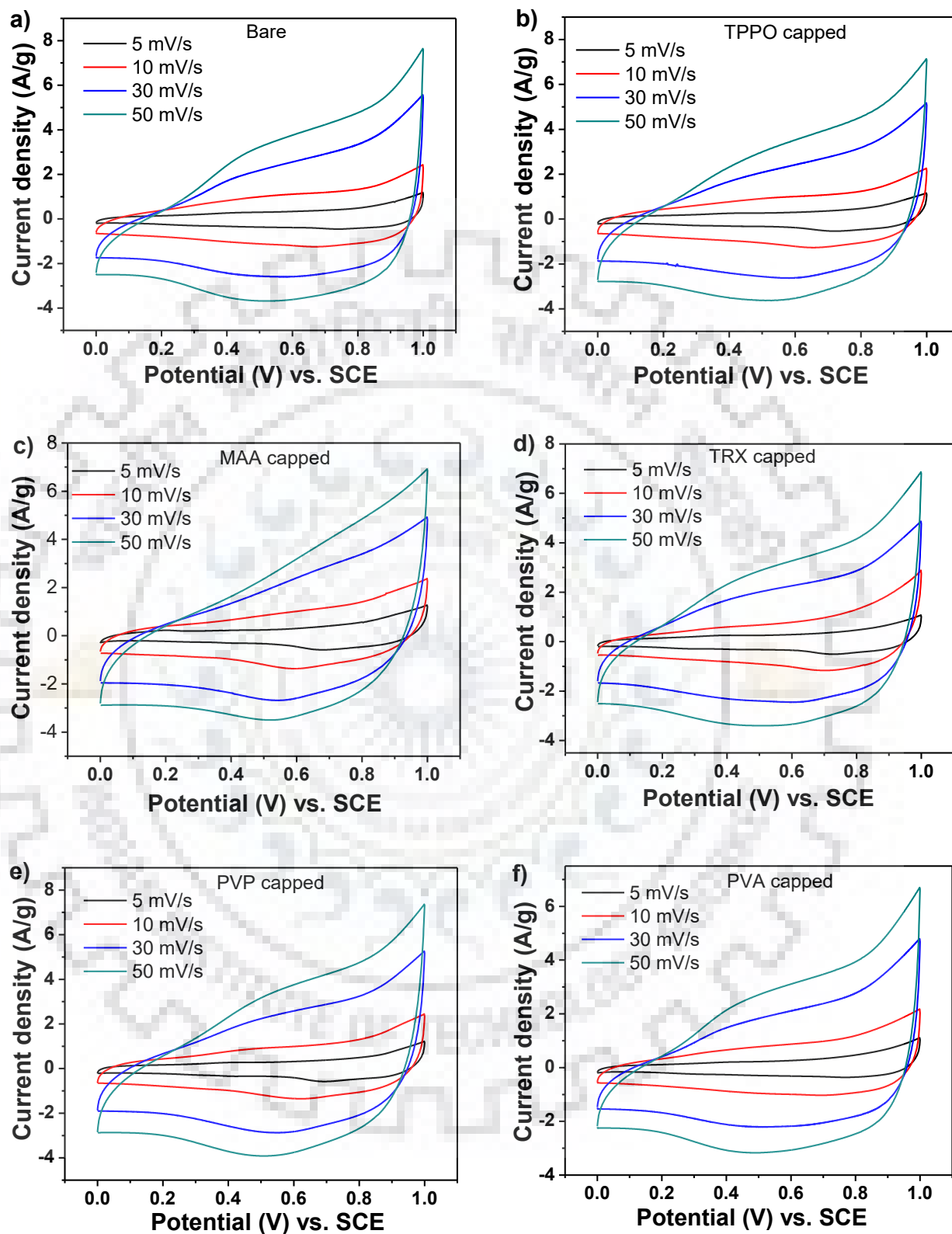


Fig. 3.10 Continued to next page.

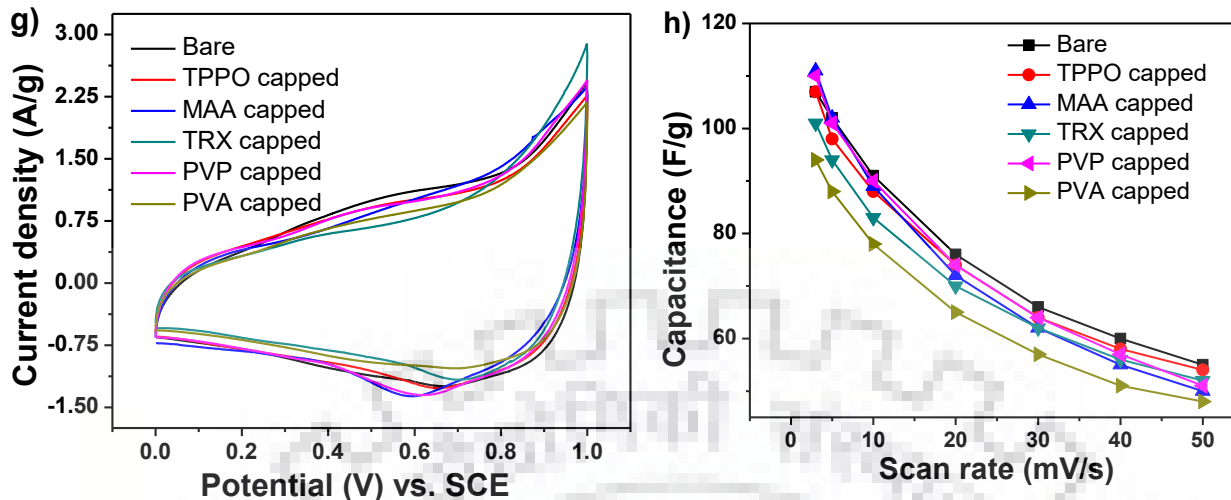


Fig. 3.10 Cyclic voltammograms of (a) bare, (b) TPPO capped, (c) MAA capped, (d) TRX capped, (e) PVP capped, (f) PVA capped CuO NPs. (g) Cyclic voltammograms of bare and all capped CuO NPs at scan rate of 10 mV/s. (h) Specific capacitance at different scan rates.

The area under the CV curves of the respective batches of capped CuO nanoparticles varied to a very small extent. In other words, the oxidation current varied for the batch of bare, TPPO capped and MAA capped CuO NPs in the potential window of 0.3 to 0.8 V, which is due to faradaic redox reaction taking place at the surface of the CuO NPs. The specific capacitances at different scan rates were calculated for the batches of CuO NPs. The plot of specific capacitance vs. scan rate revealed a gradually decreasing trend (Fig.3.10h), which is consistent with different metal oxides as supercapacitor [93, 231, 232]. The decrease in the specific capacitance at higher scan rates is attributable to inefficient interaction of electrolyte ions with active materials owing to lesser interaction time. Further, the specific capacitance was decreased to nearly 50-55% at higher scan rate of charging (i.e., 50 mV/s). Let's take the case of MAA capped, TPPO capped and PVP capped CuO NPs to examine their trend of specific capacitance at different scan rates. Initially the specific capacitance of MAA capped CuO NPs was more than that of TPPO capped CuO NPs. But the specific capacitance of MAA capped CuO NPs was lesser than that of TPPO capped CuO NPs for 50 mV/s scan rate. This is attributable to various features e.g., faster redox reaction process, electrosorption and intercalation of charges at the surface layers of the NPs [233]. The other reason for low specific capacitance in MAA at higher scan rate can be attributed to less surface area as compared to TPPO capped CuO NPs due to which the interaction of charges are inefficient. However the

same reason can't be given for explaining low capacitance at scan rate of 50 mV/s for PVP capped CuO NPs, as PVP capped CuO NPs exhibited higher BET surface area. In this case, the functional group of PVP interacting with surface of CuO might play significant role. In that case the carbonyl group of pyrrolidone ring in PVP might affect the charge transport properties. In addition molecular structure of the polymer might also affect the charge transport phenomena between electrolyte ions and Cu atoms. Notably, a supercapacitor store energy either by ion adsorption (EDLC) or by fast surface redox reactions (pseudocapacitance, PC). The correlation between higher variation in specific capacitance as a function of scan rate and larger BET surface area of TPPO capped, TRX capped and PVA capped CuO NPs, as compared to smaller BET surface area MAA capped CuO NPs is attributable to faster interaction of electrolyte ions with Cu atoms of these capped CuO NPs.

3.3.6.3 EDLC vs. PC contributions

The supercapacitance behavior is governed by two mechanisms, i.e., charge accumulation and transfer via electric double layer and via faradaic processes attributed to pseudocapacitance property [234-236]. The plot of $1/q$ vs. $v^{1/2}$ for the pristine and all the batches of capped CuO NPs are given in Fig. 3.11a. The linear fit of each batches was extrapolated to voltammetric charge at $v = 0$, which is measure of total accumulation charge (q_t). From the plot q vs. $v^{-1/2}$ the extrapolated value of q at $v = \infty$ corresponded to charge in the double layer (q_{dl}) (Fig. 3.12b).

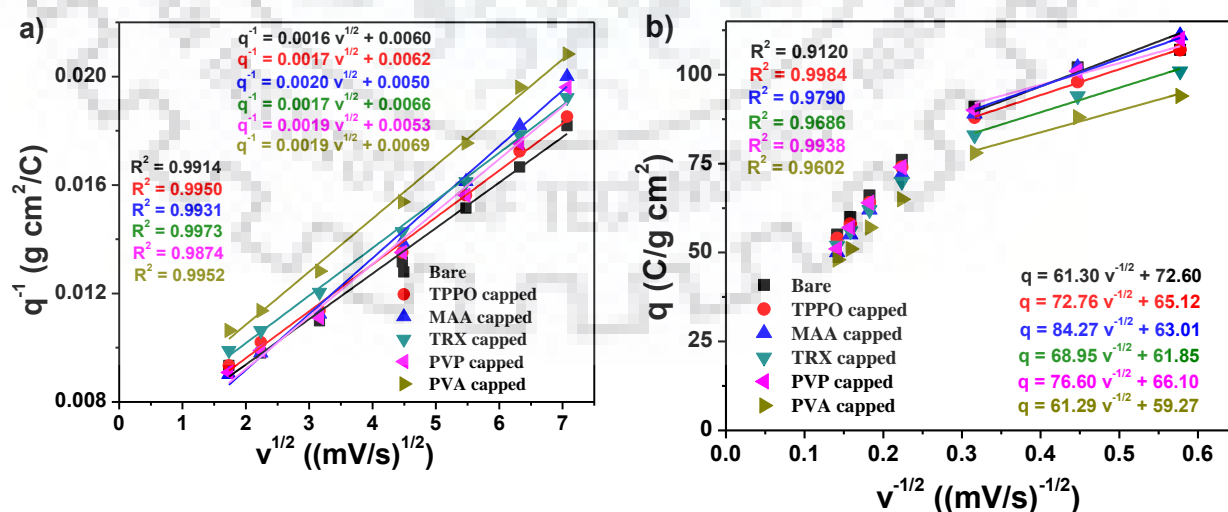


Fig. 3.11 (a) $1/q$ vs. $v^{1/2}$ and (b) q vs. $v^{-1/2}$ dependence of bare and capped CuO NPs.

Table 3.3 Summary of maximum total charge (q_t), double layer capacitance (q_{dl}), and charge associated with pseudocapacitance (q_p) of bare and capped CuO NPs in 1 M Na₂SO₄ solution.

Sample	q_t (C/g)	q_{dl} (C/g)	q_p (C/g)	q_p/q_t (%)
Bare	167	73	94	56.3
TPPO capped	161	65	96	59.6
MAA capped	200	63	137	68.5
TRX capped	152	62	90	59.2
PVP capped	187	66	121	64.7
PVA capped	145	59	86	59.3

As the potential window for electrochemical measurement of our material is from 0 to 1 V, therefore charge accumulated on electrode is equal to capacitance of the electrode material. The total specific capacitance (C_t), specific capacitance due to double layer (C_{dl}) and specific capacitance due to pseudocapacitance (C_p) values are given in the Table 3.3. The relative contribution of PC can be estimated by

$$C_p = \frac{C_p}{C_t} \times 100. \quad (3.2)$$

The C_t , C_{dl} and C_p are given in Table 3.3, which suggested that the all the capped CuO NPs revealed higher PC contribution as compared to pristine CuO NPs. In fact all have more than 59% PC contribution. The MAA capped and PVP capped CuO NPs revealed 68.5% and 64.7%, respectively, which were highest among all capped samples. This could be due to agglomeration of nanoparticles which provide more excess to electrolyte ions to interact with Cu atom. This result was consistent with previously discussed decrease in the specific capacitance with increase in scan rate.

3.3.6.4 Galvanostatic charge –discharge (GCD) studies

Further the electrochemical studies of these bare and batches of capped CuO NPs were examined by galvanostatic charge–discharge (GCD) measurements. All the charge-discharge curves of bare and batches of capped CuO NPs electrode were recorded at different current density varying from 0.2 A/g to 5 A/g (Fig. 3.12 a-f). Triangular shaped charge-discharge

curves were observed which are typical for a good supercapacitor [93]. This triangular shape revealed the constant charging and discharging nature of the bare and capped CuO NPs as supercapacitive materials with proper reversibility [237]. The specific capacitance could be also calculated from GCD study using following equation:

$$C_s = \frac{I \times t}{m \times \Delta V} \quad (3.3)$$

In the equation, the terms I , t , m and ΔV represents the applied current, charge-discharge time period, active mass of the materials and operating potential window respectively. The specific capacitance of bare, TPPO capped, MAA capped, TRX capped, PVP capped and PVA capped CuO NPs from GCD measurements were found to be 139 F/g, 134 F/g, 132 F/g, 119 F/g, 131 F/g and 103 F/g, respectively at a fixed current density of 0.2 A/g. Expectedly the results obtained from charge-discharge based capacitance were of similar trend with those of cyclic voltammetry based capacitance results. It is further noted that the specific capacitance of the bare, TPPO capped, MAA capped and PVP capped CuO NPs were of similar order i.e., 139 F/g, 134 F/g, 132 F/g and 131 F/g, respectively at constant 0.2 A/g current density. These results were better than reported literature (Table 3.4). However, the surface areas of these nanoparticles were different (e.g., 66 m²/g, 90 m²/g, 53 m²/g and 81 m²/g, respectively). Therefore, the capacitance performances of these CuO NPs are not only dependent on surface area of the nanoparticles, but other factors are likely to contribute.

In this regard, surface modification on the nanoparticles by different capping agents might have an impact on supercapacitor behavior. Capping agents tend to decrease the specific capacitance as compared to bare CuO NPs. This is attributable to conducting or non-conducting nature of capping agent. The capping agents on the CuO NPs tend to reduce the interaction of electrolyte ions with the copper atoms present on the surface.

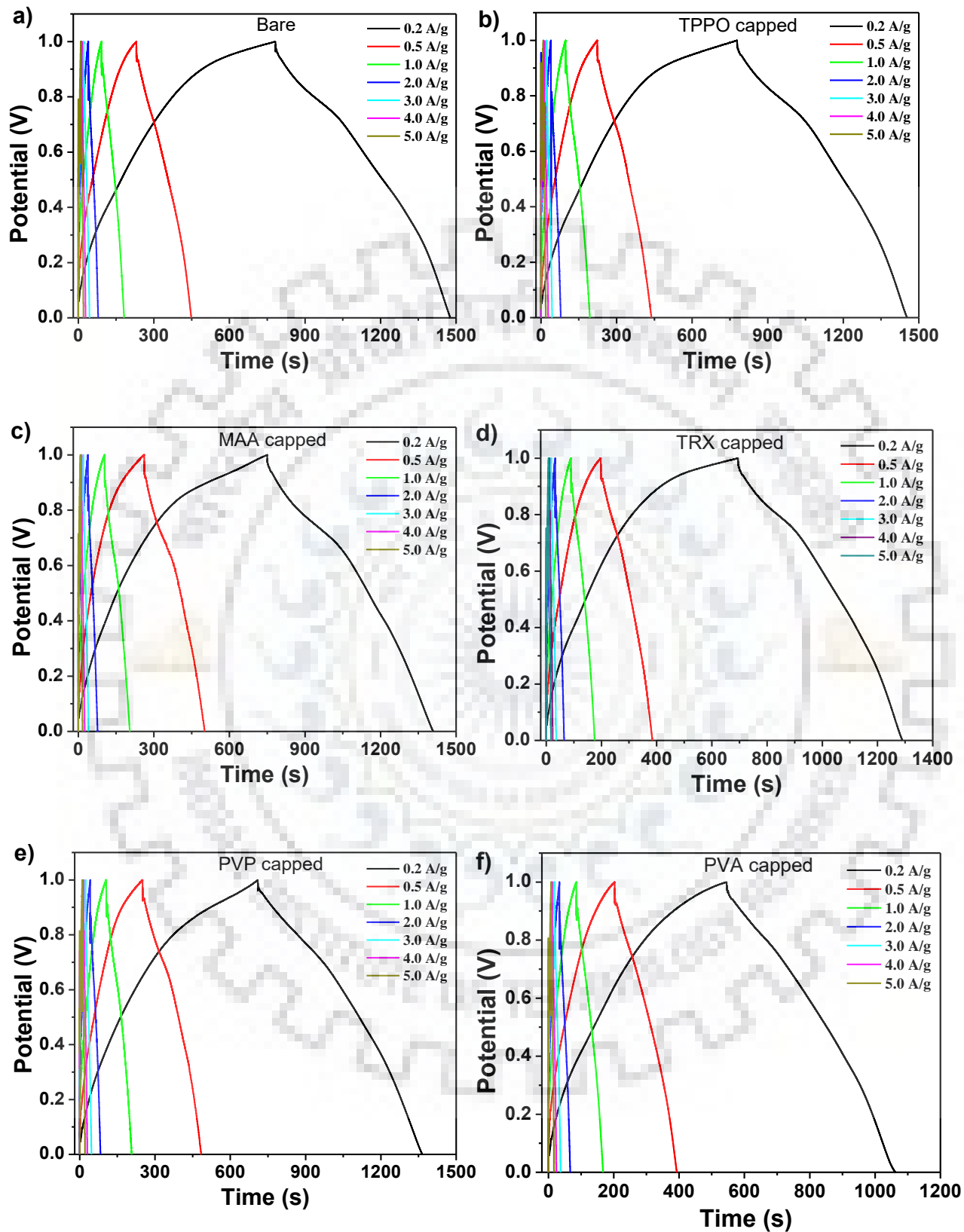


Fig. 3.12 Continued to next page

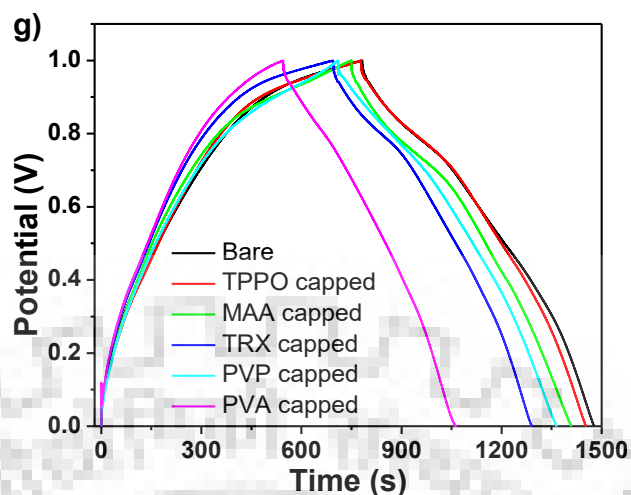


Fig. 3.12 Galvanostatic charge-discharge curves of (a) bare, (b) TPPO capped, (c) MAA capped, (d) TRX capped, (e) PVP capped, (f) PVA capped CuO NPs. and (g) Galvanostatic charge-discharge curves of bare and all capped CuO NPs at current density 0.2 A/g.

Table 3.4 Specific capacitance of CuO nanostructures reported in literature

Nanostructure	Methods of fabrication	Specific capacitance	Scan rate	Electrolyte	References
Hierarchical	Crystallization of Cu foil in alkaline medium	47 F/g	5 mV/s	1 M Na ₂ SO ₄	118
Multilayer nanosheets thin films	Chemical bath deposition (CBD) on stainless steel	22 F/g	10 mV/s	1 M Na ₂ SO ₄	119
Vertical copper oxide (CuO) nanoflakes	Surface oxidation of Cu foil	190 F/g	2 mA/cm ²	1 M KOH	129
CuO/rGO nanosheet and CuO nanosheet	Hydrothermal	40 F/g 10 F/g CuO	10 mV/s	1 M Na ₂ SO ₄	238
Capped CuO	Precipitation	135 F/g	0.2 A/g	1 M Na ₂ SO ₄	Present work

The charge-discharge curves of bare and batches of capped CuO NPs as electrodes measured at a fixed 0.2 A/g current density are given in Fig 3.12g. The time required for charging-discharging pattern is evident from Fig. 3.12. It is noted that the batch made of PVA as capping agent exhibited the worst property as it discharged quickly. On the other hand the rate of discharging was slower for bare, TPPO capped and MAA capped CuO NPs and they are considered to be better supercapacitor.

3.3.6.5 Electrochemical Impedance spectroscopy

Further, electrochemical impedance spectroscopy studies of bare and all the batches of capped CuO NPs recorded at 0.5 V bias potential vs. SCE with 5 mV amplitude in the frequency range 0.01 Hz to 1 MHz are given in Fig. 3.13a.

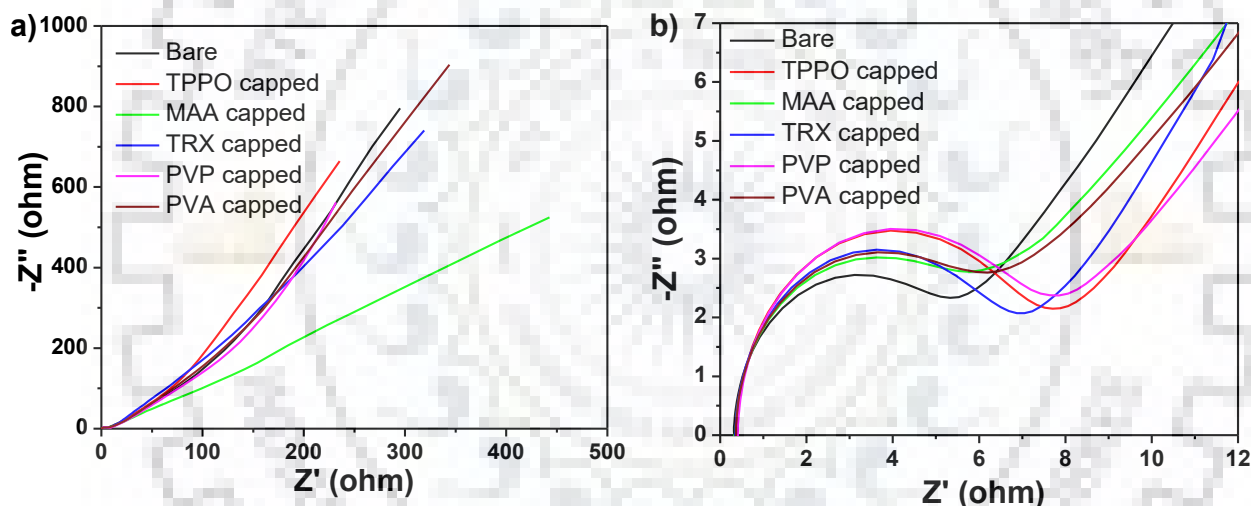


Fig. 3.13 (a) Electrochemical impedance spectroscopy of bare and batches of capped CuO NPs. (b) represent the zoom EIS of all sample in higher frequency range.

The Nyquist plot of bare, TPPO capped, TRX capped, PVP capped and PVA capped CuO NPs revealed three important regions, e.g. the semicircle at high frequency owing to charge transfer, mid frequency due to diffusion of charge and the large scale vertical line in the low frequency region due to ionic mobility. The results for high frequency and mid frequency region are given as insert of Fig. 3.13 b. For example, the equivalent series resistance (ESR) is obtained for the Z' value at which the imaginary part is zero and corresponded to higher frequency region. In addition the EIS plot also reveals the conductivity of the material in

electrolyte. The ESR of bare and the batches of capped CuO were observed to be similar, i.e., 0.4 ohm (Fig. 3.13). Notably for an ideal supercapacitor, the ESR must be as small as possible and preferably equivalent to zero. The ESR value obtained for our CuO NPs is by far the lowest among all the CuO nanostructures reported till date as per existing literature report [239]. Such low ESR values in our batches of CuO NPs is attributable to higher electric conductivity and lower ionic resistance of the electrolyte ions in the pores during charging and discharging [240]. This is attributable to interfacial properties of CuO and capping agent. The specific capacitance can also be determined from the EIS studies by the equation [241]:

$$C_s = \frac{1}{2\pi f Z'' m} \quad (3.4)$$

where, f , Z'' and m represents the frequency, imaginary component of impedance and active mass of the material respectively. In other words, C_s is inversely proportional to f and Z'' . In spite of similar specific capacitance for MAA capped and TPPO capped CuO NPs, the slope in the low frequency region for MAA capped CuO NPs is striking less as compared to TPPO capped CuO NPs. This implies that the ionic mobility in MAA capped CuO NPs was much slower than that of the electrode made of TPPO capped CuO NPs. The slower kinetics could be due to several reasons; one of the main reasons could be the thickness of MAA coating on the capped CuO NPs. In addition structural defects in nanoparticles can play important role in slower kinetics of charges. In this regard, it may be remarked that the PL studies of MAA capped CuO NPs revealed more surface defects than TPPO CuO NPs. Particularly copper/oxygen vacancies are more in MAA capped CuO NPs which may act as potential trap sites of charges. Since the BET surface area of MAA capped CuO NPs was significantly lesser than the TPPO capped CuO NPs whereas their specific capacitance were of same order, therefore it may be commented that that the pseudocapacitive behavior of MAA capped CuO NPs was more than that of TPPO capped CuO NPs. The pseudocapacitance behavior is attributable to faradaic process at the electrode. The current vs. potential plot clearly revealed the signature of redox events at the electrodes. Thus, owing to similar specific capacitance but different supercapacitive behavior, the MAA capped and TPPO capped CuO NPs were selected as electrode material for cyclic stability test and the results were compared with bare CuO NPs.

3.3.6.6 Cycle stability

The stability of the electrode material was investigated by charging-discharging process for 500 cycles at a current density of 1 A/g. The ratio of specific capacitances measured at first cycle to its last cycle is known as capacitance retention.

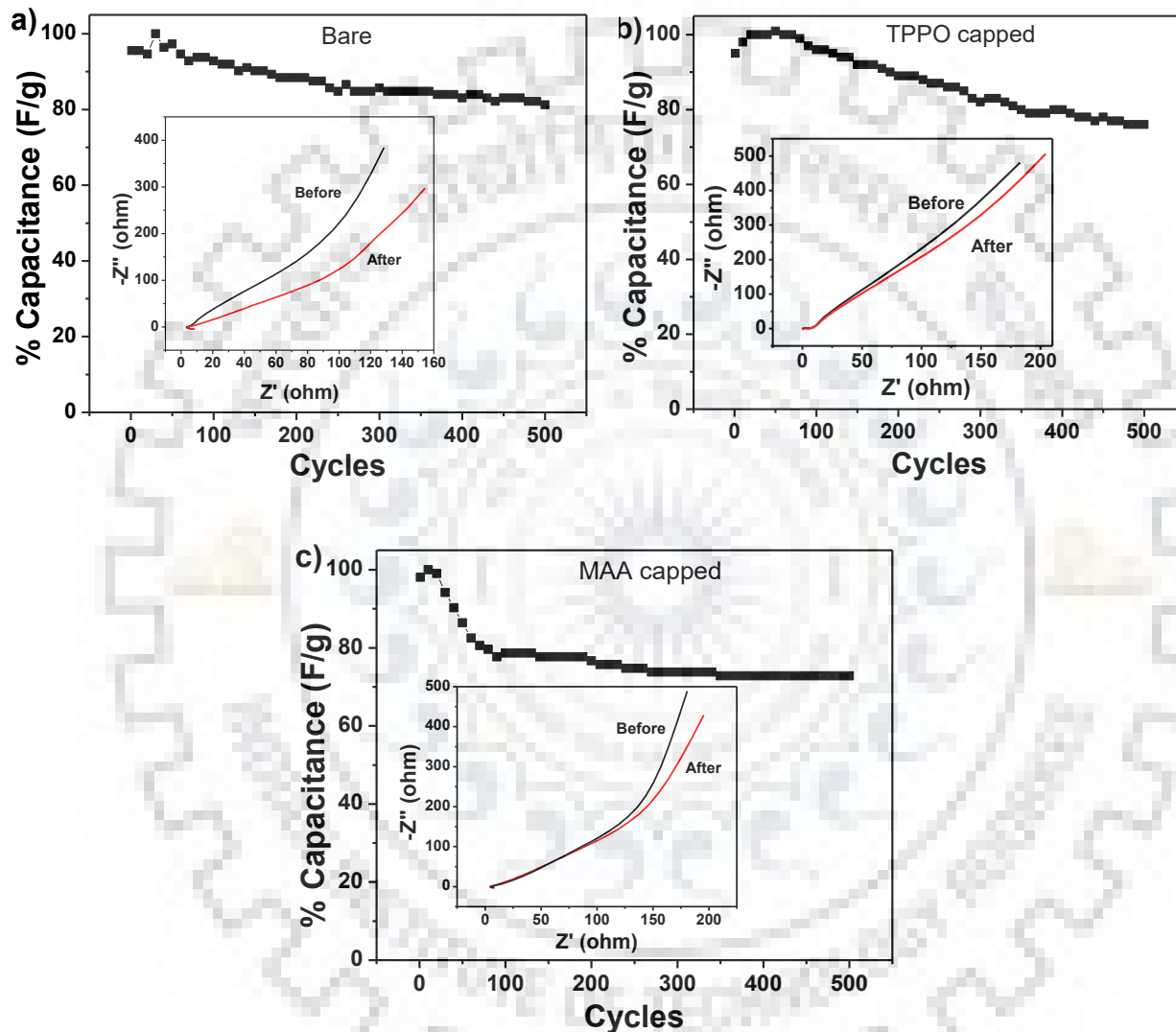


Fig. 3.14 Capacitance retention (in %) of bare (a) TPPO capped (b) and MAA capped (c) for 500 cycles of GCD at current density of 1 A/g. and EIS of samples before and after the 500 cycles inset in respective figures.

The capacitance retention plots for bare and capped CuO NPs revealed 6% enhancement in capacitance during the first few cycles. This is attributable to the initial

activation period within which pores get progressively wet. Similar phenomenon is also reported in literature [93]. Overall, the capacitance retention after 500 cycles was found to be 87% for the bare CuO NPs, 84% for TPPO capped and 73% MAA capped CuO NPs. These capacitance retention are so far very promising results among any form of CuO NPs reported so far as supercapacitor [107, 242, 243]. The decrease in the cycle stability observed here could be attributed to changes in the electrochemical properties at the surface of the CuO NPs. This could be related to degradation of capping agents during intercalation and de-intercalation of ions [242, 243].

The proposed degradation of capping agent is reflected from the comparison of the impedance spectroscopy study of these working electrodes before and after 500 cycles (Fig. 3.15). It can be seen from the Z' vs. Z'' plot (inserted plot in each of the Fig. 3.14) that the imaginary part of each plot revealed decrease in the Z'' component. This is due to decrease in the intercalation of electrolyte ions within the electrode materials. In addition, swelling and shrinking of pores, formation of inactive layer at the surface of the electrode due to charging and discharging effect could also reduce the specific capacitance of the materials [244]. The swelling and shrinking of capping agent is a significant factor, which occurs as a consequence of potential applied between electrode made of CuO NPs and the counter electrode. Here the electrolyte ions are considered to move into the pores of the electrode for intercalation process and vice-versa during de-intercalation process.

3.4 Studies of calcined capped CuO NPs

In order to improve the stability of the capped CuO NPs we have adopted calcinations of the as-synthesized capped CuO NPs at 450 °C. Further by calcination process it is expected that the structural defects of the NPs would be minimized and the pore would tend to be more stable against swelling and shrinkage during charging-discharging process. There is sufficient scope for improving the stability of the capped CuO NPs in order to realize these materials as real time supercapacitors. Henceforth, the batch of bare and capped CuO NPs after calcinations will be referred to as calcined bare CuO NPs and calcined capped CuO NPs.

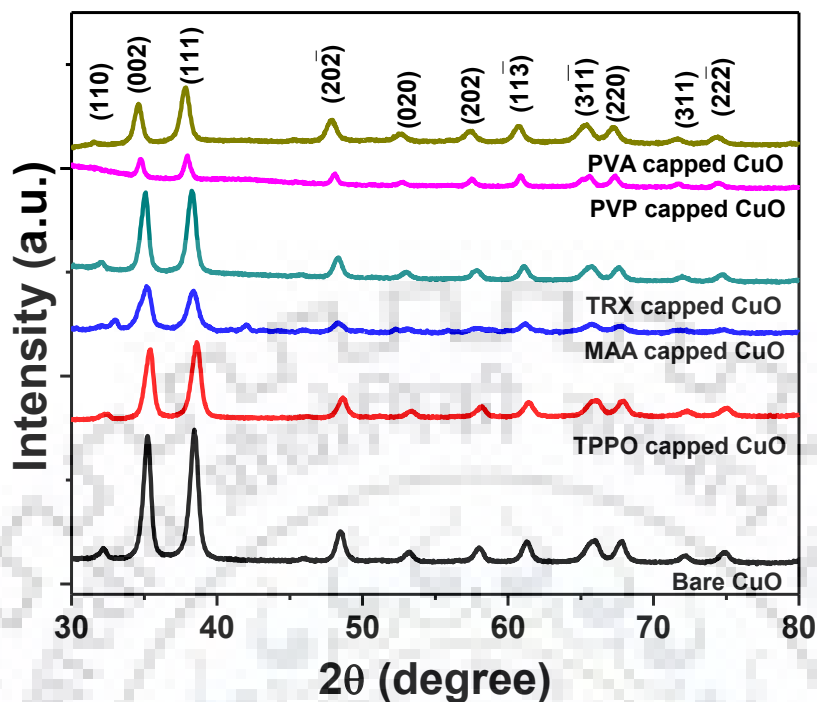


Fig. 3.15 XRD pattern corresponding to the monoclinic structure of bare, TPPO capped, MAA capped, TRX capped, PVP capped and PVA capped CuO NPs after calcination.

3.5 Result and discussion of calcined capped CuO NPs

3.5.1 X-ray diffraction

The XRD patterns of these calcined bare and the batches of calcined capped CuO NPs revealed characteristic peaks of monoclinic phase of CuO NPs which are similar to the uncalcined CuO NPs (Fig. 3.15). The crystallite size of all calcined batches of bare and capped CuO NPs were calculated from Debye Scherrer formula and listed in Table 3.5. The calcined batches reveal larger crystallite size owing to the growth of the particle size of the nanoparticles. The growth in the crystallite size due to heating is lesser for capped batches as compared to bare CuO NPs. The reason for increase in the crystallite size due to heating is attributed to the thermal degradation of the capping agent. Consequently, the nanoparticles collapsed to form larger crystallite size by rearrangement of atoms.

3.5.2 Surface morphology

The FE-SEM image of calcined bare and all batches of calcined capped CuO NPs showed agglomeration of nanoparticles (Fig. 3.16). Their respective EDAX spectrum is given alongside the FE-SEM images which confirmed the purity of calcined CuO NPs (Fig. 3.16).

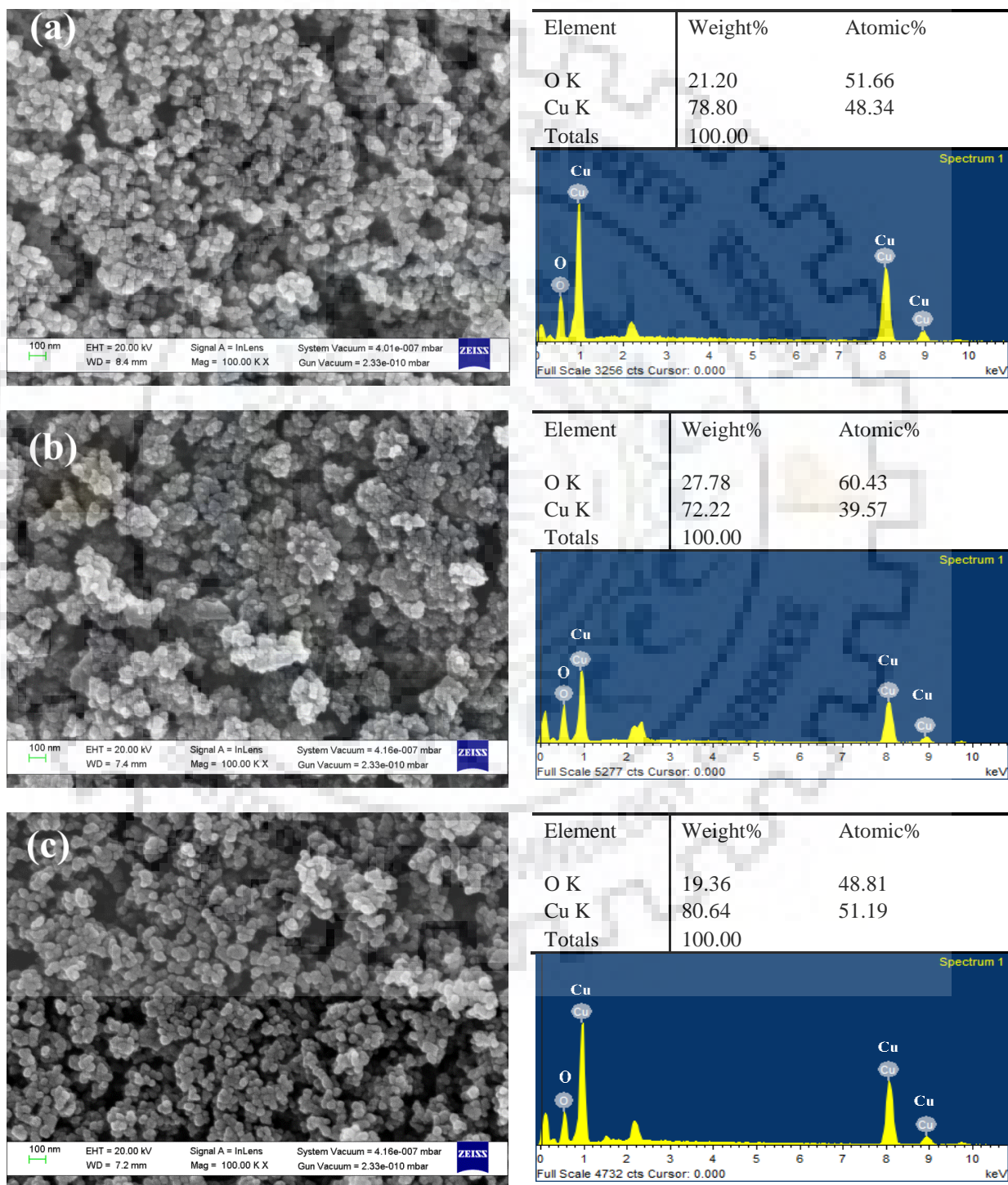


Fig. 3.16 (Figure continued to next page)

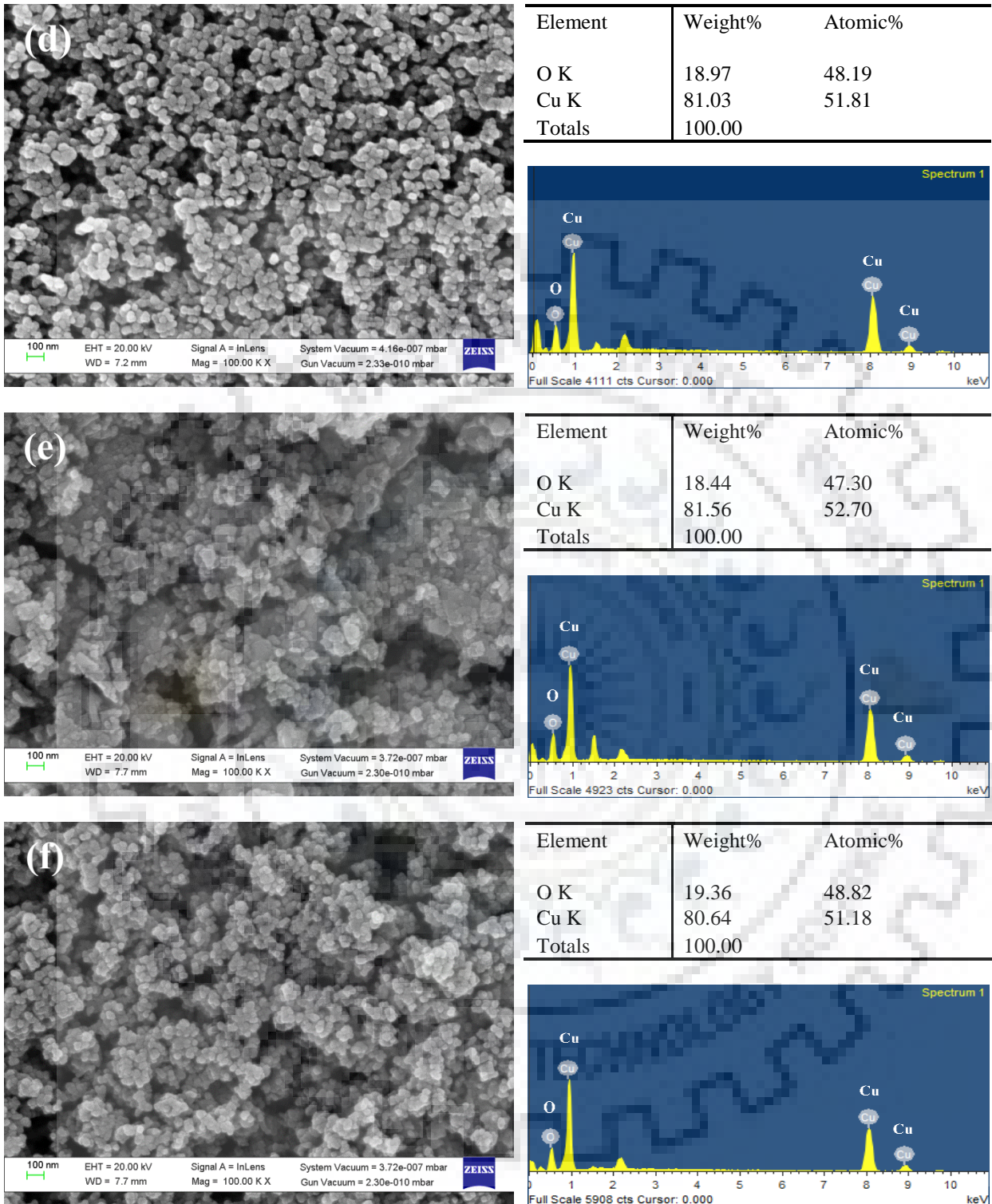


Fig. 3.16 Field Emission Scanning Electron Microscopy images showing morphology of (a) Bare, (b) TPPO, (c) MAA, (d) TRX, (e) PVP, (f) PVA capped CuO NPs after calcination and their corresponding energy dispersive X-ray analysis spectrum showing characteristic K and L X-rays and atomic% of Cu and O.

3.5.3 BET Surface area and pore size

The TPPO capped CuO NPs were also calcined to study the effect of calcinations of capped NPs. The N₂ sorption isotherm of the calcined batch of TPPO capped CuO NPs was found to be similar to the uncalcined batch. The hysteresis is in the region of 0.45 to 0.84 which also revealed mesoporous structure. The pore size distribution is given in Fig. 3.17, which revealed decrease in the pores frequencies than the uncalcined samples. The pore sizes were 1.3 nm, 2.2 nm, 3.1 nm and 4.0-4.3 nm. The average pore size is 3.89 nm. The pore volume of this CuO NPs was measured to be 0.01616 cc/g.

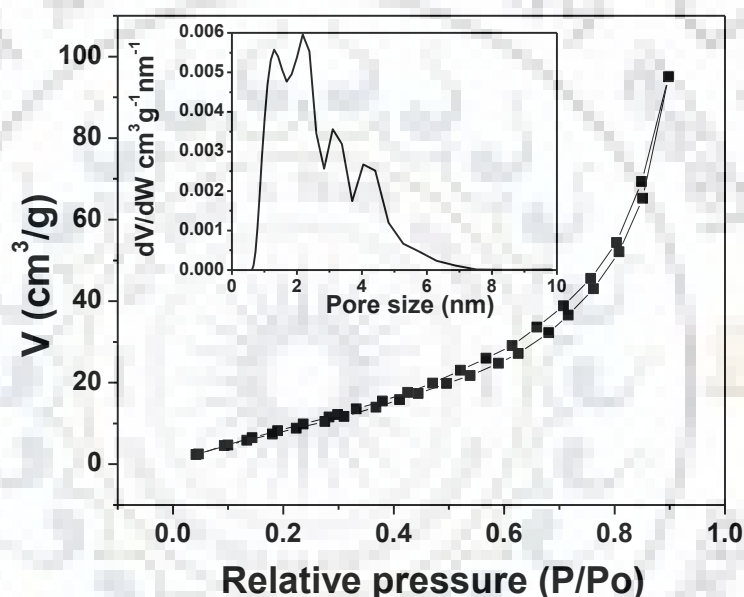


Fig. 3.17 BET isotherm of calcined TPPO capped CuO NPs. inset represent pore size distribution plot.

3.5.4 Electrochemical study of calcined capped CuO NPs

3.5.4.1 Cyclic voltammetry studies

The CV measurement of calcined bare and all the batches of calcined capped CuO NPs at different scan rates 5 mV/s, 10 mV/s, 20 mV/s, 30 mV/s, 40 mV/s and 50 mV/s (Fig. 3.18). Unlike the uncalcined samples, the oxidation and reduction peaks are not very prominent in the CV plots of the calcined sample. This implies that faradaic processes were not favored at the surface of the calcined samples. The quasi rectangular shapes of all the calcined capped CuO NPs were found to be enhanced as compared to that of calcined bare CuO NPs. The area inside the quasi rectangular shape reflected the capacitance of the electrode materials.

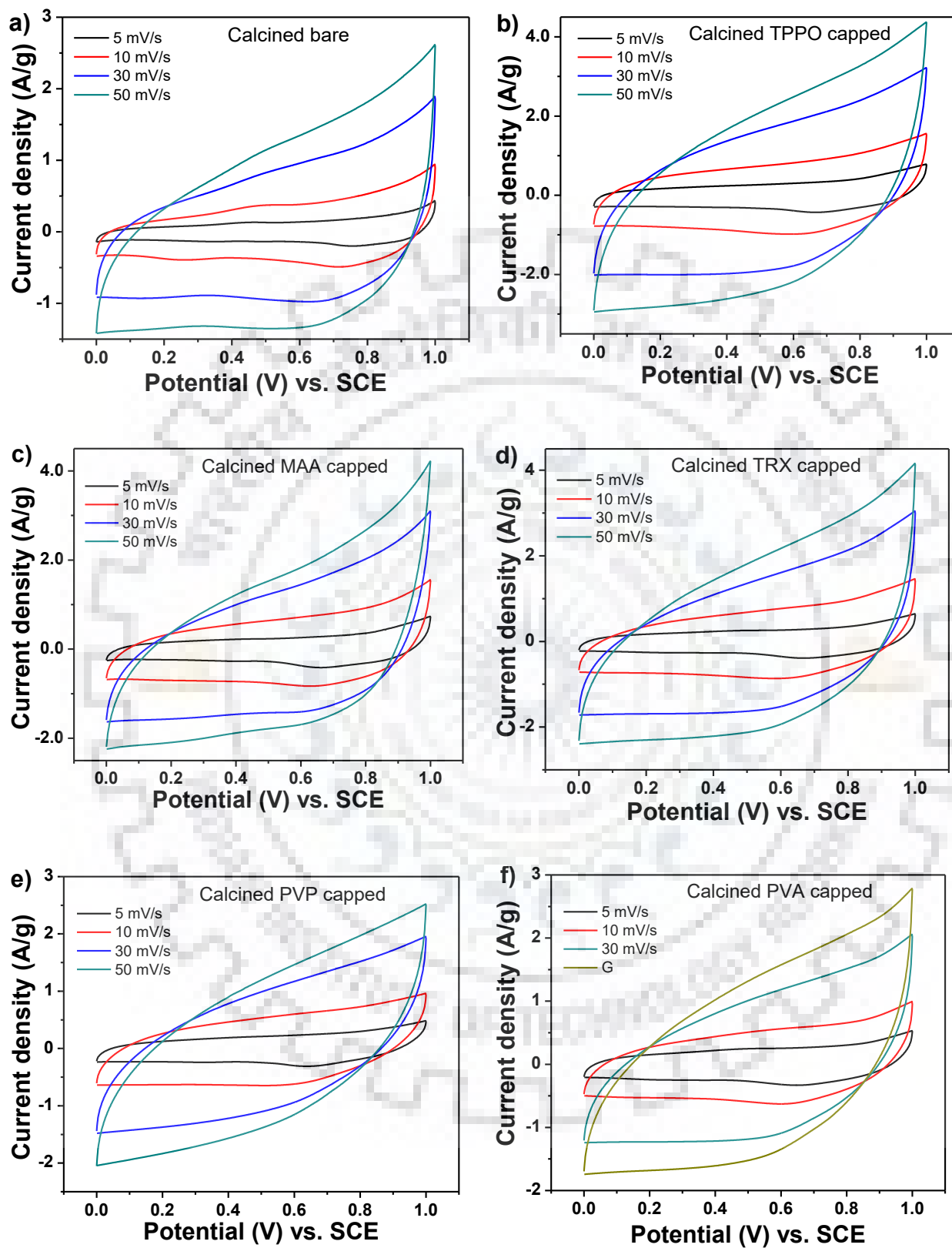


Fig. 3.18 (Continued to next page)

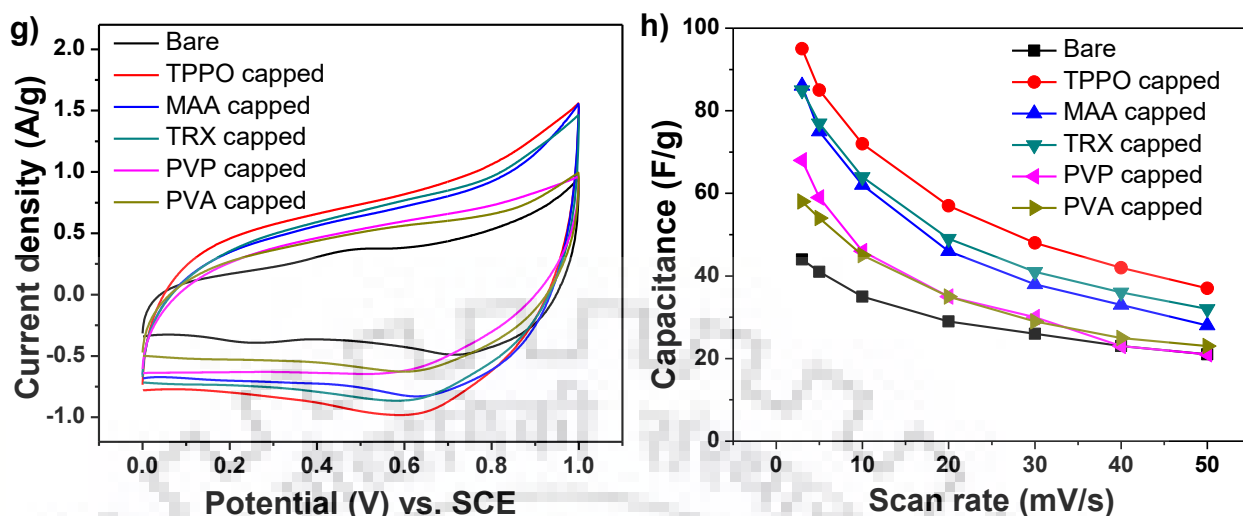


Fig. 3.18 Cyclic voltammograms of (a) bare, (b) TPPO capped, (c) MAA capped, (d) TRX capped, (e) PVP capped, (f) PVA capped CuO NPs. (g) Cyclic voltammograms of calcined bare and all batches of calcined capped CuO NPs at 10 mV/s scan rate. (h) Specific capacitance vs. scan rates plot.

Table 3.5 Crystallite size and specific capacitance of calcined bare and calcined capped CuO NPs

Sample	Crystallite size(nm)	Specific Capacitance (F/g)	
		CV (5mV/s)	GCD (0.2 A/g)
Bare	15.0	41	40
TPPO capped	15.7	85	125
MAA capped	12.9	75	97
TRX capped	12.4	77	112
PVP capped	16.6	59	71
PVA capped	12.6	54	70

The specific capacitance of each calcined batch of CuO NPs was determined as discussed earlier and the values are listed in Table 3.5. Compared to uncalcined bare CuO NPs, the specific capacitance for calcined bare CuO NPs was significantly decreased to 42 F/g. On the other hand the specific capacitance of TPPO capped, MAA capped and TRX capped CuO NPs were in the range of 75-85 F/g which were nearly similar to the uncalcined batches.

However, the specific capacitance against increasing scan rate revealed poor capacitance retention for the all the batches (Fig. 3.18h).

3.5.4.2 EDLC vs. PC contributions

The supercapacitance behavior with respect to EDLC and PC contributions was studied from $1/q$ vs. $v^{1/2}$ and q vs. $v^{-1/2}$ plots, as shown in Fig. 3.19. The C_t , C_{dl} and C_p are given in Table 3.6. Notably, the pseudocapacitance contribution was increased to 90% for the calcined samples of MAA and PVP capped CuO NPs.

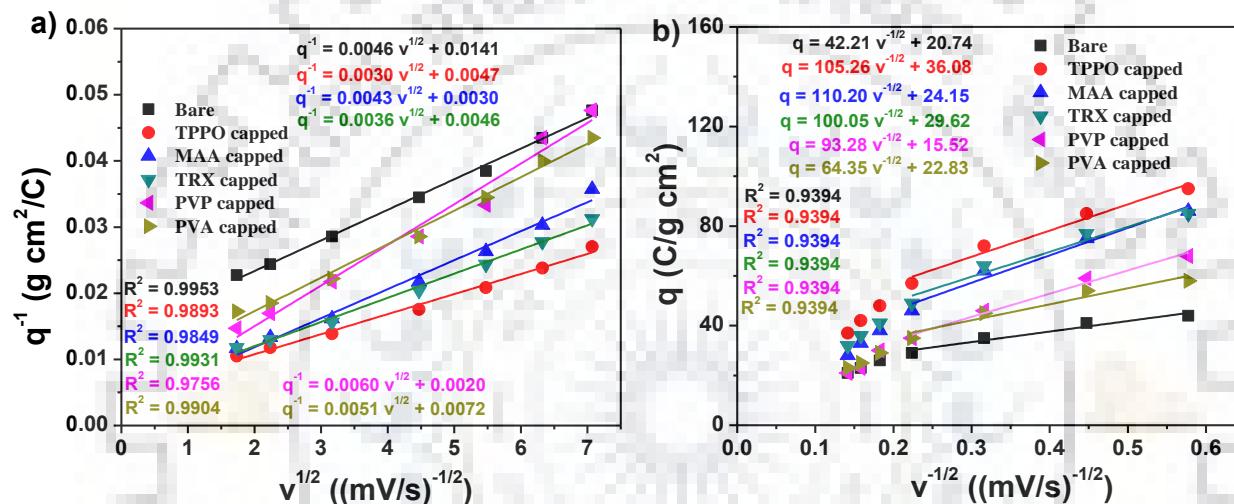


Fig. 3.19 (a) $1/q$ vs. $v^{1/2}$ and (b) q vs. $v^{-1/2}$ dependence of calcined bare and calcined capped CuO NPs.

This is consistent with our CV results and they are attributed to faradaic processes due to better interaction with cation at the surface of the electrode. The increase in PC contribution after calcination was attributable to better crystallinity, reduce the distance between electrolyte ion and Cu ions and electrolyte charge interaction for favorable intercalation and de-intercalation process. It is also noted that the calcined capped CuO NPs exhibited better PC behavior as compared to calcined bare CuO NPs. From these studies it can be remarked that the electrode material made of calcined capped CuO NPs is a promising method for achieving better supercapacitor behavior with increased pseudocapacitance contribution. The pseudocapacitance behaviors are important and necessary for devices that require faster charging and discharging

Table 3.6 Summary of maximum total charge (q_t), double layer capacitance (q_{dl}), and charge associated with pseudocapacitance (q_p) of calcined bare and calcined capped CuO NPs after calcinations in 1 M Na_2SO_4 solution.

Sample	q_t (C/g)	q_{dl} (C/g)	q_p (C/g)	q_p/q_t (%)
Bare	71	21	50	70.4
TPPO capped	213	36	177	83.1
MAA capped	333	24	309	93.0
TRX capped	217	30	187	86.2
PVP capped	500	16	484	96.8
PVA capped	139	23	116	83.5

3.5.4.3 Galvanostatic charge-discharge studies

The charge-discharge curve of calcined bare CuO NPs and the batches of calcined capped CuO NPs recorded at different current density are shown in Fig. 3.20. The charging and discharging time increased with the current density. Our GCD trends were similar to the uncalcined batches and were consistent with literature [242, 243]. The specific capacitances of these calcined CuO NPs derived from charge discharge curve at current density of 0.2 A/g are listed in Table 3.5. The specific capacitance of calcined batches of TPPO, MAA and TRX capped CuO NPs were higher than the other samples. Notably, the maximum specific capacitance is obtained for calcined TPPO capped CuO NPs (125 F/g). In addition the specific capacitance of MAA capped CuO NPs after calcination was also high, i.e., 97 F/g. These batches were selected for stability test.

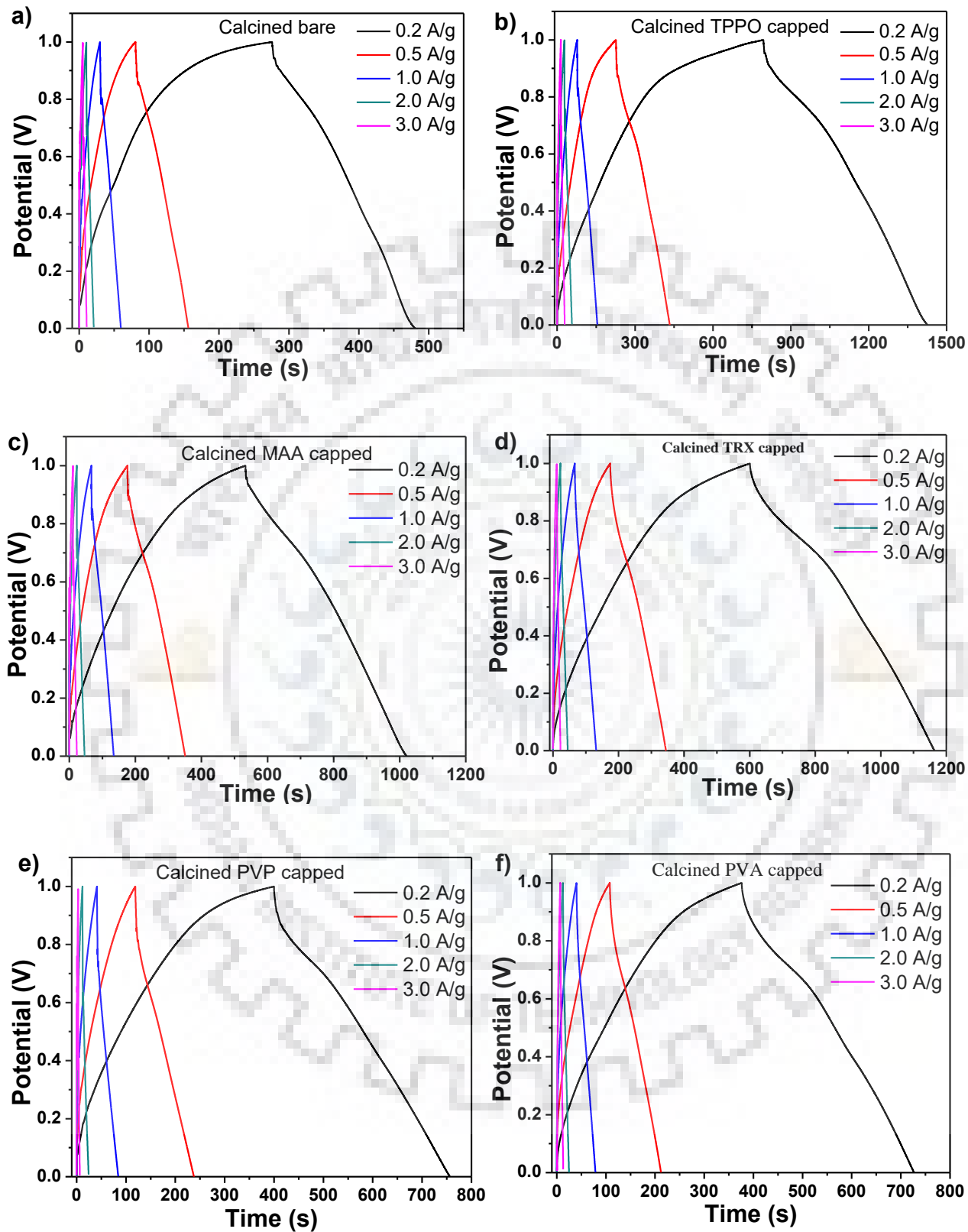


Fig. 3.20 (continued to next page)

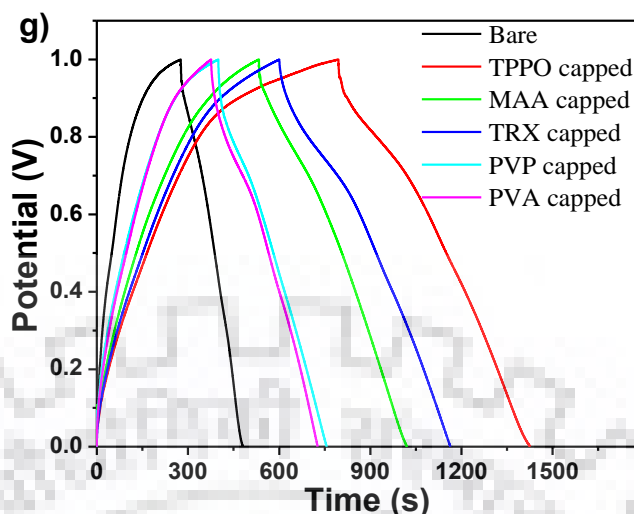


Fig. 3.20 Galvanostatic charge-discharge curves of (a) bare, (b) TPPO capped, (c) MAA capped, (d) TRX capped, (e) PVP capped, (f) PVA capped CuO NPs, (g) Galvanostatic charge-discharge curves of calcined bare and all batches of calcined capped CuO NPs at current density 0.2 A/g.

3.5.4.4 Cyclic stability

The calcined bare, calcined TPPO capped and calcined MAA capped CuO NPs are studied for stability by 500 cycles of charge-discharge process at current density of 1 A/g. The capacitance retention of calcined MAA capped CuO NPs was 80% and calcined TPPO capped CuO NPs was 102% which are improved by several fold as compared to the uncalcined batches (Fig. 3.21).

This enhancement in stability is attributed to increase crystallinity of the NPs and minimizing of defects at the surface of NPs due to heating. It may be commented here that the capacitance retention of calcined TPPO capped CuO NPs is much better than CuO based electrode reported in literature [107, 242, 243].

The impedance spectroscopy of the calcined batches after first cycle and after 500 cycles is given in Fig. 3.21. The deterioration of the electrode for MAA capped calcined CuO NPs during the cyclic charging-discharging processes is revealed from the decrease in the slope of the vertical line corresponding to low frequency region. It implied that the ionic mobility was decreased with the progress of charging-discharging.

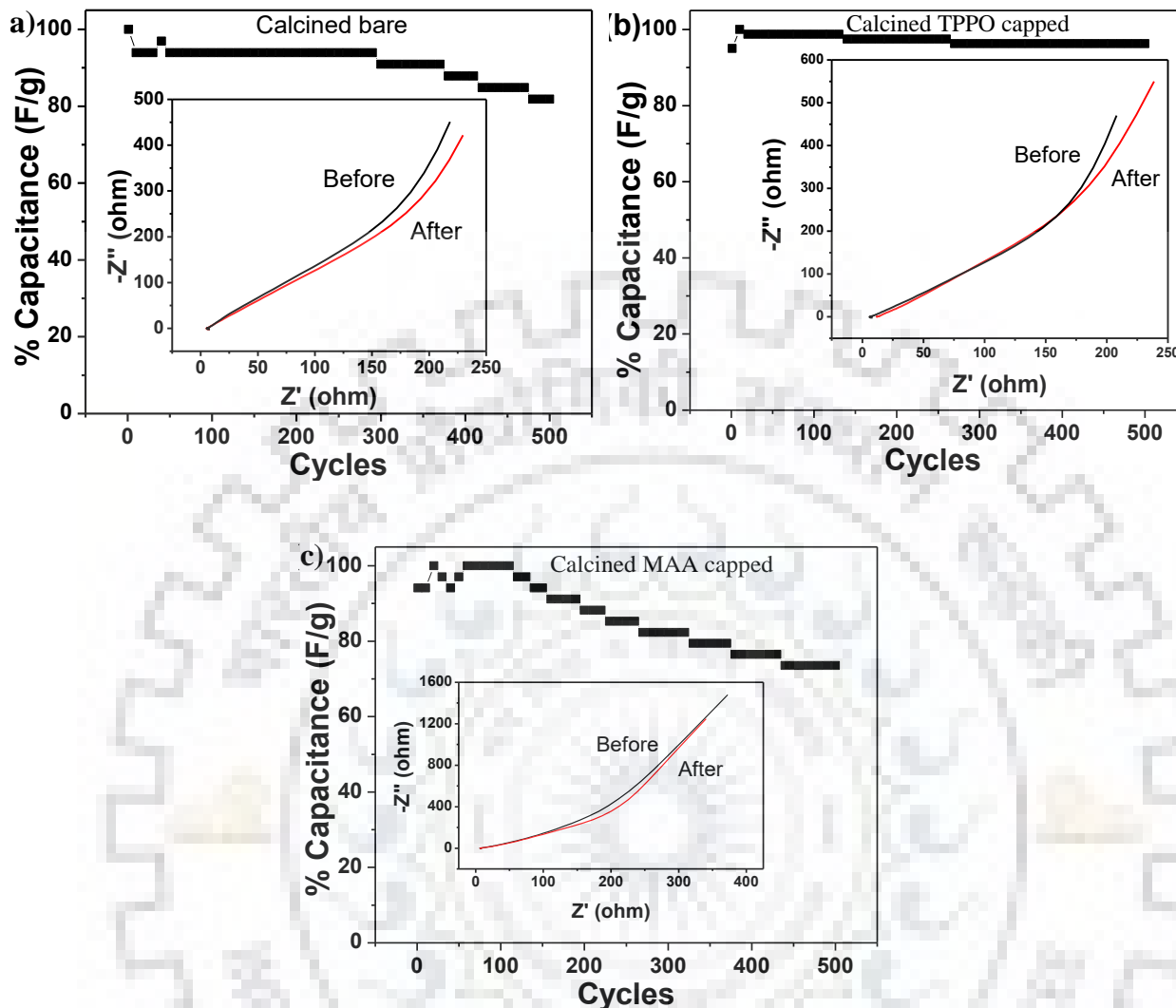


Fig. 3.21 Cycling stability test (a) calcined bare (b) calcined TPPO capped and (c) calcined MAA capped CuO NPs at current density of 1 A/g. Inset shows the Nyquist impedance spectrum of samples before and after 500 cycles.

3.6 Capped and calcined capped CuO NPs as glucose sensor

Since pseudocapacitance contribution by calcined capped batches of CuO NPs were much higher than EDLC contribution, so it was envisaged that these CuO NPs might also work as good electrode as glucose sensor via oxidation reactions at the electrode. To confirm our assumption we studied both uncalcined and calcined batches of MAA capped and TPPO capped CuO NPs as electrode for glucose sensor.

The electrocatalytic performances of the bare and the capped CuO NPs towards glucose sensing via oxidation reaction at the respective anodes in alkaline medium were studied by CV at a scan rate of 50 mV/s. The CV measurements were recorded using an arbitrary 0.9 mM glucose concentration and the results are given in Fig. 3.22 a-c. Similarly, the CV measurements of glucose oxidation by the bare and capped CuO NPs after calcination at 450 °C are given in Fig. 3.22 d-f. A control CV measurement of glucose oxidation by graphite sheet without CuO NPs did not exhibit any oxidation current in the potential window of 0 to 0.7 V. A small background current was obtained for graphite electrode which is attributable to very small double layer capacitance with electrolyte ions. Compared to the control graphite electrode, the oxidation current due to glucose oxidation increased drastically for the electrode made of bare and capped CuO NPs in the potential window ranging between 0.25 V and 0.70 V vs. SCE Fig. 3.22.

The background current was large for all the batches of electrode made of bare and capped CuO NPs, owing to high electrochemical activity of glucose [245]. Our results on glucose sensing by capped and batches of calcined capped CuO NPs are consistent with the literature [145, 146, 246, 247]. A possible mechanism involved in electrocatalytic oxidation of glucose by capped and calcined capped CuO NPs in alkaline medium is assumably similar these discussed in literature [145, 157, 246]. It is worth monitoring here that the oxidation current increased significantly for the electrodes made of calcined capped CuO NPs as compared to the uncalcined counterparts. This is attributable to enhanced electrical conductivity at the surface of the calcined capped CuO NPs as discussed in the previous section (3.3.6.5)

3.6.1 Effect of glucose concentration

The CV measurements of glucose oxidation by capped CuO NPs, calcined capped CuO NPs and their comparison with bare and calcined bare CuO NPs for increasing glucose concentration are given in Fig. 3. 23. The CV measurements of 0.9 mM glucose were recorded at different scan rates varying between 20 mV/s and 300 mV/s. As expected, the potential corresponding to peak current was observed shifted towards positive direction with the increase in scan rate. The peak current also increased linearly with the square root of scan rate (inset of Fig. 3.23). These results are consistent with quasi reversible diffusion controlled process [248].

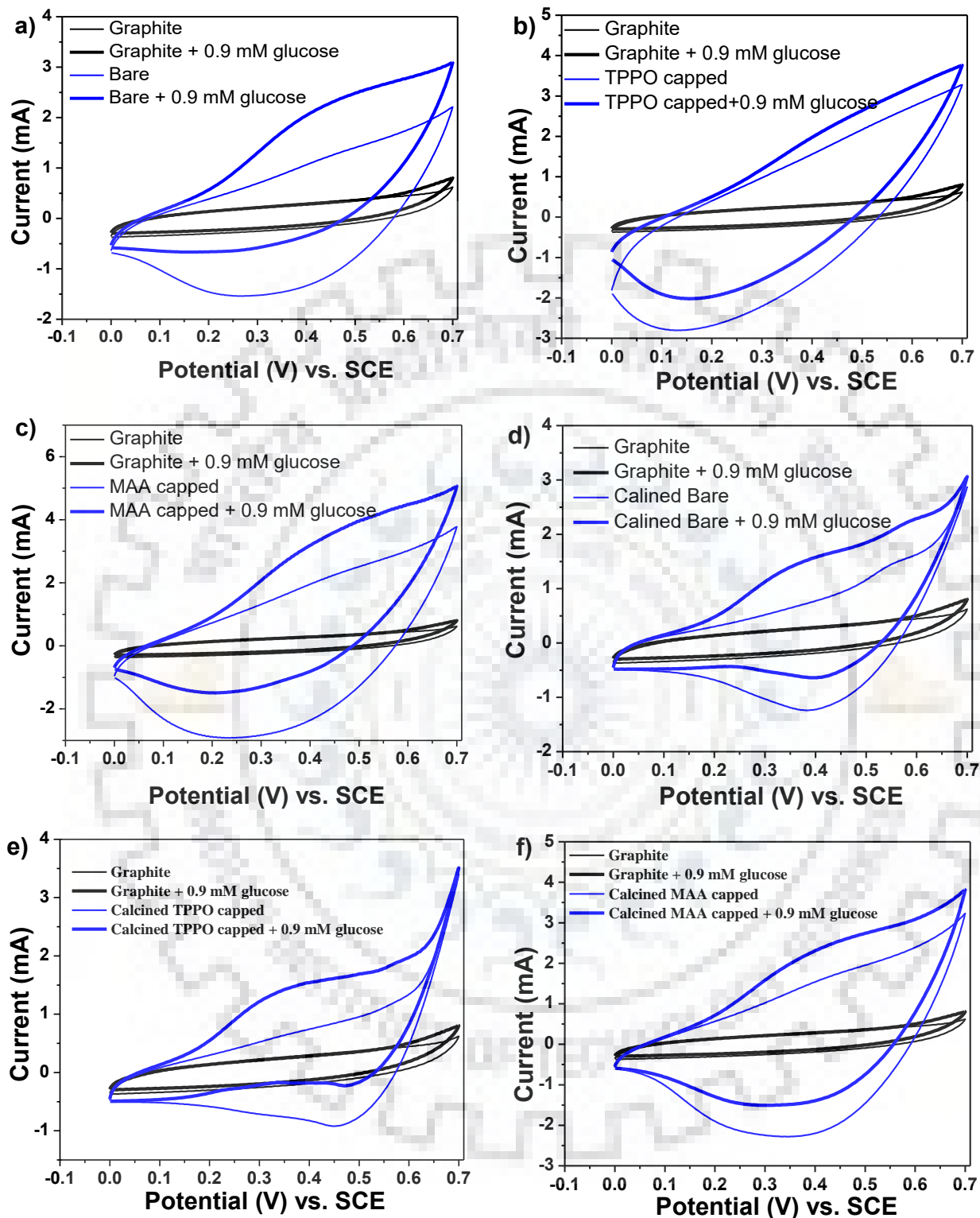


Fig. 3.22 CV curves of graphite sheet and, (a) bare, (b) TPPO capped, (c) MAA capped, (d) calcined bare, (e) calcined TPPO and (f) calcined MAA capped CuO NPs electrode in the presence and absence of glucose in 0.1 M NaOH solution measured at scan rate of 50 mV/s.

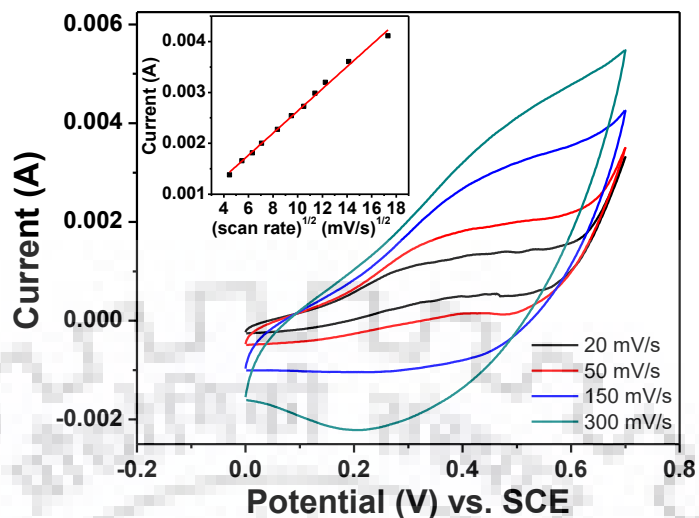


Fig. 3.23 The electrochemical behavior of glucose oxidation on the calcined TPPO capped CuO NPs electrode recorded in 0.1 M NaOH solution containing 1 mM glucose concentration at different scan rates ranging from 20 mV/s to 300 mV/s. Inset shows the dependence of the peak oxidation current on the square root of the scan rate.

3.6.2 Sensitivity

The effect of glucose concentration on the CV response of all the batches of bare, capped and their calcined counterparts were studied in the potential window of 0 to 0.7 V. The concentration of glucose was taken in the range of 9 μM to 7.1 mM and the results are given in Fig. 3.23. The oxidation current profiles for 0.9 mM glucose in selected potential window are given in the insert of Fig. 3.23. The plot of oxidation current vs. overall chosen glucose concentration was non-linear in nature (Fig. 3.24). On careful analysis, the linear part of the plot corresponded to a lesser glucose concentration range. The linear range data for all the batches of CuO NPs are given in Table 3.7. For example, the linear range for the batch of calcined TPPO capped CuO NPs was 9 μM to 4.2 mM. The sensitivity of each type of CuO NP as electrode was obtained from the slope of the linear fitted plot in Fig. 3.24. The sensitivity is given as slope/surface of the electrode and the values are listed in Table 3.7. It is noted that, the sensitivity of capped and calcined capped CuO NPs were better than the bare CuO NPs for both with and without calcination. The improved sensitivity in the capped batches is due to higher oxidation current which is attributable to the efficient faradaic redox process as discussed in the previous section. It may be commented here that the sensitivity of our electrode i.e. calcined capped CuO NPs was better than those represented in the literature (Table 3.8).

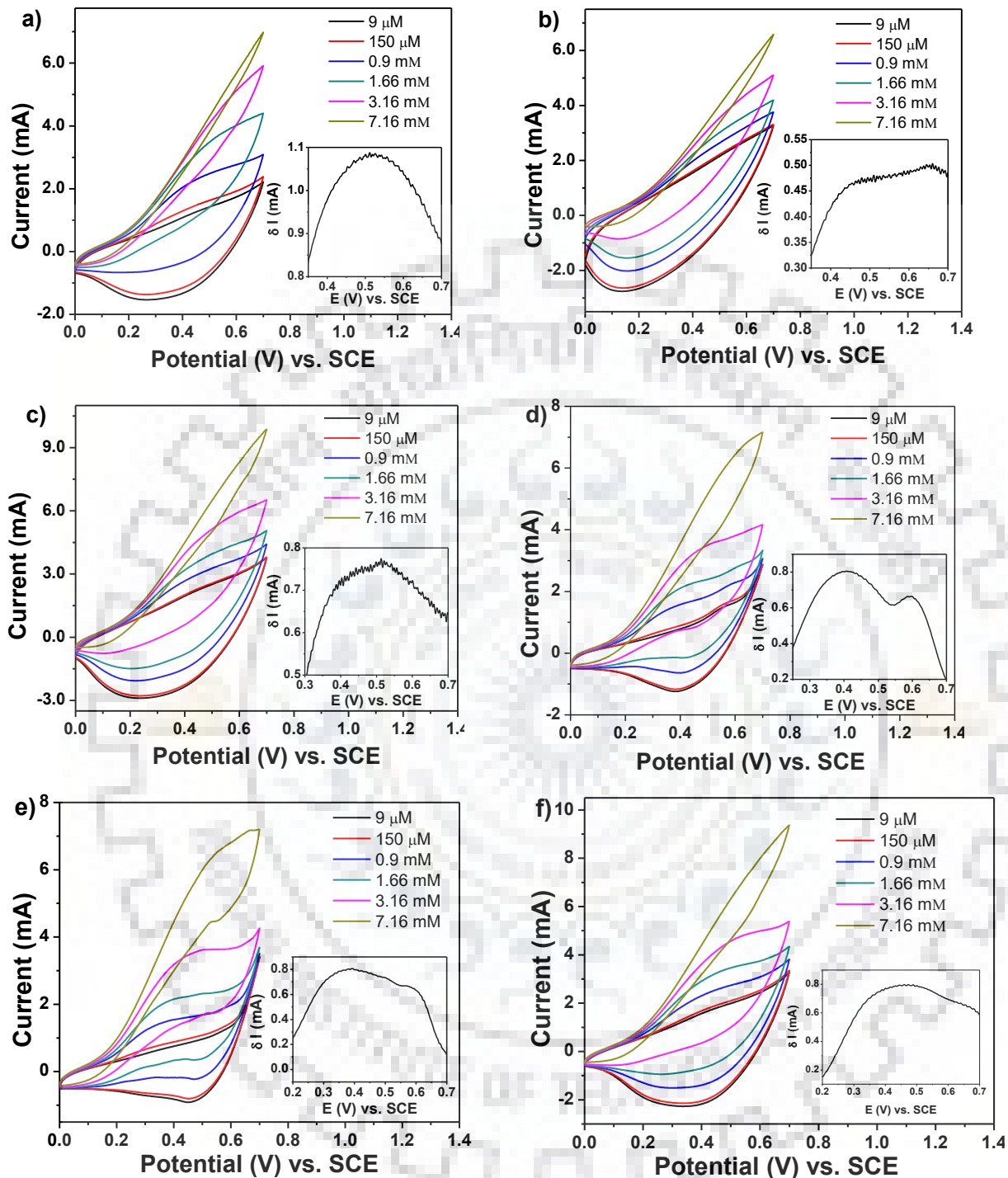


Fig. 3.24 CV curves of bare, TPPO capped, MAA capped, calcined bare, calcined TPPO and calcined MAA capped CuO NPs electrode recorded at scan rate of 50 mV/s in 0.1 M NaOH solution with successive addition of different concentration of glucose. Inset showing plot of change in anodic current versus potential

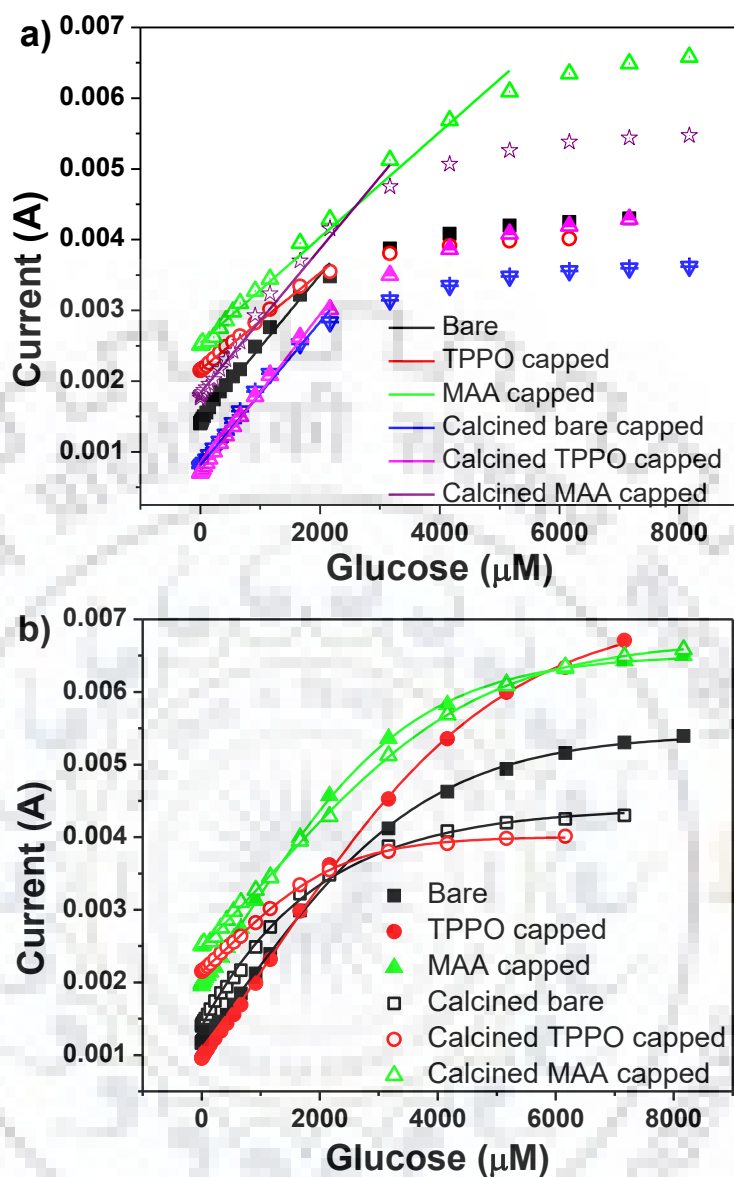


Fig. 3.25 Calibration curve of all six batches CuO NPs electrodes based on current recorded on successive addition of different amount of glucose concentration into 0.1 M NaOH solution at different oxidation potential e.g., 0.5 V for pristine, TPPO capped and MAA capped CuO NPs electrodes, 0.4 V for calcined pristine and calcined TPPO capped CuO NPs, and 0.45 V for calcined MAA capped CuO NPs.

3.6.3 Limit of detection (LoD)

The LoD was calculated for each batch of CuO NPs from the equation $\text{LoD} = 3\sigma/s$ where, σ is standard deviation of the linear coefficient and s is slope. The estimated LoD of each batch of CuO NPs are listed in Table 3.7. The LoD for calcined TPPO capped was 0.04

μM which is much better than those reported in literature (Table 3.8). The response time for glucose sensing by all batches of CuO NPs were less than 5 seconds, which is an important parameter for real time monitoring.

Table 3.7 Characteristic features of glucose sensors of all batches of CuO NPs electrodes

Electrodes	Response speed (s)	Linear range (mM)	LOD (μM)	Sensitivity ($\mu\text{A}/\text{mM cm}^{-2}$)	Oxidation potential (V)
Pristine CuO NPs	<5	0.0009 to 2.2	0.11	1024	0.50
TPPO capped CuO NPs	<5	0.0009 to 2.2	0.75	668	0.50 to 0.65
MAA capped CuO NPs	<5	0.0009 to 5.2	0.33	752	0.50
Calcined pristine CuO NPs	<5	0.0009 to 3.2	0.12	993	0.40 and 0.60
Calcined TPPO capped CuO NPs	<5	0.0009 to 4.2	0.04	1100	0.38 and 0.60
Calcined MAA capped CuO NPs	<5	0.0009 to 3.2	0.33	1143	0.45 and 0.60

3.6.4 Amperometric study

3.6.4.1 Sensitivity

The sensitivity of glucose by the capped and calcined capped batches of CuO NPs was also estimated from amperometric studies. The stepwise increase in oxidation current due to periodic spiking of very low concentration of glucose e.g., 2.5 μM , 5.0 μM and 10.0 μM in 0.1 M NaOH under stirring condition, for respective batches of CuO NPs are shown in Fig. 3.26. From this study, it may be remarked that glucose concentration of 2.5 μM can be determined from measurable increase in the current. The best response was observed for the calcined batches of TPPO capped and MAA capped CuO NPs. A constant current was measured

between any two glucose spikes which indicated the feasibility of using calcined capped CuO NPs as non-enzymatic glucose sensor.

Table 3.8 Comparison of studied CuO NPs electrode as glucose sensor reported in literature.

Electrode	LoD	Linear range (mM)	Sensitivity ($\mu\text{A}/\text{mMcm}^{-2}$)	Oxidation potential (V)	Ref.
Sandwich-structured CuO	1	3	5342.8	0.6	249
CuO nanoflowers	1.71	5	2657	0.5	250
CuO nanosheets	-	1	520	0.5	251
CuO nanoparticles	0.5	18.45	2762.5	0.6	147
CuO nanowires	0.3	18.8	2217.4	0.35	252
CuO nanocubes-graphen	0.7	4	1360	0.59	159
CuO/MWCNTs modified electrodes	4	14.5	1211	0.55	253
CuO/grapheme nanocomposites	1	8	1065	0.6	254
CuO NFs	0.8	2.5	431.3	0.40	248
Cu _x O/PPy/Au	6.2	8	232.22	0.6	255
CuO/CNFs	0.2	11	2739	0.5	256
CuO/MWCNTs	0.2	1.2	2596	0.4	257
CuO NWs	2	3	684.2	0.55	258
Cu-CuO nanowire	500	12	-	0.3	259
CuO nanoplatelets	0.5	0.8	3490.7	0.55	260
CuO nanowires	0.049	2	0.49	0.33	145
CuO biscuits/SPCE	0.1	4.03	308.71	0.5	246

3.6.4.2 Selectivity

The selectivity of non-enzymatic glucose sensing by calcined capped CuO NPs was investigated by amperometric method in the presence of easily oxidizable compound e.g., starch, sucrose, hydrogen peroxide (H_2O_2), ascorbic acid (AA), dopamine (DA) and uric acid (UA). Though normal glucose level in blood is in the range of 3 to 8 mM but oxidation currents for such glucose concentrations are very high. Because of this we have taken 250 μM glucose solutions as a test solution. The concentrations of interfering compounds were taken at 25 μM to maintain 10:1 ratio of analyte: interferent.

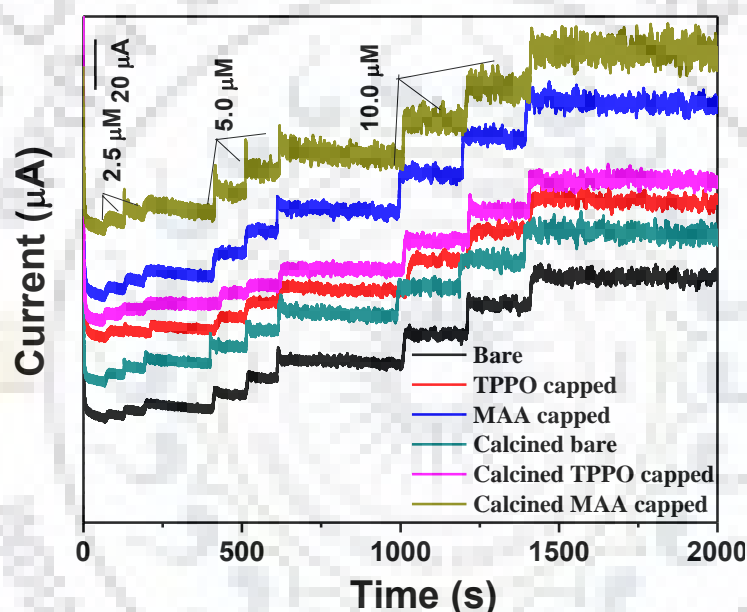


Fig. 3.26 Amperometric current responses of the all the batches of CuO NPs electrode at different oxidation potentials in 0.1 M NaOH solution with dropwise addition of 2.5 μM , 5.0 μM and 10.0 μM glucose.

The oxidation current due to oxidation of 250 μM glucose in 0.1 M NaOH under stirring condition were recorded and the results are given in Fig. 3.27. Notably, the current due to glucose oxidation was significantly higher than those of the interfering compounds. Similarly, the glucose sensing at lower glucose concentration such as 2.5 μM and 5 μM in presence of 10 times lower concentration of interfering compound were also measured (Fig. 3.27). It may therefore be summarized that the calcined TPPO and MAA capped CuO NPs are

suitable electrocatalytic material for glucose sensing in presence of common interfering agents that are usually present in human fluids.

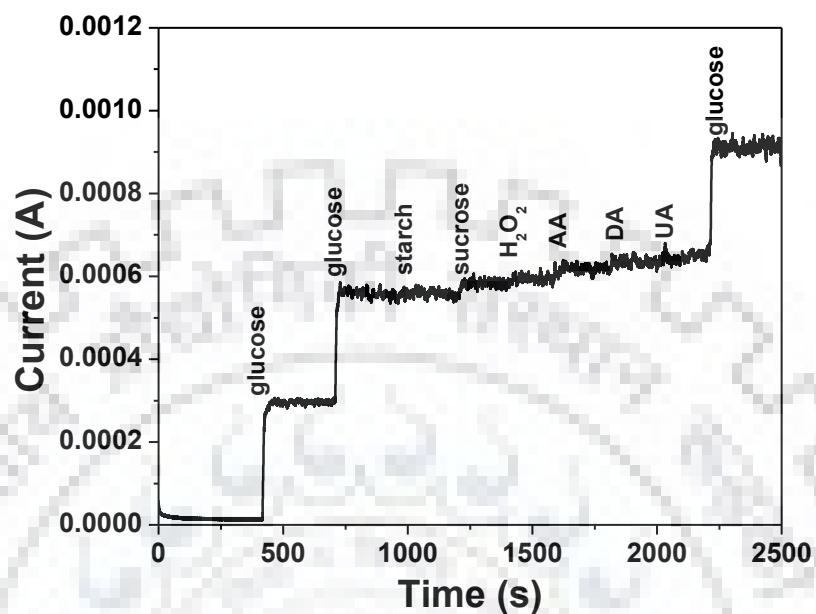


Fig. 3.27 Amperometric current responses of glucose oxidation with interfering compounds such as starch, sucrose, H₂O₂, ascorbic acid (AA), dopamine (DA) and uric acid (UA) in 0.1 M NaOH solution.

3.6.4.3 Real time analysis

The applicability and reliability of calcined TPPO capped CuO NPs as electrodes were investigated for sensing glucose levels in human blood and urine samples. The amperometric response to blood samples was analyzed with respect to 10 μ M concentration of glucose. The oxidative current for blood sample in stirring condition was nearly double as compared to that of 10 μ M glucose. By correcting a dilution factor (1000 \times), the glucose level in the blood was estimated as 20 mM (Fig. 3.28a). Similarly glucose levels in human urine sample were analyzed using calcined MAA capped CuO NPs after spiking with different concentrations of glucose in human urine sample (Fig. 3.28b). The CV measurements of urine sample spiked with glucose concentration of 50 μ M, 100 μ M and 150 μ M given in Fig. 3.29a. The increase in current at 0.36 V is attributable to glucose oxidation. The amperometric response of blank 25 μ M glucose and that of a test solution comprising 25 μ M glucose spiked in urine are shown in Fig. 3.29b.

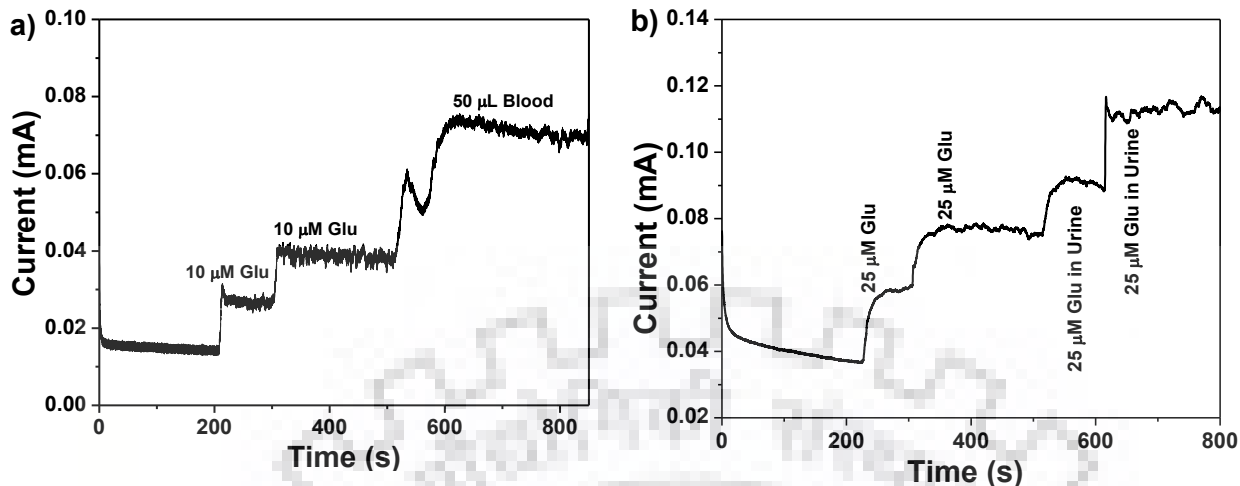


Fig. 3.28 Amperometric current response of blood sample over calcined TPPO capped CuO NPs electrode (a) and urine sample (b) over calcined MAA capped CuO NPs electrode in 0.1 M NaOH solution.

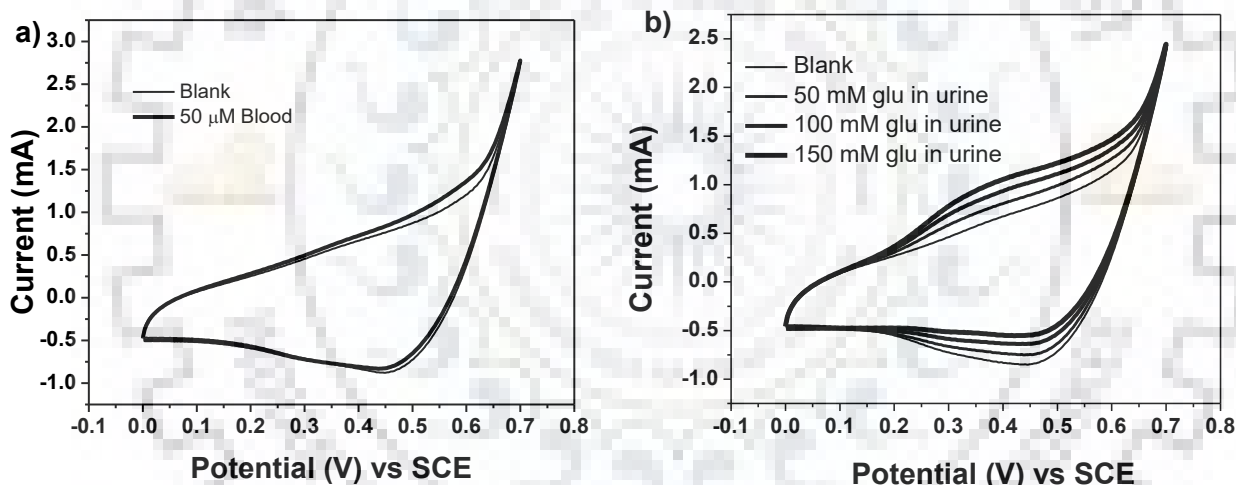


Fig. 3.29 CV curves of blood samples (a) over the calcined TPPO capped CuO NPs electrode and urine (b) over the calcined MAA capped CuO NPs electrode in 0.1 M NaOH solution at scan rate of 50 mV/s.

The possibility of using the calcined TPPO capped CuO as electrode for repeated estimation of glucose in urine sample is demonstrated in Fig. 3.30. After each measurement, the electrode was washed with deionized water (Millipore) and the glucose concentration was determined from CV measurement at a scan rate of 50 mV/s for six times. Each measurement revealed reproducible result. Therefore it may be inferred that calcined TPPO and MAA capped CuO NPs can be successfully used as a glucose sensor in blood and urine sample.

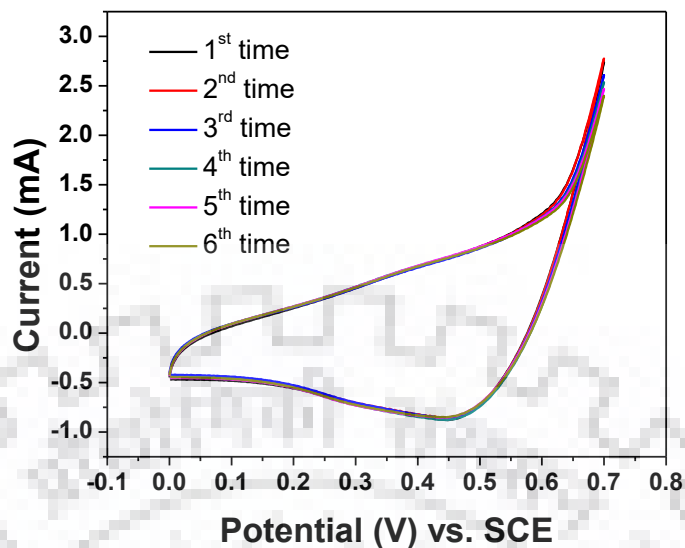


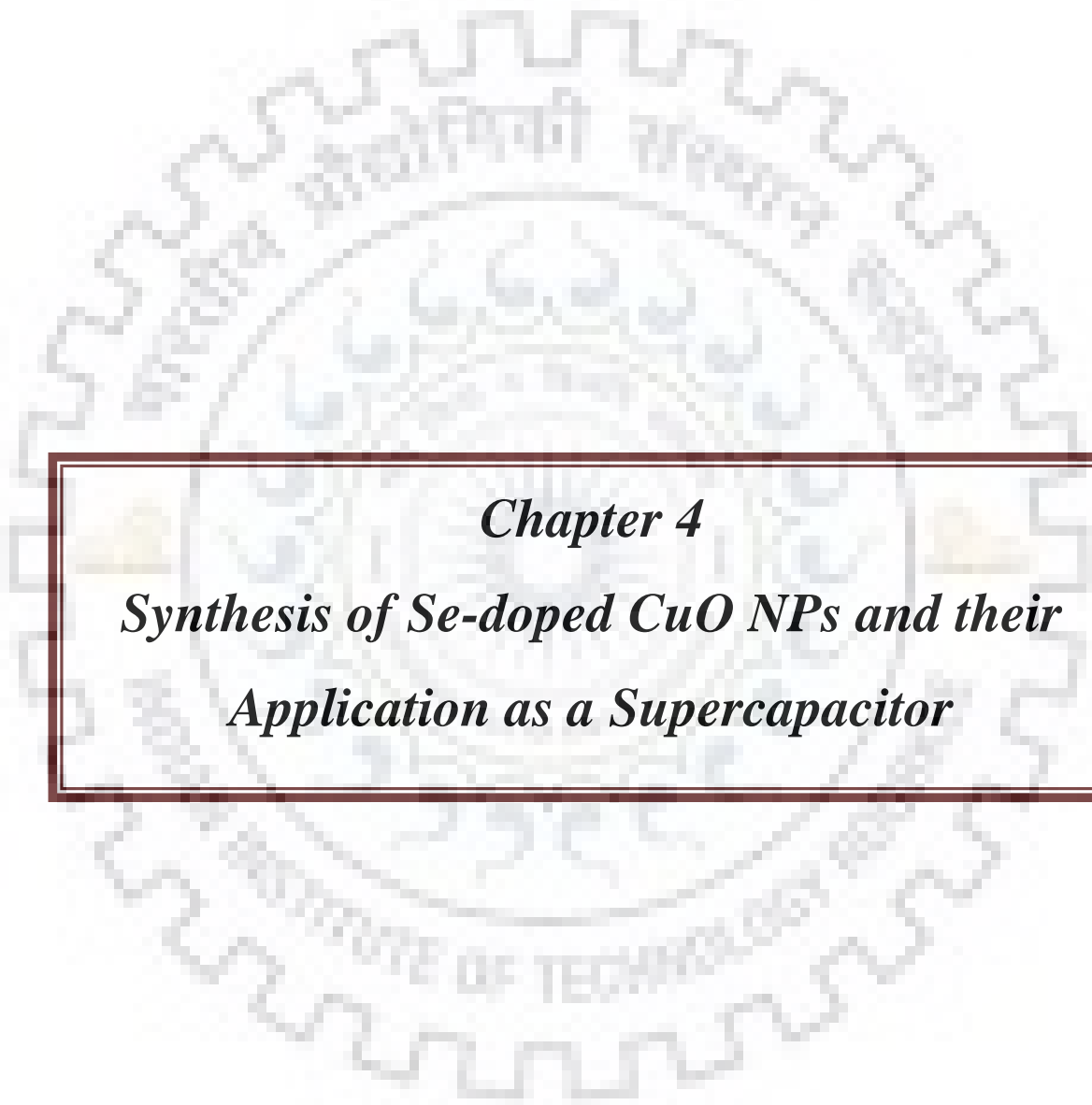
Fig. 3.30 CV curves showing re-usability of the calcined TPPO capped CuO NPs electrode for glucose determination in urine samples.

3.7 Conclusions

Batches of CuO nanoparticles capped with different types of capping agents were successfully synthesized by co-precipitation method and were thoroughly characterized. The molecular structure of capping agent is important for interacting with the surface of CuO to control the band gap, surface defect, surface morphology as well as surface area of the respective batches of CuO NPs. These surfaces modified CuO NPs were found to exhibited good supercapacitor behavior as reflected from specific capacitance of the order of 131-134 F/g for TPPO capped, MAA capped, TRX capped and PVP capped, respectively at current density of 0.2 A/g. However, the stability of these capped CuO NPs was poor and was attributed to unstable pores of the NPs. In order to improve the specific capacitance behavior, the capped CuO NPs were calcined at 450 °C. The supercapacitance behavior was investigated in terms of EDLC and PC contribution from cyclic voltammetry studies. All the batches of calcined capped CuO NPs revealed higher pseudocapacitance behavior (90%) and hence it may be concluded that the TPPO capped CuO NPs after calcination at 450 °C exhibited excellent electrode stability (102%) with high specific capacitance.

The MAA capped and TPPO capped CuO NPs before and after calcination at 450 °C were then tested for glucose sensing. The calcined batches of MAA capped and TPPO capped CuO NPs exhibited excellent glucose sensing. The LoD for calcined TPPO capped CuO NPs was 0.04 μM which is a significant better than those reported LoD values in literature. Amperometric studies also demonstrated the sensitivity and selectivity of the calcined capped CuO NPs. The glucose sensing by our method was not affected in the presence of early oxidisable compounds such as starch, sucrose, H_2O_2 , ascorbic acid, dopamine, uric acid. Finally, the applications of the calcined capped CuO NPs were demonstrated to be successful for estimating glucose concentration in the human blood and urine samples.





Chapter 4

Synthesis of Se-doped CuO NPs and their Application as a Supercapacitor

4.1 Introduction

In the previous Chapter TPPO capped CuO NPs exhibited the best electrochemical properties and were good for supercapacitor. In the present Chapter, we have studied modification of TPPO capped CuO NPs with selenium doping for supercapacitor behavior. The emphasis is on development of temperature elevated supercapacitor using CuO Nps. Among all transition metal oxides, CuO has good thermal stability and is a good thermal conductor [238]. Therefore, CuO nanostructures can be a potential material for a temperature elevated supercapacitor because it can sustain ion conductivity of electrolyte, viscosity variation and solubility limits. These factors are the major causes for lowering the device performance at high temperature [261].

For this study, doping of selenium is employed as it is expected to enhance the conductivity as well as generates defects sites in the CuO NPs to improve the supercapacitor behavior [28]. Doping in the metal oxide can developed strain, metal vacancy defect and increase charge transport over the surface. This was confirmed by Se doped ZnO nanoparticles being used for photocatalytic application [66]. The as-synthesized batches of Se-doped CuO NPs were thoroughly characterized and were studied for supercapacitor behavior at room temperature as well as at elevated temperature.

4.2 Materials and Methods

4.2.1 Chemicals

The chemicals used for CuO NPs were almost same as those mentioned in Chapter 3 sodium selenate (Na_2SeO_4 , > 98%), from HiMedia Pvt. Ltd., India.

4.2.2 Synthesis of Se-doped CuO NPs

The batches of Se-doped CuO NPs were synthesized by the coprecipitation method by adding 0, 2, 5, 10 and 20 wt% of sodium selenate in 150 mL of aqueous solution of copper acetate (20 mM) followed by addition of 0.01 g TPPO and 1mL of acetic acid. This reaction was refluxed at 100 °C for 1 hour in a round-bottomed flask. Then 1.0 M NaOH was added to the solution until a black colored precipitate was formed at pH 7.7 to 8.0. The precipitate was centrifuged at room temperature, washed 3 times with ethanol, and eventually dried at 80 °C

overnight in a temperature controlled oven. The exact amount of sodium selenate taken for respective batches was listed in Table 4.1.

Table 4.1 Concentration of selenium taken during synthesis of Se-doped CuO NPs

Weight taken of copper acetate (g)	Weight taken of sodium selenate (g)	Amount of Se dopant (mg)	Batches	Dopant amount by ICP-OES
0.6	0	0	Pristine	0 wt%
0.6	0.012	5.0	2 wt%	0.14 wt%
0.6	0.030	12.5	5 wt%	0.23 wt%
0.6	0.060	25.0	10 wt%	0.45 wt%
0.6	0.120	50.0	20 wt%	0.31 wt%

The batches of Se doped CuO NPs prepared with 2 wt%, 5 wt%, 10 wt% and 20 wt% of Se precursor were analyzed by ICP-OES technique to obtain the actual Se concentration in the respective doped CuO NPs. The concentrations of selenium in the respective batches of the acid digested nanoparticles followed by serial distribution were determined against the calibration plot obtained by analyzing known concentrations of standard selenium ion solution (Sigma Aldrich). The concentration of selenium in Se-doped CuO NPs was calculated using the formula given below:

$$Se (wt\%) = \frac{[mass\ of\ Se\ in\ acid\ digested\ (mg)]}{[mass\ of\ Se-doped\ CuO\ NPs\ digested\ (mg)]} \times 100 \quad (4.1)$$

where, mass of Se in acid digest = Se concentration measured by ICP-OES (mg/L) times total volume of digest (i.e., 1000 mL).

4.2.3 Characterization techniques

All Characterization techniques and measurement parameters are same as discussed in Chapter 3, except temperature elevated electrochemical studies, which were observed in temperature controlled set up. The cyclic stability measurement at 55 °C was found to decrease after 50-100 cycles signify decrease in the specific capacitance. This was due to increase in electrolyte concentration [241, 262], which resulted in the decrease observed. To avoid this water level in electrolyte was compensated by adding water heated at 55 °C. This was the reason behind the fluctuation in cyclic stability measurements at 55 °C temperature.

4.3 Result and discussion of Se doped CuO NPs

4.3.1 Analysis of Se doped CuO NPs

It is found that the actual doped Se concentration in the batches of CuO NPs prepared with 2 wt% Se precursor was only 0.14 wt% with respect to the weight of CuO NPs. Similarly, the actual doped Se concentration in the batches prepared with 5 wt% Se, 10 wt% Se and 20 wt% Se in CuO NPs were 0.23 wt%, 0.45 wt% and 0.31 wt%, respectively. Thus, the Se doping in the CuO NPs was poor as only about 0.14- 0.45% of the Se is incorporated in the doped CuO NPs. In a previous study by our research group, it has been discussed that the Se doped CuO synthesized by hydrothermal method revealed Se atoms to be mostly accumulated at the grain boundaries of CuO NPs and hence controlled the size of NPs [28]. However, in the present study the Se-doped CuO NPs were synthesized by co-precipitation method. The batches of CuO NPs synthesized with very high Se precursor (20 wt%) showed doped concentration lesser than the one synthesized with 10 wt% precursor concentration.

This is only possible when the doping of Se is not diffusion controlled process [263]. Such higher Se concentration in the reaction medium perhaps hindered the Se doping in CuO NPs owing to faster nucleation process. So from elemental analysis it is deduced that optimized Se doping concentration in CuO NPs was 0.45 wt%.

4.3.2 X-ray diffraction

The XRD patterns of pristine CuO NPs and the batches of CuO NPs doped with different concentration of selenium revealed characteristic peaks at (110), (002), (111), (20 $\bar{2}$) (020), (202), (11 $\bar{3}$), (31 $\bar{1}$), (220), (311) and (22 $\bar{2}$) planes corresponding to monoclinic phase of CuO nanoparticles (Fig. 4.1). These XRD patterns matched well with JCPDS file, card no. 48-1548. Compared to the pristine CuO NPs, the XRD peaks of the Se doped CuO NPs were observed to be broader and of lesser intensity for the batches of 0.14 wt%, 0.23 wt%, 0.45 wt% Se doped CuO NPs. This observed peak broadening and lowering of peak intensities are attributable to decrease in its crystallite size. This might be due to structural defects cause by Se doping in CuO NPs. For the batch of 0.45 wt% Se dopant concentration, the major peak at (111) plane was observed to be shifted towards lower 2 θ value (Fig. 4.1). This is attributable to replacement of Cu²⁺ (0.73 nm) with that of larger sized selenium species. However, the basic monoclinic crystal structure of CuO was not altered. The crystallite size of pristine and all the

batches of Se doped CuO NPs corresponding (111) plane was calculated from Debye Scherrer formula, are given in Table 4.2.

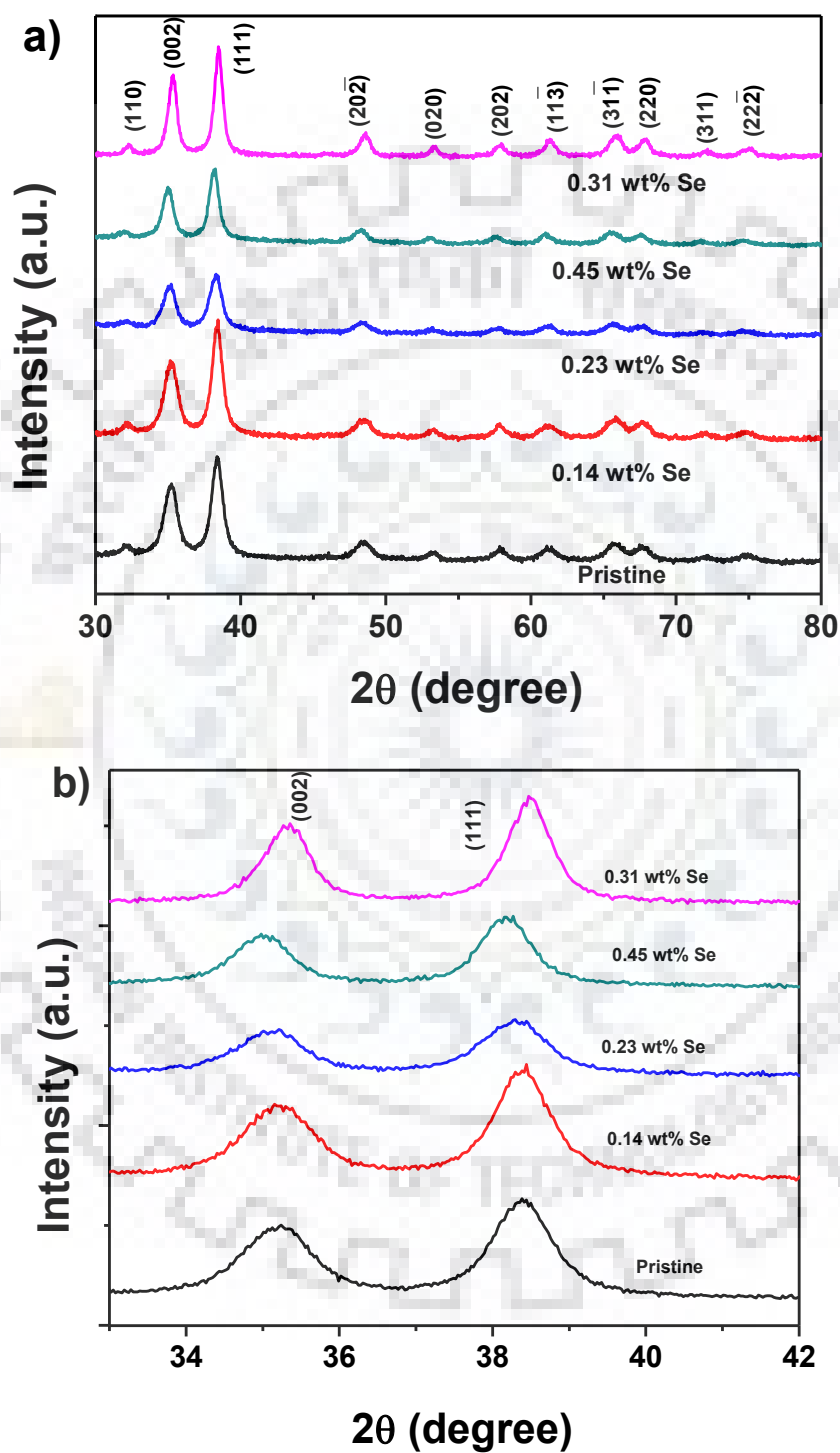


Fig. 4.1 (a) XRD pattern corresponding to the monoclinic structure of pristine and Se doped CuO NPs, (b) Zoom XRD of Se doped CuO NPs

It is noted that the crystallite size decreased with increase in Se doping concentration. This clearly indicated that Se species hindered the growth of CuO NPs. However, the crystallite size for 0.31 wt% CuO NPs was found to be more than the other batches. This anomaly is perhaps due to formation of different morphology of 0.31 wt% Se-doped CuO NPs which will be discussed later

Table 4.2 Crystallite size, band gap, surface area and specific capacitance of pristine and Se-doped CuO NPs

Sample	Crystallite size(nm)	Band gap (eV)	Surface area(m ² /g)	Specific capacitance (F/g)	
				CV (5mV/s)	GCD (0.2 A/g)
Pristine	11.4	2.9	90	99	133
0.14 wt% Se	9.9	2.8	77	96	128
0.23 wt% Se	8.3	3.0	91	80	118
0.45 wt% Se	10.7	2.9	50	120	145
0.31 wt% Se	13.4	2.8	46	98	138

4.3.3 Surface morphology

The surface morphology of pristine and all the batches of Se doped CuO NPs were studied by FE-SEM and the results are given in Fig. 4.2. It is observed that pristine and the Se doped batch (except 0.31 wt%) of CuO NPs showed agglomeration of spherical shape nanoparticles. Whereas, the batch prepared by taking very high Se concentration (20 wt% Se precursor) during synthesis i.e., 0.31 wt% Se doped CuO NPs revealed formation of flake like structure. So, the morphology of the Se doped CuO NPs depended on the Se precursor concentration. The overall composition and the purity of all batches of CuO NPs reflected from the energy dispersive X-ray analysis (EDAX) spectrum given alongside each FE-SEM image, which revealed characteristic X-ray peaks of Cu and O. This EDAX spectrum did not reveal any X-ray peak of Se in the batches of Se doped CuO NPs owing to of its lower concentration in the doped CuO NPs.

The Transmission electron microscopy (TEM) studies of Se-doped CuO NPs supported the morphological features revealed by FE-SEM. The particle sizes were determined from TEM images. The TEM images of pristine CuO NPs and 0.45 wt% Se doped CuO NPs are given in Fig. 4.3.

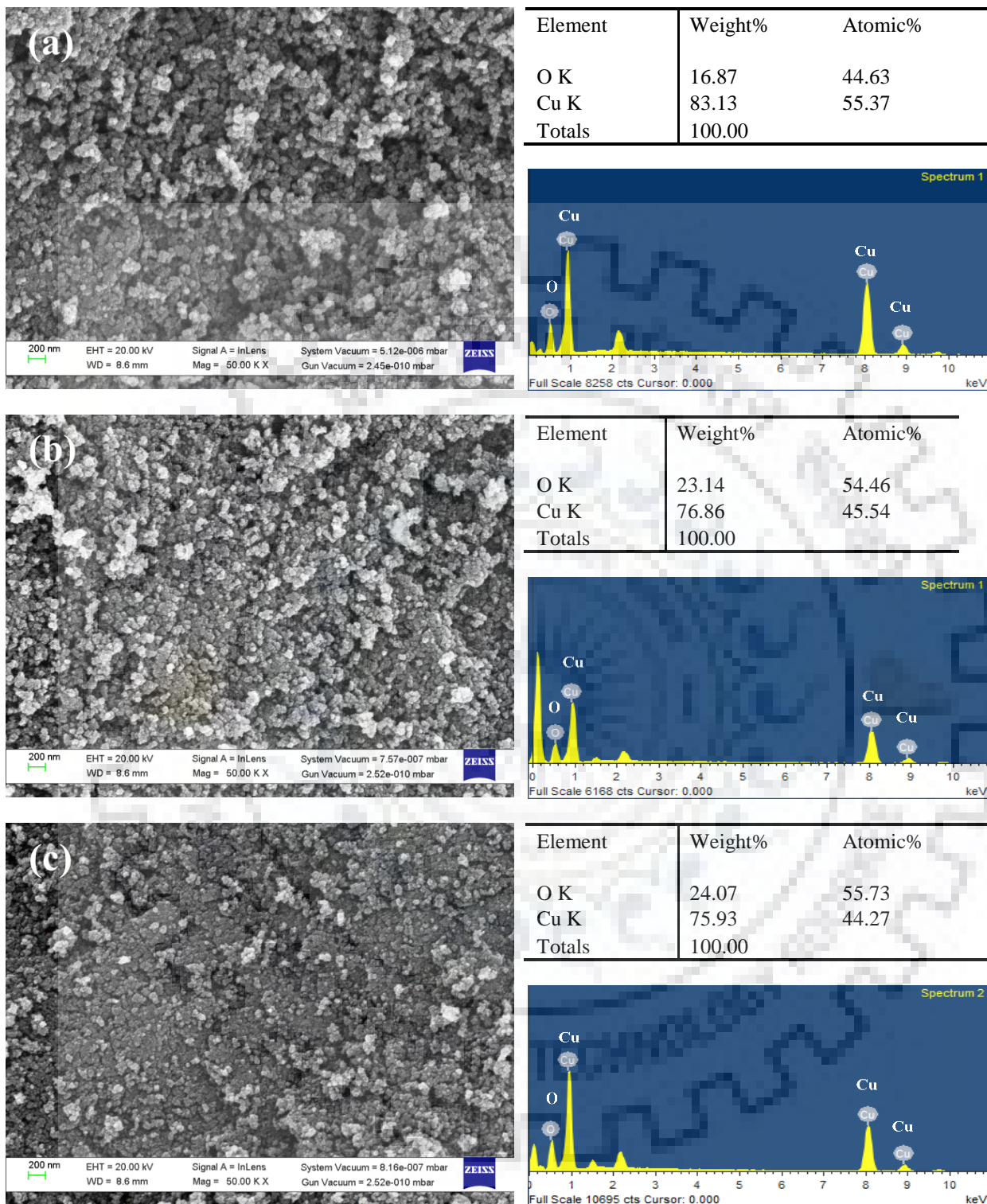


Fig. 4.2 continued in next page

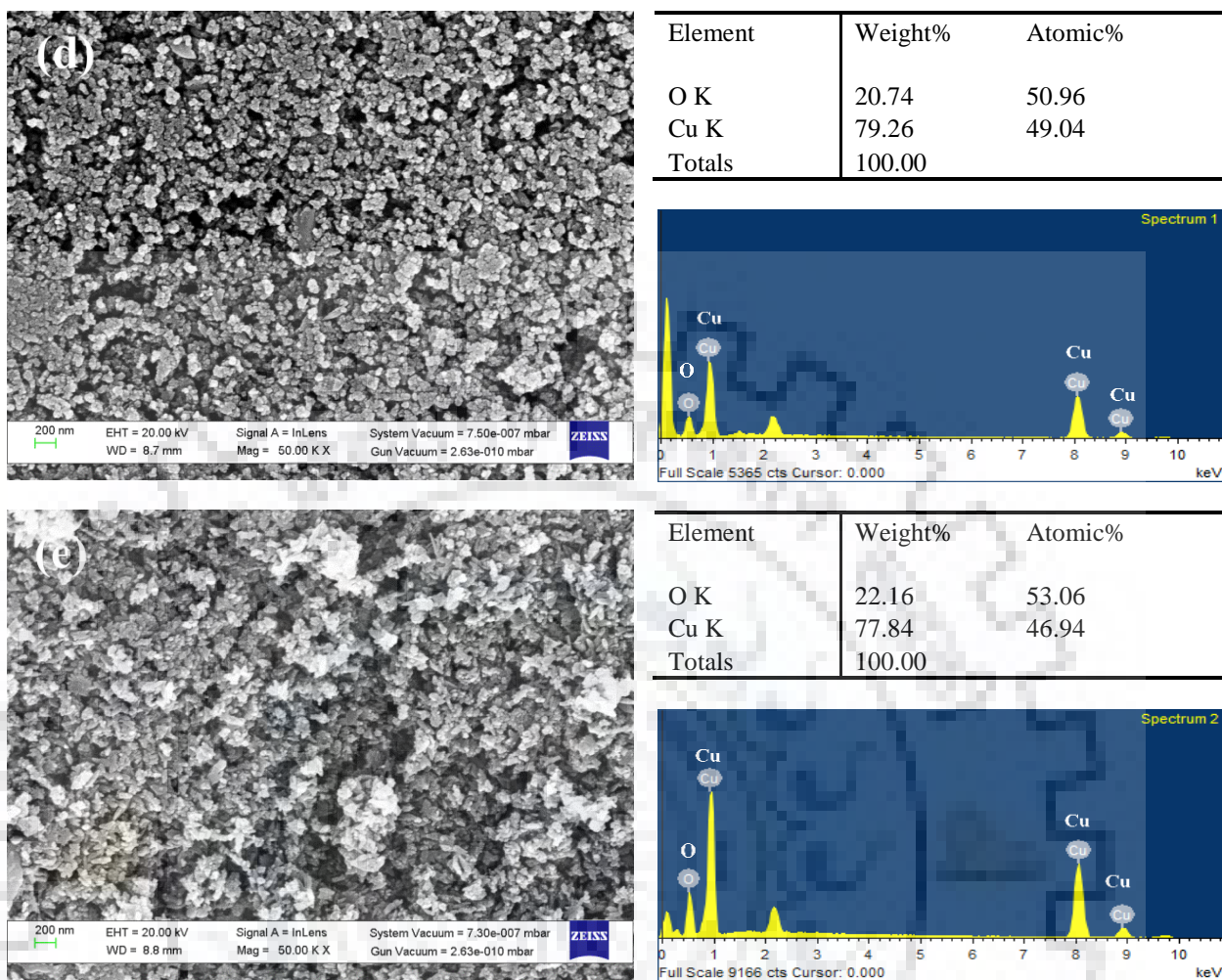


Fig. 4.2 Field Emission Scanning Electron Microscopy images of (a) Pristine, (b) 0.14 wt% Se doped, (c) 0.23 wt% Se doped, (d) 0.45 wt% Se doped and (e) 0.31 wt% Se doped CuO NPs and their corresponding energy dispersive X-ray analysis spectrum of respective nanoparticles showing characteristic K and L X-rays and atomic% of Cu and O.

The lower resolution image for both the samples revealed formation of more or less uniform sized spherical shaped nanoparticles. The higher resolution TEM images revealed particle size in the range of 10-12 nm for pristine CuO NPs. Our results were consistent with the crystallite size measurement obtained from XRD studies. However, higher resolution image of the Se doped CuO NPs did not show prominent spherical shaped nanoparticles. This could be due to formation of poorly crystalline CuO NPs due to incorporation of Se in the crystal lattice. Our assumption is further strengthened from the SAED image which clearly reflected poorly crystalline structure of Se doped CuO NPs. The particle size of Se doped CuO NPs

could not be accurately determined from TEM images. So, we would consider the crystallite size as a more appropriate particle size indicator in our studies.

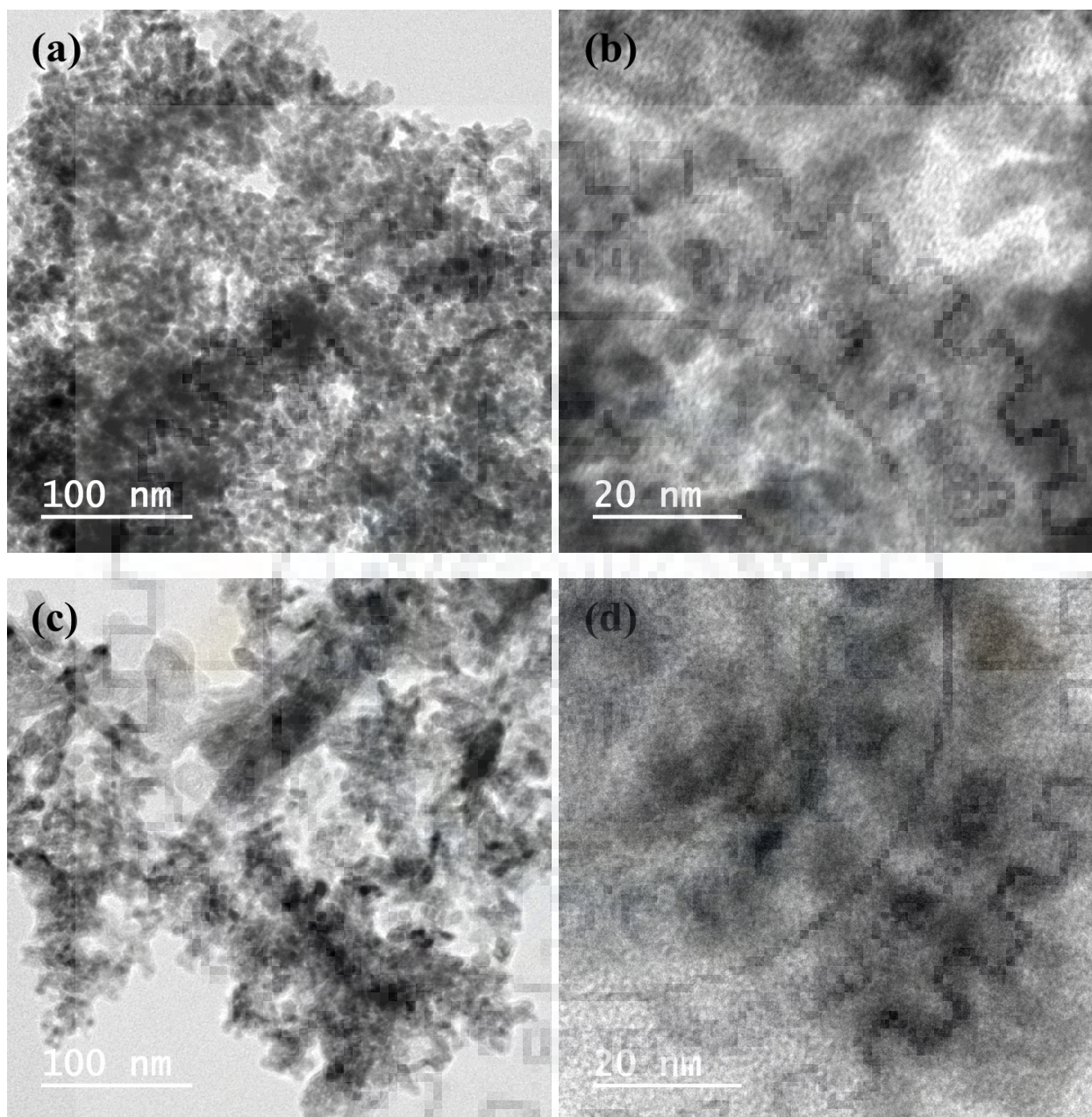


Fig. 4.3 Transmission Electron Microscopy (TEM) images of (a) pristine, (b) high resolution image of pristine, (c) Se doped CuO NPs and (d) high resolution image of Se-doped CuO NPs.

4.3.4 Optical studies

The optical properties of pristine and batches of doped CuO NPs were studied by diffuse reflectance spectroscopy (DRS) in the wavelength range 200-800 nm. The

photoluminescence spectroscopy studies were performed in wavelength range 315-575 nm, using excitation wavelength $\lambda_{\text{ex}} = 300$ nm.

4.3.4.1 Diffuse reflectance spectroscopy (DRS)

The diffuse reflectance spectroscopy studies revealed band gaps of pristine as well as for the batches of Se doped CuO NPs. The Tauc plots of these samples corresponding to Kubelka Munk formula are shown in Fig. 4.4.

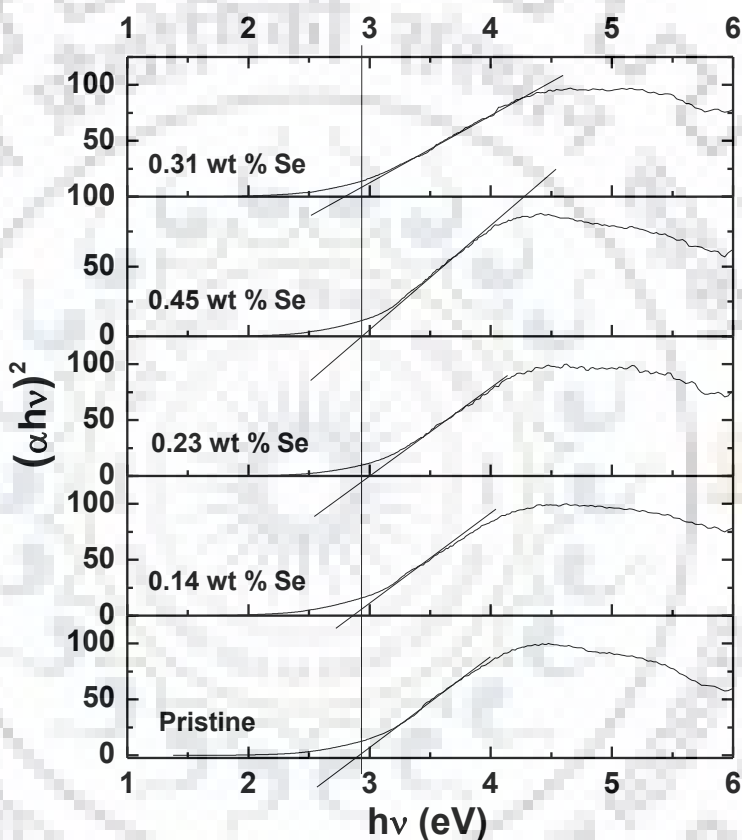


Fig. 4.4 Tauc plot obtained from diffuse reflectance spectroscopy of pristine and the batches of Se doped CuO NPs.

The band gap energy of pristine and batches of Se doped CuO NPs were in the range of 2.8 eV and 3.0 eV, listed in Table 4.2. Among the Se-doped CuO NPs studied here, the batch of 0.23 wt% Se doped CuO NPs revealed maximum band gap (3.0 eV). While the batch of 0.45 wt% Se doped CuO NPs reveal band gap of 2.9 eV. The band gap measurement was useful to select the wavelength of excitation for measuring photoluminescence property of the pristine and Se doped CuO NPs. Form DRS study, the maximum band gap was found to be 3.0 eV,

which is equivalent to 413 nm. So for photoluminescence studies we have selected at excitation wavelength of 300 nm, which is much higher than the band gap of CuO NPs.

4.3.4.2 Photoluminescence studies

The photoluminescence spectra of pristine and batches of Se doped CuO NPs are given in Fig. 4.5.

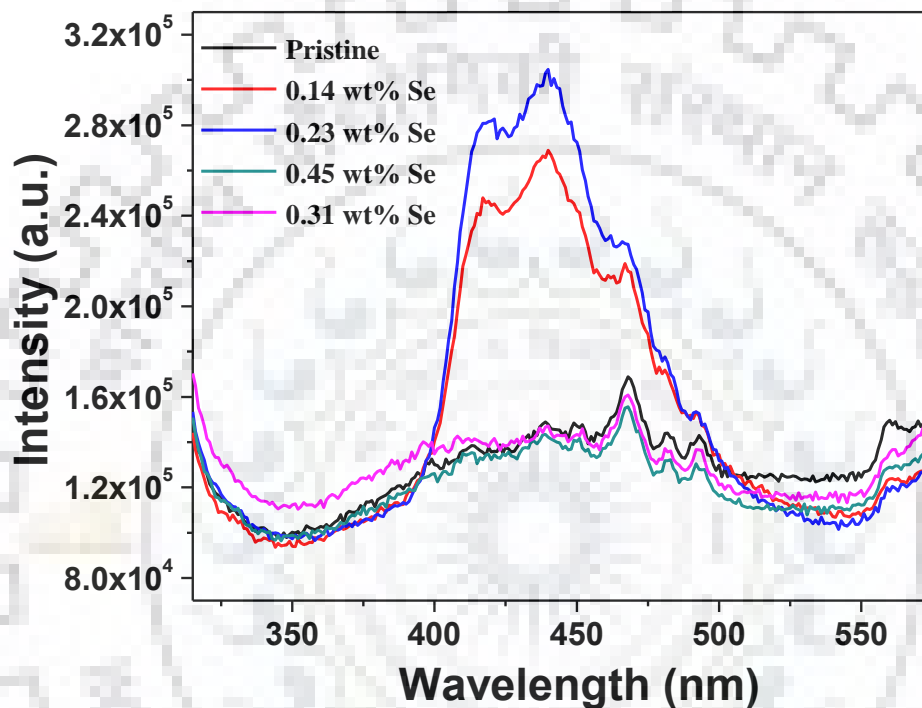


Fig. 4.5 Photoluminescence spectra of pristine and batches of Se doped CuO NPs.

Notably, the batch comprising 0.14 wt% Se and 0.23 wt% Se in CuO NPs revealed intense PL peaks at 418 nm, 440 nm and 467 nm. The peaks at 418 nm and 440 nm corresponded to electron holes recombination and near edge emission. Interestingly, these peaks were not observed for the batches of pristine CuO NPs and in the 0.45 wt% Se-doped CuO NPs. While all the batches exhibited low intensity PL peaks at 467 nm owing to Cu vacancy defect.

4.3.5 Se-doped CuO NPs as supercapacitor

The supercapacitor behavior of pristine and the batches of Se doped CuO NPs are studied by cyclic voltammetry (CV), galvanostatic charge-discharge (GCD) and electrochemical impedance spectroscopy (EIS) measurement.

1.3.5.1 Cyclic voltammetry studies

The CV curves for pristine and all the batches of Se doped CuO NPs were recorded at different scan rates e.g., 5 mV/s, 10 mV/s, 20 mV/s, 30 mV/s, 40 mV/s and 50 mV/s and results are given in Fig. 4.6. The CV curves were quasi-rectangular in shape and consistent with literature reported on various types of CuO nanostructures [242, 243]. The shapes of cyclic voltammograms were observed to be independent of applied scan rate but area under the curve is directly proportional to the scan rate. The CV curves are attributed to restriction free movement of electrolyte ions into the pores of active material and reversible feature to the electrolyte ions interaction of with the active materials [73, 244]. The oxidation peak is obtained at 0.4 V and the reduction peak at 0.5 V which are attributed to faradaic redox interaction between electrolyte and active materials. The specific capacitances of the as synthesized pristine and all the batches of Se doped CuO NPs were calculated using equation 3.1 (given in previous chapter).

The specific capacitance of pristine, and the batches of Se doped CuO NPs (0.14 wt%, 0.23 wt%, 0.45 wt% and 0.31 wt%) are calculated to be 99 F/g, 96 F/g, 80 F/g, 120 F/g and 98 F/g, respectively. From the CV studies, the specific capacitance was found to be maximum (120 F/g) for the batch of 0.45 wt% Se doped CuO NPs and minimum for the batch of 0.23 wt% Se doped CuO NPs. The observed variation in the specific capacitances was not due to surface area, but it is due to the presence of vacancy defects as revealed by near band edge emission spectra. The surface defects in the 0.23 wt% Se doped CuO NPs acted as trap sites of charges, which resulted in poor specific capacitance. The measured specific capacitances at different scan rates were presented in form of specific capacitance vs. scan rate plot. It was found that the specific capacitance of the batches of CuO NPs decreased with scan rate (Fig. 4.6f). This is due to lesser interaction behavior and pores of active material of electrolyte ions at higher scan rate.

4.3.5.2 EDLC vs. PC contributions

Further, to understand the effect of dopant on the supercapacitor behavior of pristine and Se doped CuO NPs, it is necessary to measure the charge associated with (a) electric double layer capacitance and (b) with pseudocapacitance in these materials. Form the I/q vs. $v^{1/2}$ plot, the total voltammetric charge (q_t) was calculated by extrapolating voltammetric charge to $v = 0$ (Fig. 4.7a).

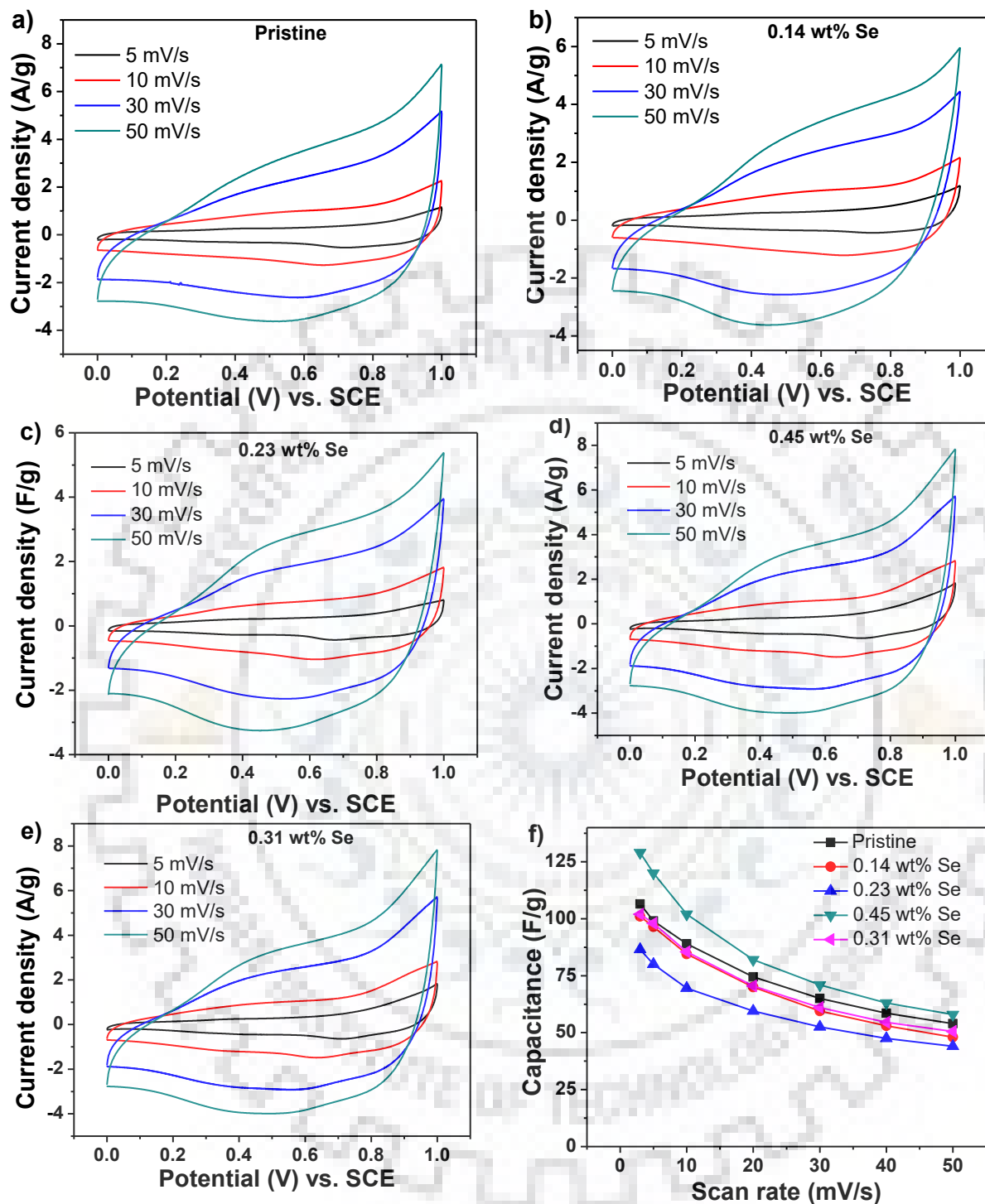


Fig. 4.6 Cyclic voltammety plots of (a) pristine, (b) 0.14 wt% Se (c) 0.23 wt% Se (d) 0.45 wt% Se, (e) 0.31 wt% Se doped CuO NPs and (f) specific capacitance vs. scan rate plot.

Total charge associated with double layer (q_{dl}) is calculated from the q_{dl} vs. $v^{-1/2}$ plot by the extrapolation of voltammetric charge to $v = \infty$ (Fig. 4.7b). Thus, charge associated with PC (q_p) can be calculated as:

$$q_p = q_t - q_{dl} \quad (4.2)$$

The contribution of PC can be estimated as:

$q_p\% = (q_p/q_t) * 100$ and the values are listed in Table 4.3.

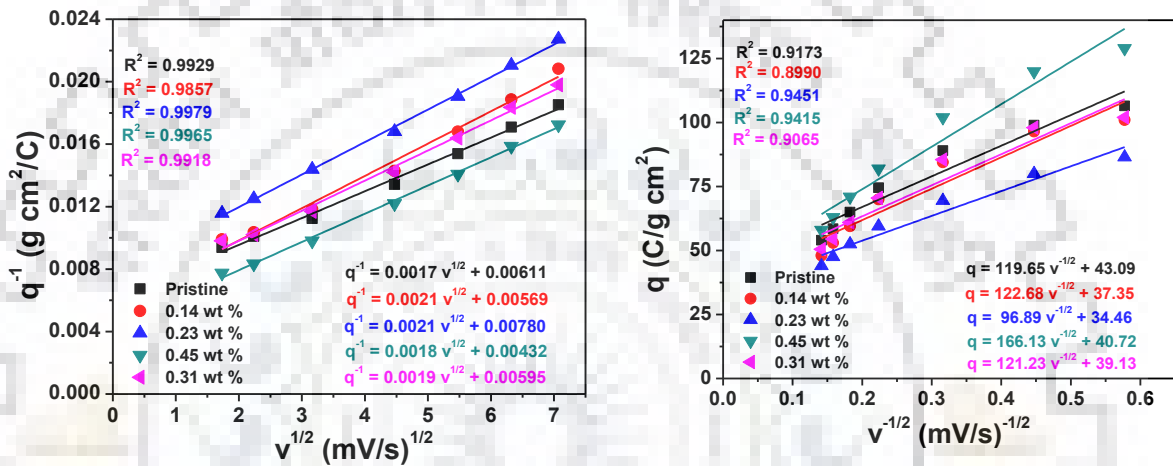


Fig. 4.7 (a) $1/q$ vs. $v^{1/2}$ and (b) q vs. $v^{-1/2}$ dependence of the batches of Se doped CuO NPs

Table 4.3 Summary of maximum total charge (q_t), double layer capacitance (q_{dl}), and charge associated with pseudocapacitance (q_p) of pristine and Se doped CuO NPs in 1 M Na_2SO_4 solution.

Sample	q_t (C/g)	q_{dl} (C/g)	q_p (C/g)	q_p/q_t (%)
Pristine	163	43.09	120	73.6
0.14 wt% Se	176	37.35	138	78.4
0.23 wt% Se	128	34.46	94	73.4
0.45 wt% Se	231	40.72	190	82.3
0.32 wt% Se	168	39.13	129	76.8

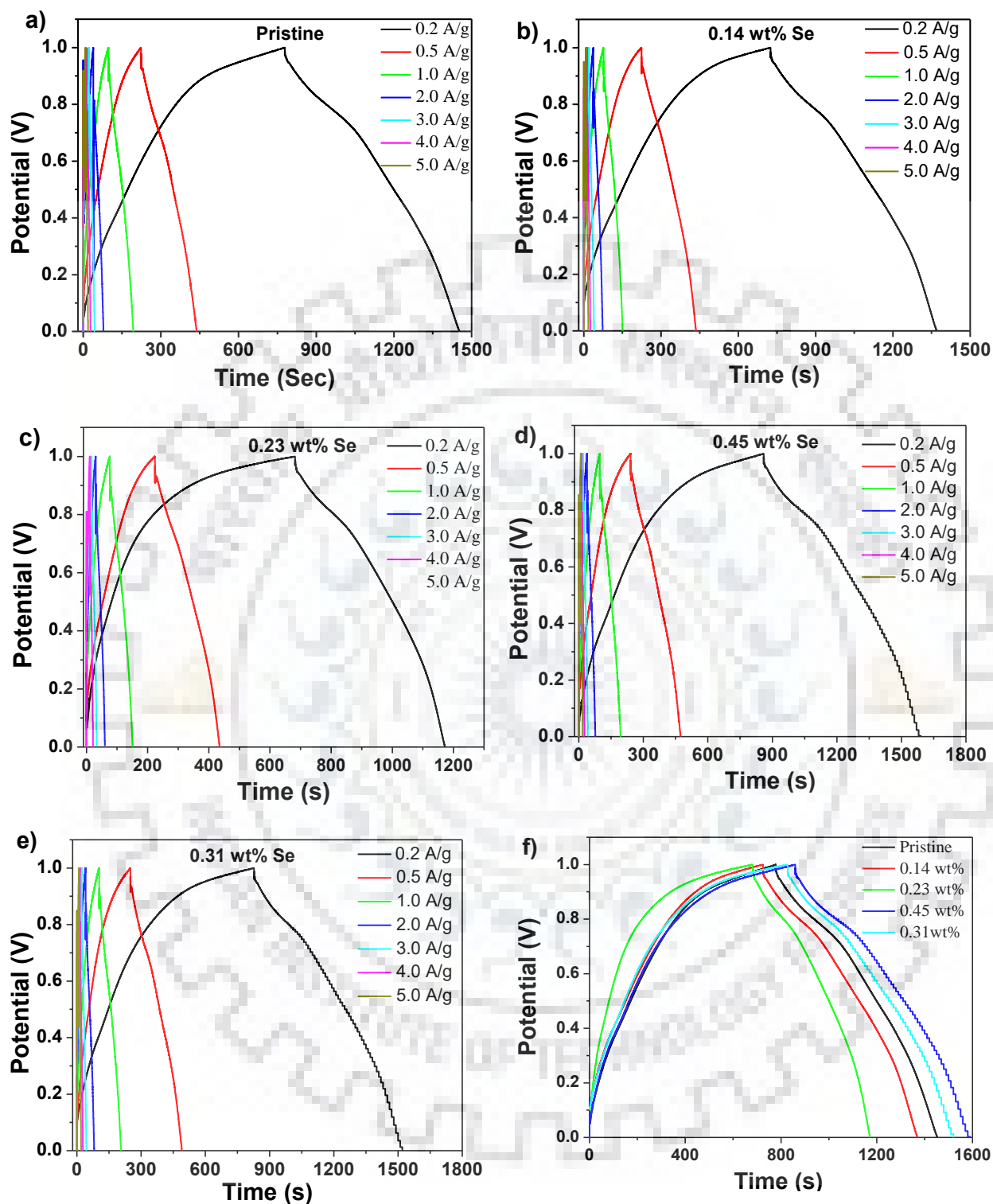


Fig. 4.8 Galvanostatic charge-discharge curves of (a) pristine, (b) 0.14 wt% Se doped, (c) 0.23 wt% Se doped, (d) 0.45 wt% Se doped, (e) 0.31 wt% Se doped CuO NPs and (f) Comparison study of GCD of the batches of Se-doped CuO NPs at current density of 0.2 A/g.

It is observed that all batches of Se doped CuO NPs exhibited higher PC contribution than the pristine batch. Notably, the PC contribution was maximum for the batch of 0.45 wt% Se doped CuO NPs, which also revealed maximum specific capacitance (as discussed earlier). The EDLC contribution is directly dependent on surface area of electrode material [264, 265]. This implied that the specific capacitance of Se-doped CuO NPs is primarily due to faradaic redox reaction involved at the surface of the electrode material. The importance of PC contribution is also indirectly revealed from the non-consistent relation between surface area and specific capacitance. In this case, the specific capacitance of 0.45 wt% Se-doped CuO NPs was 50 m²/g while the surface area of pristine CuO NPs is 90 m²/g, whereas, the specific capacitance of 0.45 wt% Se-doped CuO NPs was 20% more than the pristine. This also supported that the PC contribution was more important to explain the supercapacitor behavior of Se-doped CuO NPs.

4.3.5.3 Galvanostatic charge–discharge (GCD) studies

The electrochemical activities of the pristine and all the batches of Se doped CuO NPs were examined by galvanostatic charge-discharge studies. The charge-discharge curves of pristine and batches of Se doped CuO NPs used as electrode were recorded at different current density varying from 0.2 A/g to 5 A/g (Fig. 4.8). The charge-discharge curves revealed typical triangular shape which corresponded to constant charging and discharging behavior of the batch of Se doped CuO NPs and was consistent with feature of a supercapacitor [107, 243]. The specific capacitance for each batch was calculated from equation 3.3 (given in Chapter 3)

The specific capacitance of pristine, 0.14 wt%, 0.23 wt%, 0.45 wt% and 0.31 wt% Se doped CuO NPs are calculated to be 133 F/g, 128 F/g, 98 F/g, 145 F/g and 138 F/g, respectively at current density of 0.2 A/g. It is noted that specific capacitances calculated from GCD also followed the same trends as that of their CV studies and the maximum specific capacitance was obtained for the batch of 0.45 wt% Se doped CuO NPs, which corresponded to Se doping concentration.

4.3.5.4 Electrochemical Impedance spectroscopy (EIS) studies

The EIS studies were recorded for pristine and all the batches of Se doped CuO NPs in the frequency region 0.01 Hz to 1 MHz at 0.5 V bias voltages vs. SCE and the respective Nyquist plots are given in Fig. 4.9. The Nyquist plot provides important electrochemical

behavior of an active material used as electrode. The Nyquist plots of the Se-doped CuO NPs are consistent with literature reports of various types of CuO nanostructures [266, 267]. Typically, the Nyquist plot can be seen with three features, i.e., a) high frequency semi-circle; b) medium frequency Warburg impedance; c) low frequency capacitive behavior [268]. The semi-circle behavior was corresponded to charge transfer resistance found at the interface of electrode and electrolyte. It is seen as the initial barrier of charge transfer for carrying electrochemical reaction.

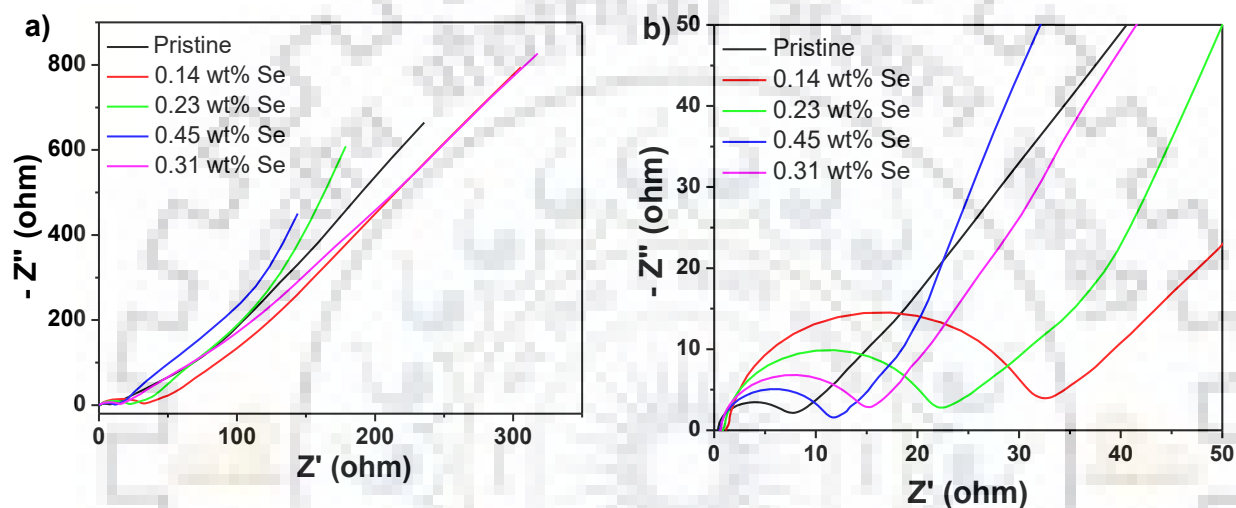


Fig. 4.9 (a) Electrochemical impedance spectroscopy of pristine and Se doped CuO NPs, (b) represent the zoom EIS of all the batches of CuO NPs in higher frequency range.

The mid-frequency region is due to solid state diffusion process. There are different opinions about the diffusion region which is governed by applied potential. Some researchers have attributed the absence of diffusion region in their active materials due to pseudocapacitor property, as they are not diffusion controlled [268]. However, Song and Bazant provided theoretical insight of the impedance behavior and suggested that all three regions would be obtained when the electrode is made up of uniform particles [269]. As we have observed all the three parts in EIS plots, so we may conclude that our Se-doped CuO NPs are of uniform features.

The ESR values were determined (as explained in chapter 3) for pristine, 0.14 wt%, 0.23 wt%, 0.45 wt% and 0.31 wt% Se doped CuO NPs were 0.4 ohm, 1.1 ohm, 0.8 ohm, 0.5

ohm and 0.6 ohm, respectively. Notably, ESR value of an ideal supercapacitor should be least and it should tend to zero [268]. However, the ESR of Se doping in the CuO NPs were marginally higher. The ESR is given as a sum of electronic and ionic resistance. The electronic resistance is exhibited by the electrode material, contacts, etc. Ionic resistance is due to the morphology of the electrode materials, mainly contribution by the resistance inside and outside the pores. For a fixed charge collector geometry of active material (1 cm × 1 cm) and same mass loading of electrode, the changes in ESR will be only due to the changes in ionic resistance. The ESR of 0.14 wt% and 0.23 wt% Se-doped CuO NPs were higher, which are consistent with defects or voids in the sample as reflected from the PL studies. The PL studies also revealed that such defects were minimized for 0.45 wt% Se-doped CuO NPs and also reflected smaller ESR values. The same was observed for the batch of concentration 0.31 wt% Se-doped CuO NPs.

The semi-circle part due to charge transfer resistance was more for the batch of 0.14 wt% Se and 0.23 wt% Se doped CuO NPs. This is attributable to higher defects in the electrode material. The charge transfer region was very small for pristine and 0.45 wt% Se doped CuO NPs. The pristine batch did not show the diffusion part corresponding to the mid frequency region. On the other hand the diffusion part was distinctly identified for 0.45 wt% se doped CuO NPs. From this it may be concluded that 0.45 wt% Se doped CuO NPs would make a better supercapacitor material owing to the diffusion of charges at the surface of electrode material. Further, the slope of the vertical line at low frequency for 0.45 wt% Se doped CuO NPs was also much higher than rest of the doped CuO NPs as well as pristine CuO NPs. This implied that 0.45 wt% is the optimized concentration for the attaining best supercapacitor behavior. Therefore, from all electrochemical studies it noted that 0.45 wt% Se doped CuO NPs exhibited maximum specific capacitance and highest conductivity as reflected from the maximum slope of low frequency data. So it was selected for electrochemical cyclic stability test.

4.3.5.5 Cyclic stability

The cyclic stability measurement of 0.45 wt% Se doped CuO NPs for supercapacitive behavior was studied by performing for 500 charge-discharge cycle at a current density of 1 A/g. The capacitance retention for the pristine and 0.45 wt% Se doped CuO NPs exhibited enhanced capacitance during the first 50 cycles. This is attributable to the initial activation

period within which pores get progressively wet and hence fewer interaction with electrolyte ions [268]. However, the capacitance decreased gradually after 50 cycles and finally found to be 85% for pristine CuO NPs and only 63% for 0.45 wt% Se doped CuO NPs electrode. The electrochemical properties of the pristine and Se-doped CuO NPs before and after 500 cycles of charging-discharging were studied and the Nyquist plots are given in the inset of Fig. 4.10. It is observed that the slopes of the low frequency region decreased for both the materials. Compared to the slopes of the material before the cyclic stability test, the slopes of the material recorded after completion of 500 cycles were less. This implied decrease in specific capacitance due to deterioration of the pores in the electrodes. The pores tend to swell and shrink during the entire period of charging–discharging cycles and affect the mobility of the electrolyte ions in the electrode material.

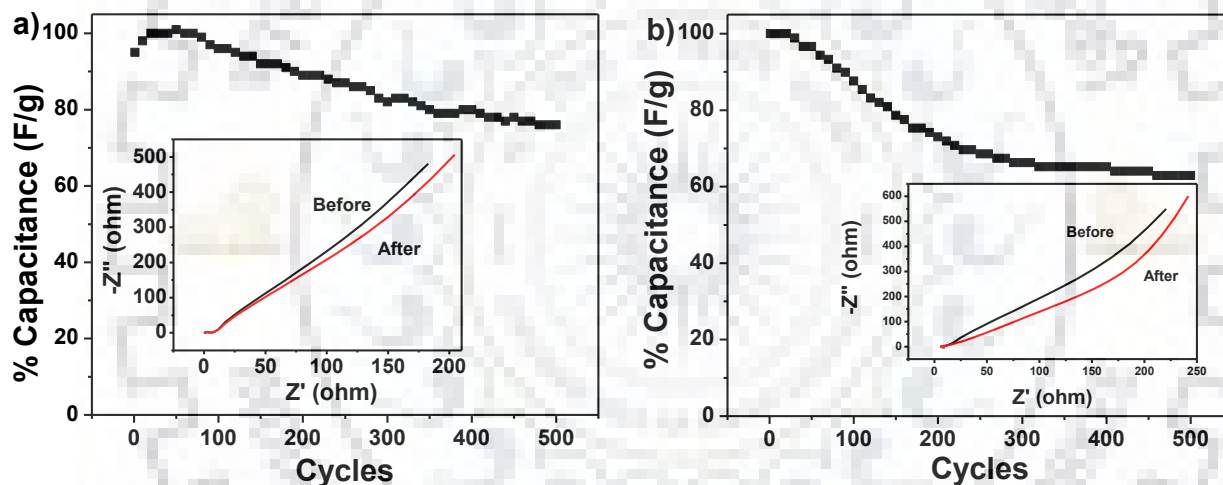


Fig. 4.10 Capacitance retention of (a) pristine and (b) 0.45 wt% Se-doped CuO NPs; Inset showing EIS plot of samples before and after the 500 cycles at current density 1 A/g.

The life of supercapacitor depends on the cyclic stability of the electrode materials. So, if the cycle stability of electrode material is short then it cannot be used in portable devices. Notably, the cycle stability of the best batch i.e., 0.45 wt% Se doped CuO NPs was found to be very poor capacitance 63%. To improve this we calcined the sample at 450 °C. The sample was calcined in air to improve the structural properties including the stability of the pores in the NPs and consequently improve the electrochemical properties. The electrochemical study was

carried out for calcined 0.45 wt% Se-doped CuO NPs and was compared with calcined pristine CuO NPs.

4.4 Result and discussion of calcined Se-doped CuO NPs

4.4.1 X-ray diffraction

The XRD pattern of calcined pristine and calcined 0.45 wt% Se doped CuO NPs are given in Fig. 4.11. The peaks particularly at (111) plane was more intense and narrower as compared to uncalcined samples. This increased peak intensity is attributed to improved crystallinity of CuO NPs. The narrower peaks corresponded to increase in crystallite size. From Debye Scherrer formula the crystallite sizes of calcined pristine and calcined 0.45 wt% Se doped CuO NPs were calculated as 15.7 nm and 12.9 nm, which were more than uncalcined samples.

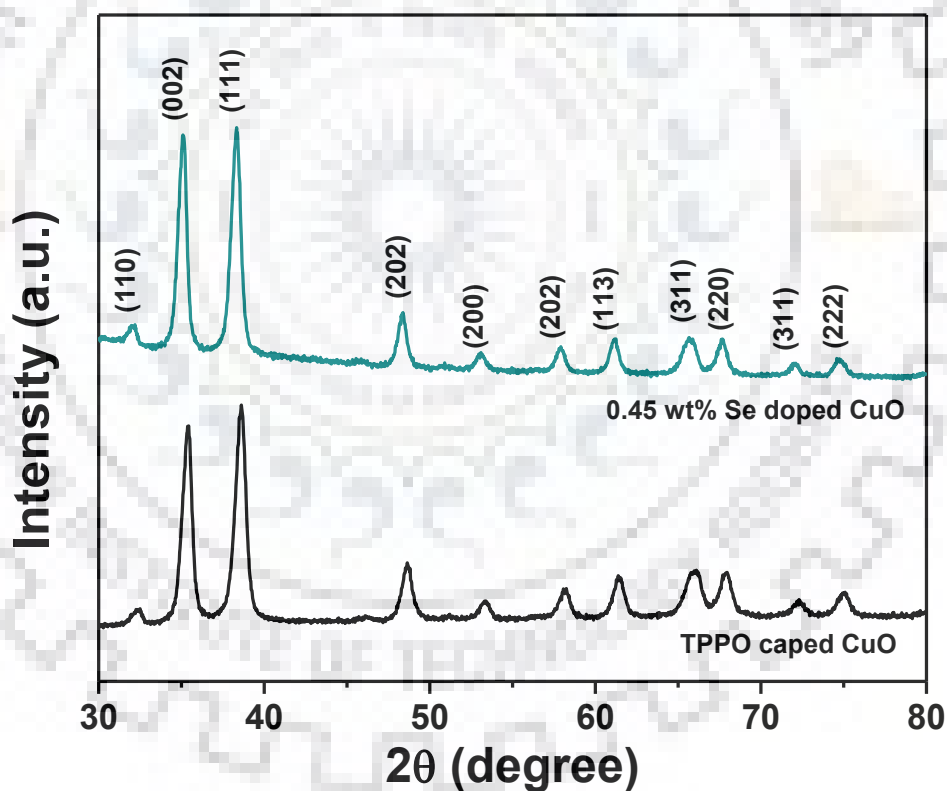


Fig. 4.11 XRD pattern corresponding to the monoclinic structure of calcined pristine and calcined Se doped CuO NPs.

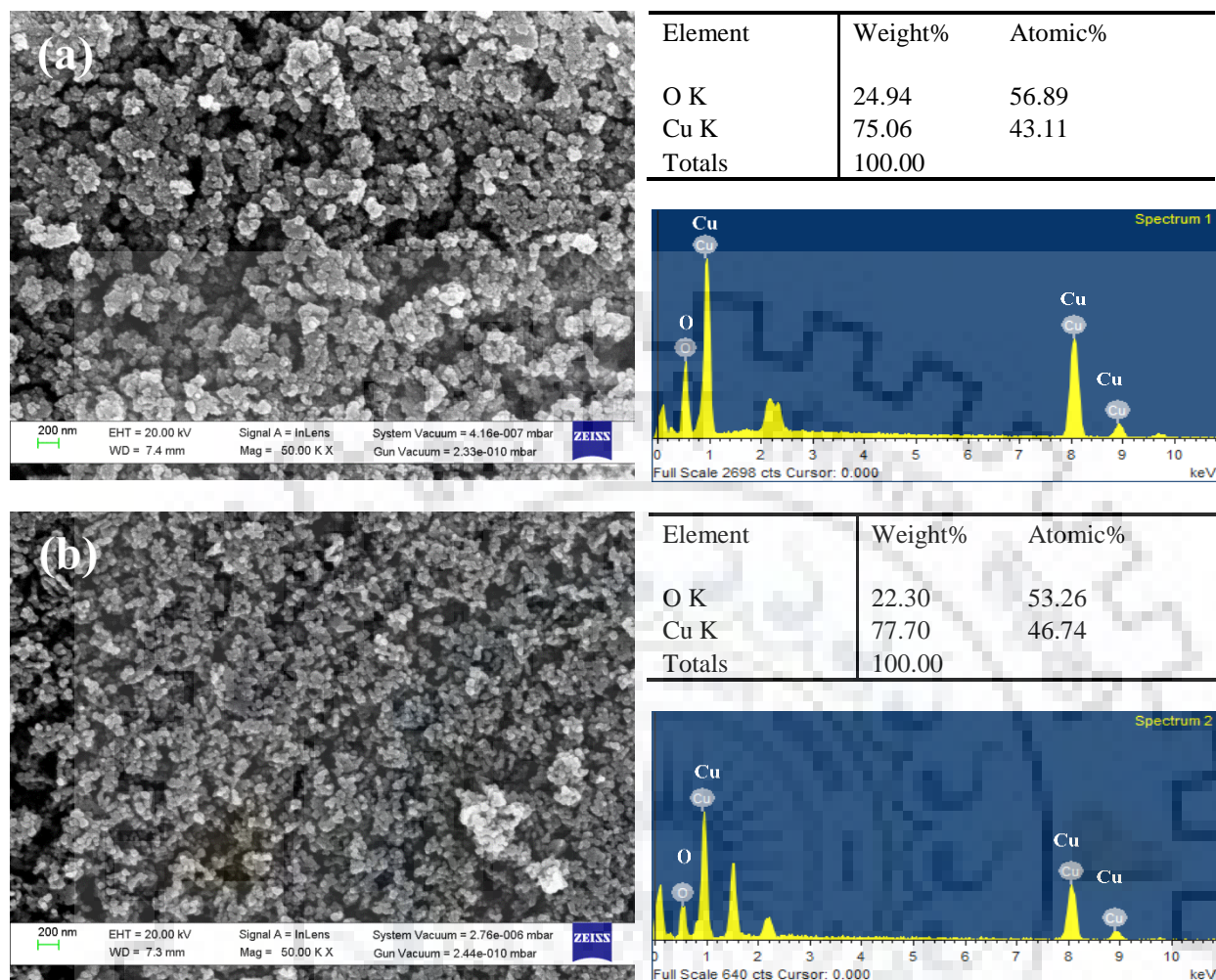


Fig. 4.12 Field Emission Scanning Electron Microscopy images of (a) calcined pristine, (b) calcined 0.45 wt% Se doped CuO NPs and their corresponding energy dispersive X-ray analysis spectrum of representative nanoparticles showing characteristic K and L X-rays and atomic% of Cu and O.

4.4.2 Surface morphology

The surface morphology of pristine and Se-doped CuO NPs was recorded by FE-SEM and the result images are shown in Fig. 4.12. The nanoparticles were agglomerated. The energy dispersive X-ray analysis (EDAX) spectrum revealed the characteristic X-ray peaks of Cu and O.

4.4.3 Calcined Se-doped CuO NPs as supercapacitor

4.4.3.1 Cyclic voltammetry studies

The effect of calcination on pristine and the Se doped CuO NPs on their electrochemical properties were studied.

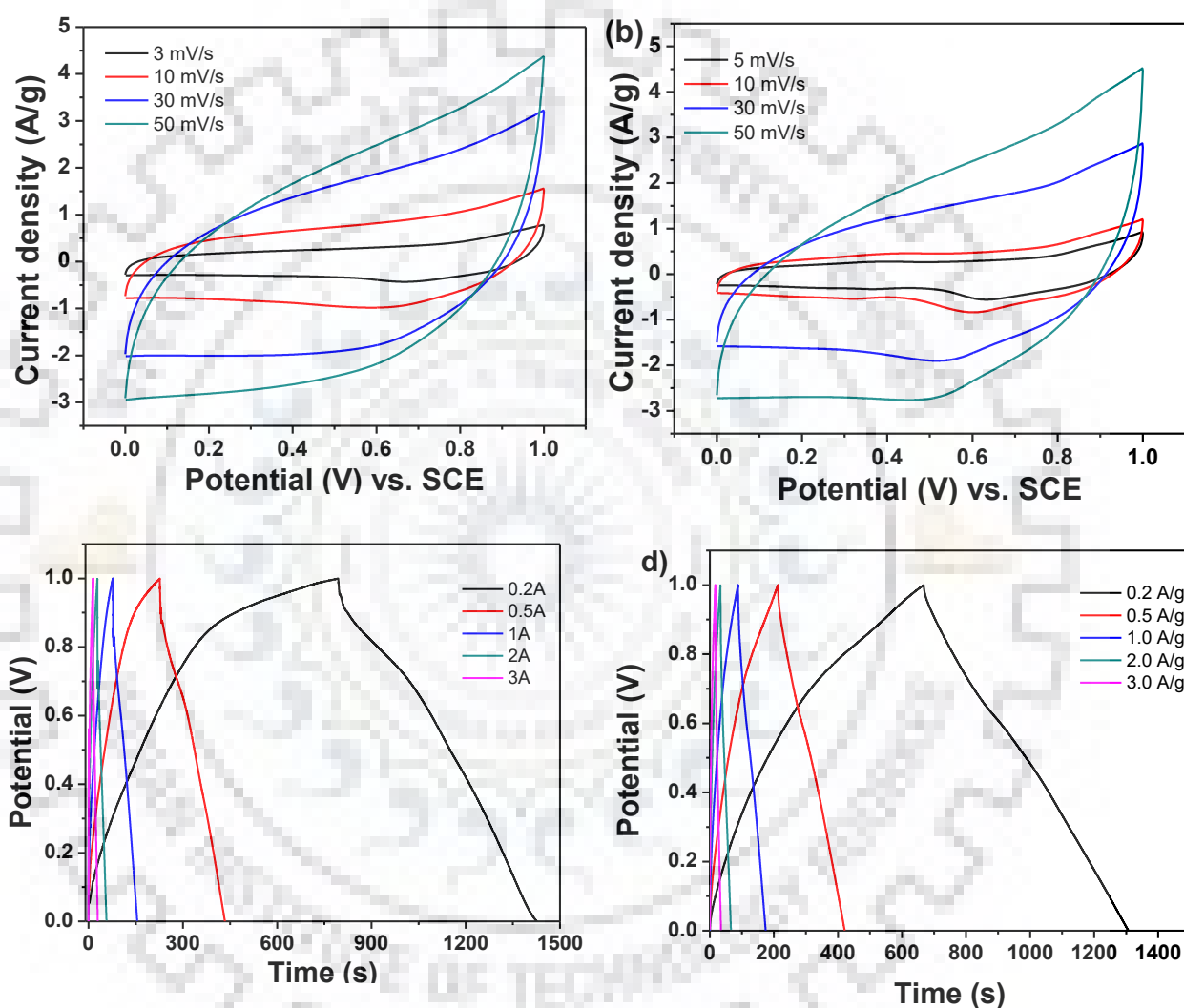


Fig. 4.13 Cyclic voltammograms of (a) calcined pristine (b) calcined 0.45 wt% Se doped CuO NPs. Galvanostatic charge-discharge curves of (c) calcined pristine and (d) calcined 0.45 wt% Se doped CuO NPs.

The CV measurements were recorded at different scan rates ranging from 5 mV/s to 50 mV/s and the results are given in Fig. 4.13. These CV curves are similar to the uncalcined counterparts, which revealed quasi rectangular shape, and hence satisfied the condition required

for a good reversible supercapacitor. The area of the CV curves increased as the scan rate was increased from 5 mV/s to 50 mV/s. However, the shapes of the curve remained unchanged with the increase in the scan rate, which is an important feature of a supercapacitor. The specific capacitance of calcined pristine and calcined Se doped CuO NPs at arbitrary 5 mV/s scan rate were found to be 90 F/g and 96 F/g, respectively. Notably, under similar measurement conditions, the specific capacitance of the Se-doped CuO NPs was decreased due to calcinations. This could be due to increase in the particles/sizes of the calcined samples.

4.4.3.2 Galvanostatic charge-discharge studies

The charge-discharge curve of calcined pristine CuO NPs and calcined Se doped CuO NPs recorded at different current density are shown in Fig. 4.13. As expected, these electrodes exhibited triangular shape charge-discharge curves and are attributed to a good supercapacitive nature of material. The specific capacitances of CuO NPs were also determined from the charge discharge curve, which were 124 F/g for pristine and 126 F/g for calcined 0.45 wt% Se doped CuO NPs at a current density of 0.2 A/g.

4.4.3.3 Cyclic stability

The cycle stability performance of calcined pristine and calcined Se doped CuO NPs were studied for 500 cycles of charge-discharge at current density of 1 A/g (Fig. 4.14). Notably, the capacitance retention was significantly improved to 96% and 93% for calcined pristine and calcined Se doped CuO NPs, respectively. The enhancement in stability can be attributed to annealing of defects and stabilizing the pores. It should be mentioned here that both the batches of calcined pristine and calcined Se-doped CuO NPs were synthesized by chemical precipitation method using TPPO as a capping agent. During calcination the TPPO is likely to be thermally decomposed, but the phosphorous of TPPO is likely to be incorporated at the surface of the CuO NPs after calcination. This would also result in surface modification of CuO NPs. As phosphorous is an n-type material, so it may impact the charge transportation property of CuO NPs for better capacitance retention. Our assumption is supported by the EIS measurement of the calcined pristine and calcined Se doped CuO NPs. The slope of the vertical line in the low frequency region is reduced, which is attributable to decrease in electrolyte interaction and increase in ionic mobility resistance after 500 cycles due to deterioration of pores of active materials. The capacitance retention of calcined pristine and calcined 0.45 wt%

Se doped CuO NPs were better than several CuO nanostructures reported in literature [238, 268, 270].

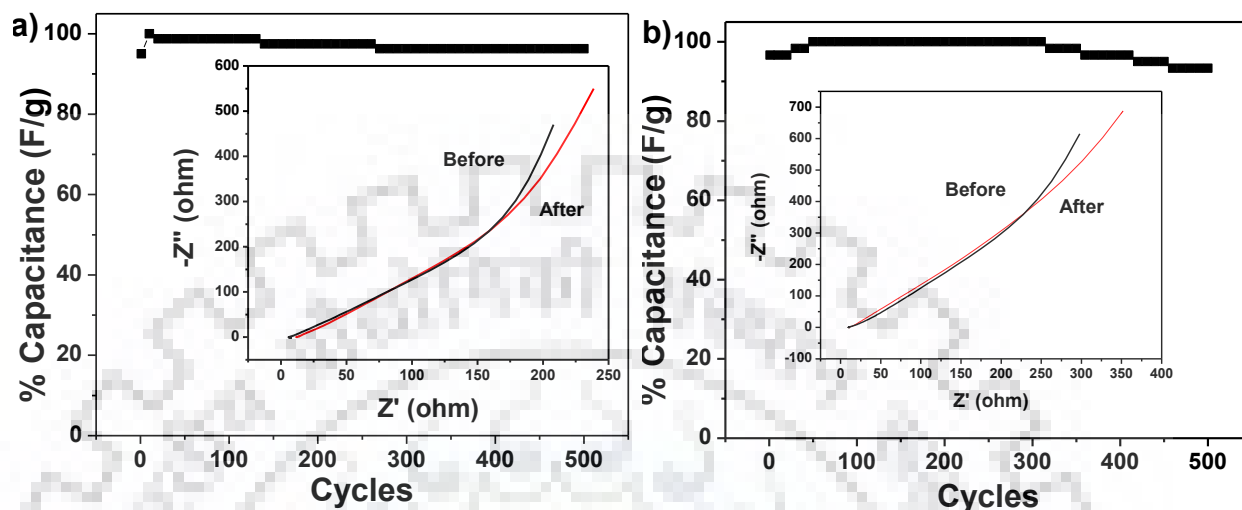


Fig. 4.14 Capacitance retention of (a) calcined pristine and (b) calcined Se doped CuO NPs, inset showing EIS plot of samples before and after the 500 cycles at current density 1 A/g.

4.5 Calcined Se doped CuO NPs as elevated temperature supercapacitor

The supercapacitor performance at elevated cell temperatures is very important for several applications including the automobile industrial applications [271]. At elevated temperatures electrolyte ion conductivity, viscosity, thermal stability, solubility limits are change and consequently affect supercapacitor behavior of the active material [241, 262]. Notably, in the last few years studies are being reported dealing with effect of temperature on aqueous based supercapacitors performance [241]. In this context copper oxide supercapacitor can be a good option because copper oxide is well known for thermal stability and as a bulk material it is being used in several industrial applications as a thermal energy transfer material [261]. For this we have selected calcined batches of pristine and calcined Se doped CuO NPs for investigating the effect of elevated cell temperature on their supercapacitor behavior from cyclic voltammetry measurement and electrochemical impedance spectroscopy studies.

4.5.1 Cyclic voltammetry studies

The elevated temperature cyclic voltammetry study of calcined pristine and calcined 0.45 wt% Se doped CuO NPs were recorded for cell temperatures ranging between 25 °C and 75 °C with an increment of 10 °C in presence of 1.0 M Na₂SO₄ electrolyte solution at different

scan rates 10 mV/s to 70 mV/s. The CV at each cell temperature was recorded at different scan rates ranging between 10 mV/s and 70 mV/s, and the results are given in Fig. 4.15 & 4.16. As expected the quasi rectangular shaped of CV curves were obtained which are signature of good supercapacitive behavior. The CV plots of calcined pristine CuO NPs are different cell temperature recorded at 10 mV/s scan rate are given in Fig. 4.17a. The shape and sizes of the CV curves were found to increase with increase in cell temperature. This indicated that the specific capacitance increases with increase in cell temperature. But according to Gouy-Chapman theory, the specific capacitance is inversely related to temperature, which is given by expression:

$$C_d = \left(\frac{\alpha}{T}\right) \cosh\left(\frac{\beta}{T}\right) \quad (4.3)$$

where, C_d represent specific capacitance, α is function of the concentration and the dielectric property of electrolyte, and β represents electrode potential. Therefore, the obtained increase in the specific capacitance of these materials cannot be explained by Gouy-Chapman theory. This implies that there are other contributions for increasing the specific capacitance with increase in temperature. It may be remarked that at high temperature the ionic mobility is increased and the contributions from faradaic redox cannot be ruled out. Prominent redox peaks observed at higher cell temperature measurements. This is because of improved mobility and rapid diffusion of electrolyte ions into the electrode materials at higher temperature. The specific capacitances of calcined pristine CuO NPs at different temperatures corresponding to each scan rate were determined. The specific capacitance vs. scan rate graph at different cell temperature is shown in Fig. 4.17b. It is observed that the specific capacitance decreased with increase in scan rate for all measured temperatures.

Similarly, the effect of cell temperature on CV curves of calcined Se doped CuO NPs, recorded at 10 mV/s (Fig. 4.17c). The specific capacitance was found to decrease with increase in scan rate (Fig. 4.17d), for all the cell temperature.

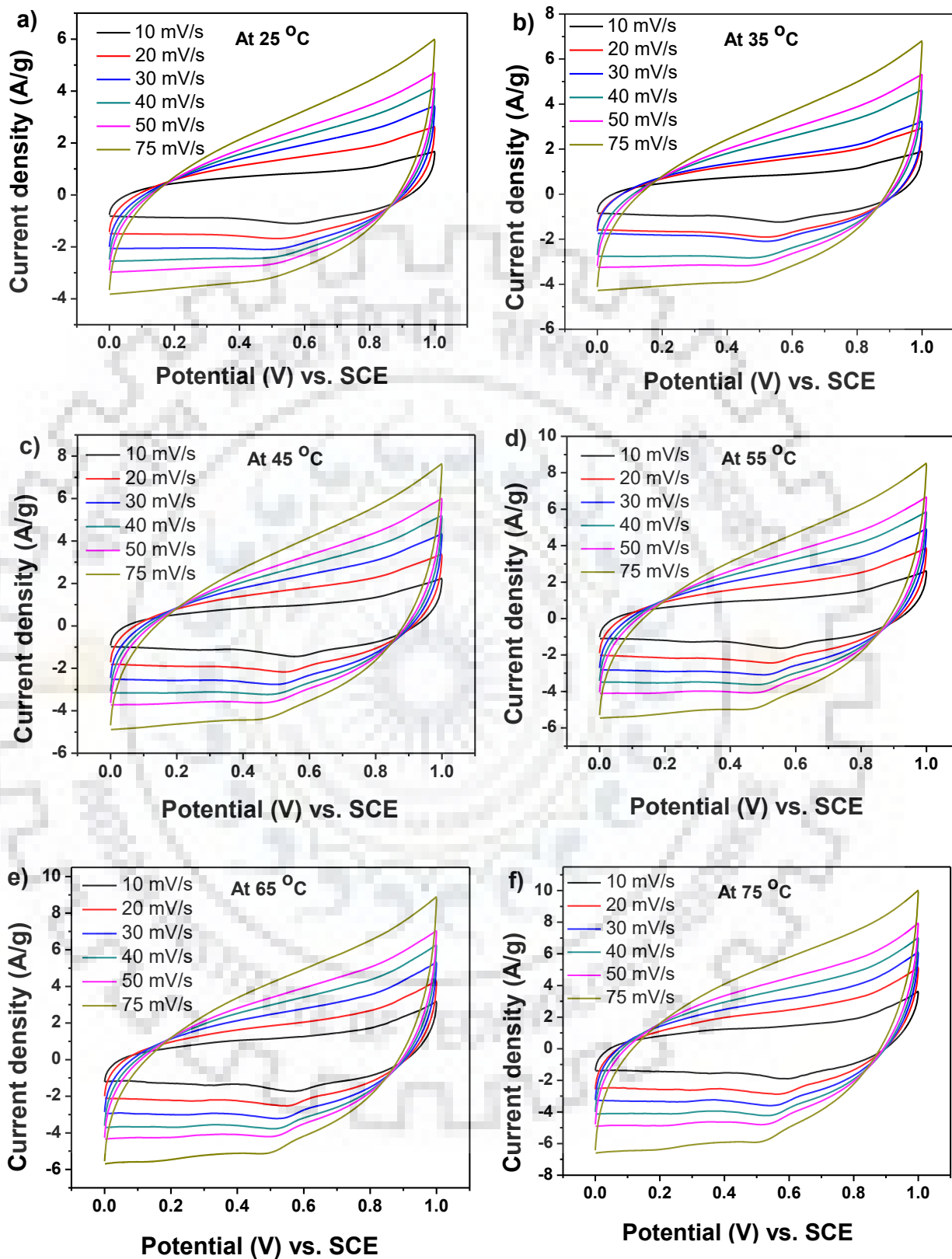


Fig. 4.15 Cyclic voltammetry of calcined pristine CuO NPs at (a) 25 °C, (b) 35 °C, (c) 45 °C, (d) 55 °C, (e) 65 °C, and (f) 75 °C.

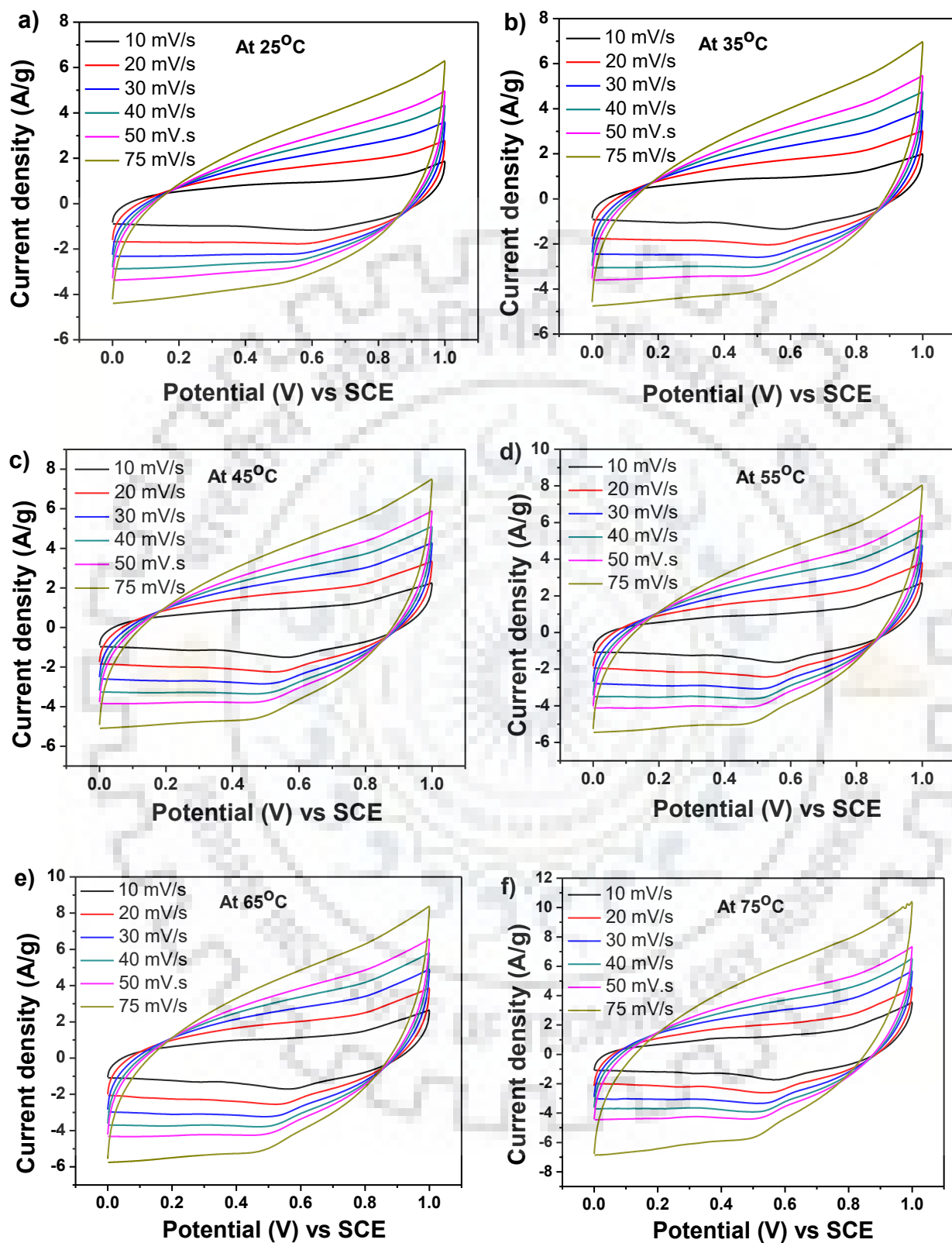


Fig. 4.16 Cyclic voltammetry of calcined Se-doped CuO NPs at (a) 25 °C, (b) 35 °C, (c) 45 °C, (d) 55 °C, (e) 65 °C, and (f) 75 °C.

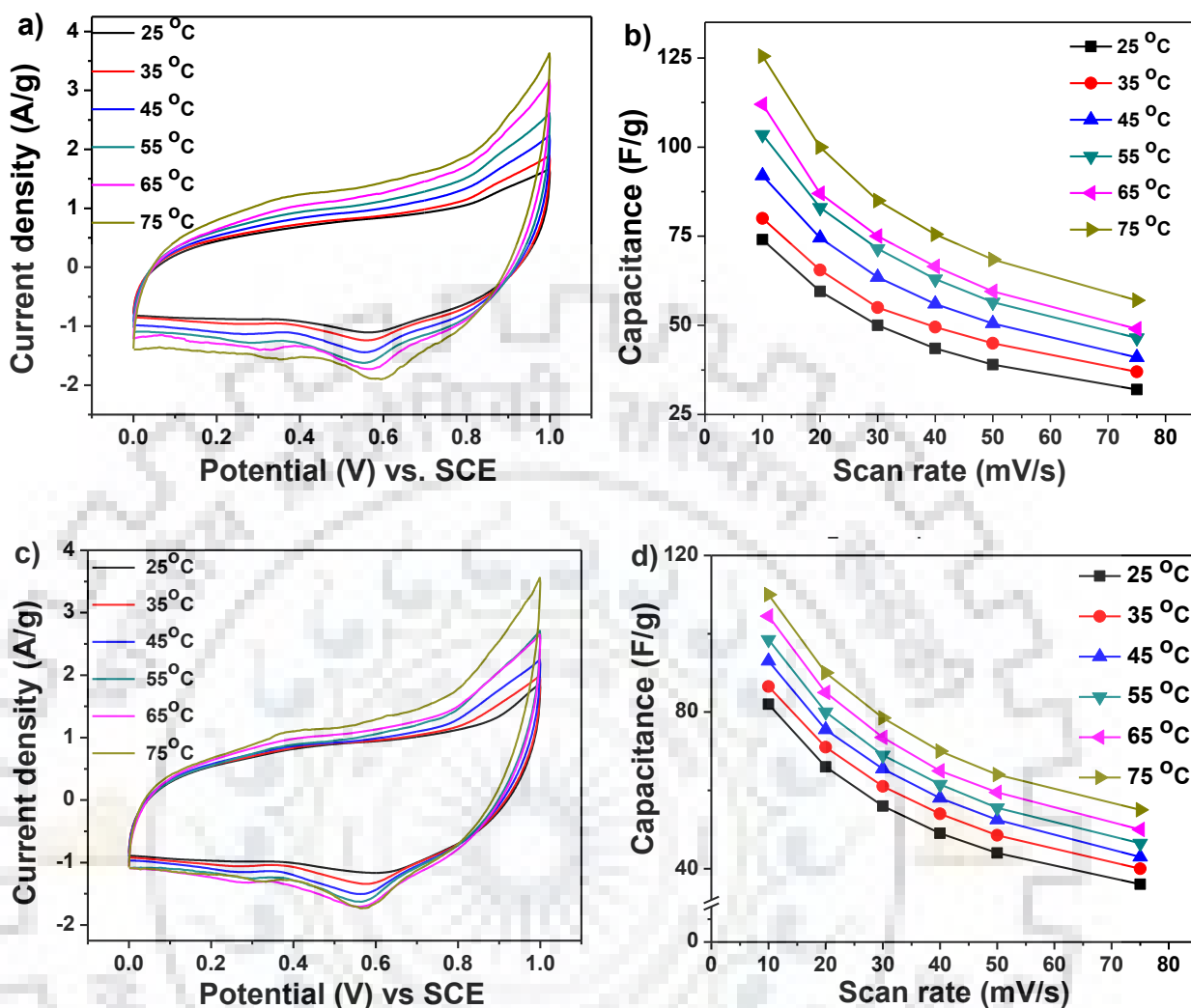


Fig. 4.17 (a) Comparison plot of CV curves of calcined pristine CuO NPs at different temperature at scan rate of 10 mV/s (b) capacitance vs. scan rate plot, (c) Comparison plot of CV curves of calcined Se doped CuO NPs at different temperature at scan rate of 10 mV/s and (d) capacitance vs. scan rate plot.

It is noted from Fig. 4.17 b, d, that the specific capacitance of calcined Se doped CuO NPs is 115 F/g and that of pristine CuO NPs is 125 F/g at 75 °C for scan rate of 10 mV/s. From these studies it is concluded that the specific capacitance of our material is increased by 67% to 45% at elevated cell temperature.

4.5.2 EDLC vs. PC contributions

Further, to understand the effect of temperature on the supercapacitor behavior of pristine and Se doped CuO NPs, it is necessary to measure the charge associated with (a) electric double layer capacitance and (b) with pseudocapacitance in these materials.

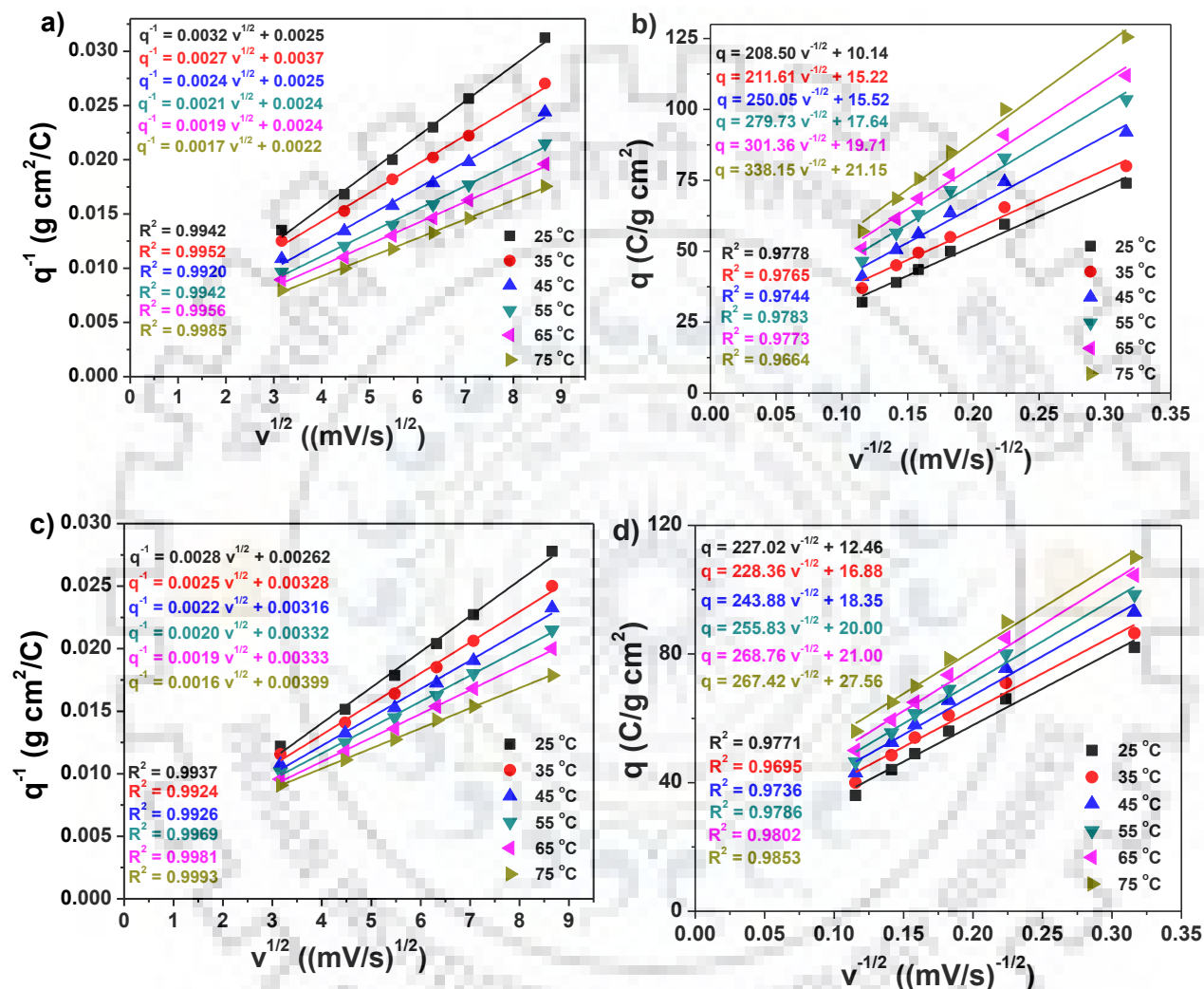


Fig. 4.18 (a) $1/q$ vs. $v^{1/2}$, (b) q vs. $v^{-1/2}$ dependence of calcined pristine CuO NPs on temperature. (c) $1/q$ vs. $v^{1/2}$ (d) q vs. $v^{-1/2}$ dependence of calcined Se doped CuO NPs on temperature.

From the $1/q$ vs. $v^{1/2}$ plot, the total voltammetric charge (q_t) was calculated by extrapolating voltammetric charge to $v = 0$ (Fig. 4.18a). Total charge associated with double layer (q_{dl}) is calculated from the q_{dl} vs. $v^{-1/2}$ plot by the extrapolation of voltammetric charge to $v = \infty$ (Fig. 4.18b). Thus, charge associated with PC (q_p) can be calculated as:

$$q_p = q_t - q_{dl} \quad (4.4)$$

The contribution of PC can be estimated as:

$q_p\% = (q_p/q_t) \times 100$ and the values are listed in Table 4.4. The PC and EDLC contribution in the calcined batches of pristine and calcined Se doped CuO NPs were determined as explained in section 4.3.5.2. From the I/q vs. $v^{1/2}$ the total voltammetric charges were determined as 400 F/g and 390 F/g, respectively.

Table 4.4 Summary of maximum total charge (q_t), double layer capacitance (q_{dl}), and charge associated with pseudocapacitance (q_p) of calcined pristine and calcined Se doped CuO NPs in 1 M Na₂SO₄ solution.

Sample	q_t (C/g)	q_{dl} (C/g)	q_p (C/g)	q_p/q_t (%)
Pristine at 25°C	400	10	390	97.5
Pristine at 35°C	270	15	255	94.4
Pristine at 45°C	400	16	384	96.0
Pristine at 55°C	417	18	399	95.7
Pristine at 65°C	417	20	397	95.2
Pristine at 75°C	455	21	434	95.4
Se doped at 25°C	381	12	369	96.8
Se doped at 35°C	305	17	288	94.4
Se doped at 45°C	316	18	298	94.3
Se doped at 55°C	301	20	281	93.4
Se doped at 65°C	300	21	279	93.0
Se doped at 75°C	251	28	223	88.8

The total charges associated with double layer were only 10 and 12 C/g, respectively. These are nearly four times less than their uncalcined counterparts. This indicated that double layer charge transfer process is significantly less. This also implied that the PC contribution for the calcined sample is high. The charge associated with PC in the calcined batches of pristine and Se doped CuO NPs (q_p) were 390 and 369 F/g, respectively. The PC contributions for these samples were 97.5% and 96.8%, respectively. The enhance charge accumulation for calcined batches are therefore, related to pseudocapacitance property. The enhanced specific capacitance

is attributable to better faradaic redox reaction at the surface of the calcined samples. Owing the improved electrochemical behavior, the calcined batches of pristine and Se doped CuO NPs were studied at higher cell temperature. For calcined pristine CuO NPs, total voltammetric charge increased with cell temperature. Whereas, total voltammetric charge at higher cell temperature for Se doped CuO NPs is decreased. The charge accumulation via double layer mechanism is systematically increased with cell temperature. This can be attributed to the dynamics of pore volume with cell temperature, which could form accumulation of charges. In addition, the diffusion of charges at higher cell temperature is not ruled out. Compared to pristine batch, the Se doped batch contrasting exhibited lowering of the total charge with increase in cell temperature. In this case also, the charge accumulation via double layer is increased by the same extent as that of the pristine batch. Further, the charge accumulation by pseudocapacitance mechanism for calcined pristine batch also increases with cell temperature. However, the net PC contribution is found to remain same or it was decreased by very small extent. This is due to increased charge accumulation contribution via double layer. The charge accumulation by PC mechanism decreased with cell temperature. This indicated that the faradaic redox reaction decreased at the surface of the Se doped CuO NPs. This could be attributed to poorer stability as revealed from the cyclic charging and discharging measurements recorded at higher cell temperature (55 °C). The decrease in the net PC contribution more for Se doped CuO NPs (9%) as compared to pristine batch (~2.3%).

4.5.3 Electrochemical impedance spectroscopy studies

The effect of temperature on supercapacitive behavior of calcined pristine and calcined Se doped CuO NPs were further investigated by electrochemical impedance spectroscopy. The Nyquist plots are shown in Fig. 4.19a and Fig. 4.19b, respectively. It is found that as the cell temperature increases from 25 °C to 75 °C, the equivalent series resistance (ESR) decreased. This reflected thermally activated ions with lesser activation energy favoring diffusion [272]. The vertical component of imaginary impedance became shorter as temperature increase from 25 °C to 75 °C for both calcined pristine and Se doped CuO NPs. The low frequency impedance is related to specific capacitance of material by following equation:

$$C_s = 1/(2\pi fZ''m) \quad (4.5)$$

Where, f , Z'' and m represents the frequency, imaginary component of impedance and active mass of the material, respectively. In other words, C_s is inversely proportional to f and Z'' . So, the observed shorter Z'' value for high temperature measurement reflected higher specific capacitance. This is in agreement with the CV results discussed above.

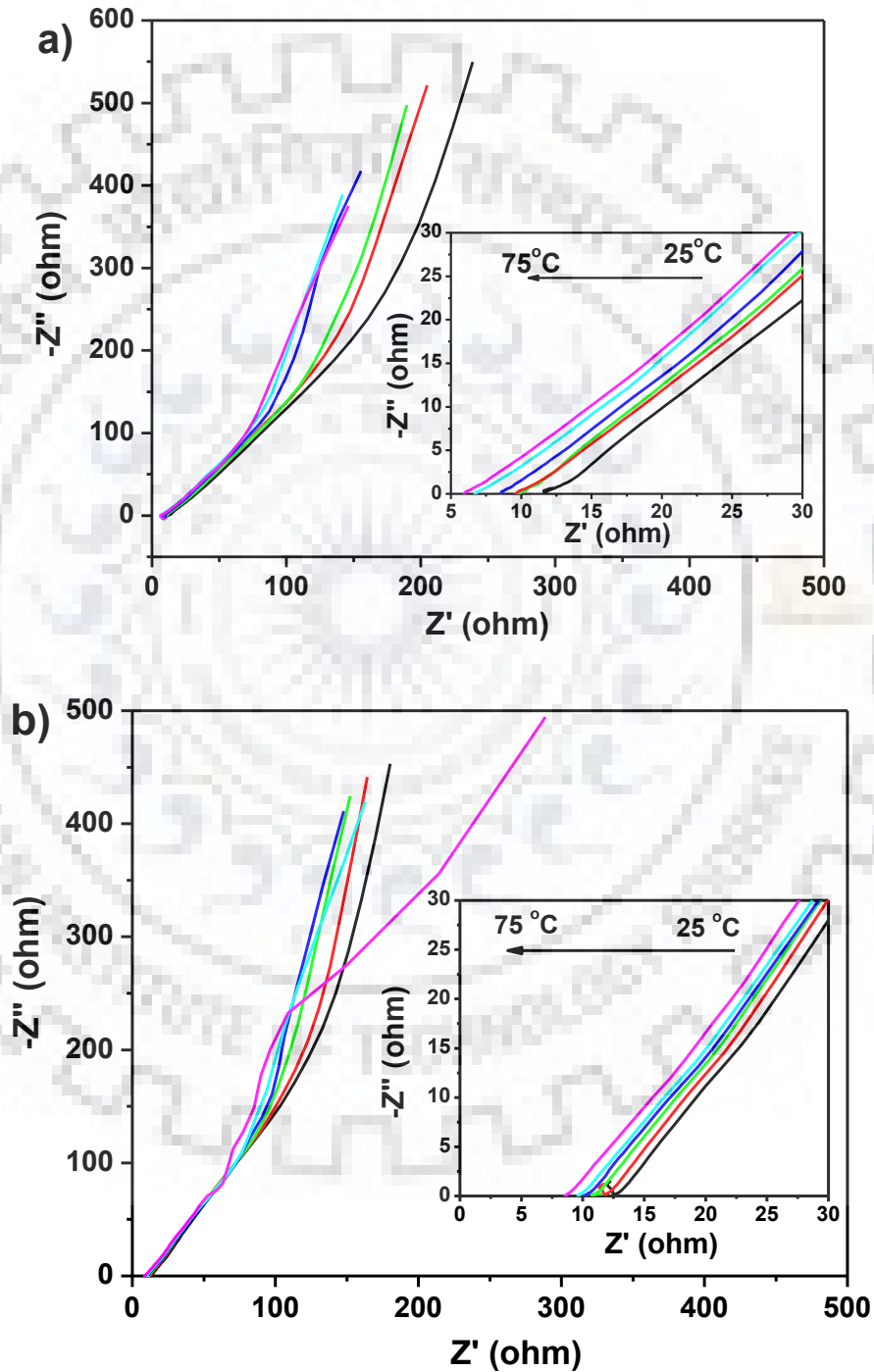


Fig. 4.19 Electrochemical impedance spectroscopy (EIS) of (a) pristine (b) Se doped CuO NPs at different temperature.

4.5.4 Cycle stability at elevated temperature

The stability of calcined pristine and calcined Se doped CuO NPs supercapacitor at elevated cell temperature was investigated by recording 500 cycles of charging-discharging process as at current density of 3 A/g.

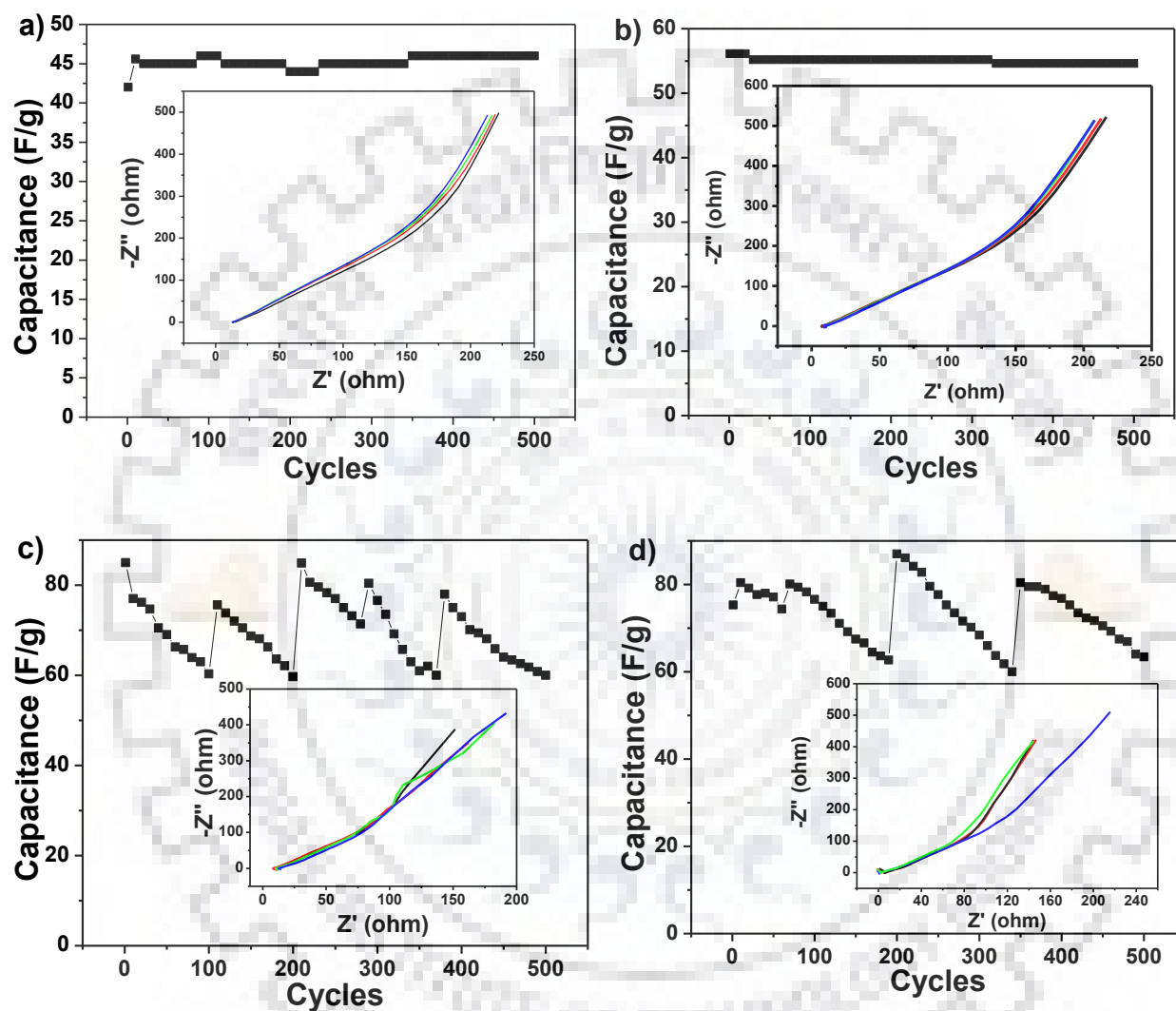


Fig. 4.20 Cycle stability of (a) pristine and (b) Se doped CuO NPs at 25 °C, (c) pristine and (d) Se doped CuO NPs at 55 °C after 500 cycles at current density 3 A/g. The inset in each figure represents EIS plot of pristine and Se doped CuO NPs recorded at respective cell temperatures.

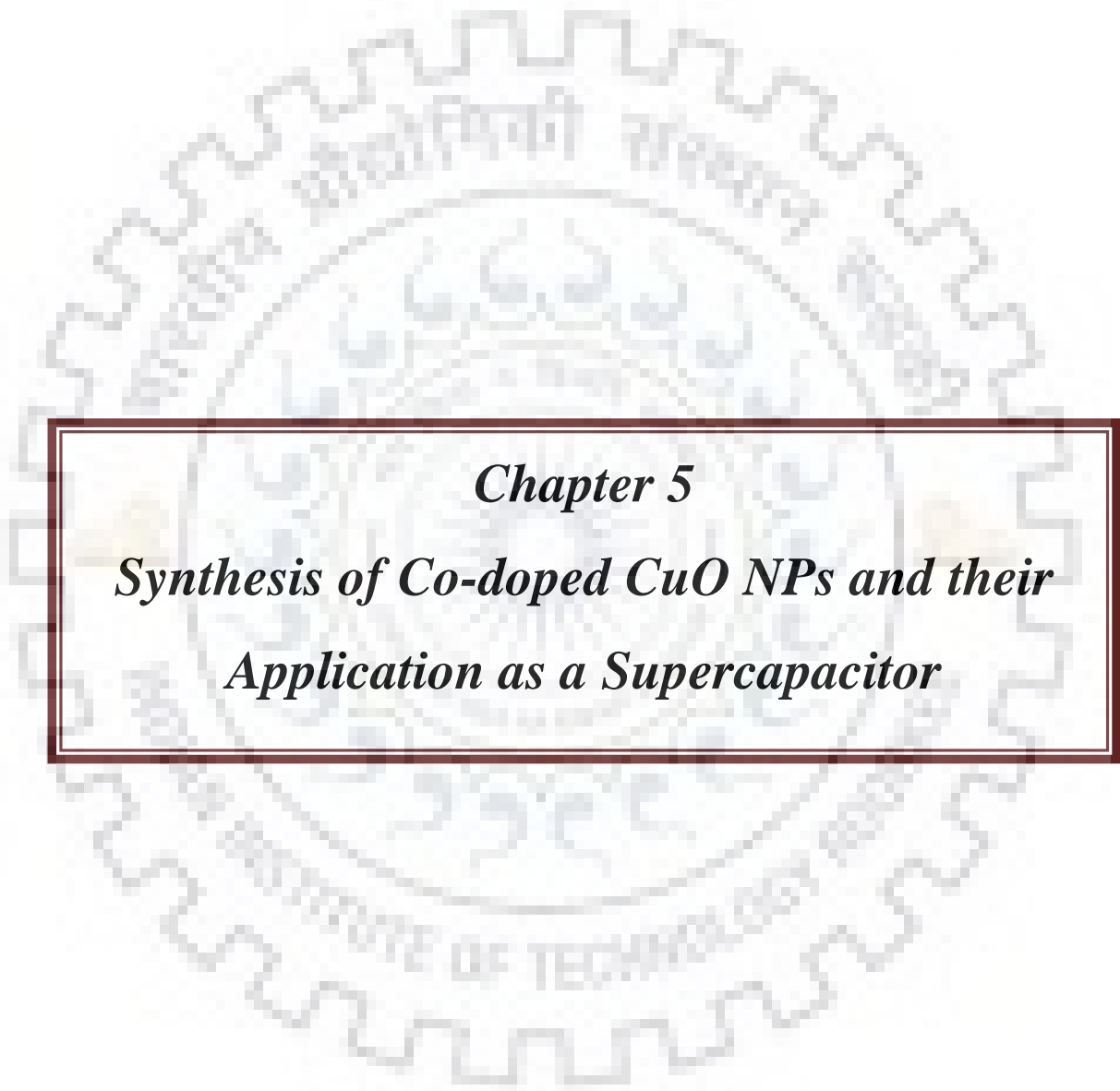
This measurement was done at 25 °C and 55 °C cell temperature. The capacitance retention after 500 charge discharge cycles at 25 °C for calcined pristine and calcined Se doped CuO NPs were found to be 100% and 98% respectively (Fig. 4.20 a, b). Similarly, the

capacitance retention of calcined pristine and calcined Se doped CuO NPs observed after 500 cycles for 55 °C were between 95% and 98%, respectively (Fig. 4.20 c, d) . These results are very encouraging for our Se-doped CuO NPs as supercapacitor at high temperature and at high current density. Further, the impedance measurements of both the samples were recorded after 1 cycle, 10 cycle, 100 cycle and 500 cycles, at 25 °C and 55 °C cell temperatures. The corresponding Nyquist plots are inserted in the respective plots given in Fig. 4.20. It is noted that there was not much change in the plots of both calcined pristine and calcined Se doped CuO NPs at 25 °C. This signified that the Se-doped CuO NPs as supercapacitor are electrochemically stable. However, changes at lower frequency region are observed in the impedance measurement of calcined pristine and calcined Se doped CuO NPs at 55 °C. This is attributable to difference in specific capacitance of the both materials at 55 °C. This difference in mostly contributed by faradaic reaction at elevated temperature. From this study, we can conclude that Se doped CuO NPs prepared by our method is suitable for application as supercapacitor at different cell temperature.

4.6 Conclusion

TPPO capped CuO NPs were successfully doped with Se of different concentration by chemical precipitation method. The dopant concentration in each of Se doped CuO NPs were determined by ICP-OES, which revealed only 0.14 to 0.45 wt% of Se presence in doped CuO NPs. Such poor Se-doping is most likely attributed to capping of CuO nanocrystals by Se species. This assumption is supported by observing less particles size of Se-doped CuO NPs as compared to pristine CuO NPs. The PL studies of batches of doped CuO NPs synthesized with lesser Se precursor revealed more Cu vacancies and oxygen vacancies, while the optimum doping corresponding to 0.45 wt% Se dopant concentration and the said defects were minimum. The batches of doped CuO NPs synthesized with 20 wt% precursor exhibited flakes like structure instead of spherical shape particles. All the batches of Se-doped CuO NPs were investigated for supercapacitive behavior by study their CV, GCD, and EIS measurements. The batch of 0.45 wt% Se doped CuO NPs exhibited highest specific capacitance (144 F/g) at current density of 0.2 A/g. It is attributed to increase in the conductivity as compared to pristine due to Se doping owing to minimized vacancy based defects. The supercapacitor mechanism of the 0.45 wt% Se-doped CuO NPs were discussed from EIS studies, which revealed structural and pseudocapacitance contribution. This implied that the surface area of the doped CuO NPs

was not very important; rather the faradaic reaction at the surface of the doped CuO NPs was more important phenomena to explain supercapacitor behavior. The capacitance retention of pristine and 0.45 wt% Se doped CuO NPs was only 73% and 63%. In order to improve the capacitance retention, the as-synthesized batches of CuO NPs were calcined at 450 °C. These calcined batches exhibited about 10-15% decrease in specific capacitance but their capacitance retention were improved to 93-96%. These calcined pristine and 0.45 wt% Se doped CuO NPs were chosen for investigation of their supercapacitive behavior at higher cell temperatures. The specific capacitance increased for higher cell temperature (i.e., 25 °C, 35 °C, 45 °C, 55 °C, 65 °C and 75 °C). The enhancement in specific capacitance as a function of temperature is attributed to reduce kinetic barrier for the redox reaction and enhance diffusivity of electrolyte ions. The cycle stability of these samples was excellent and about 92% to 95% at 55°C temperature after 500 cycles of GCD process at current density of 3 A/g. The supacacitor behavior was mostly attributed to PC contribution. However, the PC contribution was reduced for the calcined pristine and calcined 0.45 wt% Se-doped CuO NPs exhibited decrease in PC contribution as a function of temperature. This is attributable to opening of micro-pores at elevated temperatures. It may be concluded that the Se-doped CuO NPs can be used in wide range of cell temperature and can be used for practical applications.



Chapter 5

*Synthesis of Co-doped CuO NPs and their
Application as a Supercapacitor*

5.1 Introduction

In continuation of our investigation on CuO NPs as electrode material for supercapacitor behavior, we present here a systematic study on synthesis, characterization and supercapacitor behavior of a novel cobalt doped CuO NPs. Cobalt doping is reported to offer excellent supercapacitor behavior is manganese oxide [273], NiO [274], etc owing to its variable valency. So we choose Co as a dopant to modify the structural and physicochemical properties of CuO NPs. Only few reports are there which deals with dopants effect in CuO nanostructure and their utilization as supercapacitors [172, 173, 275, 181]. Cobalt is well known material that has been used in supercapacitor from long time. So cobalt doping in CuO NPs exhibit multi oxidation state effect on supercapacitor behavior and it increased the conductivity as well as electron transport properties of CuO NPs. We have discussed the effect of presence of defects sites in the electrode material. The best performing Co-doped CuO NPs were used for the first time in the fabrication of symmetric solid state supercapacitor.

In this study we have synthesized cobalt doped CuO NPs with different concentration of Co by chemical precipitation method. These batches were thoroughly characterization and studies for supercapacitor behavior. Symmetric solid state capacitor made of optimized Co-doped CuO NPs was studied to determine varying working potential window and energy density which are important factor for practical application as devices.

5.2 Materials and methods

5.2.1 Chemicals

Chemicals used in this study were same as discussed in Chapter 3, in a addition cobalt acetate ($\text{Co}(\text{CH}_3\text{COO})_2 > 98\%$) from HiMedia Pvt. Ltd., India. was used as cobalt precursor.

5.2.2 Synthesis of Co-doped CuO NPs

The batches of Co-doped CuO NPs were synthesized by the coprecipitation method by adding different concentration 0, 2, 5, 10 and 20 wt% of cobalt acetate in 150 mL of aqueous solution of copper acetate (20 mM) followed by addition of 0.01 g TPPO and 1ml of acetic acid (Table 5.1). This reaction was refluxed at 100 °C for 1 hour in a round-bottomed flask. Then 1.0 M NaOH was added to the solution until a black colored precipitate was formed at pH 7.7

to 8.0. The precipitate was centrifuged at room temperature, washed 3 times with ethanol, and eventually dried at 80 °C overnight in a temperature controlled oven.

Table 5.1 Concentration of cobalt taken during synthesis of Co-doped CuO NPs

Weight taken of copper acetate (g)	Weight taken of cobalt acetate (g)	Amount of Co dopant (g)	Batches	Dopant amount by ICP-OES
0.6	0	0	Pristine	0 wt%
0.6	0.01865	1.86	2 wt%	1.14 wt%
0.6	0.0373	3.73	5 wt%	4.14 wt%
0.6	0.0647	6.47	10 wt%	5.77 wt%
0.6	0.1294	12.94	20 wt%	8.33 wt%

The batches of Co doped CuO NPs prepared with 2 wt%, 5 wt%, 10 wt% and 20 wt% of Co precursor were analyzed by ICP-OES technique to obtain the actual Co concentration in respective batches of doped CuO NPs. The concentrations of cobalt in the respective batches of the acid digested nanoparticles were determined against the calibration plot obtained by analyzing known concentrations of standard cobalt ion solution (Merck). The concentration of cobalt in Co-doped CuO NPs was calculated using the formula given below:

$$Co \left(\frac{w}{w} \% \right) = \frac{[mass\ of\ Co\ in\ acid\ digest\ (mg)]}{[mass\ of\ Co-doped\ CuO\ NPs\ digest\ (mg)]} \times 100 \quad (5.1)$$

where, mass of Co in acid digest = Co concentration measured by ICP-OES (mg/L) times total volume of digest (i.e., 1000 mL).

5.2.3 Fabrication of symmetric solid state supercapacitor

The batch Co-doped CuO NPs was used to fabricate symmetric solid state supercapacitor. The gel electrolyte was prepared by mixing H₂SO₄ and PVA in 1:1 ratio in water at room temperature followed by 6 hour stirring at 80 °C. This electrolyte was used in between two electrodes in sandwich form with a layer of whatman filter paper.

5.3 Result and discussion of Co-doped CuO NPs

5.3.1 Analysis of Co doped CuO NPs

It is observed that the actual doped concentration of cobalt in the batches of CuO NPs prepared with 2 wt%, 5 wt%, 10 wt% and 20 wt% Co precursor was 1.14 wt%, 4.10 wt%, 5.77 wt% and 8.33 wt%, respectively with respect to the weight of CuO NPs. In a previous study by our research group, it has been investigated that the Co dopant occupied the grain boundaries of CuO NPs and leads to reduce the particles size. [105].

5.3.2 X-ray diffraction

The XRD patterns of pristine and different batches of cobalt doped CuO NPs revealed their characteristic peaks corresponding to (110), (002), (111), (20 $\bar{2}$), (020), (202), (11 $\bar{3}$), (31 $\bar{1}$), (220), (311) and (22 $\bar{2}$) planes of monoclinic structure of CuO NPs (Fig. 5.1). These XRD patterns matched with JCPDS file corresponding to card no. 48-1548. Compared to the pristine batch, the XRD patterns of Co-doped CuO NPs revealed decrease in peak intensities and broadening as a function of dopant concentrations. The broadening of the peaks and decrease in peak intensities are attributed to (a) decrease in crystallite size as a function of Co dopant concentration, (b) increase in defects in the lattice structure, and (c) increase in lattice strain. No peak shift was observed in the XRD plots of Co-doped CuO NPs. This implied substitution of Co²⁺ in the lattice position of Cu²⁺ sites of CuO NPs (Fig. 5.1b).

Table 5.2 Crystallite size, band gap, surface area and specific capacitance of pristine and Co-doped CuO NPs

Sample	Crystallite size (nm)	Band gap (eV)	Surface area (m ² /g)	Specific capacitance (F/g)	
				CV (5mV/s)	GCD (0.2 A/g)
Pristine	11.4	2.90	90	99	133
1.14 wt% Co	9.3	2.43	66	107	137
4.14 wt% Co	9.5	2.67	71	99	132
5.77 wt% Co	9.6	2.79	81	118	160
8.33 wt% Co	9.8	2.86	70	103	141

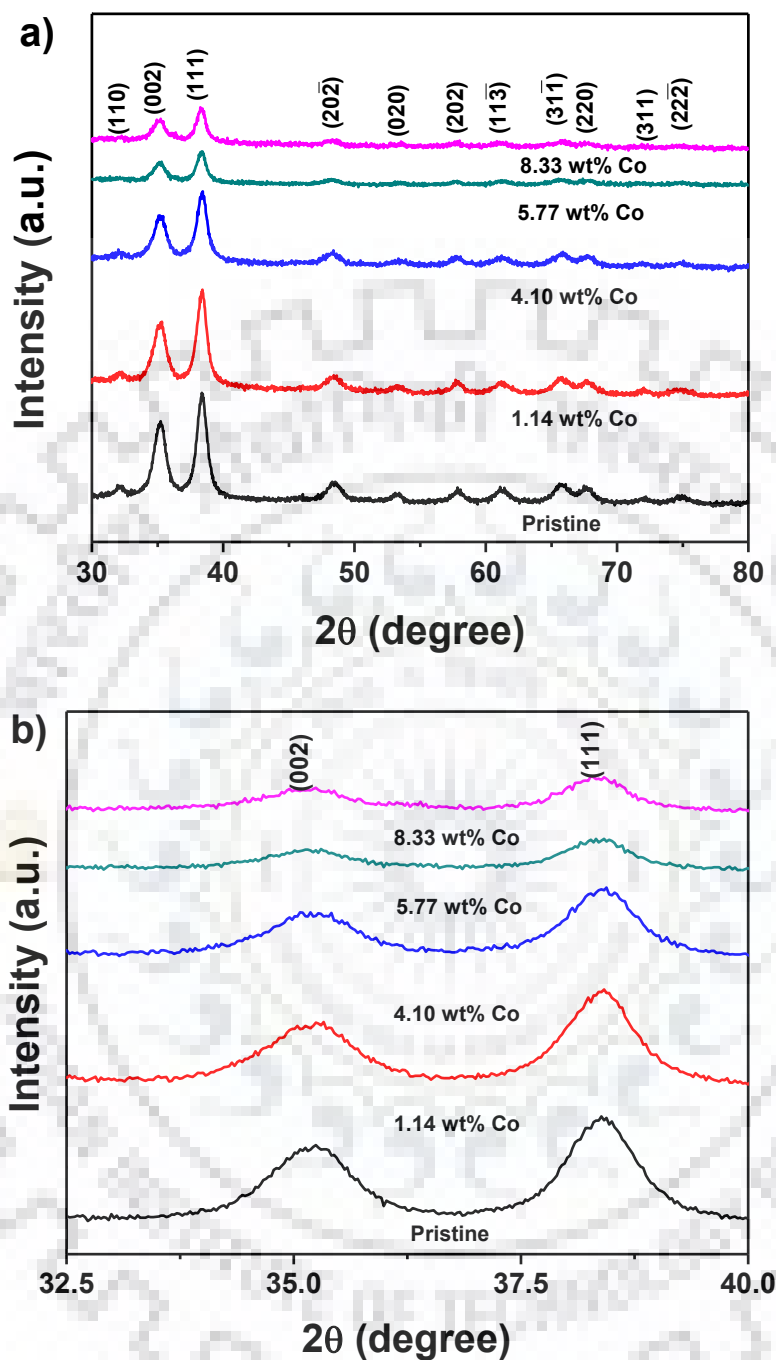


Fig. 5.1 (a) XRD pattern corresponding to the monoclinic structure of pristine and Co-doped CuO NPs, (b) Zoom XRD of Co-doped CuO NPs

The dopant substitution is favourable as the ionic radii of Cu^{2+} and Co^{2+} are similar i.e., 0.73 nm and 0.70 nm, respectively. The crystallite size of all the batches of CuO NPs were studied here

calculated from Debye Scherrer formula and the results are given in Table 5.2. The crystallite size of Co-doped CuO NPs were smaller than that of pristine CuO NPs. Similar observation is also reported in the literature [105].

5.3.3 Surface morphology

The surface morphology of pristine and all the batches of Co-doped CuO NPs were studied by FE-SEM and the results are given in Fig. 5.2. The FE-SEM images revealed agglomeration of the as-synthesized nanoparticles.

The overall chemical composition and purity of the NPs were reflected from the energy dispersive X-ray analysis (EDAX) measurements, which corresponded to imaged nanoparticles. The corresponding EDAX spectra are given along site the respective FE-SEM images. This analysis revealed characteristic X-ray peaks of Cu, Co and O. Further, the transmission electron microscopy (TEM) studies revealed agglomeration of the NPs (Fig. 5.3). High resolution TEM image of pristine CuO NPs revealed spherical shaped nanoparticles of sizes in the range of 10-12 nm size. This result is consistent with the crystallite size measurements by XRD studies. Whereas, the batch of 5.77 wt % Co-doped CuO NPs revealed irregular shaped nanoparticles.

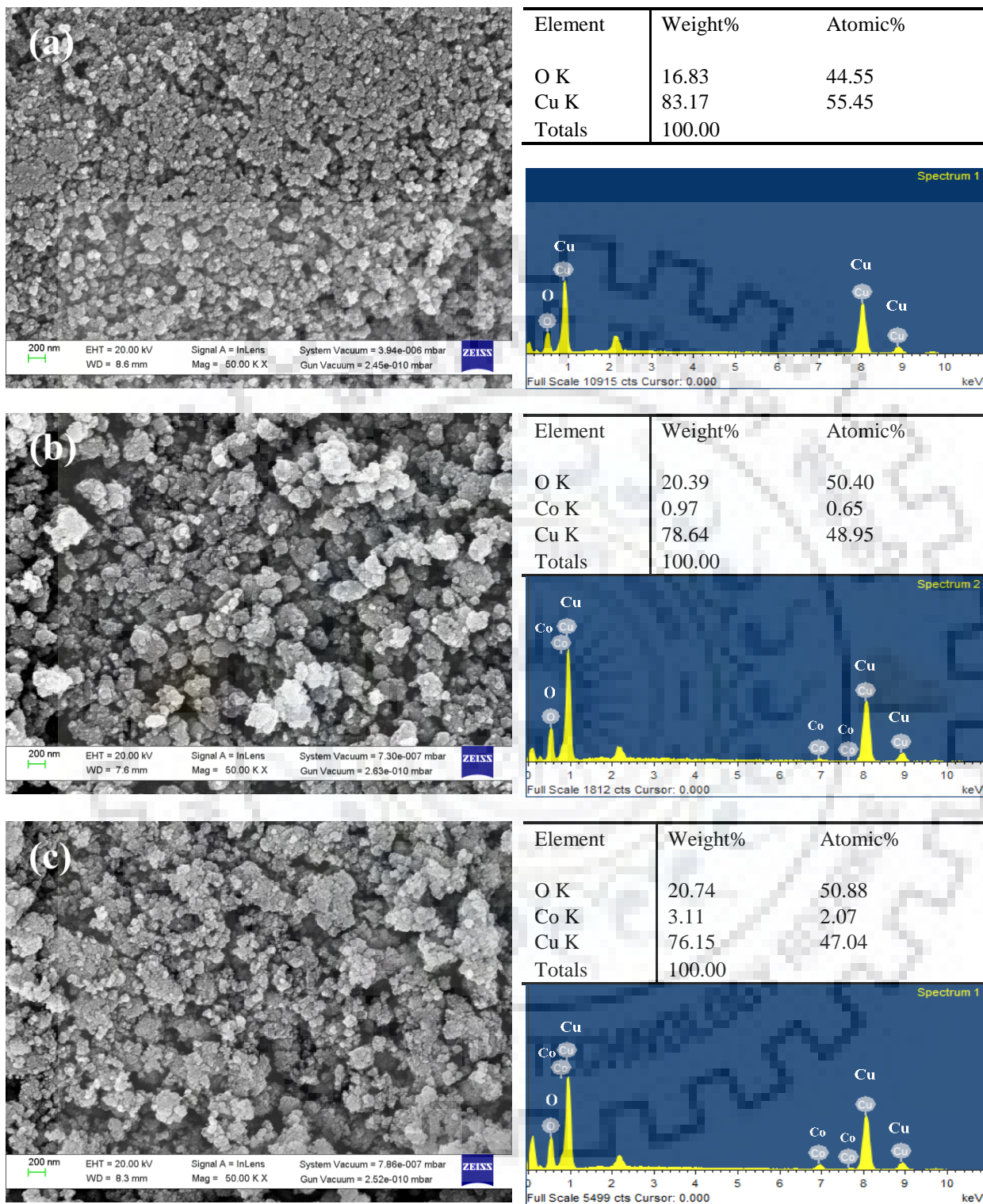


Fig. 5.2 continued in next page

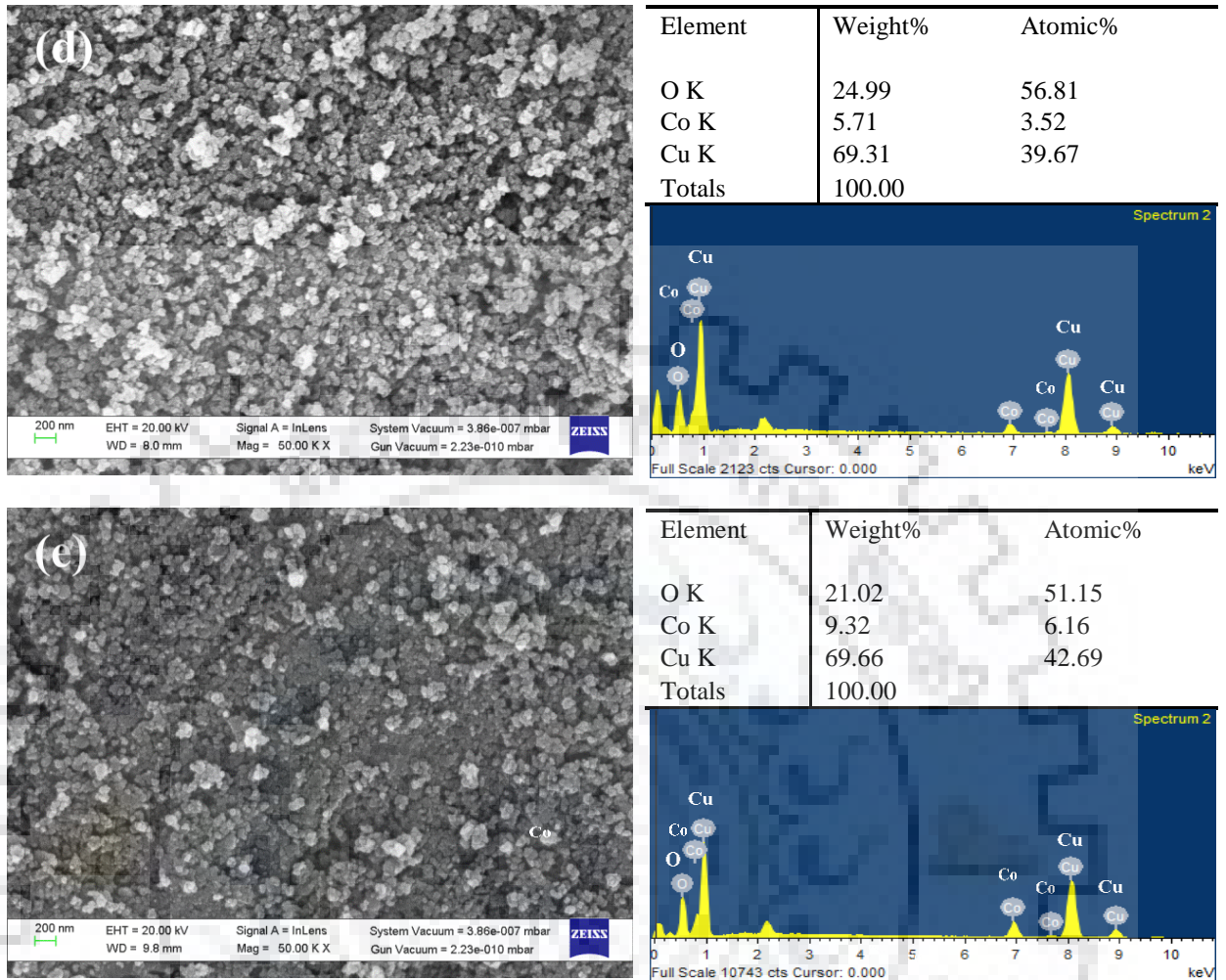


Fig. 5.2 Field Emission Scanning Electron Microscopy images of (a) Pristine; (b) 1.14 wt% Co doped; (c) 4.10 wt% Co doped; (d) 5.77 wt% Co doped; and (e) 8.33 wt% Co doped CuO NPs. Their corresponding energy dispersive X-ray analysis spectra are given next to the respective FE-SEM images, which revealed characteristic K and L X-rays and atomic% of Cu, Co and O.

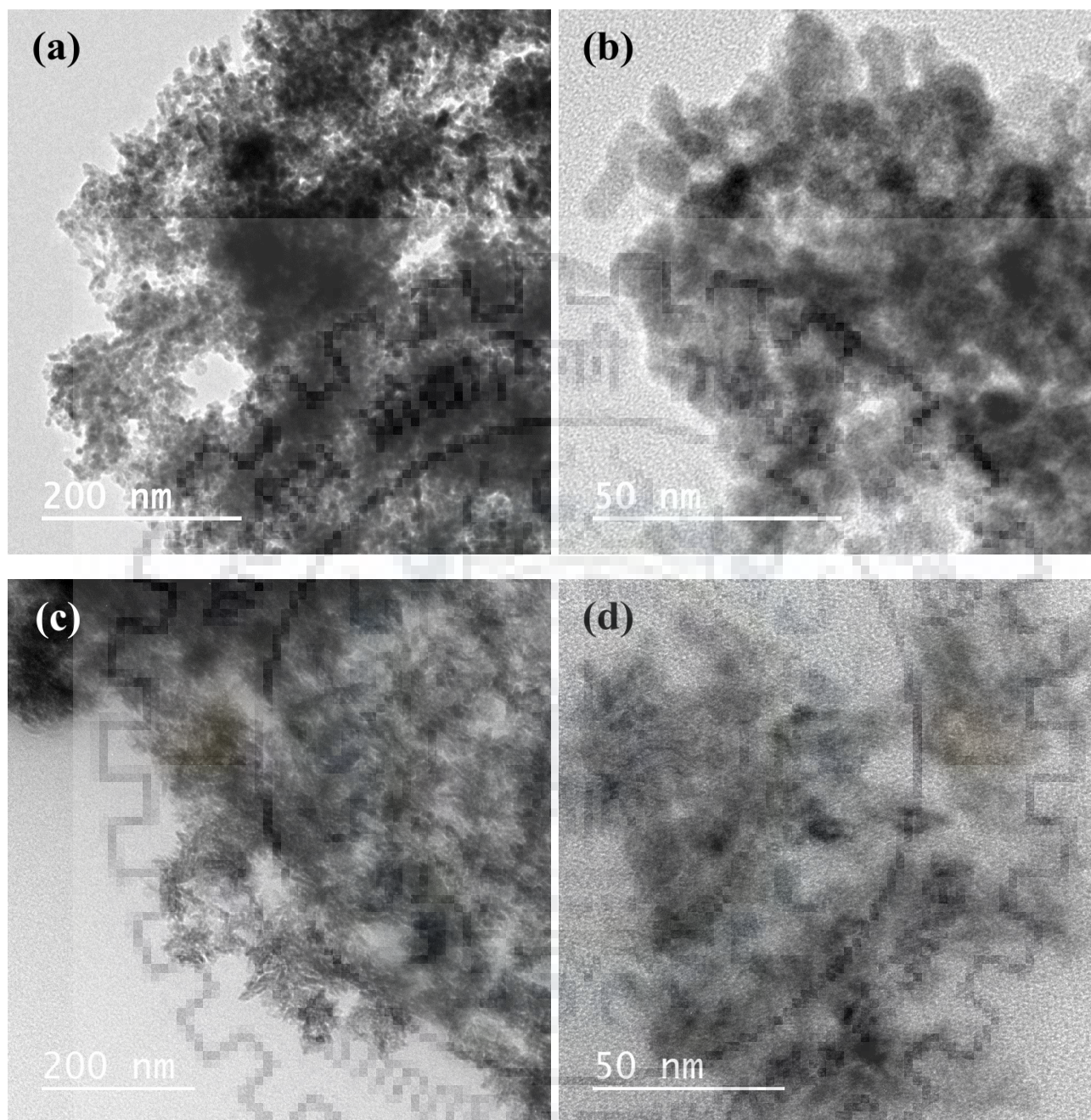


Fig. 5.3 Transmission Electron Microscopy (TEM) images of (a) pristine; (b) high resolution images of pristine CuO NPs; (c) Co-doped CuO NPs; and (d) high resolution images of Co-doped CuO NPs.

5.3.4 Optical studies

The optical properties of bare and batches of capped CuO NPs were studied by diffuse reflectance spectroscopy (DRS) in the wavelength range 200-800 nm. The photoluminescence spectroscopy studied was recorded in wavelength range 315-575 nm.

5.3.4.1 Diffuse reflectance spectroscopy (DRS)

The diffuse reflectance spectroscopy was used for the determination of band gap of pristine as well as batches of the Co-doped CuO NPs.

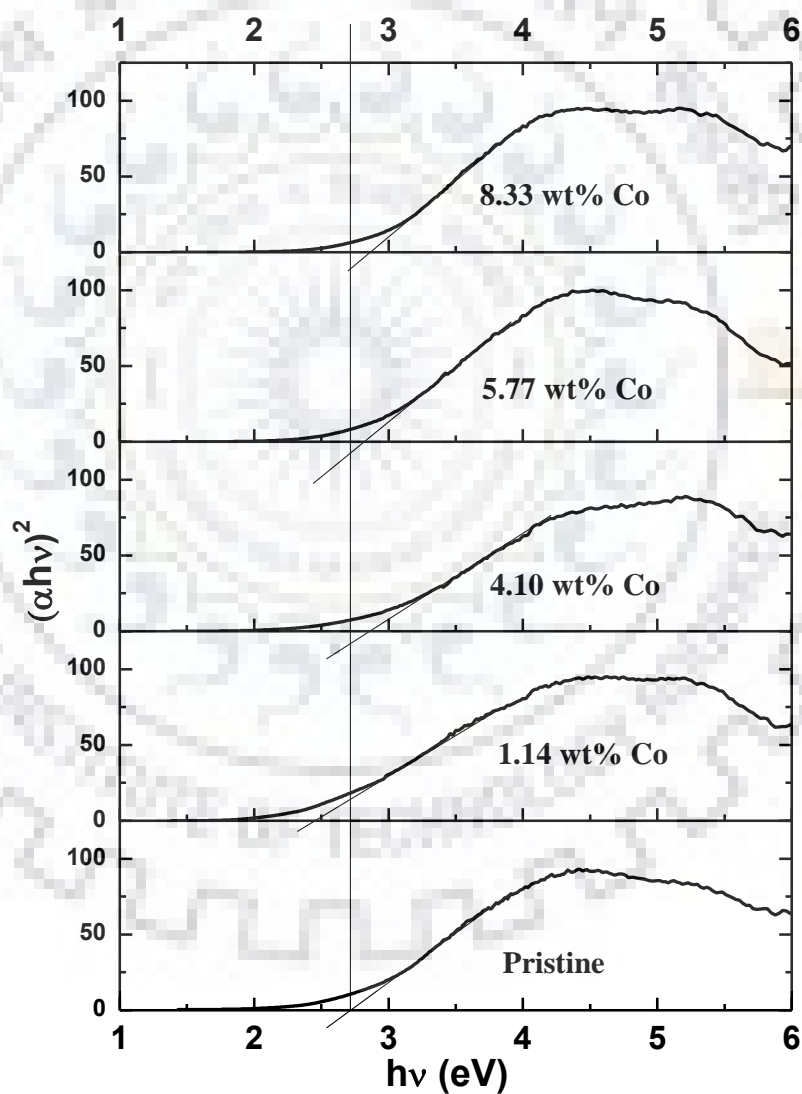


Fig. 5.4 Tauc plot obtained from diffuse reflectance spectroscopy of pristine and the respective batches of Co-doped CuO NPs.

The estimated band gap will provide the information about excitation energy needed for photoluminescence study. The Tauc plots of these samples corresponding to Kubelka Munk formula are shown in Fig. 5.4. The band gap energy of pristine was determined as 2.9 eV. Similarly, the band gaps of Co-doped CuO NPs were in the range of 2.43-2.86 eV, in order to increasing order of Co-dopant concentration. The band gap energy of the respective batches of pristine and Co-doped CuO NPs are listed in Table 5.2. The band gap of all the batches of Co-doped CuO NPs is lesser than that of pristine CuO NPs. Moreover, the band gap of Co-doped CuO NPs increased as a function of Co dopant concentration. This increasing trend of band gap energy in the Co-doped CuO NPs is found to be directly correlated with crystallite size. The band gap-crystallite size relation observed in our study is anemology to the several inverse relations between band gap and particles size relationship. This could be attributed to Jahn Teller distribution.

5.3.4.2 Photoluminescence Spectroscopy Studies

The photoluminescence (PL) spectra of pristine and the batches of Co-doped CuO NPs were studied to get information about defect sites. The PL peaks corresponded to radiative transition between the energy states, where the splitting of e.g., orbital of Cu^{2+} play a role. The transfer energies less than the re-combination of exaction indicate defect levels [53].

The photoluminescence spectra of pristine and the batches of Co-doped CuO NPs are recorded using excitation wavelength $\lambda_{\text{ex}} = 300$ nm and the results are given in the Fig. 5.5. The batches of 1.14 wt% Co, 4.10 wt% Co and 8.77 wt% Co-doped CuO NPs revealed intense PL peaks at 418 nm, 440 nm and 467 nm in the visible region. These intense peaks are attributable to near band edge emission, may be due to electronic transition in defects levels e.g., V_{Cu} (copper vacancies), C_{ii} (copper interstitial) V_{o} oxygen vacancy. The Pristine and 5.77 wt% Co-doped CuO NPs did not reveal such intense near band edge emission, instead they revealed weak peak at 467 nm. This indicated lesser defect population in these samples as compared to other batches of Co-doped CuO NPs. Further it is reported in the literature that the material with defects exhibited higher electrical resistance as compared to materials with lesser defects [185]. So, the batches of 5.77 wt% Co-doped CuO NPs are more conductive than pristine and other Co-doped CuO NPs. This defect sites are considered to be as a trapping sites for the generated charge at the NPs surface during interaction with electrolyte ions.

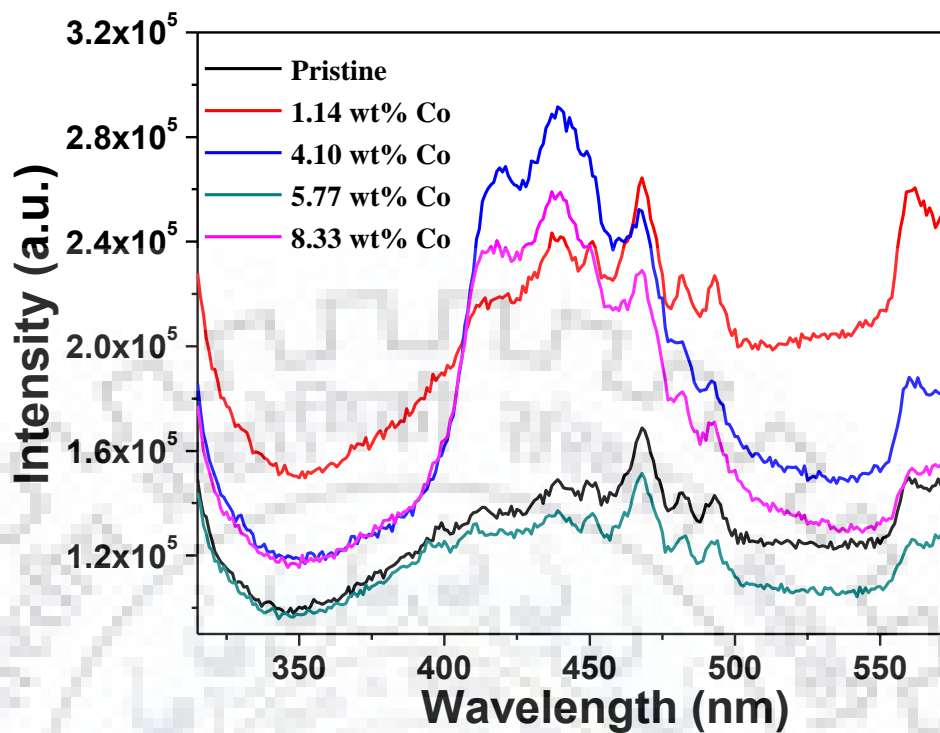


Fig. 5.5 Photoluminescence spectra of pristine and the batches of Co-doped CuO NPs.

5.3.5 Electrochemical studies

The electrochemical properties of pristine and the batches of Co-doped CuO NPs are studied by cyclic voltammetry, galvanostatic charge-discharge and electrochemical impedance spectroscopy in three electrode configuration measurements

5.3.5.1 Cyclic voltammetry study

The CV curves for pristine and the batches of Co-doped CuO NPs are recorded at different scan rates e.g., 5 mV/s, 10 mV/s, 20 mV/s, 30 mV/s, 40 mV/s and 50 mV/s (Fig. 5.6). The shapes of CV curve were quasi-rectangular shape and corresponded to literature reported on CuO nanostructures [238, 267, 270]. The shapes of cyclic voltammograms are observed to be independent of applied scan rate. This suggested that our pristine and Co-doped CuO NPs are favorable material for supercapacitor. These features are also observed in capped and Se-doped CuO NPs discussed earlier.

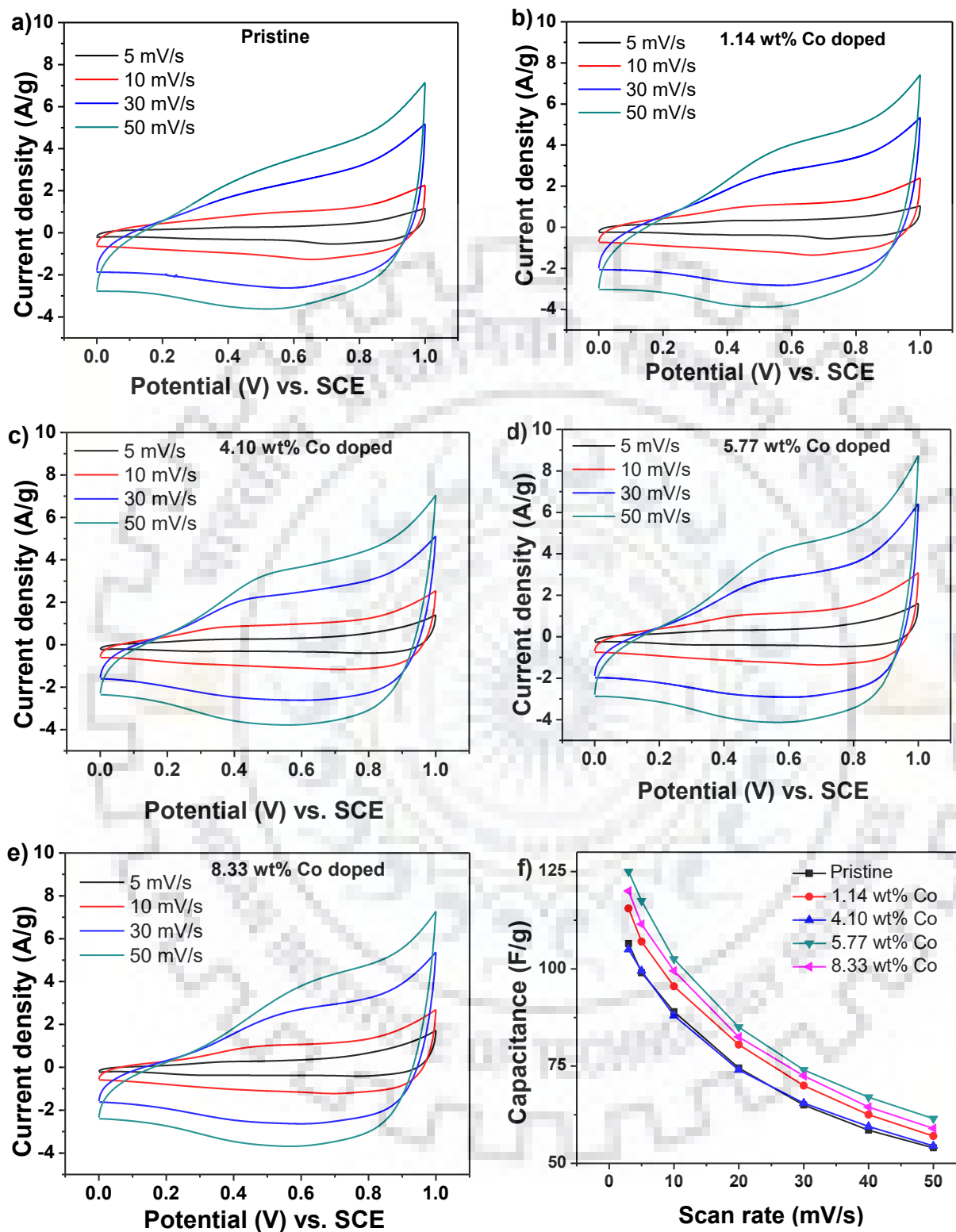


Fig. 5.6 Cyclic voltammograms of (a) pristine; (b) 1.14 wt% Co (c) 4.10 wt% Co (d) 5.77 wt% Co and (e) 8.33 wt% Co doped CuO NPs, (f) specific capacitance vs. scan rate plot.

The similar shapes of CV curves are attributed to restriction free movement of electrolyte ions into the pores of electrode and reversible feature to the electrolyte ion interactions with the Co-doped CuO NPs based electrode materials.

The specific capacitance of pristine and all the batches of Co-doped CuO NPs were calculated using the equation (3.2) discussed in Chapter 3. The specific capacitance of pristine, 1.14 wt%, 4.10 wt%, 5.77 wt% and 8.33 wt% Co-doped CuO NPs determined as 99 F/g, 107 F/g, 99 F/g, 118 F/g and 103 F/g, respectively. The maximum specific capacitance was found for the batch of 5.77 wt% Co-doped CuO NPs. This is correlated with lesser defects and hence more conductivity. Furthermore, among all the Co-doped CuO NPs, the BET surface area was maximum for 5.77 wt% Co-doped CuO NPs. This also explains the higher specific capacitance for 5.77 wt% Co-doped CuO NPs as specific capacitance is directly proportional to surface area of the electrode material. The specific capacitance of all the batches of doped CuO NPs decreased with increase in scan rate (Fig. 5.6f). This is due to lesser interaction of electrolyte ions with the pores of the active material. Notably, from CV measurements it is observed that all the Co-doped CuO NPs exhibited higher specific capacitance than the pristine CuO NPs in spite of lesser surface area. This can be attributed to incorporation by multiple oxidation state cations in the system via doping of the Co^{2+} [4, 68].

5.3.5.2 EDLC vs. PC contributions

The CV plots of all the batches of doped and pristine CuO NPs at varying scan rate indicates charge transport between electrolyte and electrode and hence provides useful insights to understand supercapacitor mechanism. For this it is necessary to measure the charge associated with (a) electric double layer capacitance particularly in the pores and (b) with faradaic process which is given as pseudocapacitance. The EDLC contribution is directly proportional to surface area of electrode [268]. The total voltammetric charge (q_t) was obtained from the plot of $1/q$ vs. $v^{1/2}$ by extrapolating voltammetric charge to $v = 0$ (Fig. 5.7a). The total charge associated with double layer (q_{dl}) was calculated from q_{dl} vs. $v^{-1/2}$ plot by extrapolation of voltammetric charge to $v = \infty$ (Fig. 5.7b). So the charge associated with pseudocapacitance (q_p) can be determined as:

$$q_p = q_t - q_{dl} \quad (5.2)$$

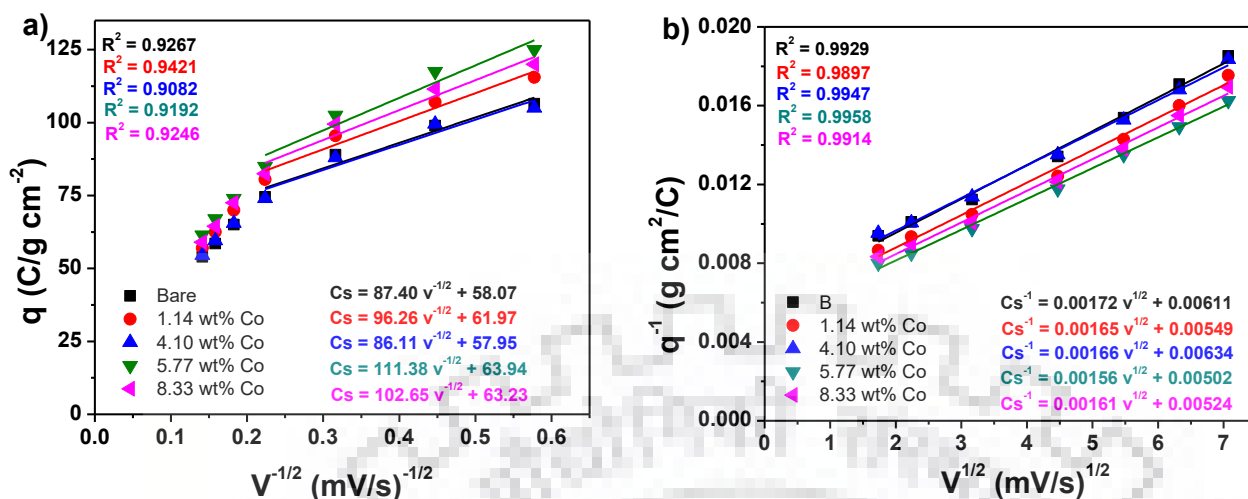


Fig. 5.7 (a) $1/q$ vs. $v^{1/2}$ and (b) q vs. $v^{-1/2}$ dependence of the batches of Co-doped CuO NPs

The relative charge due to pseudocapacitance contribution is determined as:

$q_p\% = q_p \cdot 100/q_t$, since the voltage window for these measurement were 0 – 1.0 V. So pseudocapacitance contribution is given as:

$$q_p\% = q_p \cdot 100/q_t \quad (5.3)$$

Table 5.3 Summary of maximum total charge (q_t), double layer capacitance (q_{dl}), and charge associated with pseudocapacitance (q_p) of pristine and Co-doped CuO NPs in 1 M Na₂SO₄ solution.

Sample	q_t (C/g)	q_{dl} (C/g)	q_p (C/g)	q_p/q_t (%)
Pristine	163	43.09	120	73.6
1.14 wt% Co	182	61.97	120	65.9
4.10 wt% Co	158	57.95	100	63.3
5.77 wt% Co	199	63.94	135	67.8
8.33 wt% Co	191	63.23	128	67.0

The C_p value for the all the batches are listed in Table 5.3. It is noted that the PC contribution of all the doped batches are more than the EDLC contribution. This is also suggested that from the observed oxidation peak match the electrode in the CV plots (Fig. 5.6).

Notably, the maximum PC contribution was obtained for the batch of 5.77 wt% Co-doped CuO NPs. It should be remarked here that the PC contribution did not follow any trend with surface area. For example the surface area of pristine CuO NPs was 90 m²/g whereas the PC contribution was 64.4% as compared to 5.77 wt% Co-doped CuO NPs 67.8% (surface area 81 m²/g). So the higher specific capacitances measured for the doped CuO NPs is also correlated to with higher PC contribution. In other word, the supercapacitor behavior of the Co-doped CuO NPs was mostly contributed by pseudocapacitance character.

5.3.5.3 Galvanostatic charge-discharge (GCD) studies

The electrochemical activities of the pristine and all the batches of Co-doped CuO NPs were determined by galvanostatic charge-discharge studies. The charge-discharge curves of electrodes made of pristine and batches of Co-doped CuO NPs were recorded at different current density varying from 0.2 A/g to 5 A/g (Fig. 5.8). The charge-discharge curves of these CuO NPs revealed typical triangular shape which corresponds to constant charging and discharging behavior of a supercapacitor [244]. The specific capacitance of pristine, 1.14 wt%, 4.10 wt%, 5.77 wt% and 8.33 wt% Co-doped CuO NPs were calculated using equation 3.3 (discussed in Chapter 3) as 133 F/g, 137 F/g, 132 F/g, 160 F/g and 141 F/g, respectively at current density of 0.2 A/g. It is noted that specific capacitances calculated from GCD also followed the same trends as the CV studies and the specific capacitance for the batch of 5.77 wt% Co-doped CuO NPs was significantly higher than others. Further, for the comparison of pristine and the batches of Co-doped CuO NPs charging-discharging curves at current density of 0.2 A/g is plotted and given in Fig. 5.8f. It reflected that the batches of Co-doped CuO NPs took longer time for charging-discharging as compared to pristine CuO NPs and are advantageous for certain applications. This could be attributed to the presence of Co²⁺ ion in the active materials owing to increase the presence of multi oxidation state cations in the sample [18].

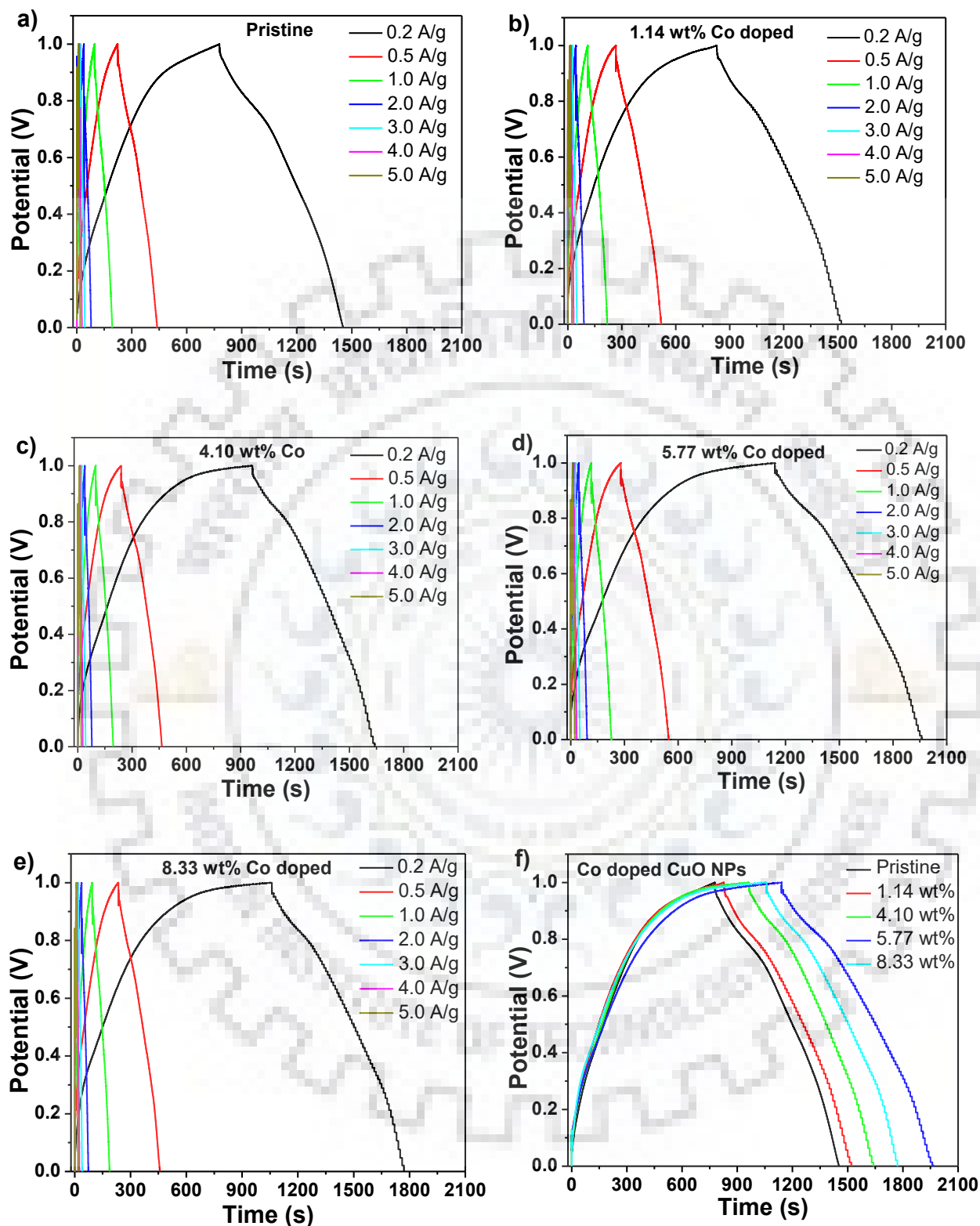


Fig. 5.8 Galvanostatic charge-discharge curves of (a) pristine, (b) 1.14 wt% Co-doped, (c) 4.10 wt% Co-doped, (d) 5.77 wt% Co-doped, (e) 8.33 wt% Co-doped CuO NPs and (f) Comparison study of GCD of all batches of CuO NPs at current density of 0.2 A/g.

5.3.5.4 Electrochemical impedance spectroscopy (EIS)

The EIS measurements were recorded for the pristine and all the batches of Co-doped CuO NPs in the frequency range 0.01 Hz to 1 MHz with 0.5 V bias voltages vs. SCE with 5 mV amplitude (Fig. 5.9).

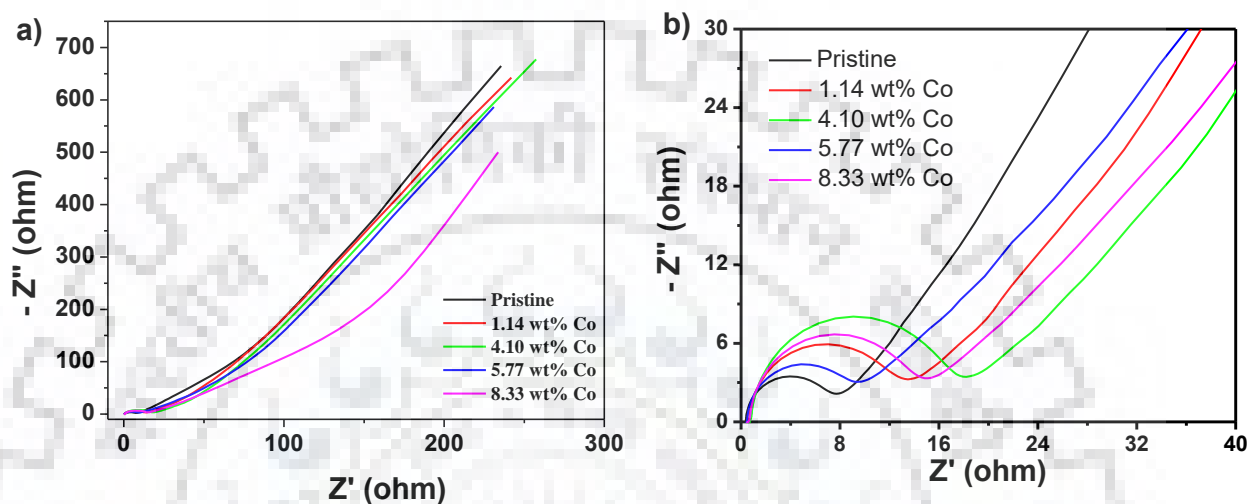


Fig. 5.9 (a) Electrochemical impedance spectroscopy of pristine and Co-doped CuO NPs, (b) represent the zoom EIS of all the batches of CuO NPs in higher frequency range.

From these studies we would understand several important electrochemical events, e.g., reveals about charge transfer, electrolyte ions interaction with pores of material, electrolyte/electrode interface resistance, electrolyte ions diffusion resistance in the pores of the electrode and specific capacitance of the active material at particular frequency [268]. The EIS response of all the Co-doped CuO NPs and pristine CuO NPs were typical for a supercapacitor material which can be categorized into three regions, e.g., high frequency, mid frequency and low frequency. The high and mid frequency regions for each batch of CuO NPs are given in the insert of the respective EIS plots. Notably, the high frequency region revealed typical semi-circular trend which reflected charge transfer resistances in the CuO NPs as electrode material, while the mid frequency region corresponded to diffusion of charge in the pores of electrodes. The radius of curvature of pristine and 5.77 wt% Co-doped CuO NPs were much lesser than those of other batches of Co-doped CuO NPs. This is due to the nature of defects present in the respective CuO NPs. However, all the batches of CuO NPs revealed shift in the centre of semi

circle with respect to the Z' axis. This is attributed to deviation from an ideal Debye's model, which is based on single relaxation time. The non-Debye type relaxation are said to obey Cole-Cole's formation given as [276]

$$Z^*(\omega) = Z' + iZ'' = R/[1+(i\omega/\omega_0)^{1-n}] \quad (5.4)$$

$\omega_0 = \omega_{\max}$ in the peak relaxation frequency

When n tends to zero, the above equation corresponded to Classical Debye formation. The value of 'n' is an indication of the extent of departure from the ideal condition. The non-ideal condition is mainly governed by grain size, grain distribution and grain boundary effect. In our studies the deviation of the centre of the semi circle from the Z' axis can therefore be attributed to non ideal system due to alteration of structural properties of CuO NPs due to cobalt doping. The batches of 1.14 wt%, 4.10 wt% and 8.33 wt% Co-doped CuO NPs revealed depressed semi-circle (i.e., their centre lies away from Z') which is due to multiple relaxation time. The larger average relaxation time for these batches of Co-doped CuO NPs is not suitable for charging-discharging process. This is confirmed from the GCD studies (Fig. 5.8). Further, equivalent series resistance (ESR) values were obtained from the semi-circle region. Among all the Co-doped CuO NPs the ESR was minimum for the batch of 5.77 wt% Co-doped CuO NPs (0.47 ohm) which was nearly similar to the pristine CuO NPs. Interestingly both of these batches revealed lesser extent of non-ideal system and hence they are better promising supercapacitor material.

The mid frequency region were more or less similar for all the batches except that of 8.33 wt% Co-doped CuO NPs. This frequency region is attributed to diffusion of electrolyte ions in the electrode material. This can be attributed to higher surface defects in the material as revealed from the PL studies. Since the specific capacitance of 8.33 wt% Co-doped CuO NPs was poor among the batch studied here so further analysis of this batch was not considered here.

The low frequency studies revealed a typical straight vertical line with almost similar slope. This region is associated with the grain boundary of the electrode material and relaxation phenomenon at the interface. So it is evident that the grain boundaries of all the Co-doped CuO NPs were more or less similar; except the batch consisting of very high cobalt concentration

(i.e., 8.33 wt%). Further specific capacitance can be estimated from the low frequency plot, which is inversely proportional to the imaginary part of the impedance (Z''), frequency (f) and active mass of the material (m). It is given as:

$$C_s = 1/(2\pi f Z'' m) \quad (5.5)$$

The vertical component corresponding to Z'' was found to be minimum for the batch of 5.77 wt% Co-doped CuO NPs. So it may be remarked the EIS studies also confirmed that specific capacitance was maximum for the batch of 5.77 wt% Co-doped CuO NPs.

5.3.5.5 Cyclic stability

The batch of 5.77 wt% Co-doped CuO NPs showing the best supercapacitance behavior was subjected to cyclic stability measurement. The cyclic stability was performed by charging-discharging the chosen CuO NPs for 500 cycles at current density of 1 A/g. The results were compared with pristine CuO NPs (Fig. 5.10). The capacitance retention of pristine and 5.77 wt% Co-doped CuO NPs increased during starting first few cycles. This is attributable to the initial activation of period within which pores get progressively wet and hence favoured the electrolyte ion interaction. After 50 cycles, that capacitance retention started to decrease due to degradation and deterioration of pores owing to repeated electrolyte ions interaction. At the end of 500 cycles, the capacitance retention of pristine and 5.77 wt% Co-doped CuO NPs were found to be 85% and 50%, respectively. The decrease in capacitance retention was faster in the batch of 5.77 wt% Co-doped CuO NPs, which can be attributed to presence of weak pore structures due to doping.

The Nyquist plots for batch before and after the end of 500 cycles of charging-discharging measurement are provided as in set of respective figures. It is observed that after 500 cycles the slope of the both samples decreased. This is attributable to lower interaction of electrolyte ions with active materials due to degradation and deterioration of pores. This implies that the specific capacitance decreased with increase the number of charging-discharging cycles, resulted for the lowering the capacitance retention. Apart from quasi rectangular shaped CV curve and triangular shaped GCD curve, it is necessary to achieve capacitance retention of the order of 95%-100%, in order to qualify for device applications.

Though the CV and GCD curves of Co-doped CuO NPs were favorable as supercapacitor materials but their capacitance retention was poor. This could be due to unstable pores in the material as the nanoparticles were prepared by co-precipitation method and stabilized by TPPO capping agent. So it was decided to stabilize the pores (if possible) by calcining the pristine and 5.77 wt% Co-doped CuO NPs for improving their supercapacitor behavior. In order to test these samples, further we tested their electrochemical properties by same steps i.e., by CV, GCD and EIS measurements. Henceforth, batch 5.77 wt% Co-doped CuO NPs will be referred to as Co-doped CuO NPs.

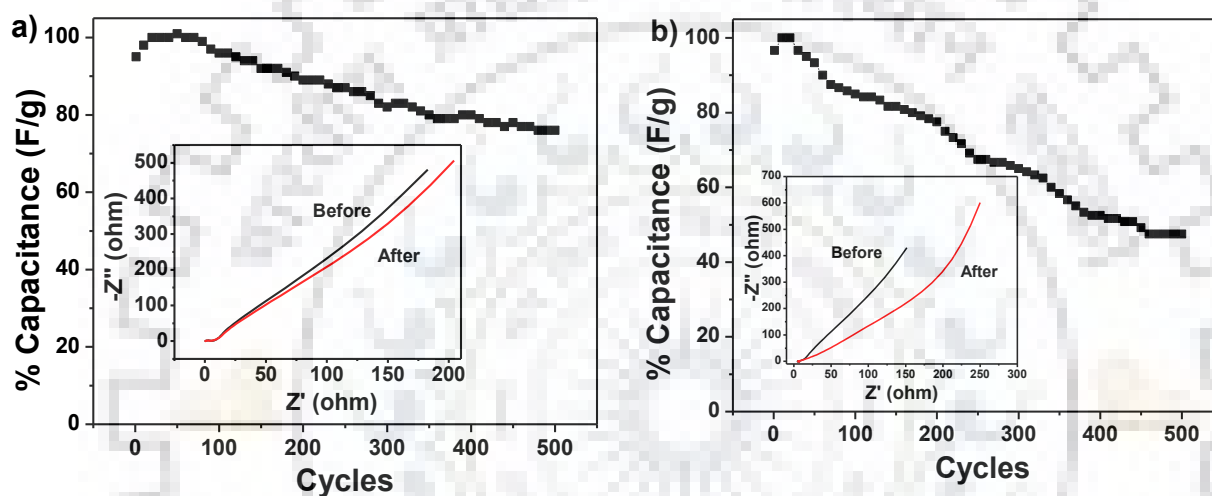


Fig. 5.10 Capacitance retention of (a) pristine and (b) Co-doped CuO NPs; Inset shows EIS plot of samples before and after the 500 cycles at current density 1 A/g.

5.4 Characterization of calcined Co-doped CuO NPs

5.4.1 XRD studies

The pristine and the batch of 5.77 wt% Co-doped CuO NPs were calcined at 450 °C. Their XRD patterns reflected increase in the peak intensities and narrowing of the peaks (Fig. 5.11). From Debye Scherrer equation, the crystallite sizes of the calcined batches were found to be larger than the un-calcined counterparts (Fig. 5.11). This is due to merging of grains during calcinations.

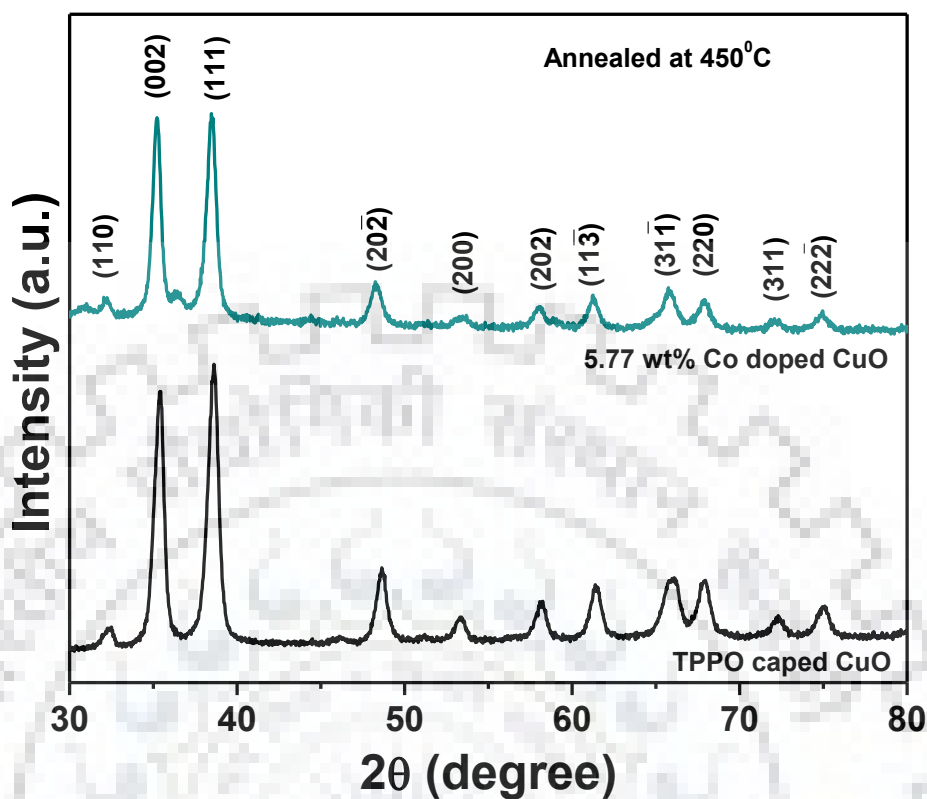


Fig. 5.11 XRD pattern corresponding to the monoclinic structure of calcined pristine and calcined Co doped CuO NPs.

5.4.2 Surface morphology

The morphology of pristine and the batch of 5.77 wt% Co-doped CuO NPs after calcination was studied with FE-SEM (Fig. 5.12). The observed FE-SEM images of these sample revealed agglomeration of nanoparticles. The EDAX spectrum revealed the presence of Cu, Co and O.

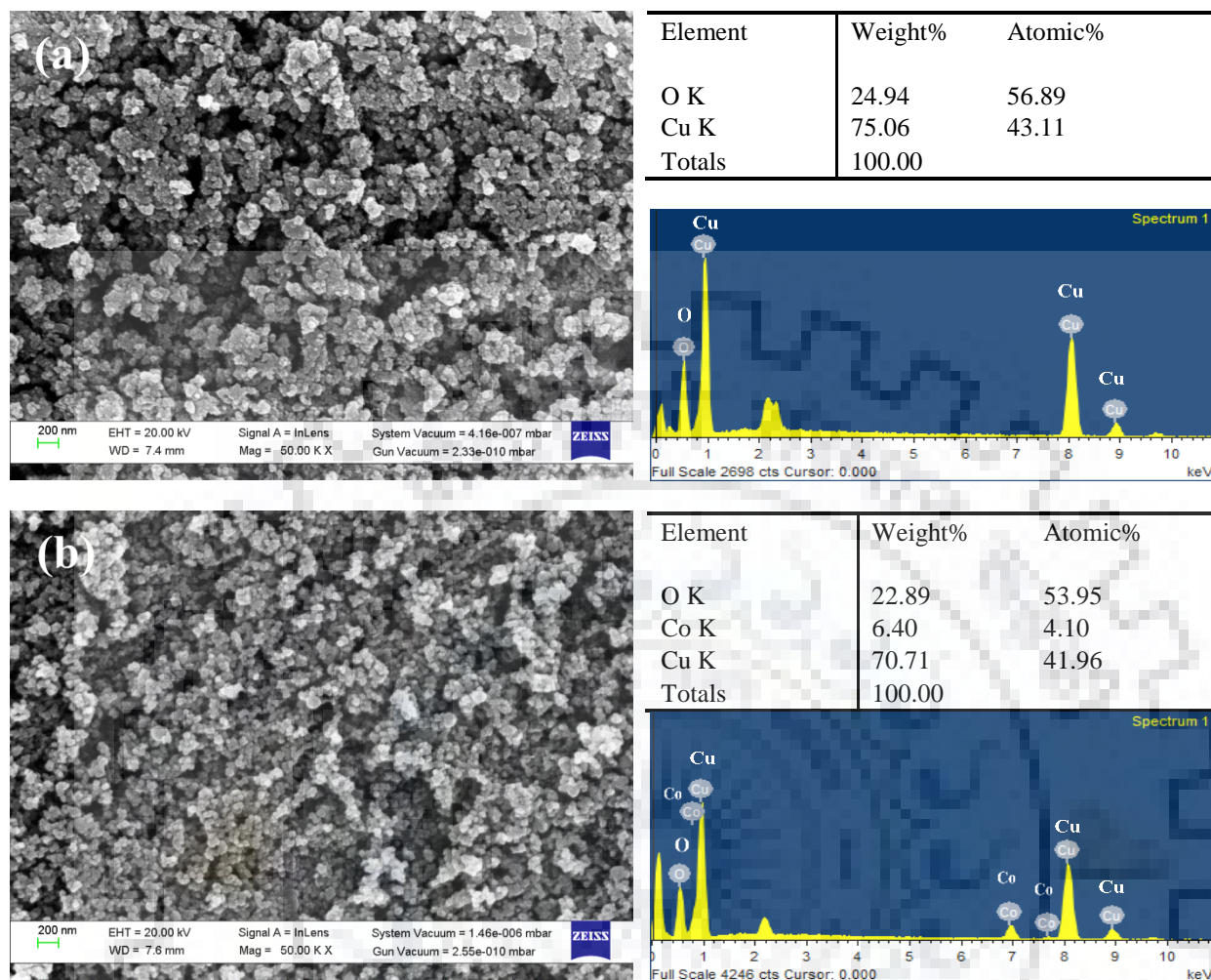


Fig. 5.12 Field Emission Scanning Electron Microscopy images of (a) calcined pristine, (b) calcined 5.77 wt% Co doped CuO NPs. Their corresponding energy dispersive X-ray analysis spectrum of respective batches of nanoparticles are given adjacent to FE-SEM images, which revealed characteristic K and L X-rays and atomic% of Cu, Co and O.

5.4.3 Electrochemical study of calcined Co-doped CuO NPs

5.4.3.1 Cyclic voltammetry studies

The cyclic voltammetry (CV) studies of pristine and Co-doped CuO NPs after calcination recorded at different scan rates ranging between 5 mV/s to 50 mV/s are given in Fig. 5.13 a, b. The CV curves were similar to the uncalcined batches of CuO NPs. As expected these CV plots revealed quasi rectangular shape with increase in scan rate, the slope of the CV did not change. However, area under the curve increased with scan rate, which is a

characteristic feature of a supercapacitor material. The specific capacitance of calcined pristine and calcined Co-doped CuO NPs determined as 90 F/g and 95 F/g, respectively at scan rate of 5 mV/s were however less than those of their uncalcined counterparts under similar measurement conditions. The decrease in the specific capacitance is attributable to increase in particle size. This was confirmed from the XRD measurements of calcined samples (Fig. 5.12).

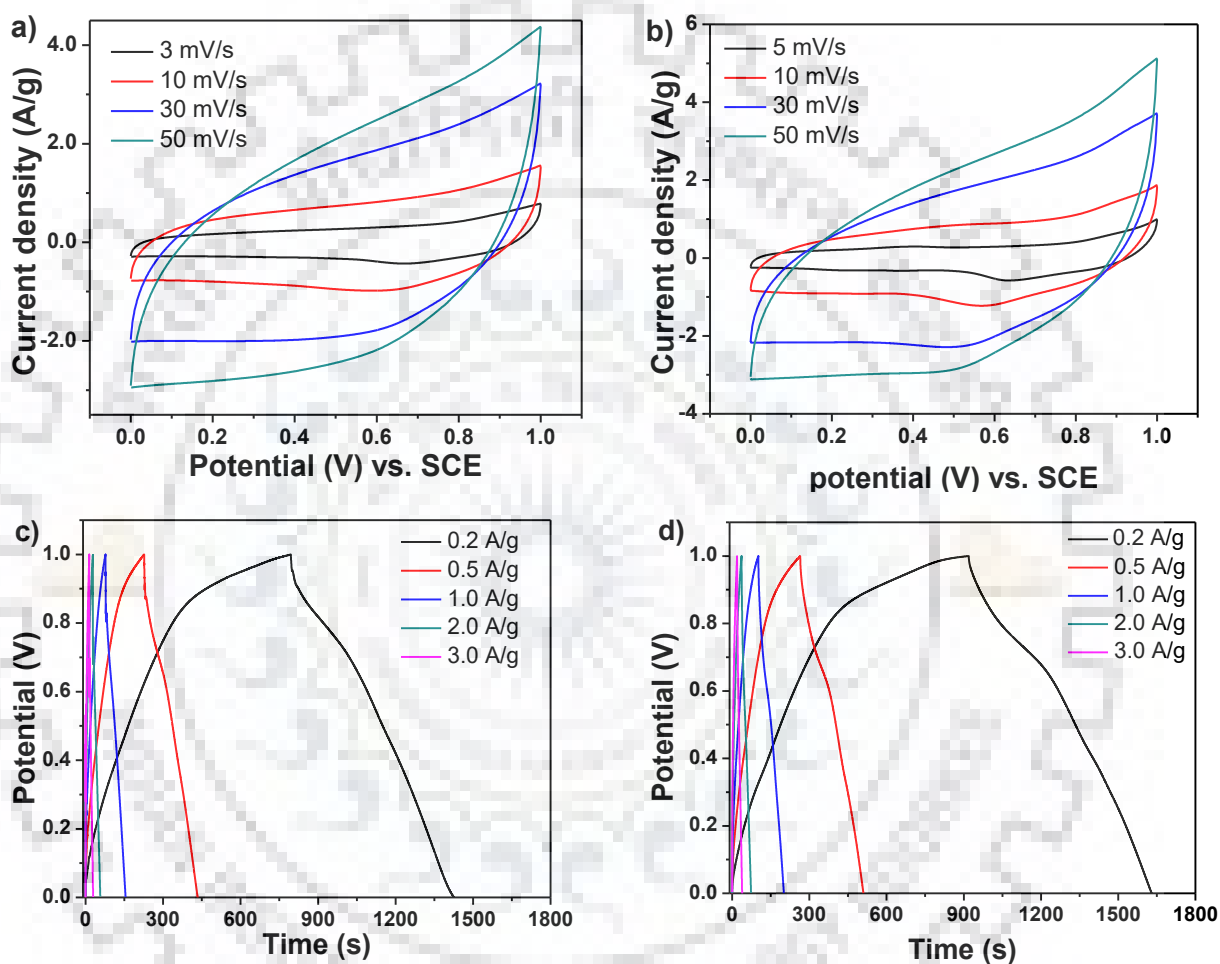


Fig. 5.13 Cyclic voltammograms of (a) calcined pristine (b) calcined 5.77 wt% Co-doped CuO NPs; Galvanostatic charge-discharge curves of (c) calcined pristine and (d) calcined 5.77 wt% Co-doped CuO NPs

5.4.3.2 Galvanostatic charge-discharge studies

The charge-discharge studies of calcined pristine and calcined Co-doped CuO NPs recorded at different current densities i.e., 0.2 A/g, 0.5 A/g, 1.0 A/g, 2 A/g and 3 A/g are given

in Fig. 4.13 c, d. As expected the galvanostatic charge-discharge curves revealed triangular shaped plots. The charging-discharging time decrease with increase in current density. The specific capacitances of these calcined samples were calculated using the equation number 3.1 (Chapter 3). The specific capacitance of calcined pristine and calcined Co dope CuO NPs 126 F/g and 140 F/g, respectively at current density of 0.2 A/g. Notably these specific capacitance were also lesser than the uncalcined counterparts measured at 0.2 A/g current density. The observed decrease in the specific capacitance is also attributable to increase in crystallite size or grain size due to calcinations.

5.4.3.3 Cyclic stability

The cyclic stability of calcined pristine and calcined Co-doped CuO NPs were studied for 500 cycles of charge-discharge at current density of 1 A/g (Fig. 5.14). After 500 cycles, the capacitance retention of calcined pristine and calcined Co-doped CuO NPs were measured to be 96% and 92%, respectively. As expected the stability of the electrode materials made of pristine and Co-doped CuO NPs were significantly increased. We have to also keep in mind that the stability tests were done at much higher current density (1 A/g) which testifies that the pores in the electrode after calcinations were stable as compared to the uncalcined samples. The EIS plots of these calcined samples before and after 500 cycles are given in the inset of Fig. 5.14. Notably, the EIS plots were similar for high and mid frequency region. Only at low frequency regions the slope was less for the sample after 500 cycles. This is attributed to lower interaction of electrolyte ions with the electrode material pores as pores get deteriorated with increase in charging-discharging cycles.

It may be summarized that upon calcination, the specific capacitance is decreased by nearly 20% but the most important feature was improvement of capacitance retention from 50% to 92% after 500 cycles of charging-discharging. Therefore, CuO NPs doped with cobalt followed by calcination at 450 °C resulted in development of stable supercapacitors.

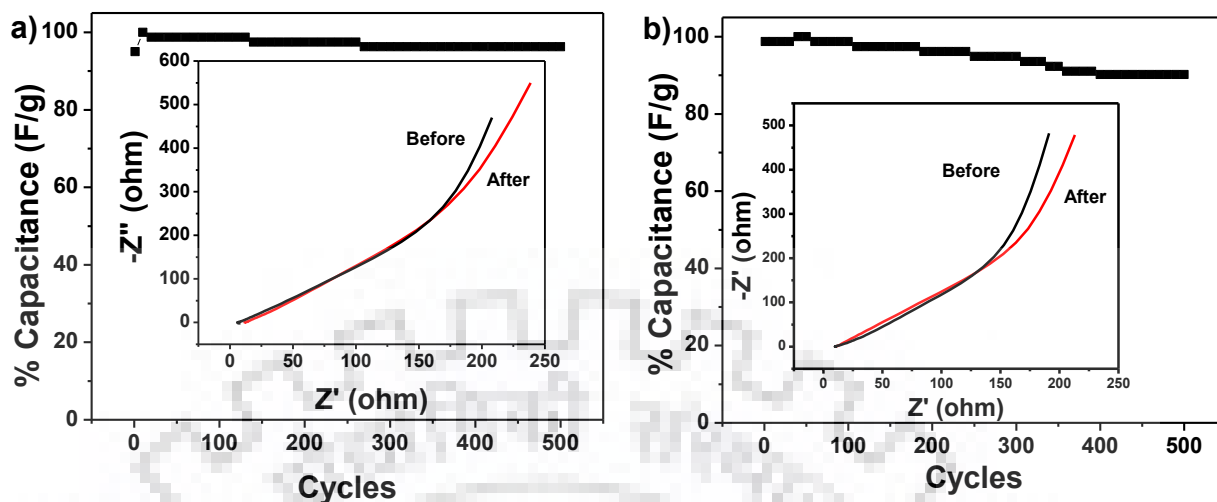


Fig. 5.14 Capacitance retention of (a) calcined pristine and (b) calcined Co-doped CuO NPs, inset showing EIS plot of samples before and after 500 cycles at current density of 1 A/g.

5.5 Symmetric solid state supercapacitor

Supercapacitors i.e., EDLC and PC can provide higher power density than batteries due to their charge storage process on the surface of the material without ion diffusion inside the material. But the restriction of charge storage on the surface makes supercapacitor weak in terms of energy density as compared to batteries. The energy (E) of the supercapacitor depends on the specific capacitance (C) and cell voltage (V), as given in expression:

$$E = (CV^2)/2 \quad (5.6)$$

So, the energy of a supercapacitor can be increased by two ways, e.g., (1) increase the specific capacitance by modifying surface of the material, (2) increase the working cell voltage of the material by using the different working potential of materials.

The cell voltage can be increased by fabricating symmetric, asymmetric or hybrid supercapacitors. Here we have fabricated symmetric supercapacitor of Co-doped CuO NPs. The detailed of fabrication process is discussed in material and methods (section 5.2.4). The photograph of fabricated solid state supercapacitor is given in Fig. 5.15. Their electrochemical behavior was studied from CV and GCD measurements.



Fig. 5.15 Photograph of symmetric solid state supercapacitor made of 5.77 wt% Co-doped CuO NPs.

5.5.1 Cyclic voltammetry

The CV studies of the fabricated symmetric supercapacitor were carried out at different potential window range. The CV curve of the fabricated cell was recorded at different scan rates e.g., 5 mV/s, 10 mV/s, 20 mV/s, 30 mV/s, 40 mV/s and 50 mV/s at working potential window 0–1.0 V (Fig. 5.16). The area and slope of the quasi rectangular shaped CV curve increased with increase in scan rate. This is attributed to reversible and faster interaction of ions with the pores of the materials. This signified functioning of the fabricated cell as a good supercapacitor within the potential window of 0-1.0 V. Next the CV plot was recorded at a fixed arbitrary scan rate of 20 mV/s over potential window range of 0-3.5 V (Fig. 5.17). With increase in voltage the measured current drastically increased specially for potential greater than 2.5 V. This is most likely to be due to oxygen evolution phenomenon. A careful observation of the CV plot up to 2.4 V revealed that there was not drastic increase in the oxidation current up to 2.0 V (Fig. 5.18). However reduction peaks were observed for the measurements recorded at 1.25 V onwards. So our fabricated symmetric supercapacitor can work up to 2.0 V.

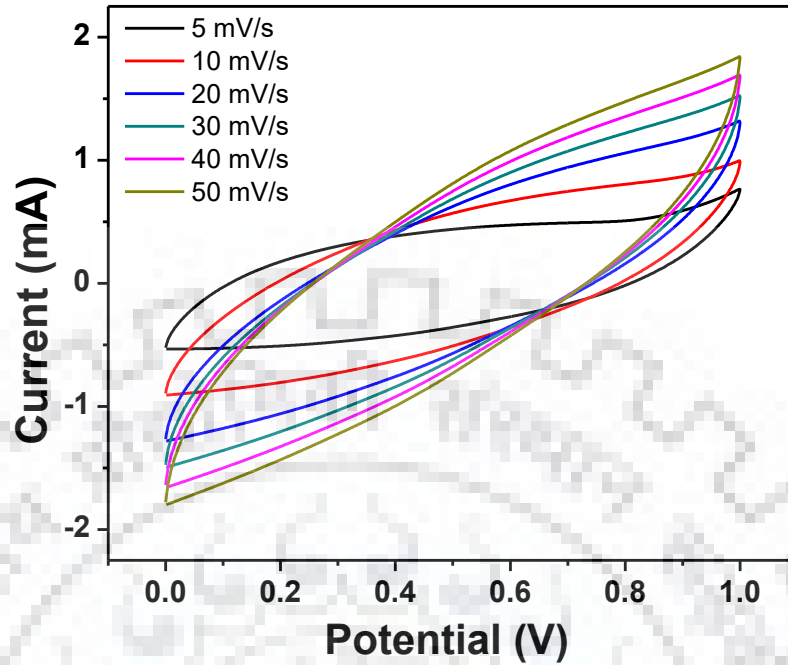


Fig. 5.16 CV curve of symmetric solid state supercapacitor at different scan rate in the cell voltage range 0 to 1.0 V

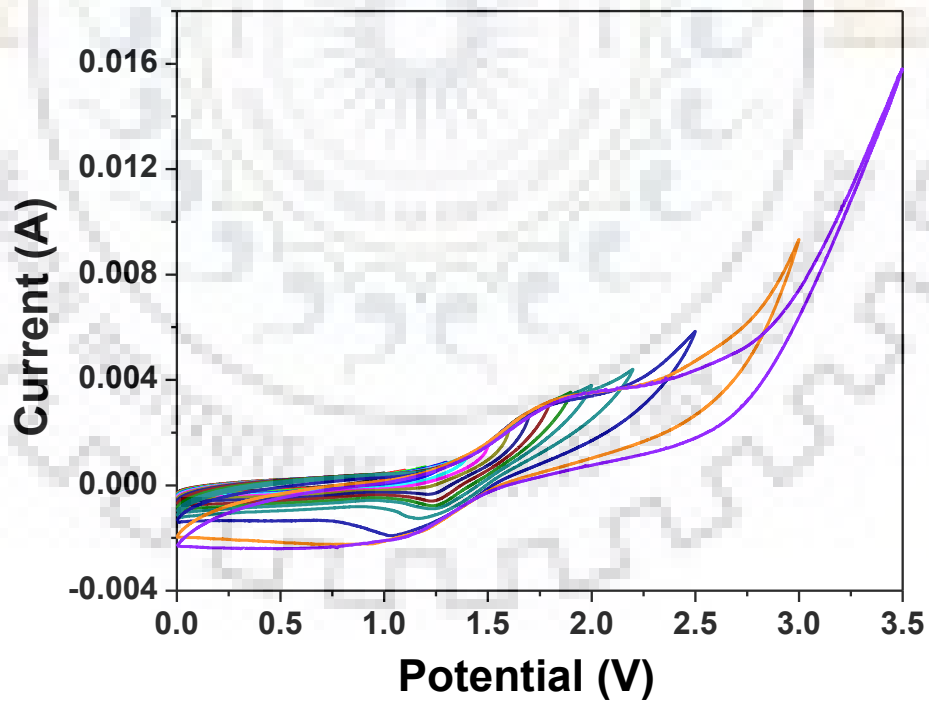


Fig. 5.17 CV curves of symmetric solid state supercapacitor at a fixed scan rate of 20 mV/s in different cell voltage range of 0 to 3.5 V

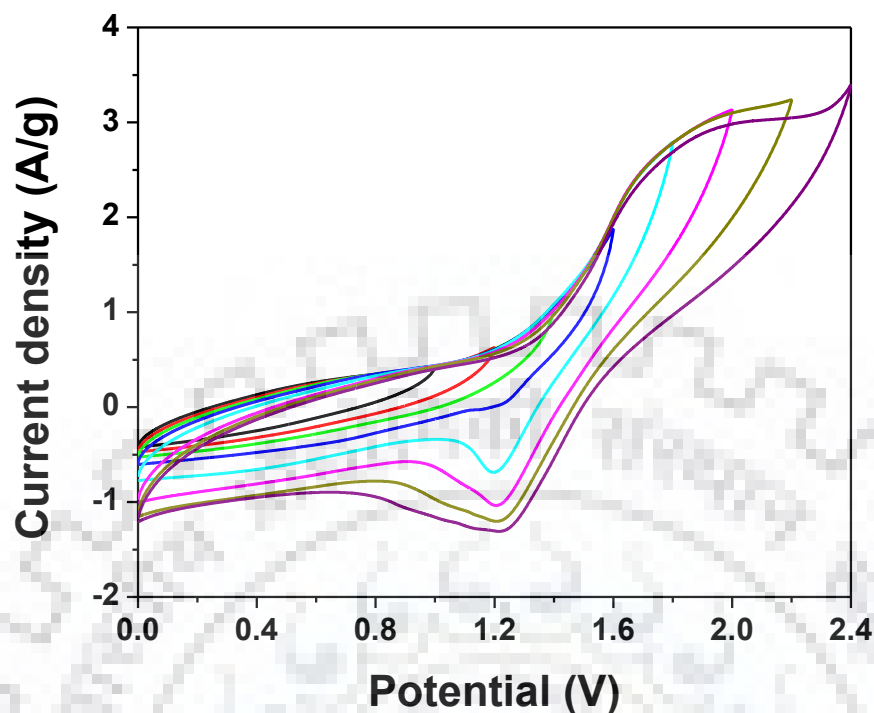


Fig. 5.18 CV curves of symmetric solid state supercapacitor at 20 mV/s scan rate in the different cell voltage range of 0 to 2.4 V

5.5.2 Charge-discharge study

Now, the GCD of the fabricated supercapacitor was studied in the potential window range of 0 to 2.0 V at current density of 0.2 A/g (Fig. 5.19). The charging was sharp during the first 5 second to reach 1.0 V followed by slow gradient charging to 2.0 V. The discharging was also fast from 2.0 V to 1.0 V followed by a gradually decreasing discharging to 0 V. This is due to faster intercalation and deintercalation of charges in the pores of the materials. The total capacitance was calculated using the given formula:

$$C_t = \frac{I\Delta t}{m\Delta V} \quad (5.7)$$

where, I , Δt , m and ΔV represents the current (A), total discharge time (s), the active mass of the materials (g) and working cell voltage (V), respectively. The calculated total capacitance of our fabricated supercapacitor was 2.6 F/g which is same as specific capacitance.

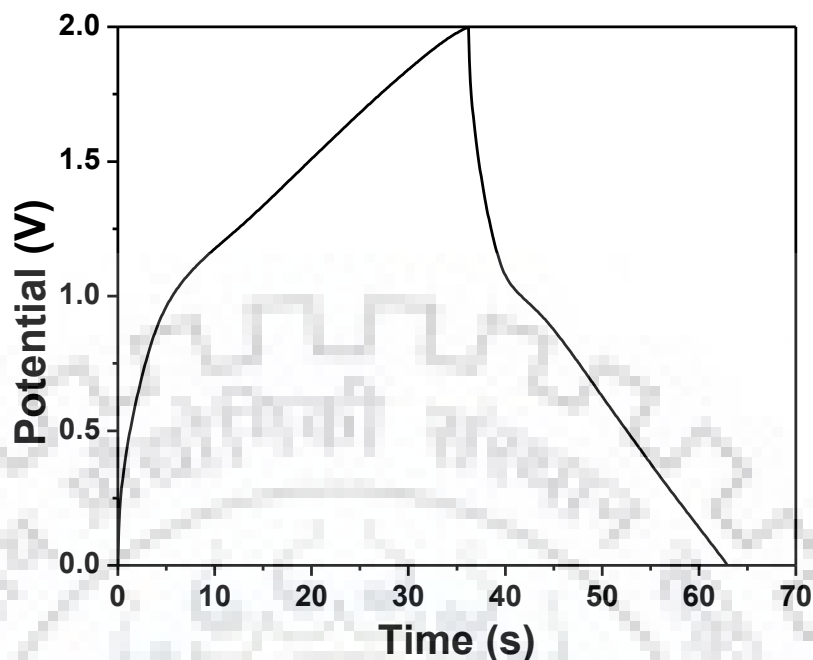


Fig. 5.19 Galvanostatic charge-discharge curve of symmetric solid state supercapacitor at 0.2 A/g current density in the cell voltage range of 0 to 2.0 V.

The energy density and power density were calculated by following formula:

$$E = C\Delta V^2/2 \quad (5.8)$$

$$P = 3600E/\Delta t \quad (5.9)$$

So, the energy density of fabricated supercapacitor was 5.2 Wh/kg, and the power density was 720 W/kg. It may be revealed that this energy density of our fabricated cell can be increased. If we made a hybrid supercapacitor in which one electrode is of PC nature and other is of EDLC nature.

5.6 Conclusion

In this Chapter we have discussed we have discussed successfully methodology for developing cobalt doped CuO NPs as supercapacitor. Batches with different concentration of cobalt dopant are synthesized by chemical precipitation method. The batch comprising of 5.77 wt% Co in the doped CuO NPs was needle shaped and was found to exhibit maximum capacitance. This has been attributed to minimum vacancy related defects in the doped CuO NPs as reflected from photoluminescence spectra. Surface area of the doped CuO NPs was not very important feature for enhanced the specific capacitance. The CV and EIS studies

suggested pseudocapacitance contribution as the most important one to account for the observed specific capacitance. The cyclic stability was however poor for 5.77 wt% Co-doped CuO NPs. Because of this, the Co-doped NPs were calcined to stabilize the pores. These led to about 20% decrease in the specific capacitance but the cyclic stability improved as revealed from more than 90% capacitance retention after 500 cycles of charging-discharging processes. Further, the batch of 5.77 wt% Co-doped CuO NPs was chosen for fabricating symmetric solid state supercapacitor and its specific capacitance and energy density was determined. Enough scope does exist to improve these two specifications to translate Co-doped CuO NPs as a energy storage devices.





Summary and Future Scope

Summary

The worldwide demand for energy has led to development of energy storage materials. In this regard, supercapacitors have emerged as an excellent option which led to development wide range of materials for optimum charge storage. Surface area, morphology, porous nature and conductivity are some of the critical features to be met for qualifying as a good supercapacitor. Literature survey suggested CuO as poorly studied material as supercapacitor, in spite of low cost, high conductivity, large abundance and high theoretical specific capacitance (higher than MnO₂ and RuO₂, which are widely studied). This thesis work was therefore designed aimed at investigating different options for improving CuO nanoparticles as supercapacitors. For this purpose, CuO nanoparticles were subjected to physical and chemical modification.

The physical modification was done implanting with low energy (50 keV) N⁵⁺ ion beam on CuO thin film prepared by pulsed laser deposition (PLD). Different phases of copper oxide with varying crystalline or amorphous nature were formed on glass substrate owing to different partial pressure of oxygen gas. For example, the batch prepared with 80 mTorr oxygen pressure did not produce any crystalline copper oxide phase, but Cu₂O phase was formed after implantation with N⁵⁺ of particle fluence = 1.0×10^{16} particles/cm². Whereas, the copper oxide thin film prepared at 100 mTorr oxygen partial pressure resulted in formation of mixed phase of copper oxide, which was transformed to a single phase of Cu₂O after implanting with 2.5×10^{15} particles/cm². However, CuO phase was formed after implanting with 1.0×10^{16} particles/cm². These ion implanted CuO/Cu₂O thin film revealed increase in electrical conductivity as function of implanted particle fluence. However, their supercapacitor behavior was not investigated.

Further CuO nanoparticles modification studies were conducted by chemical route. In this regard, two approaches were used: (a) modification by capping agents; and (b) modification by doping with p and d block elements. In both the cases CuO host nanoparticles were synthesized by simple chemical precipitation method. Five different capping agents, e.g., triphenylphosphine oxide (TPPO), mercaptoacetic acid (MAA), triton X-100, polyvinylpyrrolidone (PVP) and polyvinyl alcohol (PVA) were used to synthesize five batches of differently capped CuO nanoparticles. These batches of as synthesized nanoparticles were

characterized by X-ray diffraction, field emission scanning electron microscope, transmission electron microscope, BET surface area, diffused reflectance spectroscopy, photoluminescence spectroscopy. The MAA and PVP capped CuO nanoparticles comprised of more copper/oxygen vacancy defects as compared to other capped CuO nanoparticles. All the batches of capped CuO nanoparticles were investigated for supercapacitor behavior and were compared with pristine CuO NPs which was prepared by the same precipitation method but without any modification. The cyclic voltammetry (CV) studies revealed typical quasi-rectangular shaped curve with varying specific capacitances. Among these batches, the mercaptoacetic acid (MAA) capped and triphenyl phosphine oxide (TPPO) capped CuO nanoparticles exhibited higher specific capacitance recorded at 0.2 A/g current density. The TPPO capped CuO nanoparticles comprised of minimum defects as revealed from photoluminescence spectra. So higher specific capacitance for TPPO capped CuO NPs was due to minimal loss of charges in the “less defect” CuO NPs. On the other hand, the MAA capped CuO was associated with certain order of vacancy based defects. In spite of this higher specific capacitance for MAA capped CuO NPs is attributable to favorable defects. This can be due to oxygen vacancies which favored the transportation of charges as compared to metal vacancy defects in other PVP, TRX and PVA capped CuO NPs. So the nature of defects is found to play an important role in the charge transport property and hence impacted supercapacitor behavior. The electrochemical impedance spectroscopy studies revealed the tentative mechanism for supercapacitor behavior of capped CuO NPs. It was found that the faradaic process due to redox reactions at the surface of the electrode made of TPPO capped CuO was improved and hence the supercapacitor behavior was mostly due to pseudocapacitance contribution.

Performance of a supercapacitor is a measure of retention of specific capacitance after several cycles of charging and discharging. The specific capacitance is primarily controlled by the stability of the pores and electrocatalytic activity at the surface of the electrode, so the charging discharging cycles could affect the specific capacitances. The retention capacitance for TPPO capped CuO NPs were poor (84%). In order to improve the retention capacitance, the as-synthesized batches of TPPO capped CuO NPs were calcined to 450 °C for 3 h. This led to increase in the crystallinity as revealed from the XRD studies and the pores were stable. This is reflected from drastic improvement of retention capacitance to 102% after 500 cycles of charging and discharging processes.

The EIS studies clearly revealed the pseudocapacitance contribution responsible for improved supercapacitor behavior of calcined batches of TPPO capped and MAA capped CuO NPs. Because of this, we extended our studies on calcined TPPO capped and calcine MAA capped CuO NPs for glucose sensing. Their limits of detection of glucose detection by electrocatalytic process were 0.04 μM and 0.33 μM , respectively. The linear detection ranges were 9 μM to 3.2 mM and 9 μM to 4.2 mM, respectively. The electrodes made of calcined TPPO capped and calcined MAA capped CuO NPs were demonstrated for successful determination of glucose levels in human blood and urine samples.

Next, batches of chemically doped CuO NPs were synthesized for studying supercapacitor behavior. From literature, selenium (Se) doped in metal oxides revealed excellent applications, such as enhanced photocatalytic and catalytic activity. Though Se exists in different oxidation states but Se doped metal oxides have not been explored for electrochemical studies. Batches of CuO NP doped with different Se concentrations were synthesized by chemical precipitation method. They were thoroughly characterized and their electrochemical responses were studied from cyclic voltammetry (CV), galvanostatic charging-discharging (GCD) and electrochemical impedance spectroscopy (EIS). The CV measurement of the batches of Se-doped CuO NPs exhibited good supercapacitance behavior. The CV studies based charge storage calculations revealed that maximum specific capacitance of 144 F/g was recorded for an arbitrary 0.2 A/g current density for the batch of 0.45 wt% Se-doped CuO NPs. Notably, the specific capacitance of 0.45 wt% Se doped CuO NPs (capped with TPPO) was more than the batch of without doped TPPO capped CuO NPs. The ESR value and the slope of the impedance in the low frequency region revealed that 0.45 wt% Se-doped CuO NPs is more conducting than other batches CuO NPs. However, similar to the capped CuO NPs, the capacitance retention for 0.45 wt% Se-doped CuO NPs after 500 cycles of charging and discharging was poor. This is attributed to more degradation of pores in 0.45 wt% Se-doped CuO NPs samples during the cycles of charging and discharging. In order to improve the retention capacitance, the batch of 0.45 wt% Se doped CuO NPs was calcined at 450 $^{\circ}\text{C}$ for 3 h. The capacitance retention after 500 cycles of charging and discharging was improved to 96%, which happened to one of the highest retention capacitance for CuO NPs as supercapacitor.

The calcined batches of 0.45 wt% Se-doped CuO NPs and the pristine CuO NPs were chosen for the investigating higher cell temperature supercapacitor behavior over a temperature

range of 25 °C to 75 °C. These samples revealed increase in specific capacitance as a function of cell temperature. It is attributed to reduce kinetic barrier for the redox reaction and enhance diffusivity of electrolyte ions. The improvement in the supercapacitor behavior was due to decrease in the pseudocapacitance contribution owing to redox reactions at the surface of the electrode. In other words, the EDLC contribution was enhanced due to opening of micro-pores at elevated temperatures which favored accumulation of charges in the pores of the calcined CuO NPs, and consequently the specific capacitance was increased. These observations reflected that doped CuO NPs can work in wider cell temperature range.

In another chemical modification study, we have chosen electroactive metal cobalt as a dopant to modify CuO NPs. Though the starting precursor concentration of cobalt was similar to that of selenium, but the actual cobalt dopant concentrations in the batches of doped CuO NPs were more than 10 times higher than those of Se doped ones. This can be attributed to favorable co-precipitation of Co in CuO NPs and also favorable diffusion of cobalt ions in CuO. This cobalt (Co) doped CuO NPs exhibited increase in crystallite size and band gap as a function of cobalt concentration. The batches of 1.14 wt% and 4.10 wt% Co-doped CuO NPs revealed more defects as compared to 5.77 wt% and 8.33 wt% Co-doped CuO NPs.

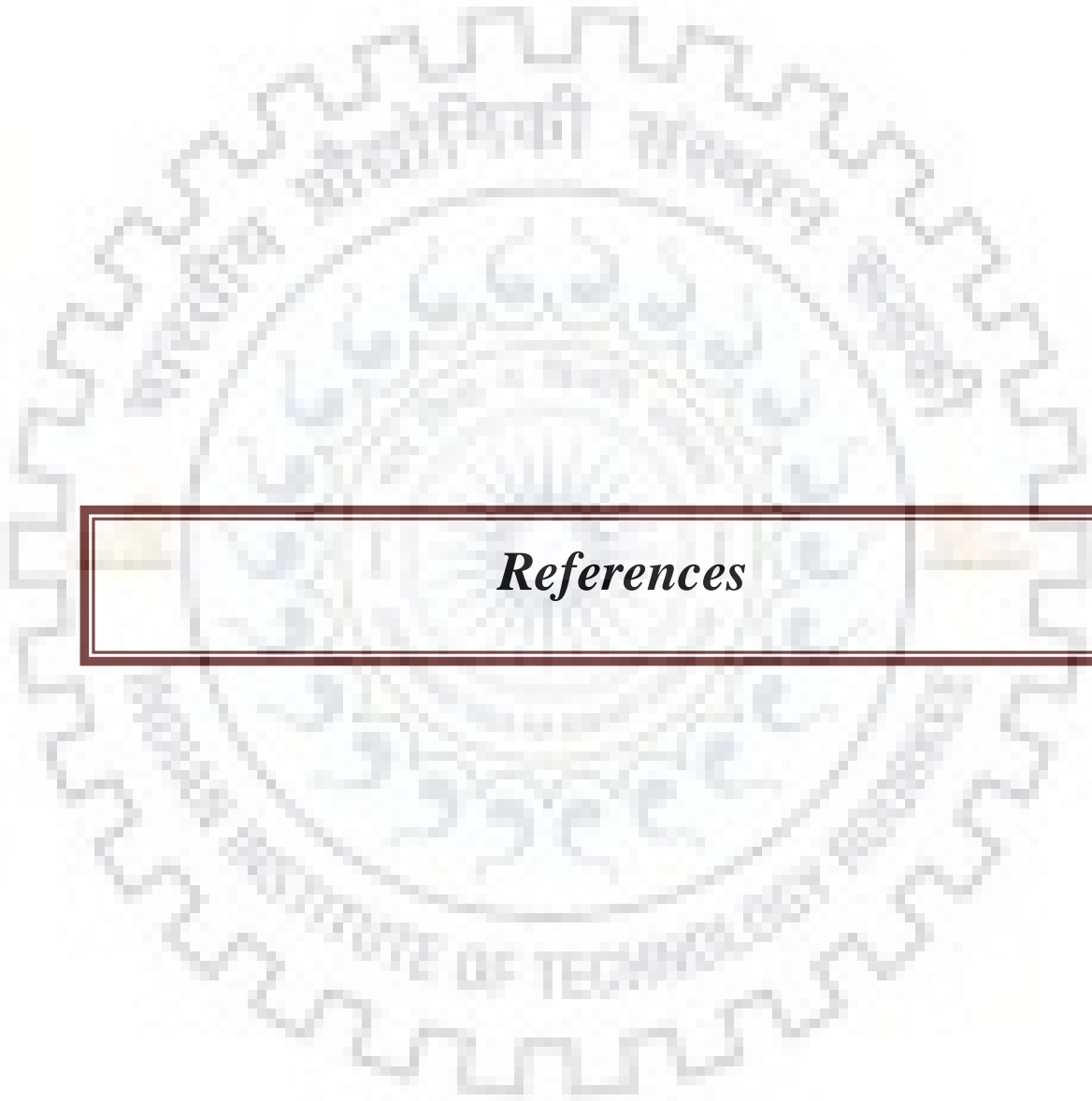
The CV measurements of all the batches of Co-doped CuO NPs revealed quasi-rectangular shaped curve and the maximum specific capacitance was determined as 160 F/g for 5.77 wt% Co doped CuO NPs recorded at an arbitrary current density of 0.2 A/g. The specific capacitance was 10% more than the optimized (0.45 wt%) Se doped CuO NPs. This could be due to better electrochemical properties of cobalt which is doped in CuO NPs. Similar to the capped and Se doped CuO NPs, the capacitance retention after 500 cycles of charging and discharging was poor. The retention capacitance was improved to 98% after calcinations of the 5.77 wt% Co-doped CuO NPs. In this case as well, the specific capacitance was mostly due to faradaic processes as evident from large pseudocapacitance contribution. The 5.77 wt% Co-doped CuO NPs was chosen for fabrication of symmetric solid state supercapacitor, which revealed 2.6 F/g specific capacitance and delivered maximum 1.4 Wh/Kg energy density in the potential window range 0 to 2.0 V.

Future Scopes

The specific capacitances derived from CuO NPs modified by capping and doping were much less than expected. This indicates that there is still enough room for investigating the strategies for achieving higher specific capacitance using CuO system. The major area to improve is enhancing EDLC character developing methods for porous CuO NPs. Further, the role of defects and its engineering in CuO has tremendous promise to impact on supercapacitor performance. However, the study on glucose sensing by surface modified CuO NPs is very encouraging. It can be explored for making electrochemical devices for sensing other environmental pollutants, like toxic gases, pesticides, etc.







References

References

- (1) Feynman, R.P. There's plenty of room at the bottom, an invitation to enter a new field of physics. *Eng. Sci.* **1960**, *23*, 22–36.
- (2) Taniguchi, N. On the basic concept of nanotechnology, *proceeding of the International Conference on production Engineering.* **1974**, 18-23.
- (3) Zhang, Q., Zhang, K., Xu, D., Yang, G., Huang, H., Nie, F., Liu, C., Yang, S. CuO nanostructures: synthesis, characterization, growth mechanisms, fundamental properties, and applications. *Prog. Mater. Sci.* **2014**, *60*, 208–337.
- (4) Korotcenkov, G. Gas Response control through structural and chemical modification of metal oxide films: state of the art and approaches. *Sensors Actuators B Chem.* **2005**, *107* (1), 209–232.
- (5) Wenderich, K., Mul, G. Methods, mechanism, and applications of photodeposition in photocatalysis: A Review. *Chem. Rev.* **2016**, *116* (23), 14587–14619.
- (6) Zhao, X., Sánchez, B.M., Dobson, P.J., Grant, P.S. The role of nanomaterials in redox-based supercapacitors for next generation energy storage devices. *Nanoscale* **2011**, *3* (3), 839.
- (7) Zhi, M., Xiang, C., Li, J., Li, M., Wu, N. Nanostructured carbon–metal oxide composite electrodes for supercapacitors: A review. *Nanoscale* **2013**, *5* (1), 72–88.
- (8) Arya, S.K., Wong, C.C., Jeon, Y.J., Bansal, T., Park, M.K. Advances in complementary-metal–oxide–semiconductor-based integrated biosensor arrays. *Chem. Rev.* **2015**, *115* (11), 5116–5158.
- (9) Wang, S., Wang, Z., Zha, Z. Metal nanoparticles or metal oxide nanoparticles, an efficient and promising family of novel heterogeneous catalysts in organic synthesis. *Dalt. Trans.* **2009**, *0* (43), 9363-9373.
- (10) Park, J.Y., Baker, L.R., Somorjai, G.A. Role of hot electrons and metal–oxide interfaces in surface chemistry and catalytic reactions. *Chem. Rev.* **2015**, *115* (8), 2781–2817.
- (11) Zhang, H., Chen, G., Bahnemann, D. Photoelectrocatalytic materials for environmental applications. *J. Mater. Chem.* **2009**, *19* (29), 5089-5121.
- (12) Sun, Y., Liu, S., Meng, F., Liu, J., Jin, Z., Kong, L. Metal oxide nanostructures and their gas sensing properties: A review. *Sensors* **2012**, *12* (3), 2610-2631.
- (13) Hajipour, M., Fromm, K., Ashkarran, A. Antibacterial properties of nanoparticles. *Trends Biotechnol.* **2012**, *10*, 499-511.
- (14) Poizot, P., Laruelle, S., Grugeon, S., Dupont, L. Nano-sized transition-metal oxides as negative-

- electrode materials for lithium-ion batteries. *Nature* **2000**, *407*, 496-499.
- (15) Jose, R., Thavasi, V. Metal oxides for dye sensitized solar cells. *J. Am.* **2009**, *92* (2), 289-301.
- (16) Martin, L., Chu, Y., Ramesh, R. Advances in the growth and characterization of magnetic, ferroelectric, and multiferroic oxide thin films. *Mater. Sci. Eng. R* **2010**, *68* (4-6), 89-133.
- (17) Rakhi, R., Chen, W., Cha, D., Alshareef, H. High performance supercapacitors using metal oxide anchored graphene nanosheet electrodes. *J. Mater.* **2011**, *21* (40), 16197-16204.
- (18) Jiang, J., Li, Y., Liu, J., Huang, X., Yuan, C. Recent advances in metal oxide based electrode architecture design for electrochemical energy storage. *Adv. Mater.* **2012**, *24* (38), 5166-5180.
- (19) Li, Y., Yang, X., Feng, Y., Yuan, Z. One-dimensional metal oxide nanotubes, nanowires, nanoribbons, and nanorods: synthesis, characterizations, properties and applications. *Crit. Rev. Solid* **2012**, *37* (1), 1-74.
- (20) Jun, Y., Choi, J., Cheon, J. Shape control of semiconductor and metal oxide nanocrystals through nonhydrolytic colloidal routes. *Angew. Chemie Int.* **2006**, *45* (21), 3414-3439.
- (21) Burda, C., Chen, X., Narayanan, R., El-Sayed, M.A. Chemistry and properties of nanocrystals of different shapes. *Chem. Rev.* **2005**, *105*, 1025-1102.
- (22) Patzke, G., Zhou, Y., Kontic, R. Oxide nanomaterials: synthetic developments, mechanistic studies, and technological innovations. *Angew. Chemie* **2011**, *50* (4), 826-859.
- (23) George, S., Pokhrel, S., Ji, Z., Henderson, B.L., Xia, T., Li, L., Zink, J.I., Nel, A.E., Madler, L. Role of Fe doping in tuning the band gap of TiO₂ for the photo-oxidation-induced cytotoxicity paradigm. *J. Am. Chem. Soc.* **2011**, *133* (29), 11270-11278.
- (24) Khairy, M., Zakaria, W. Effect of metal-doping of TiO₂ nanoparticles on their photocatalytic activities toward removal of organic dyes. *Egypt. J. Pet.* **2014**, *23* (4), 419-426.
- (25) Gusain, R., Kumar, P., Sharma, O.P., Jain, S.L., Khatri, O.P. Reduced graphene oxide-CuO nanocomposites for photocatalytic conversion of CO₂ into methanol under visible light irradiation. *Appl. Catal. B Environ.* **2016**, *181*, 352-362.
- (26) Saravanan, R., Karthikeyan, S., Gupta, V.K., Sekaran, G., Narayanan, V., Stephen, A. Enhanced photocatalytic activity of ZnO/CuO nanocomposite for the degradation of textile dye on visible light illumination. *Mater. Sci. Eng. C* **2013**, *33* (1), 91-98.
- (27) Li, B., Wang, Y. Facile synthesis and photocatalytic activity of ZnO-CuO nanocomposite. *Superlattices Microstruct.* **2010**, *47* (5), 615-623.

- (28) Sharma, A., Dutta, R.K. Se-doped CuO NPs/H₂O₂/UV as a highly efficient and sustainable photo-fenton catalytic system for enhanced degradation of 4-bromophenol. *J. Clean. Prod.* **2018**, *185*, 464–475.
- (29) Yu, K.M., Walukiewicz, W., Wu, J., Beeman, J.W., Ager III, J.W., Haller, E.E., Shan, W., Xin, H.P., Tu, C.W., Ridgway, M.C. Formation of diluted III – V nitride thin films by N ion implantation. *J. Appl. Phys.* **2001**, *90*, 2227.
- (30) Myers, M.A., Myers, M.T., General, M.J., Lee, J.H., Shao, L., Wang, H. p-type ZnO thin films achieved by N⁺ ion implantation through dynamic annealing process. *J. Appl. Phys* **2013**, *101*, 112101.
- (31) Chandramohan, S., Kanjilal, A., Sarangi, S.N., Majumder, S., Sathyamoorthy, R., Som, T. Implantation-assisted Co-doped CdS thin films: structural, optical, and vibrational properties. *J. Appl. Phys.* **2009**, *106* (6), 063506.
- (32) Stepanov, A.L., Galyautdinov, Evlyukhin, A.B., Nuzhdin, V.I., Valeev, V.F., Osin, Y.N., Evlyukhin, E.A., Kiyan, R., Kavetsky, T.S., Chichkov, B.N. Synthesis of periodic plasmonic microstructures with copper nanoparticles in silica glass by low-energy ion implantation. *Appl. Phys. A* **2013**, *111* (1), 261–264.
- (33) Watt, F., Bettioli, A.A., Van Kan, J.A., Teo, E.J., Breese, M.B.H. Ion beam lithography and nanofabrication: A review. *Int. J. Nanosci.* **2005**, *04* (03), 269–286.
- (34) Bettioli, A.A., Sum, T.C., van Kan, J.A., Watt, F. Fabrication of micro-optical components in polymer using proton beam micro-machining and modification. *Nucl. Instruments Methods Phys. Res. Sect. B Beam Interact. with Mater. Atoms* **2003**, *210*, 250–255.
- (35) Van Kan, J.A., Rajta, I., Ansari, K., Bettioli, A.A., Watt, F. Nickel and copper electroplating of proton beam micromachined SU-8 resist. *Microsyst. Technol.* **2002**, *8* (6), 383–386.
- (36) Bettioli, A.A., Jamieson, D.N., Prawer, S., Allen, M.G. Ion beam induced luminescence from diamond and other crystals from a nuclear microbeam. *Nucl. Instruments Methods Phys. Res. Sect. B Beam Interact. with Mater. Atoms* **1994**, *85* (1–4), 775–779.
- (37) Chandramohan, S., Kanjilal, A., Tripathi, J.K., Sarangi, S.N., Sathyamoorthy, R., Som, T. Structural and optical properties of Mn-doped CdS thin films prepared by ion implantation. *J. Appl. Phys.* **2009**, *105* (12), 123507.
- (38) Chandramohan, S., Kanjilal, A., Strache, T., Tripathi, J.K., Sarangi, S.N., Sathyamoorthy, R.,

- Som, T. Modifications in structural and optical properties of Mn-ion implanted CdS thin films. *Appl. Surf. Sci.* **2009**, 256 (2), 465–468.
- (39) Chandramohan, S., Kanjilal, A., Sarangi, S.N., Majumder, S., Sathyamoorthy, R., Som, T. Effect of Fe-ion implantation doping on structural and optical properties of CdS thin films. *Appl. Phys. A* **2010**, 99 (4), 837–842.
- (40) Liu, K., Pun, E.Y.B., Sum, T.C., Bettiol, A.A., van Kan, J.A., Watt, F. Erbium-doped waveguide amplifiers fabricated using focused proton beam writing. *Appl. Phys. Lett.* **2004**, 84 (5), 684–686.
- (41) Sum, T.C., Bettiol, A.A., Liu, K., Ren, M.Q., Pun, E.Y.B., Venugopal Rao, S., van Kan, J. A., Watt, F. Proton beam writing of erbium-doped waveguide amplifiers. *Nucl. Instruments Methods Phys. Res. Sect. B Beam Interact. with Mater. Atoms* **2005**, 231 (1–4), 394–399.
- (42) El-Atwani, O., Gonderman, S., Suslov, S., Efe, M., De Temmerman, G., Morgan, T., Bystrov, K., Hattar, K., Allain, J.P. Early stage damage of ultrafine-grained tungsten materials exposed to low energy helium ion irradiation. *Fusion Eng. Des.* **2015**, 93, 9–14.
- (43) El-Atwani, O., Suslova, A., DeMasi, A., Gonderman, S., Fowler, J., El-Atwani, M., Ludwig, K., Paul Allain, J. Real time x-ray studies during nanostructure formation on silicon via low energy ion beam irradiation using ultrathin iron films. *Appl. Phys. Lett.* **2012**, 101 (26), 263104.
- (44) Tian, H., Jia, M., Zhang, M., Hu, J. Nonenzymatic glucose sensor based on nickel ion implanted-modified indium tin oxide electrode. *Electrochim. Acta* **2013**, 96, 285–290.
- (45) Chiku, M., Watanabe, T., Einaga, Y. Fabrication of Cu-modified boron-doped diamond microband electrodes and their application for selective detection of glucose. *Diam. Relat. Mater.* **2010**, 19 (7–9), 673–679.
- (46) Suzuki, A., Ivandini, T.A., Yoshimi, K., Fujishima, A., Oyama, G., Nakazato, T., Hattori, N., Kitazawa, S., Einaga, Y. Fabrication, characterization, and application of boron-doped diamond microelectrodes for in vivo dopamine detection. *Anal. Chem.* **2007**, 79 (22), 8608–8615.
- (47) El-Atwani, O., Gonderman, S., Efe, M., De Temmerman, G., Morgan, T., Bystrov, K., Klenosky, D., Qiu, T., Allain, J.P. Ultrafine tungsten as a plasma-facing component in fusion devices: effect of high flux, high fluence low energy helium irradiation. *Nucl. Fusion* **2014**, 54 (8), 083013.
- (48) Hu, X., Li, G., Yu, J.C. Design, fabrication, and modification of nanostructured semiconductor materials for environmental and energy applications. *Langmuir* **2010**, 26 (5), 3031–3039.
- (49) Franke, M.E., Koplin, T.J., Simon, U. Metal and metal oxide nanoparticles in chemiresistors: does

- the nanoscale matter? *Small* **2006**, 2 (1), 36–50.
- (50) Yang, J.J., Pickett, M.D., Li, X., Ohlberg, D.A.A., Stewart, D.R., Williams, R.S. Memristive switching mechanism for metal/oxide/metal nanodevices. *Nat. Nanotechnol.* **2008**, 3 (7), 429–433.
- (51) Ueda, K., Tabata, H., Kawai, T. Magnetic and electric properties of transition-metal-doped ZnO films. *Appl. Phys. Lett.* **2001**, 79 (7), 988–990.
- (52) Khare, N., Kappers, M.J., Wei, M., Blamire, M.G., MacManus-Driscoll, J.L. Defect-induced ferromagnetism in Co-doped ZnO. *Adv. Mater.* **2006**, 18 (11), 1449–1452.
- (53) Tran, T.H., Nguyen, V.T. Copper oxide nanomaterials prepared by solution methods, some properties, and potential applications: A brief review. *Int. Sch. Res. Not.* **2014**, 2014, 1–14.
- (54) Nagarajan, R., Draeseke, A.D., Sleight, A.W., Tate, J. p-type conductivity in $\text{CuCr}_{1-x}\text{Mg}_x\text{O}_2$ films and powders. *J. Appl. Phys.* **2001**, 89 (12), 8022–8025.
- (55) Yanagi, H., Tate, J., Nagarajan, R., Sleight, A.W. Electrical and optical properties of PbCu_2O_2 . *Solid State Commun.* **2002**, 122 (6), 295–297.
- (56) Kumar, V., Govind, A., Nagarajan, R. Optical and photocatalytic properties of heavily F^- -doped SnO_2 nanocrystals by a novel single-source precursor approach. *Inorg. Chem.* **2011**, 50 (12), 5637–5645.
- (57) Aman, N., Mishra, T., Sahu, R.K., Tiwari, J.P. Facile synthesis of mesoporous N doped zirconium titanium mixed oxide nanomaterial with enhanced photocatalytic activity under visible light. *J. Mater. Chem.* **2010**, 20 (48), 10876.
- (58) Aman, N., Das, N.N., Mishra, T. Effect of N-doping on visible light activity of TiO_2 – SiO_2 mixed oxide photocatalysts. *J. Environ. Chem. Eng.* **2016**, 4 (1), 191–196.
- (59) Mishra, T., Wang, L., Hahn, R., Schmuki, P. In-situ Cr doped anodized TiO_2 nanotubes with increased photocurrent response. *Electrochim. Acta* **2014**, 132, 410–415.
- (60) Mishra, T., Hait, J., Aman, N., Gunjan, M., Mahato, B., Jana, R.K. Surfactant mediated synthesis of spherical binary oxides photocatalytic with enhanced activity in visible light. *J. Colloid Interface Sci.* **2008**, 327 (2), 377–383.
- (61) Biswal, A., Tripathy, B.C., Subbaiah, T., Meyrick, D., Ionescu, M., Minakshi, M. Effect of non-ionic surfactants and its role in K intercalation in electrolytic manganese dioxide. *Metall. Mater. Trans. E* **2014**, 1 (3), 226–238.

- (62) Kumar, M., Basu, T., Som, T. Ultra-violet absorption induced modifications in bulk and nanoscale electrical transport properties of Al-doped ZnO thin films. *J. Appl. Phys.* **2015**, *118* (5), 055102.
- (63) Chhillar, S., Acharya, R., Pai, R.V., Sodaye, S., Mukerjee, S.K., Pujari, P.K. A simple and sensitive particle induced gamma-ray emission method for non-destructive quantification of lithium in lithium doped $\text{Nd}_2\text{Ti}_2\text{O}_7$ ceramic sample. *J. Radioanal. Nucl. Chem.* **2012**, *293* (1), 437–441.
- (64) Chhillar, S., Acharya, R., Vittal Rao, T.V., Bamankar, Y.R., Mukerjee, S.K., Pujari, P.K., Aggarwal, S.K. Non-destructive compositional analysis of sol–gel synthesized lithium titanate (Li_2TiO_3) by particle induced gamma-ray emission and instrumental neutron activation analysis. *J. Radioanal. Nucl. Chem.* **2013**, *298* (3), 1597–1603.
- (65) Yang, J., Tan, W., Chen, C., Tao, Y., Qin, Y., Kong, Y. Nonenzymatic glucose sensing by CuO nanoparticles decorated nitrogen-doped graphene aerogel. *Mater. Sci. Eng. C* **2017**, *78*, 210–217.
- (66) Dutta, R.K., Nenavathu, B.P., Talukdar, S. Anomalous antibacterial activity and dye degradation by selenium doped ZnO nanoparticles. *Colloid Surface B* **2014**, *114*, 218–224.
- (67) Nenavathu, B.P., Rao, A.V.R.K., Goyal, A., Kapoor, A., Kumar, R. Synthesis, characterization and enhanced photocatalytic degradation efficiency of Se-doped ZnO nanoparticles using trypan blue as a model dye. *Appl. Catal. A* **2013**, *459*, 106–113.
- (68) Wang, Y., Song, Y., Xia, Y. Electrochemical capacitors: mechanism, materials, systems, characterization and applications. *Chem. Soc. Rev.* **2016**, *45* (21), 5925–5950.
- (69) Xu, W., Dai, S., Liu, G., Xi, Y., Hu, C., Wang, X. CuO nano flowers growing on carbon fiber fabric for flexible. *Electrochim. Acta* **2016**, *203*, 1–8.
- (70) Simon, P., Gogotsi, Y. Charge storage mechanism in nanoporous carbons and its consequence for electrical double layer capacitors. *Philos. Trans. R. Soc. A Math. Phys. Eng. Sci.* **2010**, *368* (1923), 3457–3467.
- (71) Simon, P., Gogotsi, Y. Materials for electrochemical capacitors. *Nat. mater.* **2009**, *7*, 845–854.
- (72) Wang, G., He, X., Wang, L., Gu, A., Huang, Y., Fang, B., Geng, B., Zhang, X. Non-enzymatic electrochemical sensing of glucose. *Microchim. Acta* **2013**, *180* (3–4), 161–186.
- (73) Wang, G., Zhang, L., Zhang, J. A review of electrode materials for electrochemical supercapacitors. *Chem. Soc. Rev.* **2012**, *41* (2), 797–828.

- (74) Pletcher, D. Electrocatalysis: present and future. *J. Appl. Electrochem.* **1984**, *14* (4), 403–415.
- (75) Vassilyev, Y.B., Khazova, O.A., Nikolaeva, N.N. Kinetics and mechanism of glucose electrooxidation on different electrode-catalysts: Part II. effect of the nature of the electrode and the electrooxidation mechanism. *J. Electroanal. Chem. Interfacial Electrochem.* **1985**, *196* (1), 127–144.
- (76) Bagotzky, V.S., Vassilyev, Y.B. Mechanism of electro-oxidation of methanol on the platinum electrode. *Electrochim. Acta* **1967**, *12* (9), 1323–1343.
- (77) Larew, L.A., Johnson, D.C. Transient generation of diffusion layer alkalinity for the pulsed amperometric detection of glucose in low capacity buffers having neutral and acidic pH values. *J. Electroanal. Chem. Interfacial Electrochem.* **1989**, *264* (1–2), 131–147.
- (78) Hsiao, M.W., Adžić, R.R., Yeager, E.B. Electrochemical oxidation of glucose on single crystal and polycrystalline gold surfaces in phosphate buffer. *J. Electrochem. Soc.* **1996**, *143* (3), 759.
- (79) Kokkindis, G., Leger, J.M., Lamy, C. Structural effects in electrocatalysis: oxidation of D-glucose on Pt (100), (110) and (111) single crystal electrodes and the effect of upd adlayers of Pb, Tl and Bi. *J. Electroanal. Chem. Interfacial Electrochem.* **1988**, *242* (1–2), 221–242.
- (80) Burke, L.D. Premonolayer oxidation and its role in electrocatalysis. *Electrochim. Acta* **1994**, *39* (11–12), 1841–1848.
- (81) Kano, K., Takagi, K., Inoue, K., Ikeda, T., Ueda, T. Copper electrodes for stable subpicomole detection of carbohydrates in high-performance liquid chromatography. *J. Chromatogr. A* **1996**, *721* (1), 53–57.
- (82) Yeo, I.H., Johnson, D.C. Anodic response of glucose at copper-based alloy electrodes. *J. Electroanal. Chem.* **2000**, *484* (2), 157–163.
- (83) Kano, K., Torimura, M., Esaka, Y., Goto, M., Ueda, T. Electrocatalytic oxidation of carbohydrates at copper(II)-modified electrodes and its application to flow-through detection. *J. Electroanal. Chem.* **1994**, *372* (1–2), 137–143.
- (84) Zheng, J.P., Jow, T.R. A new charge storage mechanism for electrochemical capacitors. *J. Electrochem. Soc.* **1995**, *142* (1), L6.
- (85) Conway, B.E. Transition from “Supercapacitor” to “Battery” behavior in electrochemical energy storage. *J. Electrochem. Soc.* **1991**, *138* (6), 1539.
- (86) Sugimoto, W., Iwata, H., Yasunaga, Y., Murakami, Y., Takasu, Y. Preparation of ruthenic acid

- nanosheets and utilization of its interlayer surface for electrochemical energy storage. *Angew. Chemie Int. Ed.* **2003**, *42* (34), 4092–4096.
- (87) Hu, C.C., Chen, W.C., Chang, K.H. How to achieve maximum utilization of hydrous ruthenium oxide for supercapacitors. *J. Electrochem. Soc.* **2004**, *151* (2), A281.
- (88) Trasatti, S. Physical electrochemistry of ceramic oxides. *Electrochim. Acta* **1991**, *36* (2), 225–241.
- (89) Sugimoto, W., Shibutani, T., Murakami, Y., Takasu, Y. Charge storage capabilities of rutile-type RuO_2 VO_2 solid solution for electrochemical supercapacitors. *Electrochem. Solid-State Lett.* **2002**, *5* (7), A170-A172.
- (90) Takasu, Y., Murakami, Y. Design of oxide electrodes with large surface area. *Electrochim. Acta* **2000**, *45* (25–26), 4135–4141.
- (91) Wei, W., Cui, X., Chen, W., Ivey, D.G. Manganese oxide-based materials as electrochemical supercapacitor electrodes. *Chem. Soc. Rev.* **2011**, *40* (3), 1697–1721.
- (92) Wu, Z.S., Ren, W., Wang, D.W., Li, F., Liu, B., Cheng, H.M. High-energy MnO_2 nanowire/graphene and graphene asymmetric electrochemical capacitors. *ACS Nano* **2010**, *4* (10), 5835–5842.
- (93) Bhagwan, J., Sahoo, A., Yadav, K.L., Sharma, Y. Porous, one dimensional and high aspect ratio Mn_3O_4 nanofibers: fabrication and optimization for enhanced supercapacitive properties. *Electrochim. Acta* **2015**, *174*, 992–1001.
- (94) Bhagwan, J., Sivasankaran, V., Yadav, K.L., Sharma, Y. Porous, one-dimensional and high aspect ratio nano fibric network of cobalt manganese oxide as a high performance material for aqueous and solid-state supercapacitor (2 V). *J. Power sources* **2016**, *327*, 29–37.
- (95) Yu, Y., Su, W., Yuan, M., Fu, Y., Hu, J. Electrocatalytic oxidation of formaldehyde on nickel ion implanted-modified indium tin oxide electrode. *J. Power Sources* **2015**, *286*, 130–135.
- (96) Yu, Y., Jia, M., Tian, H., Hu, J. The fabrication of silver ion implantation-modified electrode and its application in electrocatalytic oxidation of formaldehyde. *J. Power Sources* **2014**, *267*, 123–127.
- (97) Liang, F., Tian, H., Jia, M., Hu, J. Pt nanoparticles ion-implanted onto indium tin oxide electrodes and their electrocatalytic activity towards methanol. *J. Power sources* **2013**, *225* (1), 9–12.
- (98) Liu, M.S., Lin, M.C.-C., Huang, I.-T., Wang, C.-C. Enhancement of thermal conductivity with

- CuO for nanofluids. *Chem. Eng. Technol.* **2006**, *29* (1), 72–77.
- (99) Liao, L., Zhang, Z., Yan, B., Zheng, Z., Bao, Q.L., Wu, T., Li, C.M., Shen, Z.X., Zhang, J.X., Gong, H., Li, J.C., Yu, T. Multifunctional CuO nanowire devices: p-type field effect transistors and CO gas sensors. *Nanotechnology* **2009**, *20* (8), 085203.
- (100) Wang, S.B., Hsiao, C.H., Chang, S.J., Lam, K.T., Wen, K.H., Hung, S.C., Young, S.J., Huang, B.R.A CuO nanowire infrared photodetector. *Sensors Actuators, A Phys.* **2011**, *171* (2), 207–211.
- (101) Wang, K., Dong, X., Zhao, C., Qian, X., Xu, Y. Facile synthesis of Cu₂O/CuO/RGO nanocomposite and its superior cyclability in supercapacitor. *Electrochim. Acta* **2015**, *152*, 433–442.
- (102) Liu, D., Yang, Z., Wang, P., Li, F., Wang, D., He, D. Preparation of 3D nanoporous copper-supported cuprous oxide for high-performance lithium ion battery anodes. *Nanoscale* **2013**, *5* (5), 1917.
- (103) Kumar, R.V., Diamant, Y., Gedanken, A. Sonochemical synthesis and characterization of nanometer-size transition metal oxides from metal acetates. *Chem. Mater.* **2000**, *12* (8), 2301–2305.
- (104) Fan, H., Yang, L., Hua, W., Wu, X., Wu, Z., Xie, S., Zou, B. Controlled synthesis of monodispersed CuO nanocrystals. *Nanotechnology* **2004**, *15* (1), 37–42.
- (105) Sharma, A., Dutta, R.K., Roychowdhury, A., Das, D., Goyal, A., Kapoor, A. Cobalt doped CuO nanoparticles as a highly efficient heterogeneous catalyst for reduction of 4-nitrophenol to 4-Aminophenol. *Appl. Catal. A* **2017**, *543*, 257–265.
- (106) Li, Y., Chang, S., Liu, X., Huang, J., Yin, J., Wang, G., Cao, D. Nanostructured CuO directly grown on copper foam and their supercapacitance performance. *Electrochim. Acta* **2012**, *85*, 393–398.
- (107) Pendashteh, A., Mousavi, M.F., Rahmanifar, M.S. Fabrication of anchored copper oxide nanoparticles on graphene oxide nanosheets via an electrostatic coprecipitation and its application as supercapacitor. *Electrochim. Acta* **2013**, *88*, 347–357.
- (108) Nwanya, A.C., Obi, D., Ozoemena, K.I., Osuji, R.U., Awada, C., Ruediger, A., Maaza, M., Rosei, F., Ezema, F.I. Facile synthesis of nanosheet-like CuO film and its potential application as a high-performance pseudocapacitor electrode. *Electrochim. Acta* **2016**, *198*, 220–230.
- (109) Souza, E.A., dos Santos, A.O., Cardoso, L.P., Tabacniks, M.H., Landers, R., Gorenstein, A.

- Copper-vanadium mixed oxide thin film electrodes. *J. Power Sources* **2006**, *162* (1), 679–684.
- (110) Patel, M., Pati, R., Marathe, P., Kim, J., Mukhopadhyay, I., Ray, A. Highly photoactive and photo-stable spray pyrolyzed tenorite CuO thin films for photoelectrochemical energy conversion. *J. Electrochem. Soc.* **2016**, *163* (14), H1195–H1203.
- (111) Hsu, Y., Yu, C., Chen, Y., Lin, Y. Synthesis of novel Cu₂O micro/nanostructural photocathode for solar water splitting. *Electrochim. Acta* **2013**, *105*, 62–68.
- (112) Li, K., Fan, G., Yang, L., Li, F. Novel ultrasensitive non-enzymatic glucose sensors based on controlled flower-like CuO hierarchical films. *Sensors Actuators, B Chem.* **2014**, *199*, 175–182.
- (113) Dong, C., Wang, Y., Xu, J., Cheng, G., Yang, W., Kou, T., Zhang, Z., Ding, Y. 3D binder-free Cu₂O@Cu nanoneedle arrays for high-performance asymmetric supercapacitors. *J. Mater. Chem. A* **2014**, *2* (43), 18229–18235.
- (114) Li, Y., Ye, K., Cheng, K., Cao, D., Pan, Y., Kong, S., Zhang, X., Wang, G. Anchoring CuO nanoparticles on nitrogen-doped reduced graphene oxide nanosheets as electrode material for supercapacitors. *J. Electroanal. Chem.* **2014**, *727*, 154–162.
- (115) Purushothaman, K.K., Saravanakumar, B., Babu, I.M., Sethuraman, B., Muralidharan, G. Nanostructured CuO/reduced graphene oxide composite for hybrid supercapacitors. *RSC Adv.* **2014**, *4* (45), 23485.
- (116) Zhao, B., Liu, P., Zhuang, H., Jiao, Z., Fang, T., Xu, W., Lu, B., Jiang, Y. Hierarchical self-assembly of microscale leaf-like CuO on graphene sheets for high-performance electrochemical capacitors. *J. Mater. Chem. A* **2013**, *1* (2), 367–373.
- (117) Chen, L., Zhang, Y., Zhu, P., Zhou, F., Zeng, W., Lu, D.D., Sun, R., Wong, C. Copper salts mediated morphological transformation of Cu₂O from cubes to hierarchical flower-like or microspheres and their supercapacitors performances. *Sci. Rep.* **2015**, *5*, 1–7.
- (118) Krishnamoorthy, K., Kim, S.J. Growth, characterization and electrochemical properties of hierarchical CuO nanostructures for supercapacitor applications. *Mater. Res. Bull.* **2013**, *48* (9), 3136–3139.
- (119) Dubal, D.P., Dhawale, D.S., Salunkhe, R.R., Jamdade, V.S., Lokhande, C.D. Fabrication of copper oxide multilayer nanosheets for supercapacitor application. *J. Alloys Compd.* **2010**, *492* (1–2), 26–30.
- (120) Patake, V.D., Joshi, S.S., Lokhande, C.D., Joo, O.S. Electrodeposited porous and amorphous

- copper oxide film for application in supercapacitor. *Mater. Chem. Phys.* **2009**, *114* (1), 6–9.
- (121) Shinde, S.K., Dubal, D.P., Ghodake, G.S., Fulari, V.J. Hierarchical 3D-flower-like CuO nanostructure on copper foil for supercapacitors. *RSC Adv.* **2015**, *5* (6), 4443–4447.
- (122) Dubal, D.P., Gund, G.S., Holze, R., Lokhande, C.D. Mild chemical strategy to grow micro-roses and micro-woolen like arranged CuO nanosheets for high performance supercapacitors. *J. Power Sources* **2013**, *242*, 687–698.
- (123) Zhang, J., Feng, H., Qin, Q., Zhang, G., Cui, Y., Chai, Z., Zheng, W. Interior design of three-dimensional CuO ordered architectures with enhanced performance for supercapacitors. *J. Mater. Chem. A* **2016**, *4* (17), 6357–6367.
- (124) Zhang, X., Shi, W., Zhu, J., Kharistal, D.J., Zhao, W., Lalia, B.S., Hng, H.H., Yan, Q. High-power and high-energy-density flexible pseudocapacitor electrodes made from porous CuO nanobelts and single-walled carbon nanotubes. *ACS Nano* **2011**, *5* (3), 2013–2019.
- (125) Yu, L., Jin, Y., Li, L., Ma, J., Wang, G., Geng, B., Zhang, X. 3D porous gear-like copper oxide and their high electrochemical performance as supercapacitors. *Cryst. Eng. Comm.* **2013**, *15* (38), 7657.
- (126) Shaikh, J.S., Pawar, R.C., Moholkar, A.V., Kim, J.H., Patil, P.S. CuO-PAA hybrid films: chemical synthesis and supercapacitor behavior. *Appl. Surf. Sci.* **2011**, *257* (9), 4389–4397.
- (127) Moosavifard, S.E., El-Kady, M.F., Rahmanifar, M.S., Kaner, R.B., Mousavi, M.F. Designing 3D highly ordered nanoporous CuO electrodes for high-performance asymmetric supercapacitors. *ACS Appl. Mater. Interfaces* **2015**, *7* (8), 4851–4860.
- (128) Dubal, D.P., Gund, G.S., Holze, R., Lokhande, C.D. Enhancement in supercapacitive properties of CuO thin films due to the surfactant mediated morphological modulation. *J. Electroanal. Chem.* **2014**, *712*, 40–46.
- (129) Endut, Z., Hamdi, M., Basirun, W.J. Pseudocapacitive performance of vertical copper oxide nanoflakes. *Thin Solid Films* **2013**, *528*, 213–216.
- (130) Huang, L.S., Yang, S.G., Li, T., Gu, B.X., Du, Y.W., Lu, Y.N., Shi, S.Z. Preparation of large-scale cupric oxide nanowires by thermal evaporation method. *J. Cryst. Growth* **2004**, *260* (1–2), 130–135.
- (131) Xu, P., Liu, J., Liu, T., Ye, K., Cheng, K., Yin, J., Cao, D., Wang, G., Li, Q. Preparation of binder-free CuO/Cu₂O/Cu composites: a novel electrode material for supercapacitor applications.

- RSC Adv.* **2016**, *6* (34), 28270–28278.
- (132) Choudhury, T., Saied, S.O., Sullivan, J.L., Abbot, A.M. Reduction of oxides of iron, cobalt, titanium and niobium by low-energy ion bombardment. *J. Phys. D. Appl. Phys.* **1989**, *22* (8), 1185–1195.
- (133) Öztaş, M., Bedir, M. Effect of nitrogen ion implantation on the sprayed ZnSe thin films. *Mater. Lett.* **2007**, *61* (2), 343–346.
- (134) Zheng, S.K., Wang, T.M., Hao, W.C., Shen, R. Improvement of photocatalytic activity of TiO₂ thin film by Sn ion implantation. *Vacuum* **2002**, *65* (2), 155–159.
- (135) Parretta, A., Jayaraj, M.K., Di Nocera, A., Loreti, S., Quercia, L., Agati, A. Electrical and optical properties of copper oxide films prepared by reactive RF magnetron sputtering. *Phys. Status Solidi* **1996**, *155* (2), 399–404.
- (136) Christenson, H.K. DLVO (Derjaguin-Landau-Verwey-Overbeek) theory and solvation forces between mica surfaces in polar and hydrogen-bonding liquids. *J. Chem. Soc., Faraday Trans. 1*, **1984**, *9* (7), 1933–1946.
- (137) Sharma, A., Dutta, R.K., Roychowdhury, A., Das, D. Studies on structural defects in bare, PVP capped and TPPO capped copper oxide nanoparticles by positron annihilation lifetime spectroscopy and their impact on photocatalytic degradation of rhodamine B. *RSC Adv.* **2016**, *6* (78), 74812–74821.
- (138) Raj, B.G.S., Asiri, A.M., Qusti, A.H., Wu, J.J., Anandan, S. Sonochemically Synthesized MnO₂ nanoparticles as electrode material for supercapacitors. *Ultrason. Sonochem.* **2014**, *21* (6), 1933–1938.
- (139) Grigore, M.E., Biscu, E.R., Holban, A.M., Gestal, M.C., Grumezescu, A.M. Methods of synthesis, properties and biomedical applications of CuO nanoparticles. *Pharmaceuticals* **2016**, *9* (4), 1–14.
- (140) Huang, M., Zhang, Y., Li, F., Wang, Z., Alamusi, Hu, N., Wen, Z., Liu, Q. Merging of kirkendall growth and ostwald ripening: CuO@MnO₂ core-shell architectures for asymmetric supercapacitors. *Sci. Rep.* **2014**, *4*, 35–40.
- (141) Torto, N., Ruzgas, T., Gorton, L. Electrochemical oxidation of mono- and disaccharides at fresh as well as oxidized copper electrodes in alkaline media. *J. Electroanal. Chem.* **1999**, *464* (2), 252–258.

- (142) Hien, V.X., You, J., Jo, K., Kim, S., Lee, J., Kim, J., Heo, Y. H₂S-sensing properties of Cu₂O submicron-sized rods and trees synthesized by radio-frequency magnetron sputtering. *Sensor Actuat. B Chem.* **2014**, *202*, 330–338.
- (143) Fu, T. CuS-doped CuO nanoparticles sensor for detection of H₂S and NH₃ at room temperature. *Electrochim. Acta* **2013**, *112*, 230–235.
- (144) Ratko, A., Babushkin, O., Baran, A., Baran, S. Sorption and gas sensitive properties of In₂O₃ based ceramics doped with Ga₂O₃. *J. Eur. Ceram. Soc.* **1998**, *18* (14), 2227–2232.
- (145) Zhuang, Z., Su, X., Yuan, H., Sun, Q., Xiao, D., Choi, M.M.F. An improved sensitivity non-enzymatic glucose sensor based on a CuO nanowire modified Cu electrode. *Analyst* **2008**, *133* (1), 126–132.
- (146) Kang, X., Mai, Z., Zou, X., Cai, P., Mo, J. A sensitive nonenzymatic glucose sensor in alkaline media with a copper nanocluster/multiwall carbon nanotube-modified glassy carbon electrode. *Anal. Biochem.* **2007**, *363* (1), 143–150.
- (147) Vaseem, M., Tripathy, N., Hahn, Y. Wide linear-range detecting nonenzymatic glucose biosensor based on CuO nanoparticles inkjet-printed on electrodes. *Anal. Chem.* **2013**, *85* (21), 10448–10454.
- (148) Hu, S., Xu, C., Wang, G., Cui, D. Voltammetric determination of 4-nitrophenol at a sodium montmorillonite-anthraquinone chemically modified glassy carbon electrode. *Talanta*, **2001**, *54*, 115–123.
- (149) Dubal, D.P., Gund, G.S., Holze, R., Jadhav, H.S., Lokhande, C.D., Park, C.J. Surfactant-assisted morphological tuning of hierarchical CuO thin films for electrochemical supercapacitors. *Dalt. Trans.* **2013**, *42* (18), 6459.
- (150) Siddiqui, H., Qureshi, M.S., Haque, F.Z. Surfactant assisted wet chemical synthesis of copper oxide (CuO) nanostructures and their spectroscopic analysis. *Optik*, **2016**, *127* (5), 2740–2747.
- (151) Zhang, H., Feng, J., Zhang, M. Preparation of flower-like CuO by a simple chemical precipitation method and their application as electrode materials for capacitor. *Mater. Res. Bull.* **2008**, *43* (12), 3221–3226.
- (152) Wang, G., Huang, J., Chen, S., Gao, Y., Cao, D. Preparation and supercapacitance of CuO nanosheet arrays grown on nickel foam. *J. Power Sources* **2011**, *196* (13), 5756–5760.
- (153) Global Report on Diabetes. World Health Organization, **2016**, 978, 88.

- (154) Dong, X.C., Xu, H., Wang, X.W., Huang, Y.X., Chan-Park, M.B., Zhang, H., Huang, W., Chen, P. 3D graphene à cobalt oxide electrode for high-performance supercapacitor and enzymeless glucose detection. *ACS nano*. **2012**, 6(4), 3206–3213.
- (155) Ikhsan, N.I., Rameshkumar, P., Huang, N.M. Controlled synthesis of reduced graphene oxide supported silver nanoparticles for selective and sensitive electrochemical detection of 4-nitrophenol. *Electrochim. Acta* **2016**, 192, 392–399.
- (156) Gülen, Y., Bayansal, F., Şahin, B., Çetinkara, H.A., Güder, H.S. Fabrication and characterization of Mn-doped CuO thin films by the SILAR method. *Ceram. Int.* **2013**, 39 (6), 6475–6480.
- (157) Saraf, M., Natarajan, K., Mobin, S.M. Non-enzymatic amperometric sensing of glucose by employing sucrose templated microspheres of copper oxide (CuO). *Dalt. Trans.* **2016**, 45 (13), 5833–5840.
- (158) Yang, Z., Feng, J., Qiao, J., Yan, Y., Yu, Q., Sun, K. Copper oxide nanoleaves decorated multi-walled carbon nanotube as platform for glucose sensing. *Anal. Methods* **2012**, 4 (7), 1924.
- (159) Luo, L., Zhu, L., Wang, Z. Nonenzymatic amperometric determination of glucose by CuO nanocubes–graphene nanocomposite modified electrode. *Bioelectrochemistry* **2012**, 88, 156–163.
- (160) Ananth, A., Dharaneedharan, S., Heo, M.-S., Mok, S.Y. Copper oxide nanomaterials: synthesis, characterization and structure-specific antibacterial performance. *Chem. Eng. J.* **2015**, 262, 179–188.
- (161) Yu, C.F., Sung, C.W., Chen, S.H., Sun, S.J. Relationship between the photoluminescence and conductivity of undoped ZnO thin films grown with various oxygen pressures. *Appl. Surf. Sci.* **2009**, 256 (3), 792–796.
- (162) Kawamura, F., Yasui, I., Kamei, M., Sunagawa, I. Habit modifications of SnO₂ crystals in SnO₂-Cu₂O flux system in the presence of trivalent impurity cations. *J. Am. Ceram. Soc.* **2004**, 84 (6), 1341–1346.
- (163) Morrison, S.R. Selectivity in semiconductor gas sensors. *Sensors and Actuators* **1987**, 12 (4), 425–440.
- (164) Meixner, H., Lampe, U. Metal oxide sensors. *Sensors Actuators B Chem.* **1996**, 33 (1–3), 198–202.
- (165) Gopel, W., Jones, T.A., Kleitz, M., Lundstrom, J., Seiyama, T. Sensors: comprehensive survey, chemical and biochemical sensors. Part 1, Vol. 2, (Eds; Gopel, W., Hesse, J., Zemel, J.N.) VCH

- Publishers Inc., New York, NY (USA) **1991**.
- (166) Madou, M.J., Morrison, S.R. Chemical sensing with solid state devices, Academic Press, **1989**.
- (167) Liu, T., Li, X., Li, F. Enhanced photocatalytic activity of Ce³⁺-TiO₂ hydrosols in aqueous and gaseous phases. *Chem. Eng. J.* **2010**, *157* (2–3), 475–482.
- (168) Tsang, S.C., Bulpitt, C. Rare earth oxide sensors for ethanol analysis. *Sens. Actuat. B* **1998**, *52*, 226–235.
- (169) Chaudhary, N.V.P., Murthy, J.K., Venimadhav, A. Absence of dipolar ordering in Co doped CuO. *Solid State Commun.* **2016**, *247* (3), 36–39.
- (170) Baturay, S., Tombak, A., Kaya, D., Ocak, Y.S., Tokus, M., Aydemir, M., Kilicoglu, T. Modification of electrical and optical properties of CuO thin films by Ni doping. *J. Sol-Gel Sci. Technol.* **2016**, *78* (2), 422–429.
- (171) Bhuvaneshwari, S., Gopalakrishnan, N. Enhanced ammonia sensing characteristics of Cr doped CuO nanoboats. *J. Alloys Compd.* **2016**, *654* (2), 202–208.
- (172) Huang, J., Wu, H., Cao, D., Wang, G. Influence of Ag doped CuO nanosheet arrays on electrochemical behaviors for supercapacitors. *Electrochim. Acta* **2012**, *75*, 208–212.
- (173) Shaikh, J.S., Pawar, R.C., Devan, R.S., Ma, Y.R., Salvi, P.P., Kolekar, S.S., Patil, P.S. Synthesis and characterization of Ru doped CuO thin films for supercapacitor based on bronsted acidic ionic liquid. *Electrochim. Acta* **2011**, *56* (5), 2127–2134.
- (174) Mariammal, R.N., Ramachandran, K., Kalaiselvan, G., Arumugam, S., Renganathan, B., Sastikumar, D. Effect of magnetism on the ethanol sensitivity of undoped and Mn-doped CuO nanoflakes. *Appl. Surf. Sci.* **2013**, *270*, 545–552.
- (175) Chiang, C.Y., Shin, Y., Ehrman, S. Dopant effects on copper oxide photoelectrochemical cell water splitting. *Energy Procedia* **2014**, *61*, 1799–1802.
- (176) Wang, W., Li, Z., Zheng, W., Yang, J., Zhang, H., Wang, C. Electrospun palladium (IV)-doped copper oxide composite nanofibers for non-enzymatic glucose sensors. *Electrochem. commun.* **2009**, *11* (9), 1811–1814.
- (177) Paul Joseph, D., Venkateswaran, C., Sambasivam, S., Choi, B.C. Effect of Fe alloying on the structural, optical, electrical and magnetic properties of spray-deposited CuO thin films. *J. Korean Phys. Soc.* **2012**, *61* (3), 449–454.
- (178) Liu, K.L., Yuan, S.L., Duan, H.N., Zheng, X.F., Yin, S.Y., Tian, Z.M., Wang, C.H., Huo, S.X.

- Exchange bias in Fe and Ni codoped CuO nanocomposites. *J. Appl. Phys.* **2010**, *107* (2).
- (179) Khmissi, H., Sayed, A.M. El, Shaban, M. Structural, morphological, optical properties and wettability of spin-coated copper oxide, influences of film thickness, Ni, and (La, Ni) co-doping. *J. Mater. Sci.* **2016**, *51* (12), 5924–5938.
- (180) Bayansal, F., Gülen, Y. CuO Nanostructures grown by the SILAR method: influence of Pb-doping on the morphological, structural and optical properties. *J. Alloy Compd.* **2015**, *619*, 378–382.
- (181) Chiang, C.Y., Shin, Y., Ehrman, S. Li doped CuO film electrodes for photoelectrochemical cells. *J. Electrochem. Soc.* **2012**, *159* (2), B227.
- (182) Chand, P., Gaur, A., Kumar, A., Gaur, U.K. Structural and optical study of Li doped CuO thin films on Si (100) substrate deposited by pulsed laser deposition. *Appl. Surf. Sci.* **2014**, *307*, 280–286.
- (183) Cretu, V., Postica, V., Mishra, A.K., Hoppe, M., Tiginyanu, I., Mishra, Y.K., Chow, L., de Leeuw, N.H., Adelung, R., Lupan, O. Synthesis, characterization and DFT studies of zinc-doped copper oxide nanocrystals for gas sensing applications. *J. Mater. Chem. A* **2016**, *4* (17), 6527–6539.
- (184) Basith, N.M., Vijaya, J.J., Kennedy, L.J., Bououdina, M. Structural, morphological, optical, and magnetic properties of Ni-doped CuO nanostructures prepared by a rapid microwave combustion method. *Mat. Sci. Semicon. Proc.* **2014**, *17*, 110–118.
- (185) Rao, G.N., Yao, Y.D., Chen, J.W. Influence of Mn substitution on microstructure and magnetic properties of $\text{Cu}_{1-x}\text{Mn}_x\text{O}$ nanoparticles. *J. Appl. Phys.* **2007**, *101*, 09H119.
- (186) Abd El-Kader, F.H.; Hakeem, N.A.; Elashmawi, I.S.; Menazea, A. A. Synthesis and characterization of PVK/Ag NPs nanocomposites prepared by laser ablation. *Spectrochim. Acta. A. Mol. Biomol. Spectrosc.* **2015**, *138*, 331–339.
- (187) Meneses, C.T., Duque, J.G.S., Vivas, L.G., Knobel, M. Synthesis and characterization of TM-doped CuO (TM = Fe, Ni). *J. Non. Cryst. Solids* **2008**, *354* (42–44), 4830–4832.
- (188) Zhu, H., Zhao, F., Pan, L., Zhang, Y., Fan, C., Zhang, Y., Xiao, J. Q. Structural and magnetic properties of Mn-doped CuO thin films. *J. Appl. Phys.* **2007**, *101*, 09H111.
- (189) Klinbumrung, A., Thongtem, T., Thongtem, S. Characterization and gas sensing properties of CuO synthesized by DC directly applying voltage, *Appl. Surf. Sci.* **2014**, *313*, 640–646.

- (190) Jindal, K., Tomar, M., Gupta, V. CuO thin film based uric acid biosensor with enhanced response characteristics, *Biosens. Bioelectron.* **2012**, *38*, 11–18.
- (191) Sanal, K.C., Vikas, L.S., Jayaraj, M.K. Room temperature deposited transparent p-channel CuO thin film transistors, *Appl. Surf. Sci.* **2014**, *297*, 153-157.
- (192) Singh, B., Mehta, B.R. Relationship between nature of metal-oxide contacts and resistive switching properties of copper oxide thin film based devices, *Thin Solid Films* **2014**, *569*, 35-43.
- (193) Jarlborg, T. Effects of spin-phonon interaction within the CuO plane of high- T_c superconductors, *Physica C* **2007**, *454*, 5–14.
- (194) Yin, Z., Ding, Y., Zheng, Q., Guan, L. CuO/polypyrrole core-shell nanocomposites as anode materials for lithium-ion batteries, *Electrochem. Commun.* **2012**, *20*, 40–43.
- (195) Gao, W., Yang, S., Yang, S., Lv, L., Du, Y. Synthesis and magnetic properties of Mn doped CuO nanowires, *Phys. Lett. A* **2010**, *375*, 180–182.
- (196) Bhaumik, A., Haque, A., Karnati, P., Taufique, M.F.N., Patel, R., Ghosh, K. Copper oxide based nanostructures for improved solar cell efficiency, *Thin Solid Films* **2014**, *572*, 126-133.
- (197) Vidyasagar, C.C., Arthoba Naik, y., Venkatesh, T.G., Viswanatha, R. Solid-state synthesis and effect of temperature on optical properties of Cu–ZnO, Cu–CdO and CuO nanoparticles, *Powder Technol.* **2011**, *214*, 337–343.
- (198) Jia, R., Lin, G., Zhao, D., Zhang, Q., Lin, X., Gao, N., Liu, D. Sandwich-structured Cu₂O photodetectors enhanced by localized surface plasmon resonances, *Appl. Surf. Sci.* **2015**, *332*, 340–345.
- (199) Malerba, C., Biccari, F., Ricardo, C.L.A., D’Incau, M., Scardi, P., Mittiga, A. Absorption coefficient of bulk and thin film Cu₂O, *Sol. Energy. Mat. Sol. C* **2011**, *95*, 2848-2854.
- (200) Parachhino, A., Laporte, V., Sivula, K., Gratzel, M., Thimsen, E. Highly active oxide photocathode for photoelectrochemical water reduction, *Nat. Mater.* **2011**, *10*, 456-61.
- (201) Minami, T., Nishi, Y., Miyata, T., Namoto, J. High-efficiency oxide solar cells with ZnO/Cu₂O heterojunction fabricated on thermally oxidized Cu₂O sheets, *Appl. Phys. express* **2011**, *4*, 062301-1-062301-3.
- (202) Balamurugan, B., Mehta, B.R. Optical and structural properties of nanocrystalline copper oxide thin films prepared by activated reactive evaporation, *Thin Solid Films* **2001**, *396* 90–96.
- (203) Saravanan, V., Shankar, P., Mani, G.K., Rayappan, J.B.B. Growth and characterization of spray

- pyrolysis deposited copper oxide thin films: Influence of substrate and annealing temperatures, *J. Anal. Appl. Pyrolysis* **2015**, *111*, 272-277.
- (204) Balamurugan, B., Mehta, B.R., Avasthi, D.K., Singh, F., Arora, A.K., Rajalakshmi, M., Raghavan, G., Tyagi, A.K., Shivaprasad, S.M. Modifying the nanocrystalline characteristics-structure, size, and surface states of copper oxide thin films by high-energy heavy-ion irradiation, *J. Appl. Phys.* **2002**, *92*, 3304-3310.
- (205) Mayer, J.W., Eriksson, L., Davies, J.A. Ion implantation in Semiconductors, *Academic Press* **1970**.
- (206) Sagalowicz, L., Fox, G.R. Planar defects in ZnO thin films deposited on optical fibers and flat substrates, *J. Mater. Res.* **1999**, *14*, 1876-1885.
- (207) Dutta, R.K., Bind, U.C., Krishna, J.B.M., Sinha, A.K., Taki, G.S. Ion beam irradiation of ZnS dispersed in PMMA and its photocatalytic application, *J. Radioanal. Nucl. Chem.* **2014**, *302*, 819-824.
- (208) Ziegler, J.F., Ziegler, M.D., Biersack, J.P. SRIM – The stopping and range of ions in matter, *Nucl. Instrum. Meth. B* **2010**, *268*, 1818-1823.
- (209) Whitney, R.D.S., Clemente, M.M., Revcolevschi, A. Growth and microstructural control of single crystal cuprous oxide Cu₂O, *J. Cryst. Growth* **1974**, *23*, 113-120.
- (210) Subramaniyan, A., Perkins, J.D., O'Hayre, R.P., Lany, S., Stevanovic, V., Ginley, D.S., Zakutayev, A. Non-equilibrium deposition of phase pure Cu₂O thin films at reduced growth temperature, *APL Mat.* **2014**, *2*, 022105-6.
- (211) Ragone, D.V. Thermodynamics of Materials *Wiley: New York*, **1995**, pp. 125-135.
- (212) Rodriguez, J.A., Hrbek, J. Decomposition of NO₂ on metal surfaces: Oxidation of Ag, Zn, and Cu films, *J. Vac. Sci. Technol. A* **1994**, *12*, 2140-2144.
- (213) Sheng, H., Hong-Ying, C., Yuh-Bin, C., Han, S.C. Phase transformations in copper oxide nanowires, *J. Vac. Sci. Technol. B* **2005**, *23*, 2557-2560.
- (214) Mishra, P., Solanki, V., Rath, A., Chakraborty, S., Lohani, H., Sahoo, P.K., Sekhar, B.R. Structural and optical study of MeV cobalt ion implanted silicon, *Adv. Mat. Lett.* **2014**, *5*, 699-705.
- (215) Zhang, X.D., Liu, C.L., Wang, Z., Lü, Y.Y., Yin, L.J. Photoluminescence and electrical properties of N-implanted ZnO films, *Nucl. Instrum. Methods Phys. Res., Sect. B* **2007**, *254*, 83-86.

- (216) Zhang, X.D., Wu, P., Shen, Y.Y., Zhang, L.H., Xue, Y.H., Zhu, F., Zhang, D.C., Liu, C.L. Structural and optical properties of Au-implanted ZnO films, *Appl. Surf. Sci.* **2011**, 258, 151–157.
- (217) Maruyama, T. Copper oxide thin films prepared by chemical vapor deposition from copper dipivaloylmethanate, *Sol. Energ. Mat. Sol. C.* **1998**, 56, 85-92.
- (218) Morigaki, K. Physics of amorphous semiconductors, *World Scientific Publishing Company, London*, **1999**, 137-171.
- (219) Nobbs, J.H., Kubelka-Munk theory and the prediction of reflectance, *Res. Prog. Coloration* **1985**, 15, 66-75.
- (220) Brandt, I.S., Martins, C.A., Zoldan, V.C., Viegas, A.D.C., da Silva, J.H.D., Pasa, A.A. Structural and optical properties of Cu₂O crystalline electrodeposited films, *Thin Solid Films* **2014**, 562, 144-151.
- (221) Lim, Y-F., Chua, C.S., Lee, C.J.J., Chi, D. Sol-gel deposited Cu₂O and CuO thin films for photocatalytic water splitting, *Phys. Chem. Chem. Phys.* **2014**, 16, 25928-25934.
- (222) Wanninayake, A.P., Gunashekar, S., Li, S., Church, B.C., Abu-Zahra, N. Performance enhancement of polymer solar cells using copper oxide nanoparticles. *Semicond. Sci. Technol.* **2015**, 30 (6), 064004.
- (223) Izaki, M., Shinagawa, T., Mizuno, K.-T., Ida, Y., Inaba, M., Tasaka, A. Electrochemically constructed p-Cu₂O/n-ZnO heterojunction diode for photovoltaic device. *J. Phys. D. Appl. Phys.* **2007**, 40 (11), 3326–3329.
- (224) Shinde, S.K., Fulari, V.J., Kim, D.Y., Maile, N.C., Koli, R.R., Dhaygude, H.D., Ghodake, G.S. Chemical synthesis of flower-like hybrid Cu(OH)₂/CuO electrode: application of polyvinyl alcohol and triton X-100 to enhance supercapacitor performance. *Colloids Surf. B Biointerfaces* **2017**, 156, 165–174.
- (225) Ballantyne, A.M., Chen, L., Dane, J., Hammant, T., Braun, F.M., Heeney, M., Duffy, W., McCulloch, I., Bradley, D.D.C., Nelson, J. The effect of poly(3-hexylthiophene) molecular weight on charge transport and the performance of polymer:fullerene solar cells. *Adv. Funct. Mater.* **2008**, 18 (16), 2373–2380.
- (226) Tauc, J., Grigorovici, R., Vancu, A. Optical properties and electronic structure of amorphous germanium. *Phys. status solidi* **1966**, 15 (2), 627–637.

- (227) Klabunde, K.J. Nanoscale materials in chemistry, *A John Wiley & Sons, Inc., Publication*. **2009**.
- (228) Gaur, U.K., Kumar, A., Varma, G.D. The synthesis of self-assembled polycrystalline 1-D CuO nanostructures in aqueous medium and a study of their multifunctional features. *Cryst. Eng. Comm.* **2014**, *16* (14), 3005-3014.
- (229) Bhaumik, A., Shearin, A.M., Patel, R., Ghosh, K. Significant enhancement of optical absorption through nano-structuring of copper based oxide semiconductors: possible future materials for solar energy applications. *Phys. Chem. Chem. Phys.* **2014**, *16* (22), 11054–11066.
- (230) Muiva, C.M., Juma, A.O., Lepodise, L.M., Maabong, K., Letsholathebe, D. Surfactant assisted chemical bath deposition based synthesis of 1-D nanostructured CuO thin films from alkaline baths. *Mater. Sci. Semicond. Process.* **2017**, *67*, 69–74.
- (231) Wu, N.L., Kuo, S.L., Lee, M.H. Preparation and optimization of RuO₂-impregnated SnO₂ xerogel supercapacitor. *J. Power Sources* **2002**, *104* (1), 62–65.
- (232) Vijayakumar, S., Nagamuthu, S., Muralidharan, G. Supercapacitor studies on NiO nanoflakes synthesized through a microwave route. *ACS Appl. Mater. Interfaces* **2013**, *5* (6), 2188–2196.
- (233) Lee, J.S.M., Briggs, M.E., Hu, C.C., Cooper, A.I. Controlling electric double-layer capacitance and pseudocapacitance in heteroatom-doped carbons derived from hypercrosslinked microporous polymers. *Nano Energy* **2018**, *46*, 277–289.
- (234) Ardizzone, S., Fregonara, G., Trasatti, S. “Inner” and “Outer” active surface of RuO₂ electrodes. *Electrochim. Acta* **1990**, *35* (1), 263–267.
- (235) Baronetto, D., Krstajić, N., Trasatti, S. Reply to “note on a method to interrelate inner and outer electrode areas” by H. Vogt. *Electrochim. Acta* **1994**, *39* (16), 2359–2362.
- (236) Chang, K.H., Hu, C.C., Chou, C.Y. Textural and capacitive characteristics of hydrothermally derived RuO₂·xH₂O nanocrystallites: independent control of crystal size and water content. *Chem. Mater.* **2007**, *19* (8), 2112-2119.
- (237) Lee, J.S.M., Wu, T.H., Alston, B.M., Briggs, M.E., Hasell, T., Hu, C.C., Cooper, A.I. Porosity-engineered carbons for supercapacitive energy storage using conjugated microporous polymer precursors. *J. Mater. Chem. A* **2016**, *4* (20), 7665–7673.
- (238) Bu, I.Y.Y., Huang, R. Fabrication of CuO-decorated reduced graphene oxide nanosheets for supercapacitor applications. *Ceram. Int.* **2017**, *43* (1), 45–50.
- (239) Singh, P.K., Das, A.K., Hatui, G., Nayak, G.C. Shape controlled green synthesis of CuO

- nanoparticles through ultrasonic assisted electrochemical discharge process and its application for supercapacitor. *Mater. Chem. Phys.* **2017**, *198*, 16–34.
- (240) Wu, F.C., Tseng, R.L., Hu, C.C., Wang, C.C. The capacitive characteristics of activated carbons-comparisons of the activation methods on the pore structure and effects of the pore structure and electrolyte on the capacitive performance. *J. Power Sources* **2006**, *159* (2), 1532–1542.
- (241) Chae, J.H., Chen, G.Z. Influences of ions and temperature on performance of carbon nanoparticles in supercapacitors with neutral aqueous electrolytes. *Particuology* **2014**, *15*, 9–17.
- (242) Lu, J., Xu, W., Li, S., Liu, W., Javed, M. S., Liu, G., Hu, C. Rational design of CuO nanostructures grown on carbon fiber fabrics with enhanced electrochemical performance for flexible supercapacitor. *J. Mater. Sci.* **2018**, *53* (1), 739–748.
- (243) Zhao, T., Yang, W., Ji, X., Jin, W., Hu, J., Li, T. In-situ synthesis of expanded graphite embedded with CuO nanospheres coated with carbon for supercapacitors. *Appl. Surf. Sci.* **2017**, *460*, 58–64.
- (244) Iro, Z.S., Subramani, C., Dash, S.S. A brief review on electrode materials for supercapacitor. *Int. J. Electrochem. Sci.* **2016**, *11* (12), 10628–10643.
- (245) Park, S., Boo, H., Chung, T.D. Electrochemical non-enzymatic glucose sensors. *Anal. Chim. Acta* **2006**, *556* (1), 46–57.
- (246) Velmurugan, M., Karikalan, N., Chen, S.M. Synthesis and characterizations of biscuit-like copper oxide for the non-enzymatic glucose sensor applications. *J. Colloid Interface Sci.* **2017**, *493*, 349–355.
- (247) Ahmad, R., Tripathy, N., Ahn, M.S., Bhat, K.S., Mahmoudi, T., Wang, Y., Yoo, J.Y., Kwon, D.W., Yang, H.Y., Hahn, Y.B. Highly efficient non-enzymatic glucose sensor based on CuO modified vertically-grown ZnO nanorods on electrode. *Sci. Rep.* **2017**, *7* (1), 2–11.
- (248) Wang, W., Zhang, L., Tong, S., Li, X., Song, W. Three-dimensional network films of electrospun copper oxide nanofibers for glucose determination. *Biosens. Bioelectron.* **2009**, *25* (4), 708–714.
- (249) Sun, S., Zhang, X., Sun, Y., Yang, S., Song, X., Yang, Z. Hierarchical CuO nanoflowers: water-required synthesis and their application in a nonenzymatic glucose biosensor. *Phys. Chem. Chem. Phys.* **2013**, *15* (26), 10904.
- (250) Meher, S.K., Rao, G.R. Archetypal sandwich-structured CuO for high performance non-enzymatic sensing of glucose. *Nanoscale.* **2013**, *5* (5), 2089–2099.
- (251) Singh, S., Lee, S., Kang, H., Lee, J., Baik, S. Thermoelectric power waves from stored chemical

- energy. *Energy Storage Mater.* **2016**, *3*, 55–65.
- (252) Li, Z., Chen, Y., Xin, Y., Zhang, Z. Sensitive electrochemical nonenzymatic glucose sensing based on anodized CuO nanowires on three-dimensional porous copper foam. *Sci. Rep.* **2015**, *5* (1), 16115.
- (253) Liu, X.W., Pan, P., Zhang, Z.M., Guo, F., Yang, Z.C., Wei, J., Wei, Z. Ordered self-assembly of screen-printed flower-like CuO and CuO/MWCNTs modified graphite electrodes and applications in non-enzymatic glucose sensor. *J. Electroanal. Chem.* **2016**, *763*, 37–44.
- (254) Hsu, Y.W., Hsu, T.K., Sun, C.L., Nien, Y.T., Pu, N.W., Ger, M.D. Synthesis of CuO/graphene nanocomposites for nonenzymatic electrochemical glucose biosensor applications. *Electrochim. Acta.* **2012**, *82*, 152–157.
- (255) Meng, F., Shi, W., Sun, Y., Zhu, X., Wu, G., Ruan, C., Liu, X., Ge, D. Nonenzymatic biosensor based on Cu(x)O nanoparticles deposited on polypyrrole nanowires for improving detection range. *Biosens. Bioelectron.* **2013**, *42*, 141–147.
- (256) Zhang, J., Zhu, X., Dong, H., Zhang, X., Wang, W., Chen, Z. In situ growth cupric oxide nanoparticles on carbon nanofibers for sensitive nonenzymatic sensing of glucose. *Electrochim. Acta.* **2013**, *105*, 433–438.
- (257) Jiang, L.C., Zhang, W.D. A highly sensitive nonenzymatic glucose sensor based on CuO nanoparticles-modified carbon nanotube electrode. *Biosens. Bioelectron.* **2010**, *25* (6), 1402–1407.
- (258) Zhang, Y., Liu, Y., Su, L., Zhang, Z., Huo, D., Hou, C., Lei, Y. CuO nanowires based sensitive and selective non-enzymatic glucose detection. *Sensors Actuators B Chem.* **2014**, *191*, 86–93.
- (259) Wang, G., Wei, Y., Zhang, W., Zhang, X., Fang, B., Wang, L. Enzyme-free amperometric sensing of glucose using Cu-CuO nanowire composites. *Microchim. Acta.* **2010**, *168* (1–2), 87–92.
- (260) Wang, J., Zhang, W.D. Fabrication of CuO nanoplatelets for highly sensitive enzyme-free determination of glucose. *Electrochim. Acta.* **2011**, *56* (22), 7510–7516.
- (261) Singh, A., Akhtar, M.A., Chandra, A. Trade-off between capacitance and cycling at elevated temperatures in redox additive aqueous electrolyte based high performance asymmetric supercapacitors. *Electrochim. Acta* **2017**, *229*, 291–298.
- (262) Roberts, A.J., Slade, R.C. Temperature dependence of key performance indicators for aqueous supercapacitors containing nanostructured birnessite. *ECS Transactions*, **2012**, *41*, 65–80.

- (263) Baral, A., Sarangi, C.K., Tripathy, B.C., Bhattacharya, I.N., Subbaiah, T. Copper electrodeposition from sulfate solutions-effects of selenium. *Hydrometallurgy* **2014**, *146*, 8–14.
- (264) Yu, Z., Tetard, L., Zhai, L., Thomas, J. Supercapacitor electrode materials: nanostructures from 0 to 3 dimensions. *Energy Environ. Sci.* **2015**, *8*, 702–730.
- (265) Ke, Q., Wang, J. Graphene-based materials for supercapacitor electrodes – A review. *J. Materiomics* **2016**, *2(1)*, 37-54.
- (266) Hameed, M.U., Khan, Y., Ali, S., Wu, Z., Dar, S.U., Song, H., Ahmad, A., Chen, Y. Tween-80 guided CuO nanostructures: morphology-dependent performance for lithium ion batteries. *Ceram. Int.* **2017**, *43*, 741–748.
- (267) Shi, L., Fu, X., Fan, C., Yu, S., Qian, G., Wang, Z. Carbonate-assisted hydrothermal synthesis of porous, hierarchical CuO microspheres and CuO/GO for high-performance lithium-ion battery anodes. *RSC Adv.* **2015**, *5*, 85179–85186.
- (268) Eftekhari, A. Mechanism of ultrafast supercapacitors. *J. Mater. Chem. A* **2018**, *6*, 2866–2876.
- (269) Song, J., Bazant, M.Z. Effects of nanoparticle geometry and size distribution on diffusion impedance of battery electrodes. *J. Electrochem. Soc.* **2012**, *160*, A15–A24.
- (270) Liu, M., Lin, M.C., Wang, C. Enhancements of thermal conductivities with Cu, CuO, and carbon nanotube nanofluids and application of MWNT/water nanofluid on a water chiller system. *Nanoscale Res. Lett.* **2011**, *6*, 297.
- (271) Gupta, R.K., Candler, J., Palchoudhury, S., Ramasamy, K., Gupta, B.K. Flexible and high performance supercapacitors based on NiCo_2O_4 for wide temperature range applications. *Sci. Rep.* **2015**, *5*, 15265.
- (272) Uematsu, M., Frank, E.U. Static dielectric constant of water and steam. *J. Phys. Chem.* **1980**, *9*, 1291–1306.
- (273) Tang, C.-L., Wei, X., Jiang, Y.-M., Wu, X.-Y., Han, L., Wang, K.-X., Chen, J.-S. Cobalt-doped MnO_2 hierarchical yolk-shell spheres with improved supercapacitive performance. *J. Phys. Chem. C* **2015**, *119*, 8465–8471.
- (274) Wang, Q., Liu, S., Sun, H., Lu, Q. Synthesis of a flower-like Co-doped $\text{Ni}(\text{OH})_2$ composite for high-performance supercapacitors. *RSC Adv.* **2015**, *5*, 48181–48186.
- (275) Durai, G., Kuppasami, P., Viswanathan, K. Investigation on microstructure and improved supercapacitive performance of Mn doped CuO thin films prepared by reactive radio frequency

magnetron sputtering. *J. Mater. Sci. Mater. Electron.* **2018**, 29, 2051–2058.

- (276) Ram, M. Transport phenomena in the compound: $\text{LiFe}_{1/2}\text{Mn}_{1/2}\text{VO}_4$. *Solid State Ionics.* **2008**, 178, 1922–1929.

